NUMERICAL AND EXPERIMENTAL INVESTIGATION OF ORGANIC NANOMATERIALS FOR THERMAL ENERGY STORAGE AND FOR CONCENTRATING SOLAR POWER APPLICATIONS

A Dissertation

by

BYEONGNAM JO

Submitted to the Office of Graduate Studies of
Texas A&M University
in partial fulfillment of the requirements for the degree of

DOCTOR OF PHILOSOPHY

August 2012

Major Subject: Mechanical Engineering

Numerical and experimental investigation of organic nanomaterials for thermal energy storage and for concentrating solar power applications

NUMERICAL AND EXPERIMENTAL INVESTIGATION OF ORGANIC NANOMATERIALS FOR THERMAL ENERGY STORAGE AND FOR CONCENTRATING SOLAR POWER APPLICATIONS

A Dissertation

by

BYEONGNAM JO

Submitted to the Office of Graduate Studies of
Texas A&M University
in partial fulfillment of the requirements for the degree of

DOCTOR OF PHILOSOPHY

Approved by:

Chair of Committee,	Debjyoti Banerjee
Committee Members,	Kamran Entesari
	Devesh Ranjan
	Arun R. Srinivasa
Head of Department,	Jerald A. Caton

August 2012

Major Subject: Mechanical Engineering

ABSTRACT

Numerical and Experimental Investigation of Organic Nanomaterials for Thermal Energy Storage and for Concentrating Solar Power Applications. (August 2012)

Byeongnam Jo, B.S.; M.S., Ajou University;

M.S., University of Minnesota - Twin Cities

Chair of Advisory Committee: Dr. Debjyoti Banerjee

Concentrating solar power (CSP) plants are used to harness solar thermal energy to generate electricity. Thermal energy storage (TES) systems enable the CSP plants to be operated during disruptions in solar energy input and furthermore to extend the operating hours of the plants to match the diurnal peak in solar energy input (that typically occurs between noon to 3 p.m.) with the peak in in daily demand for power consumption (that typically occurs between 4 p.m. to 7 p.m.). Molten salts and their eutectics are employed as TES media to store the thermal energy from the solar radiation, due to their low vapor pressure at elevated temperatures. However, the molten salts have relatively poor thermo-physical properties which are an impediment to their application in TES.

In this study, the specific heat capacity of the molten salt mixture was enhanced dramatically by doping with nanoparticles. Differential scanning calorimetry was used to measure the specific heat capacity of these nanomaterial samples and the latent heat of fusion. The specific heat capacity was measured in both solid and liquid phase for these

samples. Furthermore, the rheological characteristics of the nanofluids were also studied using a concentric parallel plate (corn and plate) rheometer.

Binary carbonate salt mixtures were used as the base material (solvent) and mixed with organic nanoparticles such as carbon nanotubes, C_{60}, and graphite nanoparticles. Various parameters were varied in this study: the nanoparticle materials, mass concentrations of the nanoparticles, the composition of the solvent materials (salt mixture ratios), and the synthesis protocols for the mixtures.

Also, computational studies were performed using molecular dynamics (MD) simulations to estimate the interfacial thermal resistances between a nanoparticle and surrounding molten salt molecules. This enabled the estimation of the optimum nanoparticle size for performing the experimental measurements.

The measurements showed that the specific heat capacity of the molten salt nanomaterials was enhanced significantly (~ 20-90 %) on mixing with nanoparticles at minute concentrations (0.1-5 % mass concentration). It was observed that the nanomaterial properties are strongly sensitive to small variations in the protocols implemented in this study. This was also evident for the rheological properties of the nanomaterials in the molten state (liquid phase, i.e. for “nanofluids”).

Theoretical models demonstrate that the chemical properties (and to a lesser extent the thermo-physical properties) as well as composition of the solvent material plays a dominant role in determining the level of enhancement of the resultant values of the specific heat capacity when doped with nanoparticles. Chemical functionalization of nanoparticles can be used to optimize the resulting properties of the nanomaterials.

DEDICATION

I dedicate this dissertation to my beloved family and my friends.

ACKNOWLEDGEMENTS

I wish to express my deepest gratitude to my advisor, Dr. Banerjee for his guidance and support. I also thank my committee members, Dr. Kamran Entesari, Dr. Devesh Ranjan, and Dr. Arun Srinivasa for their guidance and advice.

Special thanks go to Dr. Robert Taylor in the Department of Veterinary Integrative Bioscience for ICP analysis. To Mr. Hyun-eun Kwak, Mr. Jiwon Yu, Mr. Hongjoo Yang for all the discussion and assistance. I would also like to extend my gratitude to Dr. Jaisuk Yoo and Dr. Hyun-Jung Kim at Ajou University. You have encouraged me with invaluable advice.

I would like to thank to Department of Energy (DOE) - Solar Energy Technology Program (SETP) - for sponsoring the research project for my Ph.D. thesis. During the completion of my Ph.D. thesis at Texas A&M University - I was also supported from the following research projects managed by Dr. Banerjee at the Texas Engineering Experiment Station (TEES) – which I gratefully acknowledge: Qatar National Research Foundation (QNRF); ADA Technologies, Inc. through the Small-Business Technology Transfer & Research (STTR) Program – Phase I, by the Office of Naval Research (ONR) under the aegis of Program Manager – Dr. Igancio Pereze De Leon; and the National Science Foundation (NSF-CBET/TTTP) under the aegis of Program Manager – Dr. Sumanta Acharyya.

To my family – you have always believed me and supported me. I would not complete my Doctoral studies without you.

NOMENCLATURE

A	surface area of nanoparticle
a	radius of primary nanoparticle
a_a	radius of nanoparticle aggregation
C	heat capacity [J/K]
c_p	specific heat capacity [J/g·K]
E	intermolecular interaction energy [kcal/mole]
K_s	bonding coefficient (stretching) [kcal/mole·Å^2]
K_b	bonding coefficient (bending) [kcal/mole·radian^2]
K_t	bonding coefficient (torsion) [kcal/mole]
m	mass [g]
q_i, q_j	charge [C]
Δq	heat flow difference [mW]
c_p	specific heat capacity [J/g·K]
R	interfacial thermal resistance [m^2·K/W]
r	distance [Å]
r_0	equilibrium bond distance [Å]
r_m	distance at which potential energy is minimum [Å]
T	temperature [K or $^\circ$C]
t	T/1000 [K]
u	potential energy
V	volume of nanoparticle
ε	depth of potential well [kcal/mole]
ϕ	volume fraction of nanoparticle
η	viscosity [Pa·s]
$[\eta]$	intrinsic viscosity [1/volume fraction]
φ_m	maximum concentration

φ_a	effective volume fraction of aggregations
θ	bond angle [radian]
θ_0	equilibrium value of the angle [radian]
ρ	density [g/cm^3]
σ	distance at which potential energy is equal to zero [Å]
τ	time constant [s]

subscripts

b	baseline (empty pan)
bf	base fluid (base material)
n	nanoparticle
nf	nanofluid
r	relative value
s	sample
st	standard material

TABLE OF CONTENTS

Page

LIST OF FIGURES

Page

LIST OF TABLES

Page

1. INTRODUCTION

1.1 Concentrating solar thermal power plants

Among the various renewable energy resources, solar thermal power is considered to be economically attractive option [1]. Solar thermal power plants, also known as concentrating solar power (CSP) plants, are comprised of four elements: a concentrator, a receiver with heat transfer fluid (HTF), thermal energy storage (TES) media, and power conversion module [1]. Although many different combinations of the systems are possible, there are three main types of the CSP plants. Fig. 1.1 illustrates [1] each type of CSP plants: parabolic trough, central receiver or solar tower, and parabolic dish.

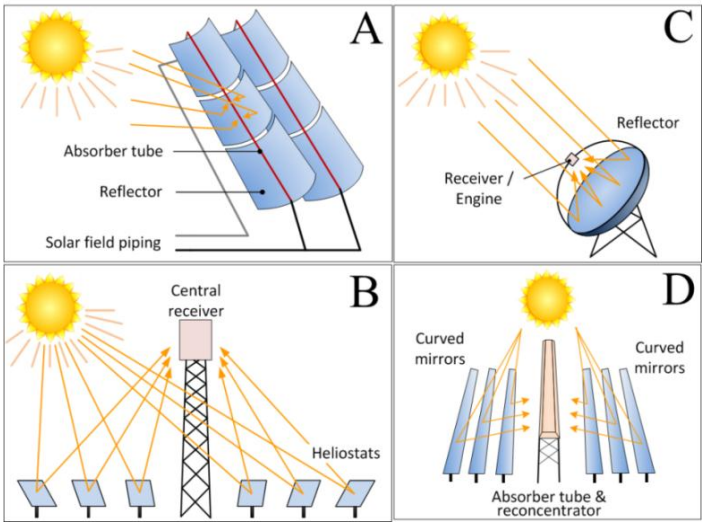

Fig. 1.1 Illustrations of current technologies for CSP plants [1]

Note: Redrawn with permission from *Global Concentrating Solar Power Outlook 09*, by Dr. C. Richter, S. Teske, and R. Short, 2009, Greenpeace International, Solar Paces, and ESTELA, Amsterdam, Copyright 2009 by Greenpeace/Markel Redondo.

This dissertation follows the style of Journal of Heat Transfer.

Parabolic troughs concentrate sunlight on to stainless steel pipes (Absorber tubes) using curved mirror reflectors (parabolic trough-shaped mirror reflectors). The absorber tubes are placed in the reflectors' focal line. Typically, oil such as Therminol VP-1 is used as HTF. With this concentrating method, the oil can be heated to approximately 400 ℃ for generating superheated steam which is used to generate electricity by driving steam turbines. In conventional solar thermal power plants, use of thermal storage systems is not in vogue yet.

In solar towers, hundreds or thousands of reflectors (called heliostats) focus the sunlight on to a central receiver that is placed on top of a tower. Hear transfer fluid (HTF) is passed through the receiver to collect the energy collected (and focused) by the heliostats. In addition, the usage of the thermal energy storage (TES) systems enables the power plants to be operated during night time (after the sun sets) or during periods of disruption in solar energy input (e.g., during cloud cover). The solar tower concept enables higher operating temperatures to be reached, and thereby enhances the efficiency of thermal energy conversion to electricity. Some plants commercially in operation use direct steam generation (DSG) in the receiver. Alternate strategies involve using molten salts or oils as HTF and/or TES media. Recently, due to the advantages conferred by the use of molten salts (e.g., molten salts enable the operating temperature of the plants to be increased), these salts and their eutectic mixtures have been employed in various solar tower systems. Typically nitrate salt eutectic (composed of eutectic mixture of sodium nitrate and potassium nitrate) has been used in many conventional solar thermal power plants.

Parabolic dish systems use a parabolic dish-shaped reflector to focus the sunlight on a receiver that is placed in front of the dish. The entire device tracks the sun in one uniform motion. Therefore, the dish platform provides the highest conversion efficiencies for transforming solar radiation to electricity. Typically, every dish unit is equipped with an independent engine in the receiver unit that operates on a Stirling cycle.

Solar thermal power plants were built and operated in various countries for pilot testing or for commercial operations. Table 1.1 [1] shows information about solar thermal power plants that were built in various countries in the early 1980s. These plants failed to reach the targeted performance levels. Since the mid 1980s, however, various CSP plants were constructed in the United States and in Spain that were commercially successful.

The factors necessary for reducing the generation costs and for scaling up the size of the CSP plants for mass production need detailed investigation. Primarily the problems arise from the unique characteristics of the power source, i.e., the sun. Since the CSP systems perform direct conversion of sunlight, they are prone to disruptions due to weather conditions and seasonal/diurnal variations in solar insolation. Also, there is another issue that arises from the difference in duration/time between the peak in power generation periods and the peak in periods of peak demand for electricity [2] (as shown in Fig. 1.2).

Table 1.1 Early solar thermal power plants

Name	Location	Size (MWe)	Type, Heat transfer fluids & Storage medium	Start-up date
Aurelios	Adrano, Sicily	1	Tower, Water-Steam	1981
SSPS/CRS	Almeria, Spain	0.5	Tower, sodium	1981
SSPS/DCS	Almeria, Spain	0.5	Trough,	1981
Sunshine	Nio, Japan	1	Tower, Water-Steam	1981
Solar One	California, USA	10	Tower, Water-Steam	1982
Themis	Targasonne, France	2.5	Tower, Molten salt	1982
CESA-1	Almeria, Spain	1	Tower, Water-Steam	1983
MSEE	Albuquerque, USA	0.75	Tower, Molten salt	1984
SEGS-1	California, USA	14	Trough, Oil	1984
Vanguard 1	USA	0.025	Dish, Hydrogen	1984
MDA	USA	0.025	Dish, Hydrogen	1984
C3C-5	Crimea, Russia	5	Tower, Water-Steam	1985

TES applications can be used as a buffer to match the peaks in demand and supply for the CSP systems. The heat energy from the solar radiation can be stored into the TES media (such as synthetic oil or molten salts) during the daytime. The CSP plants can be designed to transform the stored heat energy to electricity for up to eight hours after the sun sets. In other words, TES devices can be used for extending the operation of the CSP plants during disruptions in the availability of the energy source. Fig. 1.3 shows the effect of the storage systems in combination with hybridization [3], which extends the operation time - thereby delivering power during the periods of peak demand for

electricity. Additionally by utilizing energy storage devices the unit cost of electricity can be reduced and the stability of the CSP plants can be increased (i.e. better operational reliability can be realized).

The thermal energy storage system can also enable the operating temperature of CSP plants to be increased. Since the efficiency of thermodynamic cycles can be augmented by increasing the operating temperature, the overall efficiency of CSP plants can be also enhanced by increasing the operating temperature of the TES units. Nevertheless, conventional TES materials (such as synthetic oil) have an upper temperature limit of approximately 400 ℃ due to chemical stability issues as well as due to high vapor pressures at the elevated temperatures [4, 5]. Hence, molten salts and their eutectics have been employed as storage media in the CSP plants. These Molten salts typically melt at temperatures exceeding 200 ℃ and have low vapor pressures at elevated temperatures.

Hence, molten salts are considered to be an attractive option for reducing the generating cost of electricity. However, their relatively poor thermo-physical properties (e.g. thermal conductivity, specific heat capacity, and viscosity) are an impediment to their application in CSP plants. Therefore, enhancing the thermo-physical properties of the molten salts is the motivation of the proposed investigation. For example, enhanced thermo-physical properties increase the overall efficiency of the CSP plants and, hence, reduce the unit cost for the electricity generation.

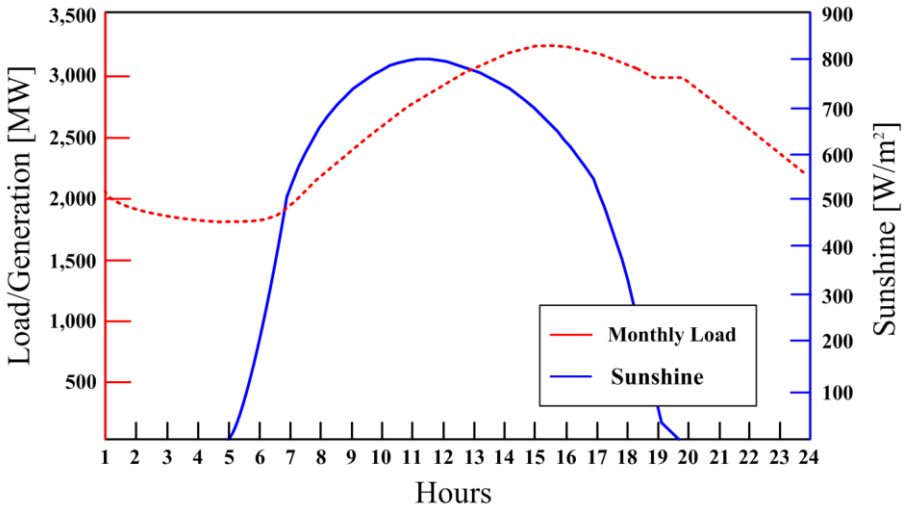

Fig. 1.2 Sun radiation profile and electricity demand profile

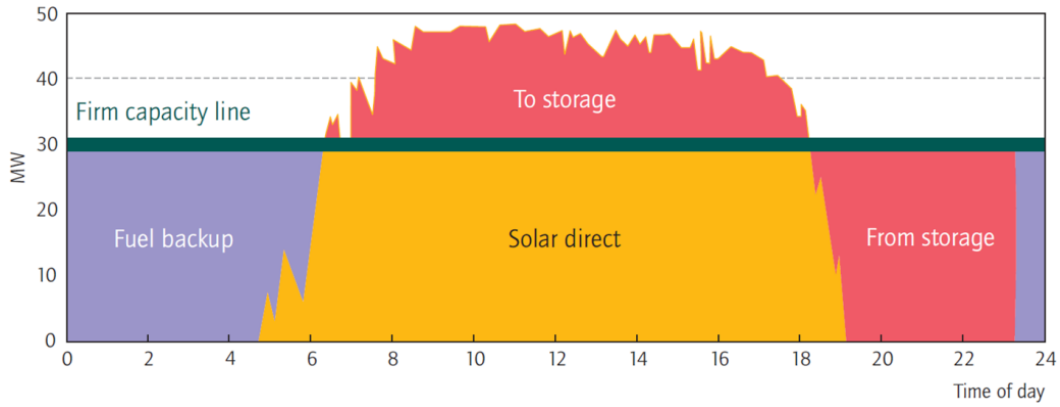

Fig. 1.3 Effect of combination of storage and hybridization in CSP plants [3]

Note: Reprinted with permission from Technology Roadmap – Concentrating Solar Power, by Nobuo Tanaka, 2010, OECD/International Energy Agency (Figure 4, Page 16), Paris, Copyright 2010 by OECD/International Energy Agency

The ultimate objective is to enable solar thermal power to be competitive with conventional power sources (e.g., coal fired power plants). In addition, exploration of alternate salt materials and their mixtures are needed for the development of next

generation of CSP plants. As mentioned before, typically, a eutectic of sodium and potassium nitrate are used in conventional CSP systems. With development in the receiver technologies and larger scale plants, however, diverse options for storage media are required to optimize the operation of the solar power plants.

1.2 Nanofluids

Solvents dispersed with stable and uniform dispersion of nanoparticles are called nanofluids. Typically the particle sizes are less than 100 nm and the dispersions are obtained at very low mass concentrations (e.g. typically less than 1 - 5 %). Nanofluids were reported for the anomalous enhancements in their thermo-physical properties. In this section a brief literature review is presented on the thermo-physical properties of nanofluids.

1.2.1 Thermal conductivity

A significant number of studies were reported on the anomalous enhancement of the thermal conductivity of the nanofluids. Typically, the transient hot wire method [6-10] was mainly used for measuring the thermal conductivity of nanofluids. Other studies employed alternate methods such as steady-state parallel-plate technique, temperature oscillation technique, micro-hot strip method, and optical beam deflection technique [11-14]. The various parameters that affect properties of nanoparticle and the thermal conductivity of nanofluids include temperature, volume fractions, material composition

(solvent and nanoparticle), particle size, particle shape and stability of the nanoparticle (dispersion/agglomeration).

In 1993, Masuda et al. dispersed Al_2O_3, SiO_2, and TiO_2 into water and measured thermal conductivity of those suspensions [15]. Authors of this study reported that the thermal conductivity linearly increased with the particle volume concentration. Lee et al., investigated the thermal conductivity enhancement at room temperature by dispersing Al_2O_3 and CuO in water and ethylene glycol (EG) [16]. They also reported a linear relationship between the thermal conductivity and particle volume concentration. Various other studies involving water or EG as base fluids concluded that the thermal conductivity of nanofluids linearly increases with the volume concentration [11, 15, 16]. However, some of these studies reported a nonlinear trend between thermal conductivity and the volume concentration, especially at low concentrations [17, 18].

In addition, material properties of the nanoparticles were also observed to affect the thermal property of the nanofluids. According to the study by Lee et al. [16], CuO nanofluids showed higher enhancement in thermal conductivity than Al_2O_3 nanofluids. In contrast, the thermal conductivity of the Al_2O_3 nanoparticles is higher than that of the CuO nanoparticles. Hence, it can be presumed that the thermal conductivity of the nanoparticle material may not be the dominant parameter for enhancing the thermo-physical properties of the solvent. Chopkar and collaborators examined the effect of nanoparticle type with Al_2Cu and Ag_2Al in water and EG [19]. A slightly higher enhancement was obtained with Ag_2Al nanoparticles. Additionally, various kinds of carbon nanotubes such as single-walled carbon nanotubes (SWNT), double-walled

carbon nanotubes (DWNT), and multi-walled carbon nanotubes (MWNT) have been used for synthesis of nanofluids and their conductivity measurements due to their outstanding thermal properties and unique characteristics, such as tunable material properties [18, 20].

In addition to the factors introduced above, various other parameters were explored to determine the dominant mechanisms that affect the thermo-physical properties of nanofluids. In particular, the effects of particle size, particle clustering (agglomeration), and pH (or dispersants such as surfactants) can affect nanoparticle dispersion. Hence, the exploration of these parameters is meaningful for understanding the inherent mechanisms responsible for the anomalous enhancement of the material properties (thermo-physical properties) of these solvent materials [6, 20-22]. A list of previous experimental studies is summarized in Table 1.2. In addition to these experimental studies, a significant number of theoretical studies were also performed [23-30]. A good review of these experimental and numerical studies was presented by Wang and Mujumdar [20].

Table 1.2 Summary of experimental studies for thermal conductivity enhancement

	Particles	Base fluid[a]	Concentration [vol. %]	Particle size [nm]	Maximum Enhancement [%]
Masuda et al. (1993) [15]	Al_2O_3 SiO_2 TiO_2	Water	1.30 - 4.30 1.10 - 2.40 3.10 - 4.30	13 12 27	32.4 1.1 10.8
Lee et al. (1999) [16]	Al_2O_3 CuO	EG	1.00 - 5.00 1.00 - 4.00	38.4 23.6	18 23
Eastman et al. (2001) [31]	Cu	EG	0.01 - 0.56	< 10	41
Choi et al. (2001) [18]	MWCNT	PAO	0.04 – 1.02	25 × 50000	57
Xie et al. (2002) [32]	SiC	EG	0.89 - 3.50 1.00 - 4.00	26 sphere 600 cylinder	13 23
Xie et al. (2002) [33]	Al_2O_3	Water/EG PO/glycerol	5.00 5.00	60.4	23/29 38/27
Das et al. (2003) [34]	Al_2O_3 CuO	Water	1.00 - 4.00 1.00 - 4.00	38.4 27.6	24 36
Assael et al. (2005) [35]	DWCNT MWCNT	Water	0.75 - 1.00 0.60	5 (ϕ) 130 × 10000	8 34
Liu et al. (2005) [36]	MWCNT	EG EO	0.20 - 1.00 1.00 - 2.00	20 ~ 50 (ϕ)	12 30
Ding et al. (2006) [37]	MWCNT	Water	0.05 - 0.49	40 (ϕ)	79
Hong et al. (2006) [38]	Fe	EG	0.10 - 0.55	10	18
Chopkar et al. (2008) [19]	Al_2Cu Ag_2Al	Water	1.00 - 2.00 1.00 - 2.00	31/68/101 33/80/120	96/76/61 106/93/75
Turgut et al. (2009) [39]	TiO_2	Water	0.2 - 3.0	21	7.4
Mintsa et al. (2009) [40]	Al_2O_3 CuO	Water	0 - 18 0 - 16	36/47 29	31/31 24

[a] EG - ethylene glycol, EO - engine oil, PO - pump oil, PAO - polyalphaolefin

1.2.2 Viscosity

Measuring the rheological properties of nanofluids is important for determining their efficacies in thermal applications, such as heating/cooling and TES. However, only a small number of studies have been reported on the experimental measurements for the rheological behavior of nanofluids. In addition, controversies exist about the shear rate-dependent rheological properties of nanofluids. In some of the previous studies nanofluids were reported to demonstrate Newtonian behavior [33, 41-43]. Das et al. measured Newtonian behaviors for aqueous Al_2O_3 nanofluids [41] and Wang et al. also showed similar rheological behaviors for both water-Al_2O_3 and EG-Al_2O_3 nanofluids [33]. However, nanofluids were also reported to have non-Newtonian (shear thinning) behavior [37, 44-47]. Chen and Ding commented on the inconsistency in the viscosity of nanofluids in their review paper [48]. They pointed out that for certain conditions the nanofluids behave like non-Newtonian fluids. Based on the literature data on the rheological behavior of nanofluids, they summarized the parameters as the following: (1) high concentration, (2) using low viscosity fluids (e.g. water), and (3) particle shape (rod-shaped particles with large aspect ratio).

In addition to the shear rate-dependent viscosity, several other parameters were examined experimentally in prior studies reported in the literature. For example, it was reported that temperature strongly affects the viscosity of nanofluids [48]. At low shear rate, the viscosity increases with temperature. The effects of particle shape and size were also reported in the literature. Chen et al. reported that the rod-shaped nanoparticles demonstrate stronger sensitivity to shear thinning behavior than spherical nanoparticles

[47]. Additionally, He et al. observed that larger particle size resulted in larger enhancement in the viscosity of nanofluids [44]. Several theoretical models [49, 50] were explored in the literature based on classical theories of mixtures that are used for estimating the viscosity of suspensions. However, the predictions from the classical models failed to match the experimental measurement for the viscosity of nanofluids. A modified theoretical model [46, 51] was developed, which incorporated the effects of nanoparticle shape and the agglomeration of the nanoparticles.

1.2.3 Specific heat capacity

A significant number of studies have been performed to experimentally and theoretically investigated the anomalous enhancement of thermal conductivity and viscosity of nanofluids. In contrast, only a few studies have been performed to measure the specific heat capacity of nanofluids. Namburu et al. reported experimental measurements of specific heat capacity of SiO_2 nanofluids as a function of the nanoparticle concentration [52]. The specific heat capacity of nanofluids was observed to linearly decrease with increase in volume concentration. In 2008, Zhou and Ni reported the same trend of decreasing specific heat capacity for aqueous dispersion of Al_2O_3 nanoparticles [53]. Similarly, Vajjha and Das performed the measurement of the specific heat capacity for water/Ethylene Glycol based-nanofluids using nanoparticles of Al_2O_3, ZnO, and SiO_2 [54]. They also reported degradation in the specific heat capacity values compared with that of the neat solvent. Recently, Zhou and collaborators

observed similar results involving degradation of the specific heat capacity for ethylene glycol-CuO nanofluids [55].

In contrast, other studies involving non-aqueous solvents showed radical enhancements in the specific heat capacity. In 2009, Nelson et al. measured the specific heat capacity of a polyalphaolefin (PAO) nanofluid mixed with graphite nanoparticle fibers [56]. They measured a drastic enhancement of up to 50 % in the specific heat capacity values on mixing with the graphite nanoparticles at a mass concentration of 0.6 %. Most recently, Shin and Banerjee have reported the enhancement in the specific heat capacity by doping with silica nanoparticles in molten salt eutectics [57-59]. Additionally, enhancements in the specific heat capacity of molten salts-based carbon nanotubes nanofluids were also observed in both solid and liquid phase [60]. Most recently, Bridges and collaborators [61] reported that the volumetric heat capacity of an ionic liquid was enhanced by doping with alumina nanoparticles by up to 45 %. These nanomaterials were termed as “NEIL” or “Nanoparticle Enhanced Ionic Liquids”. For the same solvent, however, the volumetric heat capacity was not increased by using carbon black nanoparticles.

In summary, all of the studies in which the decrease of the specific heat capacity was reported used conventional fluids such as water or EG as the solvent medium for nanofluids. In contrast, the studies which reported the enhancement of the specific heat capacity (or volumetric heat capacity) values employed different solvent materials, such as carbonate molten salt eutectic. Hence, the material properties of the solvent are expected to be the dominant parameter rather than that of the nanoparticles. Therefore,

additional studies are needed to elucidate the nature of specific heat capacity variation for nanomaterials or nanofluids.

1.2.4 Prior investigations at the Multi-Phase Flows and Heat Transfer Laboratory

Prior results from a number of investigations involving nanofluids – that were performed at the Multi-Phase Flows and Heat Transfer Laboratory (MPFHTL) and were reported in the literature - are briefly summarized in this subsection.

Using nano-coatings the phase change heat transfer was augmented significantly for both pool boiling and flow boiling [62-67]. In those studies, the pool boiling heat flux values on heater surfaces with carbon nanotube (CNT) coatings were enhanced (for both nucleate and film boiling regimes). Surprisingly, higher levels of enhancements (compared to CNT coatings) were observed for the pool boiling heat flux when using silicon nano-pillar structures [67].

Subsequently, Singh [68], Unnikrishnan et al [69] and Singh et al. [70] showed that the thermal interfacial resistance (or "Kapitza resistance") for CNT – with respect to the working fluid (or solvent liquid) was 1000 times higher than that for the silicon nano-fins. Hence, Kapitza resistance was identified as the dominant parameter for determining the level of heat flux enhancement for the nano-coatings.

A number of studies exploring the thermo-physical properties of nanomaterials (i.e., nanofluids) were also reported. In addition to the publications cited in the previous section [56-59] about the specific heat capacity for the nanofluids, such as PAO-graphite

nanofluid and the molten salt-inorganic nanofluids, a diverse range of investigations were also performed to study (experimentally measure) the:

(1) Specific heat capacity of various nanofluids or nanomaterials [60, 71-80]; and

(2) Viscosity of both aqueous nanofluids and molten salt nanofluids [81, 82].

Also, a preliminary analytical model for calculating the specific heat capacity of nanofluids was developed by modifying the simple mixture rule to include the contribution to the internal energy (of the nanofluid suspension) form a "compressed phase" of the solvent molecules that is induced on the surface of the nanoparticles [58, 83, 84].

Aqueous nanofluids were also investigated for their efficacy in enhancing convective heat transfer in microchannels [85]. An array of temperature nano-sensors or Thin Film Thermocouples (TFT) was used to calculate the axial temperature gradient in the flow direction and estimate the convective heat transfer [63-65, 86-89]. Hence, in this study the effects of several parameters on the thermal performance were also explored - such as by varying the - nanoparticle material, concentration of the nanoparticles, duration of experimentation (to explore the effect of precipitation of nanoparticles on the flow conduits as well as the heat exchanging surfaces), flow rates and surface temperature [85].

To complement these experimental studies, computational studies were conducted by using Molecular Dynamics (MD) simulations. From the MD simulations, the Kapitza resistances of both organic and inorganic nanoparticles were estimated for different

solvent compositions (e.g., organic coolants or binary molten salt mixtures) [68, 70, 90] . This is explored in more detail in the next subsection.

1.3 Molecular dynamics (MD) simulations

Various transport mechanisms have been proposed in the literature to explore the anomalous thermo-physical properties of nanofluids, which include: Brownian motion of nanoparticles, interfacial layering of liquid molecules, nanoparticle clustering, and near field radiation [23, 26-29, 91-94]. Among those, the interfacial layering of liquid molecules is considered to be a unique feature that is responsible for the enhancement of the thermal conductivity of nanofluids. In order to understand this transport mechanism, interactions between the nanoparticles and the fluid molecules should be studied. However, it is difficult to observe the liquid layering phenomena on the surface of nanoparticles. It is also difficult to measure the thickness of the liquid layer that form a distinct, yet diffuse phase. The distinct layer (or phase) of liquid molecules that forms on the surface of a nanoparticles also affects the interfacial thermal resistance between the nanoparticle and the solvent. Thus, molecular dynamics (MD) simulations have often replaced experimental measurements for estimating the thermal resistance between the nanoparticles and surrounding liquid molecules as well as for estimating the thickness of the distinct liquid layer that forms on the nanoparticle surface.

The interfacial thermal resistance (also known as thermal boundary resistance or Kapitza resistance) is an essential feature that is a significant parameter for nano-scale

heat transfer. Due to their exceptional thermal property, single-walled carbon nanotubes (SWNT) have been investigated in numerous studies using MD simulation. In 2000, Che et al. [95] studied the thermal conductivity of carbon nanotubes as a function of their structure, defects and vacancies, by utilizing the empirical bond order dependent force field. Since then, temperature dependence of the thermal conductivity of SWNT was calculated from 100 K to 500 K with the Tersoff-Brenner potential [96]. Guo and collaborators [97] compared the specific heat capacity of SWNT using various force fields. These authors also studied the temperature dependent behavior of the specific heat capacity of SWNT. MD simulations for the effect of the morphology of the surfactant aggregates of several carbon nanotubes on the specific heat capacity also performed for room temperature condition [98].

Huxtable et al. [99] experimentally measured the interfacial thermal conductance (reciprocal of interfacial thermal resistance) of carbon nanotubes suspended in water using sodium dodecyl sulfate (SDS) micelles as dispersants. The authors performed the measurements by using picosecond transient optical absorption technique. In addition to the experimental measurements, they performed MD simulations for estimating the interfacial thermal resistance of the SWNT-octane interface [99]. In 2004, Maruyama et al. performed MD simulations for heat transfer between nanotubes in a bundle and between a nanotube and water [100]. Based on the heat transfer rates, they calculated thermal boundary resistances for both cases. The interfacial thermal resistance of SWNT was also predicted by MD simulations by using a classical approach for thermal modeling between two nanotubes in mutual contact [101]. MD simulations of other

allotropes of carbon as well as carbon nanotubes were also performed. In 2006, Li et al. [102] conducted MD simulations to study the hydration of C_{60} fullerenes, carbon nanotubes, and graphene sheets in an aqueous solution and to explore the nature of water-induced interactions between these particles. Singh and Singh et al. estimated the thermal resistance of carbon nanotubes for various coolants (water, ethyl alcohol and 1-Hexene) [68, 70].

MD simulations for molten salts have also been performed for various salts. Habasaki performed MD simulation with Li_2CO_3 and Na_2CO_3 in liquid state to clarify the change of the predominant sites of alkali ions and their related properties [103]. In 2000, structural features and dynamical properties for molten Li_2CO_3 - K_2CO_3 mixtures were obtained by non-equilibrium MD simulations [104]. Using the same molten salt composition, Costa performed MD simulations to verify the effect of polarization on the structure and dynamics of the liquid eutectic, as a function of the chemical composition of each salt [105]. Carbon particles such as carbon nanotubes and fullerene have unique structures and are well known for their distinctive and tunable material properties (especially in the thermal and the electrical properties). A number of computational studies for these particles were conducted. However, the interactions of the carbon particles with molten salt eutectics have not been investigated, in as much detail. Hence, this forms the motivation for performing the MD simulations involving organic nanoparticles in this study.

The results from the study by Singh et al. [70] and for the MD simulations involving molten salt suspension of nanoparticles [90] showed that the nanoparticles induce the

formation of a "compressed phase" of solvent molecules on the surface of the nanoparticles. The density of the compressed phase was predicted to match the solid phase density of the solvent material. In addition, the MD simulations predicted that the nanoparticle can induce a concentration gradient of the molecules (for a mixture of different materials or species constituting the solvent phase). The nanoparticle is likely to have higher physical/ chemical affinity (arising from Van der Waals interactions, ionic interactions, and the combination thereof) for a particular species ("preferred species") in the solvent mixture – causing a higher concentration of the preferred species on the nanoparticle surface – compared to in the bulk.

The concentration of the preferred species on the nanoparticle surface was also predicted to vary with the changes in the composition of the bulk phase of the solvent (or neat solvent, i.e., without the nanoparticle present). The changes in concentration of the preferred species on the nanoparticle surface are also likely to cause minor perturbations in the density of the resultant compressed phase that forms on the surface of the nanoparticle. Such a complex interaction is also likely to affect the material properties and transport properties on the molecular scale for the nanoparticle suspension. This is also likely to cause spatial variation in material properties in an around (in the vicinity) of the nanoparticles in the mixture.

1.4 Objective of this study

The objective of this study is to investigate the change in the thermo-physical properties of molten salt-bases solvents when doped with organic nanoparticles.

1.5 Hypothesis

A major portion of the literature reports on the enhanced thermal conductivity of nanofluids focused on the material properties of the nanoparticles while considering the solvent material properties to be of secondary importance. Closer examination of the previous literature reports (particularly MD simulations), however, alludes to the potentially dominant role of the material properties of the solvent molecules in determining the resultant material properties of the mixture.

Therefore, the hypothesis developed in this study is that the material properties of the solvent molecules can significantly affect the properties of (in particular - the specific heat capacity) of molten salt nanomaterials (or nanofluids).

This phenomenon is especially apparent, when considering the materials properties of the “compressed phase” of the solvent molecules that are induced on the surface of the nanoparticles. Hence, the smaller the size of the nanoparticles – larger is the surface area of the nanoparticles (for the same mass fraction of nanoparticles) – which in turn can amplify the mass fraction of the compressed phase – and in turn – enable larger proportion of the contributions to the resultant material properties of the nanomaterial samples.

1.6 Overview of this study

The aim of this study is to measure the thermo-physical properties of the molten salt-based nanomaterials. The focus of this study is on enhancing the specific heat capacity of molten salt materials by doping them with organic nanoparticles such as multi-walled carbon nanotubes, graphite, and C_{60} fullerene. A variety of experiments were performed to optimize the synthesis protocol for these nanomaterials in order to maximize the enhancements in the specific heat capacity of the mixtures. Experiments were also performed to explore the dominant parameters responsible for the enhancement of the thermo-physical property values. A number of studies on thermal properties of either nanofluids or nanomaterials were aimed at exploring the effects of nanoparticles on the thermal properties (especially on the thermal conductivity) which include Brownian motion, percolation networks, etc. There were, however, significant discrepancies in these studies between the predictions by the theoretical/ analytical models and the experimental measurements. For example, literature reports show that the specific heat capacity of various solvents (such as water, ionic liquids, PAO, molten salts, etc.) were enhanced by different margins even after doing with the same nanoparticles at similar concentrations. Hence, this counter-intuitive behavior – of the dominant contribution of the solvent material properties on the specific heat capacity of the molten salt mixture-based nanomaterials was thoroughly explored and investigated in this study.

In the CSP plants, the pumping cost of the heat transfer fluids or storage fluids is a significant factor that affects the overall efficiency and the cost of electricity. Therefore

the rheological behavior of the molten salt nanomaterials in liquid state was measured for a wide range of shear rates and was compared to that of the neat molten salt eutectic. Finally, numerical simulations were performed to study the interactions between the nanoparticles and molten salt molecules, as well as to estimate the interfacial thermal resistance between the organic nanoparticles and the liquid molecules of the solvent (molten salt eutectic) for different compositions of the solvent. These computational studies were performed using MD techniques.

1.7 Significance of this study

This study will contribute to the thermal-fluid sciences and fundamental understanding of transport phenomena for small-scale (micro/nano-scale) in the following ways:

- Development of novel synthesis protocol for molten salt-based nanomaterials
- Quantitative analysis of material properties of nanomaterials as suitable candidates for thermal energy storage and concentrating solar power plant applications
- Quantitative analysis of specific heat capacity, heat of fusion, and melting point for binary carbonate salt mixtures
- Development of novel measurement and testing protocols for obtaining thermo-physical properties of nanomaterials.

- Enable experimental and theoretical investigation of the effects of several parameters (e.g. nanoparticle material properties, solvent material properties, concentrations, sizes, and shape).
- Computational estimation of the interfacial thermal resistance between organic nanoparticle and the liquid salt molecules: effects of material properties, particle size, particle shape and numerical procedure for determining the interfacial thermal resistance.
- Numerical simulations were performed to explore the properties of the compressed phase and the concentration gradients of the solvent molecules (materials and species) that are induced on the surface of the nanoparticles.
- Quantitative analysis of the rheological properties of nanomaterials.
- Comparison of rheological measurements with behavioral models in the literature.

This study also explored the applicability of nanomaterials for thermal energy storage and concentrating solar power plant applications. The results from this study are also applicable to wider range of technologies – especially for energy conversion technologies – such as nuclear power, fuel cells, and oil/ gas explorations (such as for drilling and tracking – where molten salts as well as their nanomaterial composites with enhanced thermo-physical and chemical properties could be useful for cheaper costs and better flexibilities). This study can also have wider implications (broader impact and transformative in nature) in other technologies – such as biomedical technologies (e.g., cancer hypo- and hyperthermia) and therapeutic technologies (e.g., targeted drug delivery).

1.8 Summary

Experimental and computational studies were performed to examine the changes in the thermo-physical properties of molten salt nanomaterials. This study was geared towards thermal energy storage and concentrating solar power applications (but has broader applications in energy conversion technologies as well as other technologies). A variety of parameters which affect these material properties were examined in this study.

Section 2 provides the information about the base material (solvent) and nanoparticles used in this study. Additionally, experimental procedures, such as the determination of the specific heat capacity, were also described in the section. Finally, uncertainty analysis was also performed.

Section 3 provides the information about the computational study using molecular dynamics (MD) simulations. Interfacial thermal resistance is estimated by calculating interactions between a nanoparticle and liquid salt molecules. The effects of various parameters on the interfacial thermal resistance were explored. The effect of nanoparticle and solvent material properties on the formation of the compressed phase was explored. The chemical concentration gradients in the solvent phase that are induced by the nanoparticles are also explored using the results from the MD simulations.

Section 4 provides the experimental measurements of the thermal properties for binary carbonate salt mixtures. The effect of the composition on the thermal properties was also explored.

Section 5, 6 and 7 present the experimental measurements of the thermal properties for the carbonate molten salt nanomaterials. These sections also provide the information

on the effects of the synthesis protocol, the uniformity of the nanoparticle dispersion, and nanoparticle concentration - on the specific heat capacity enhancement. Theoretical predictions from the simple mixing rule are compared with the predictions from a novel analytical model incorporated in this study.

Section 8 describes the results from the experiments exploring the effects of the solvent properties on the resultant properties of nanomaterials – that were synthesized as a part of this study. The chemical composition, i.e., mole fraction of two molten salts (lithium carbonate and potassium carbonate) was varied in this study. In addition, the experimental results were compared with the predictions from the computational study (using MD simulations). The MD simulations provided insight into the effect of the solvent material properties on the resultant property of the nanomaterial (e.g., for specific heat capacity).

Section 9 presents the experimental measurements of the specific heat capacity for the carbonate salt eutectic-organic surfactant mixtures. The sole effect of the surfactant on the significant enhancement in the specific heat capacity of the binary molten salt mixture was explored.

Section 10 presents the results from the measurement of the rheological properties of the molten salt nanofluid. The effects of nanoparticle concentration and nanoparticle agglomeration were also examined. Theoretical analysis was also performed.

Section 11 summarizes the results obtained in this study. As an outcome of this study - the future directions (as well as potential outcome/ topics) are also explored in the final section.

2. MATERIALS SYNTHESIS PROTOCOLS AND EXPERIMENTAL METHODS

2.1 Base material[1]

Carbonate salt mixtures were used as the base material (solvent) for synthesizing the molten salt nanomaterial. Carbonate slats are typically thermally stable at temperatures exceeding 500 °C. The mixture used in this study consists of lithium carbonate (Li_2CO_3) and potassium carbonate (K_2CO_3), (procured from Sigma Aldrich and were used as received). The phase diagram of binary mixture of the carbonate salt [106] is shown in Fig. 2.1.

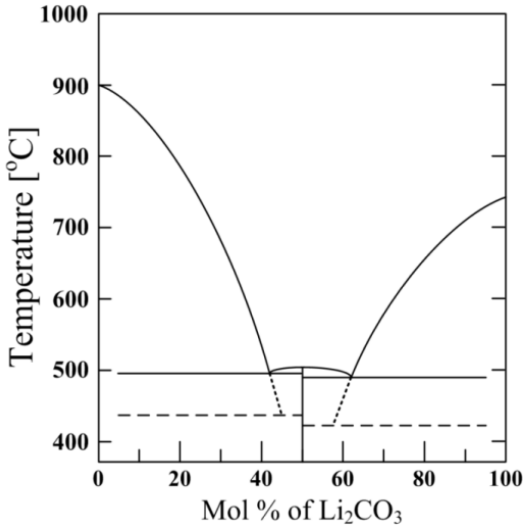

Fig. 2.1 Phase diagram of Li_2CO_3 - K_2CO_3 [106]

Note: Redrawn by permission from "NSRDS 61 Part II Physical Properties Data Compilations Relevant to Energy Storage. II. Molten Salts: Data on Single and Multi-component Systems" by G. J. Janz, C. B. Allen, N. P. Bansal, R. M. Murphy, and R. P. T. Tomkins, 1979, NSRDS-NBS 61, pp. 420, Copyright 1979 by the Secretary of Commerce on Behalf of the United States Government

[1]Contribution of the National Institute of Standards and Technology

The phase diagram shows that it has two eutectic points where the molar ratios of the two salts are 42.7:57.3 and 62:38 (Li_2CO_3:K_2CO_3). The 62:38 eutectic was chosen as a base material for the initial studies. In later studies the off-eutectic compositions of the two salts were explored in order to examine the effect of the composition of the mixture (solvent) on the specific heat capacity of the nanomaterials as well.

2.2 Nanoparticles

Organic nanoparticles - multi-walled carbon nanotubes (CNT), graphite, and C_{60} fullerene - were chosen as additives for the carbonate salt mixtures. These organic nanoparticles have specific crystal structures such as tube, disk (lamellar), and sphere, respectively. These organic nanoparticles are also known to have outstanding thermal properties [107]. The transmission electron microscope (TEM, JEOL JSM-2010) images of particles used in this study are shown in Fig. 2.2. According to manufacturer specification for the carbon nanotubes (supplier: Meliorum Technologies), their diameter range from 10-30 nm and their length is 1.5 μm. As shown in Fig. 2.2, the carbon nanotubes are consistent in the size with the manufacturer specifications. Most of the graphite nanoparticles were measured to be less than 200 nm in diameter. The situation is more complex with regard to the diameter of C_{60} nanoparticles. Basically, C_{60} aggregates and forms clusters also known as *n*-C_{60} or nano C_{60} [108]. It is, however, reported from previous studies that C_{60} has an extremely low solubility to water and furthermore sonicating water-C_{60} suspension with surfactants by ultrasonic wave does not work [109]. Hence, sodium dodecyl sulfate (SDS, Sigma Aldrich) was dissolved in

water and then C_{60} was mechanically mixed by a magnetic stirrer. The hydraulic diameter of the C_{60} nanoparticles was measured using particle size analyzer (Zetasizer Nano ZS, Malvern Instruments). The measurements were performed by varying the duration of the mechanical mixing from 1 to 4 weeks. Also, C_{60} nanoparticles were dispersed in water without SDS using the same method as described before. The hydrodynamic diameter (defined as diameter of a collection of subparticles) was 200-250 nm when using SDS and 250-300 nm in the absence of SDS. The standard deviation of the nanoparticle size distribution was also higher in the absence of SDS. Additional details about the experiments and the results are itemized in Appendix C. In this study, all nanoparticles and surfactants were used as received (i.e. without performing any explicit modification steps or for chemical functionalization of the nanoparticles)

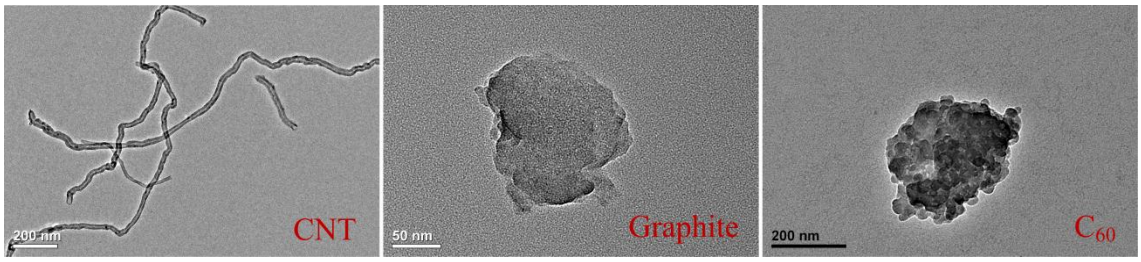

Fig. 2.2 TEM images of organic nanoparticles from samples that were used in the electron microscopy imaging before commencement of the experiments: (A) Multi-walled carbon nanotubes, (B) graphite, and (C) C_{60} fullerene

2.3 DSC measurements

The specific heat capacity values of the samples were measured using differential scanning calorimetry (DSC: Q-20, TA Instruments) for both solid and liquid states.

Based on the measured differences in heat flow, the specific heat capacity was determined by following a standard protocol established by the American Standard Test Method (ASTM E1269) [110]. According to this protocol, the difference in heat flow values between an empty pan (Tzero aluminum hermetic pans, TA Instruments) and a reference material (a sapphire disk) were recorded as a function of temperature from the DSC instrument. The measurements were repeated using the same thermo-cycling protocol multiple times in every test for the individual samples (salt mixtures or nanomaterials). A ramp rate of 20 ℃ /min was employed in the heating process and the temperature range was varied from 150 ℃ to 560 ℃. The heat flow data of the first thermal cycle in the DSC was discarded in calculation of the specific heat capacity because the first heat flow curve was often observed to be skewed, probably due to thermal non-equilibrium issues. For the DSC test runs of the empty pans and the sapphire standard, the heat flow measurements from the first run were also discarded. After the first cycle, the measurements in DSC were repeated a minimum of 5 times in order to ensure the reproducibility of the experimental results and to verify if significant variations occurred in the measurements. Two reference temperatures (250 ℃ and 400 ℃) were chosen to compare the specific heat capacity values from the solid phase measurements of the base materials to that of the nanomaterial samples. The specific heat capacity values in liquid phase were compared for the mean values between 525 ℃ and 555 ℃.

The heat of fusion was also obtained from the measured heat flow data using a software (TA Universal Analysis) provided by TA Instruments. Regarding the melting

point of the salt mixtures and the nanocomposites, it is difficult to determine the peak point of the endothermic curve (i.e. the melting peak) because the measurement uncertainty is higher at higher temperature ramp rates that were used in the experiments. Higher ramp rates were used to minimize the measurement uncertainty for the specific heat capacity data. In contrast, lower ramp rates are needed to minimize the measurement uncertainty for measuring the latent heat of fusion and the melting point values. Hence, due to the fast ramp rate that was used in this study (to be consistent with ASTM E1269), temperatures measurements (at which endothermic peaks have the lowest values) were not consistent with the reference value [106]. Therefore, the slope of the heat flow curves at the melting point (as reported in the literature) was used to estimate the values of the melting temperature for the samples (i.e., both for pure carbonate salt mixture samples and the nanomaterial samples).

2.4 Viscosity measurements

A rotational rheometer (AR 2000ex, TA Instruments) with a cone and plate test section was used to measure the rheological behaviors of the samples (pure solvent and nanofluids). These experiments were performed to measure the viscosity values over a wide range of shear rates ranging from 1 to 1000 [1/s] at a fixed temperature of 550 °C. The temperature was chosen to ensure that the carbonate salt mixtures were in liquid state. The temperature of the samples in the rheometer was controlled by an external convection-radiation oven. For the viscosity measurements, multi-walled carbon

nanotubes (CNT) were used as the nanoparticle additive. The experiments were performed for nanoparticle mass concentration of 1 %, 2 %, and 5 %. A surfactant, Gum Arabic (GA, Sigma Aldrich), was added to facilitate the uniform dispersion of the nanotubes in the salt mixtures. The mass concentration of GA was 1 %. To examine the effect of aggregation of the CNT on the viscosity, CNT nanofluid (at a mass concentration of 1 %) without GA was also tested under the same experimental conditions. These measurements were then compared with the measurements for nanofluid samples containing CNT at the same mass concentration but mixed with GA to achieve more homogeneous dispersion.

2.5 Uncertainty analysis

As mentioned above, the specific heat capacity was determined by ASTM method according to the following equation [110]:

$$c_{p,s} = c_{p,st} \frac{\Delta q_s \cdot m_{st}}{\Delta q_{st} \cdot m_s} \tag{2.1}$$

where, c is the specific heat capacity, Δq is the heat flow difference between the specimen and the empty pan, m is the mass. Subscript, s, indicates samples (pure mixtures or nanomaterials), and subscript, st, indicates the standard material (sapphire in this study). The heat flow differences were obtained by subtracting baseline (empty pan,

subscript *b*) heat flow from the heat flow of the sapphire and the sample. The measurement uncertainty is calculated as follows [111].

$$\frac{U_{c_s}}{c_{p,s}} = \sqrt{\left(\frac{U(c_{st})}{c_{p,st}}\right)^2 + \left(\frac{U(\Delta q_b)}{\delta(q_b)}\right)^2 + \left(\frac{U(\Delta q_s)}{\delta(q_s)}\right)^2 + \left(\frac{U(\Delta q_{st})}{\delta(q_{st})}\right)^2 + \left(\frac{U(m_s)}{m_s}\right)^2 + \left(\frac{U(m_{st})}{m_{st}}\right)^2} \quad (2.2)$$

Uncertainty in the measurements arise from the curve fitting of specific heat capacity of sapphire, the heat flow measurements (for the specimen and the sapphire standard), and the measurement of mass (of the sample and the sapphire standard). The uncertainties for the curve fitted values of the specific heat capacity of the sapphire standard and heat flow measurements are estimated to be ±0.3 % and ±2 %, respectively (from manufacturer specifications). The maximum value of measurement uncertainty in the determination of the specific heat capacity values for the various samples, therefore, is estimated to be ±3.5 %. The measurement uncertainty of pure carbonate salt mixture samples (pure solvent samples) is smaller than that of the nanomaterials samples. Accordingly, the measurement uncertainty for the specific heat capacity values for the pure carbonate salt mixtures was estimated to be 2.0 %.

3. COMPUTATIONAL STUDY: MOLECULAR DYNAMICS SIMULATIONS

3.1 Objective

The aim of this study is to estimate the interfacial thermal resistance for organic nanoparticles with the different crustal structures, sizes and shapes: (1) SWNT, (2) C_{60} fullerene, and (3) graphite sheets. Additionally the effects of variation in the material properties, the particle shape, and the particle size were also examined with the SWNT and the graphite sheets. The effect of the variation in the compositions of the carbonate salt mixtures on the interfacial thermal resistance was also explored for SWNT. Moreover, the effect of the cutoff radius (for the non-bonded potential) and the numerical procedure on the estimated value of the interfacial thermal resistance was also investigated. In order to understand the behavior of liquid molecules (liquid layering) near a nanoparticle, the local density of the eutectic was plotted for the simulations involving SWNT and the C_{60} fullerene.

The formation of the compressed phase occurs due to higher adhesion force between the solvent molecules and the surface atoms of the nanoparticle (compared to the mutual cohesive forces between the solvent molecules themselves). In addition, the concentration variation (spatial distribution) of the different species within the solvent phase that are induced by the nanoparticles and in the vicinity of the nanoparticles were also derived from the simulation results (meta-data). This is due to the higher (preferential) chemical and physical affinity (e.g., due to Van der Waals forces and ionic/ Coulombic force interactions) between the nanoparticle and certain species within

the solvent material. It is expected that the existence of the compressed layer in association with the concentration gradients induced in the vicinity of the nanoparticles will significantly affect the thermo-physical behavior of the nanoparticle mixtures. Such behavioral interactions on the molecular scale (between nanoparticle surface and solvent molecules) are explored using numerical models in this study.

3.2 Molecular dynamics simulations

3.2.1 Material

Carbonate salt eutectic was chosen as a solvent material for the simulations in this study due to the good thermal stability in liquid phase (at high temperatures). The feasibility for employing this solvent was also explored as a potential candidate for TES media - for the next generation of the CSP systems. The eutectic composition of lithium carbonate (Li_2CO_3) and potassium carbonate (K_2CO_3) in 62:38 molar ratio was explored initially in this numerical study. Subsequently, the composition of the two salts was varied from 34:66 to 90:10 (in molar ratio) in order to explore the effect of the composition of the base material on the interfacial thermal resistance. Three different carbon particles, an armchair SWNT, a C_{60} fullerene, and graphite sheets, were used to investigate the effect of the material properties and the particle shapes on the interfacial thermal resistance. Each particle (SWNT, C_{60}, and graphite) represents a specific shape (i.e., a cylinder, a sphere, and a disk, respectively). Fig. 3.1 shows the crystal structure of the particles. In order to examine the effect of the particle size on the interfacial thermal

resistance values, the diameters of the particles were varied from 2.7 Å to 13.6 Å for SWNT and from 7.2 Å to 18.4 Å for graphite. Diameter of the C_{60} was fixed at 7.1 Å.

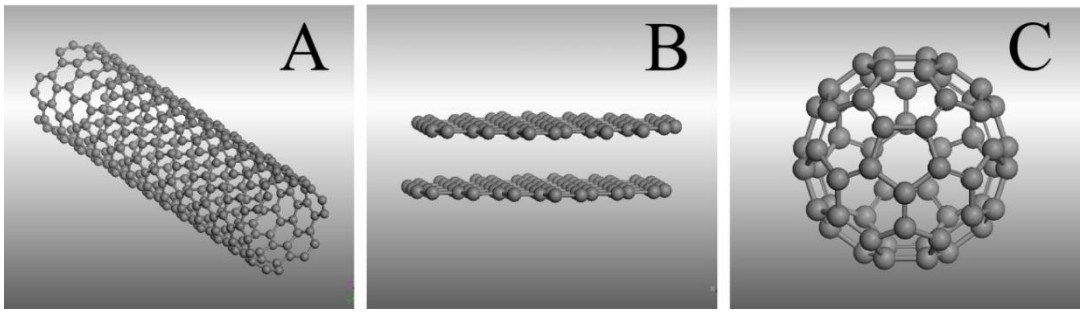

Fig. 3.1 Configuration of each carbon particle: (A) SWNT, (B) Graphite sheets, and (C) C_{60} fullerene

3.2.2 Simulation setup

The construction of the simulation box, the structure of the nanoparticle, and placement of the eutectic molecules were accomplished using a commercial tool (Materials Studio 5.0, Accelrys, Inc, 2008). The (*n*, *n*) armchair lattice structure was used for the nanotube configuration. The length of the nanotubes was chosen to fit within the simulation box and was horizontally aligned at the centroid of the box. C_{60} and graphite particles were created in the numerical models by importing basic structures embedded in Materials Studio numerical library. Based on the molar ratio between lithium carbonate and potassium carbonate, the number of molecules for each salt was determined for a chosen simulation domain. Typically, the total number of eutectic molecules is fixed to be 1500 molecules. The simulation domain (box) for these simulations was chosen to be a cube with the length of about 50 Å. In some cases

involving large particles, however, extra molecules were added to the simulation domain to be consistent with the physical properties – especially for preserving the density values of initial temperature. Table 3.1 lists the values used for nanoparticle diameters, the number of carbon atoms for a chosen carbon nanoparticle, and the number of atoms of the eutectic material (solvent phase) that was used in each simulation. Fig. 3.2 shows an initial setup of the system, showing a single crystal (lattice structure) of SWNT placed within the solvent molecules.

Table 3.1 Simulation configuration

SWNT			Graphite			Fullerene		
Diameter [Å]	N_{carbon}	$N_{eutectic}$	Diameter [Å]	N_{carbon}	$N_{eutectic}$	Diameter [Å]	N_{carbon}	$N_{eutectic}$
2.7	160	9000	7.2	44	9000	7.1	60	9000
5.4	320		9.2	74				
6.7	400		11.8	108				
8.1	480		12.8	146				
10.8	672		16.4	188	15000			
13.6*	480		18.4	242	18000			

* Simulation domain size for this case: $50 \times 50 \times 29.5$ [Å^3].

Simulation domain size for all other cases: $50 \times 50 \times 50$ [Å^3].

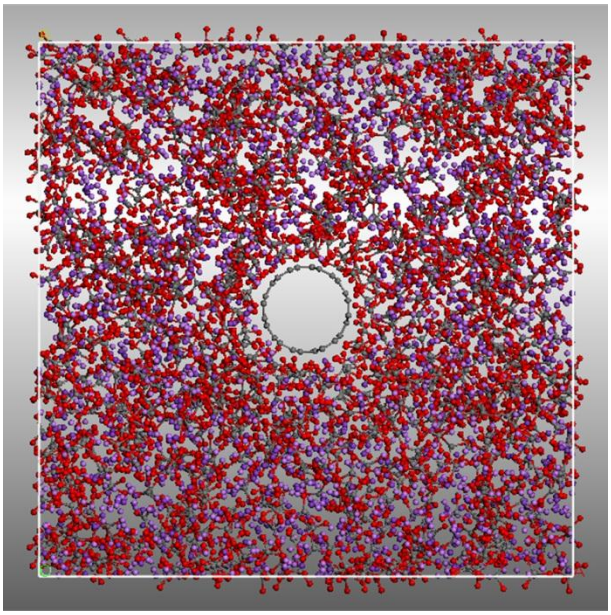

Fig. 3.2 Example of simulation domain: (5, 5) SWNT immersed in carbonate salt eutectic (Pre-simulation)

In these simulations, the interactions between any two atoms was described by Lennard-Jones (LJ) potential with Coulomb force interaction for non-bonded atoms as shown in Eq. (3.1), where r is the center-of-mass distance between the center-of-mass for any two atoms. The parameters for the LJ potential for the mutual interactions between carbon nanoparticles were obtained from various literature reports [102, 112, 113]. The parameters for the mutual interactions between the molecules of the matrix salt mixtures were obtained from Material Studio and the interaction parameters were based on the "cvff" force field, which is shown below.

$$E(r)=\frac{q_i \cdot q_j}{r}+4\varepsilon\left[\left(\frac{\sigma}{r}\right)^{12}-\left(\frac{\sigma}{r}\right)^{6}\right] \tag{3.1}$$

To account for the mutual interactions between atoms of different chemical species, the parameters for the LJ potentials were obtained by using the arithmetic mean shown in Eq. (3.2). In addition, two different cutoff radii of 12 Å and 15 Å were employed for calculating the LJ interactions. Literature reports have shown that the results of the intermolecular interactions are not affected significantly for cutoff lengths exceeding a certain threshold value [102, 112, 113]. Since the diameters of small nanotubes are, however, much smaller than the cutoff radius used, it is useful to check the differences in the results for the simulations by varying the values for the cutoff length. In the simulations the variation of the numerical parameters such as bond-stretching, bond-bending, and torsion effects are considered, as shown in Eq. (3.3). The numerical parameters for molecular interactions for each atom (for both non-bonded and bonded interactions) are listed in Table 3.2 [102, 112-114].

$$\varepsilon_{i,j} = \sqrt{\varepsilon_i \cdot \varepsilon_j} \quad , \quad \sigma_{i,j} = \frac{\left(\sigma_i + \sigma_j\right)}{2} \tag{3.2}$$

$$E = K_s \cdot \left(r - r_0\right)^2 + K_b \cdot \left(\theta - \theta_0\right) + K_t \cdot \left(1 + d \cdot \cos\left(n\phi\right)\right) \tag{3.3}$$

Table 3.2 System parameters for molecular dynamic simulations

LJ potential parameters							
Material	Interaction	ε [kcal/mol]	σ [Å]	Charge			
SWNT	C - C	0.105	3.851	0			
Graphite		0.055	3.412				
C_{60}		0.066	3.470				
Eutectic	C - C	0.148	3.617	+1.54			
	O - O	0.228	2.880	-1.18			
	Li - Li	4.735	2.839	+1			
	K - K	5.451	3.197	+1			
	Stretching		Bending		Torsion		
Material	K_s	r_0	K_b	θ_0	K_t	d	n
SWNT Graphite C_{60}	480.0	1.340	90.000	120.0	12.3700	-1	2
Eutectic	4612.0	1.290	107.4354	120.0	1.13920	-1	0

3.2.3 Simulation procedure

Large-scale Atomic/Molecular Massively Parallel Simulator (LAMMPS) distributed by Sandia National Laboratory was used for the MD simulations in the present study. Initially, a single carbon nanoparticle was placed at the centroid of the simulation box. Solvent molecules were placed randomly inside the simulation domain. As a result of the

arbitrary placement of the solvent molecules – there is a good possibility for the values for the intermolecular spacing to acquire non-physical values, even causing some of the molecules to overlap in the physical space. This initial state may not be appropriate (non-physical situation) for starting the numerical simulation. Hence, a simulation step was performed (energy minimization step) in order to separate the atoms and to avoid computational instabilities induced by high velocity of some of the atoms, thus enabling a more physically realistic situation to be obtained for the initial state of the system prior to start of the desired numerical simulation. In the minimization step, the salt atoms adjacent to the particle are moved and the temperature of the system was decreased to 0 K. After performing the energy minimization step, an equilibration procedure was implemented in two steps. First of all, a relaxation step was implemented using micro-canonical ensemble ("NVE integration"). Subsequently temperature of the system was raised to a certain starting temperature by "NPT ensemble" (isobaric-isothermal ensemble). In the present study 800 K was chosen as the starting temperature because of the high melting point of the solvent material (761 K). Following the equilibration process at the uniform temperature of 800 K, the temperature of the particles inside the simulation box was instantaneously increased to 1400 K and the final simulation ("NVE ensemble") was performed. In this process, energy (heat) was transferred from the particle to surrounding fluids (carbonate salt eutectic). Simultaneously, the average temperatures of the particle and the surrounding fluid atoms were calculated and recorded at every 50 fs.

3.2.4 Determination of interfacial thermal resistance

Based on the lumped capacitance method, the values for the interfacial thermal resistance were determined using temperature differences between the organic nanoparticle and the molten salt mixture (obtained from the last step in the simulation). Huxtable et al. applied a similar method to obtain the interfacial thermal resistance between the SWNT and the octane molecules [99]. However, the value for the heat capacity per unit area of an atomic layer of the graphite was used to calculate the interfacial thermal resistance. In this study the interfacial thermal resistance was determined from Eq. (3.4) by using the relaxation time constant, specific heat capacity, density, surface area, and nanoparticle volume (that were different for every nanoparticle explored in this study). To compare these calculation methods, the interfacial thermal resistance values were also determined using the uniform heat capacity per unit area of an atomic layer of graphite, as reported by Huxtable et al. [99].

$$R = \frac{\tau \cdot A}{C} = \frac{\tau \cdot A}{\left(\rho V c_p\right)} \tag{3.4}$$

where, R is the interfacial thermal resistance, A is the surface area of the nanoparticle, V is the volume of the nanoparticle, c_p is the specific heat capacity of the nanoparticle, ρ is the density of the nanoparticle, and τ is the time constant.

The value for time constant was obtained by a curve fitting procedure that was implemented for the transient temperature profile of the carbon nanoparticle as shown in Fig. 3.3. Regardless of the values of the particle size, material properties (such as

specific heat capacity and density) were assumed to be constant and utilized to compute the interfacial thermal resistance values for all carbon particles. Although the three particles have totally different shapes and characteristics, differences in the specific heat capacity values among the three particles are not significantly different. The specific heat capacity values for SWNT, C_{60}, and graphite were 1.750, 1.720, and 1.702 [J/g·K], respectively [115-117]. However, there are relatively large differences in the density of nanoparticles [115, 118]. As shown in Fig. 3.3, the temporal fluctuations in the temperature profile increased as the average temperature of the particle decreased. Especially, the fluctuations were too large for reliable curve fitting, for temperature values below 900 K. Therefore, the time constant (which is proportional to the slope of the line obtained from the linear fit) was calculated for temperature values exceeding 900 K (i.e., the temperature data used for calculating the linear fit was limited to the values until the heated nanoparticle cooled down to 900 K).

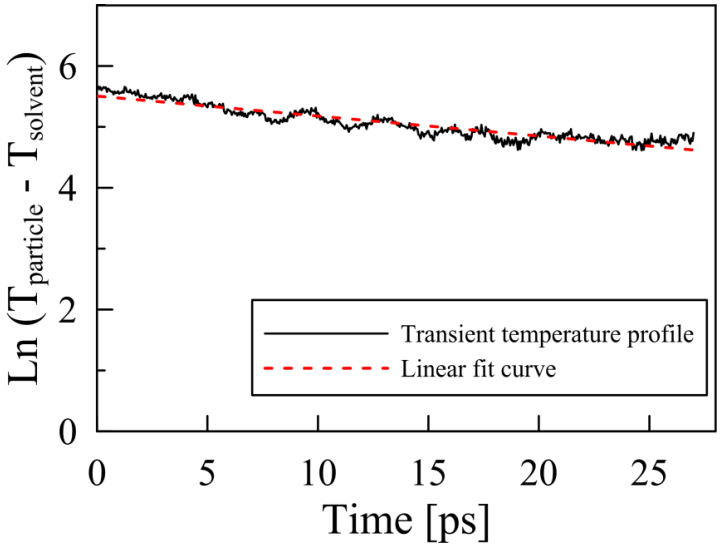

Fig. 3.3 Transient temperature profile of a carbon nanoparticle (SWNT)

3.3 Results and discussion

3.3.1 Interfacial thermal resistance

Fig. 3.4 shows the interfacial thermal resistance values between SWNT and carbonate salt eutectic, as a function of the nanotube diameter. As mentioned above, the interfacial thermal resistance was estimated from Eq. (3.4) using the dimensions and the material properties of the carbon particles. For the SWNT, the interfacial thermal resistance values were fairly uniform for the whole range of the nanotube diameters varying from 3 Å to 14 Å. The average value of 7.50×10^{-8} [$m^2 \cdot K/W$] was estimated from the simulations. This result for the SWNT simulations was found to be in a good agreement with the literature data. Maruyama reported the resistance value of 6.46×10^{-8} [$m^2 \cdot K/W$][100] for a bundle of (5, 5) SWNT. Zhong and Lukes [101] simulated heat transfer between offset parallel (10, 10) single-walled carbon nanotubes. They found the thermal resistance varies as a function of nanotube spacing, overlap, and length. For the shortly spaced nanotubes with the separation distance varying from zero to 8 [Å], they obtained the similar interfacial thermal resistance values which have the same order of magnitude (10^{-8} [$m^2 \cdot K/W$]). Huxtable et al. [99] estimated the interfacial thermal resistance of (5, 5) SWNT in the octane by MD simulations. They also measured the resistance for the SWNT-Sodium Dodecyl Sulfate (SDS) interface by short time scale optical absorption experiments. The values from the simulation and the experiments were reported to be 4×10^{-8} and 8.3×10^{-8} [$m^2 \cdot K/W$], respectively [99]. The simulation results obtained in this study are therefore consistent with the experimental measurements mentioned above.

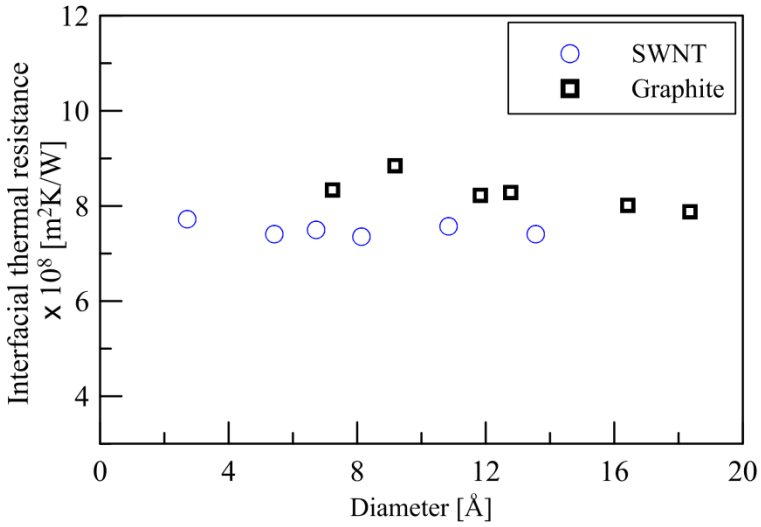

Fig. 3.4 Interfacial thermal resistances of SWNT and graphite sheets as a function of particle size

In the present MD simulation the interfacial thermal resistance values were found to be consistent with that of the literature data (i.e. having the same order of magnitude), even though the particle configurations and the solvent media were not identical in all of these simulations. Moreover, the interfacial thermal resistance values were not significantly affected by the nanotube size. However, the interfacial thermal resistance values of the SWNT in the carbonate salt eutectic were slightly higher than that of the other reports in the literature, i.e., nearly twice as high as that of liquid octane [99]. Considering that the thermal conductance values at interfaces are generally enhanced at higher temperatures (that is, the interfacial thermal resistance would decrease with increasing temperature), the thermal resistance of the SWNT is definitely higher than that of the other reports in the literature. There are several issues to be considered as reasons for these differences in the estimates for the values of the interfacial thermal

resistance. First, the solvent used in this work is different from these references. That is, the parameters incorporated to calculate the non-bonded interactions between SWNT and fluid molecules might lead to the higher values of the interfacial thermal resistance. The length of the SWNT is also an important parameter. In a reference [101], it was pointed out that the interfacial thermal resistance was affected by the length of the carbon nanotubes, and the influence disappeared after a threshold values. Therefore, the interfacial thermal resistance values reported in the literature may be influenced by the length of the nanoparticle if the parameter values used in the simulations were below the threshold values.

A similar trend in the interfacial thermal resistance was observed with the graphite sheets. As shown in Fig. 3.4 the interfacial thermal resistance values between the graphite nanoparticle and the carbonate salt eutectic were observed to be independent of the nanoparticle diameter. The mean value of the interfacial thermal resistance was obtained to be 8.27×10^{-8} [$m^2 \cdot K/W$]. In comparison with results for the SWNT, the interfacial thermal resistance of the graphite particles was higher by 10 %. Hence these results show that the nanoparticle shape has marginal effect on the value of the interfacial thermal resistance estimated by these numerical models. A similar set of numerical simulations was performed for C_{60} nanoparticle (which was modeled as a spherical nanoparticle.)

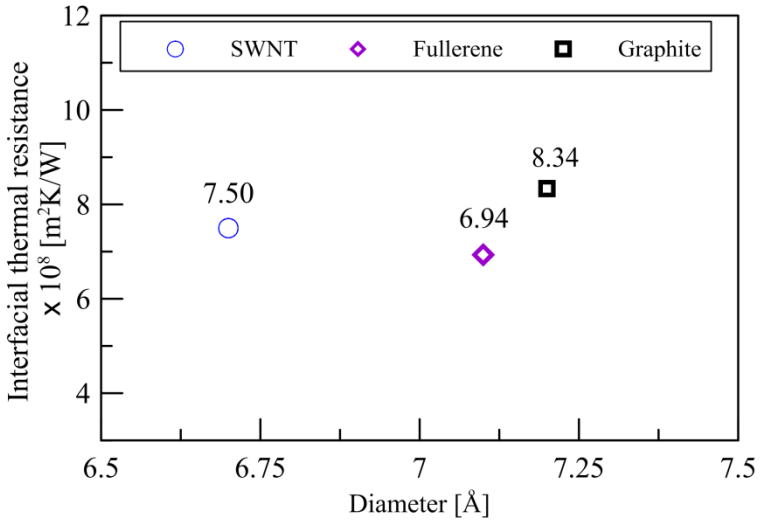

Fig. 3.5 Comparison of interfacial thermal resistances for three carbon particles with a similar diameter

Fig. 3.5 shows the interfacial thermal resistance of the fullerene nanoparticle in comparison with those of the SWNT and the graphite nanoparticles. From the simulations the resistance of C_{60} is estimated to be 6.94×10^{-8} [$m^2 \cdot K/W$], which is the smallest out of three particles but has the same order of magnitude with the SWNT and the graphite. Based on the results in Fig. 3.5, the interfacial thermal resistance varied as a function of the particle shape. It is, however, hard to conclude if the particle shape is a dominant parameter for influencing the interfacial thermal resistance between the carbon particles and the carbonate salt eutectic. In fact, the time constant of the graphite simulation was slightly lower than one from the SWNT simulation. Nevertheless, larger density of the graphite resulted in increasing the thermal resistance. Additionally, since the graphite particle was not perfectly shaped as a disk, it is possible that the radius of the particle was over-estimated. Moreover, the slightly larger parameters of the LJ

potential for the graphite (which determined non-bonding interactions between the carbon particle and the eutectic molecules) could affect the values for the interfacial thermal resistance.

3.3.2 Effect of solvent composition

The interfacial thermal resistance between SWNT and the carbonate salt mixtures was explored as a function of the chemical composition of the solvent. As shown in Fig. 3.6, the interfacial thermal resistance values decreased linearly with an increase in concentration of Li_2CO_3. The interfacial thermal resistance was estimated to be 10.3×10^{-8} [$m^2 \cdot K/W$] for 34:66 composition and it decreased down to 4.0×10^{-8} [$m^2 \cdot K/W$] for 90:10 ratio for Li_2CO_3:K_2CO_3. This trend could be explained from the non-bonded interaction parameters of the lithium carbonate and the potassium carbonate. In Eq. (3.5), the LJ potential from Eq. (3.1) is expressed as a function of the distance (r_m) at which the potential is the minimum, which is a function of σ (inter-molecular distance needed for zero potential) and ε (depth of potential well). Thus, r_m is proportional to σ.

$$u(r) = 4\varepsilon\left\{\left(\frac{\sigma}{r}\right)^{12} - \left(\frac{\sigma}{r}\right)^{6}\right\} = \varepsilon\left\{\left(\frac{r_m}{r}\right)^{12} - 2\left(\frac{r_m}{r}\right)^{6}\right\} \tag{3.5}$$

In Table 3.2, the lithium carbonate has smaller value of σ. Hence, the distance for the minimum potential is reduced as the amount of the lithium carbonate in the mixture is increased. Namely, the surrounding liquid salt molecules are located closer to the

surface of the nanoparticle. In such a situation a more effective interaction between the nanoparticle and the surrounding solvent molecules are expected. Therefore, it can be expected that the difference in values of σ for lithium and potassium is responsible for the decrease in the thermal resistance as shown in Fig. 3.6.

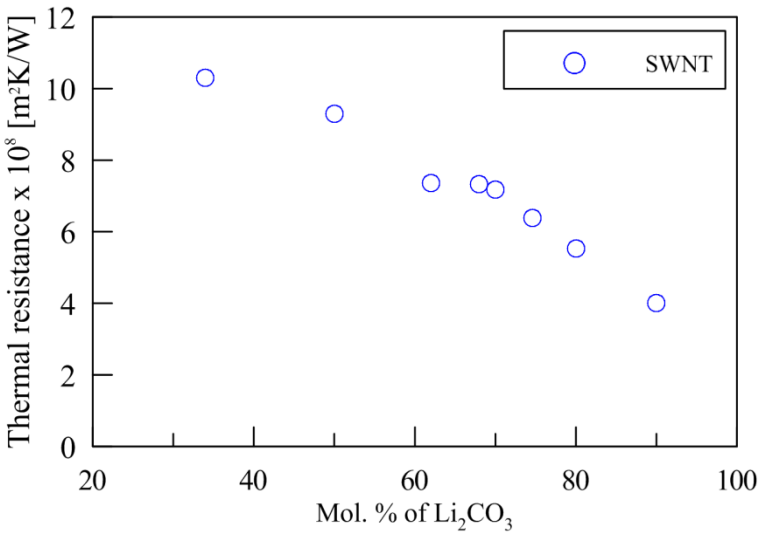

Fig. 3.6 Interfacial thermal resistance of (6, 6) SWNT as a function of chemical composition of solvent

3.3.3 Effect of cutoff radius

Identical simulations were performed by using a cutoff radius of 15 Å for all cases, in order to check the effect of the cutoff radius on the interactions between the organic nanoparticle and the salt molecules. Fig. 3.7 shows the comparison of the interfacial thermal resistance values for the cutoff length of 12 Å and 15Å for the SWNT (Top) and for the graphite (Bottom). As shown in the top figure, the resistances of the SWNT obtained for longer cutoff length (15 Å) are almost identical over the whole range of the

nanotube diameters. Unlike SWNT, for the graphite particle the interfacial thermal resistance values were affected significantly by the cutoff radius. Especially, the interfacial thermal resistance of small graphite particles whose diameter was 7 Å and 9 Å were reduced by up to 57 %, for the cutoff distance of 15 Å. For other sizes of the graphite particle, however, the interfacial thermal resistance values obtained with 15 Å cutoff length were larger than that of simulations with 12 Å. However, the differences in the results are expected considering the number of carbon atoms in the graphite crystal lattice contained within the simulation domain is quite small and the lattice structure of the nanoparticle could be easily deformed due to loading arising from thermal fluctuations. In the simulations involving larger cutoff length, the number of eutectic molecules which interact with the graphite particles was increased significantly. Since the graphite nanoparticles have significantly less number of carbon atoms than the SWNT, the graphite simulations were more sensitive to the effect of the cutoff radius.

In fact, it was reported that the cutoff distance over a certain value does not affect the interactions by LJ potential, because the Lennard-Jones interactions are negligible beyond the cutoff radius. Zhong and Lukes [101] examined the effect of the cutoff distance on the interface thermal resistance of carbon nanotubes by varying the cutoff distance from 10 Å to 20 Å. They reported negligible change in the interfacial thermal resistance when the cutoff distance was varied. Li et al. [102] also used 10 Å cutoff radius in their MD simulations for water (solvent) mixed with organic nanoparticles.

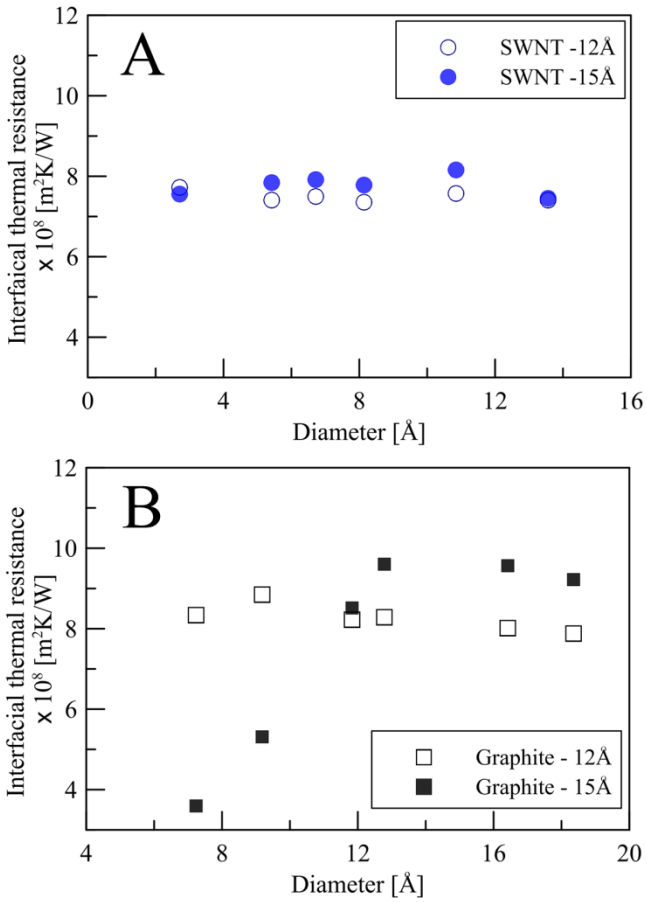

Fig. 3.7 Effect of cutoff radius on interfacial thermal resistances: (A) SWNT and (B) graphite sheets

Additionally a previous study involving MD simulations [114] for liquid Argon showed that intermolecular interactions and forces were truncated and switched to zero beyond a cutoff distance of 3σ (about 11 Å). Similarly, the SWNT simulations in this work show that the cutoff length of 12 Å did not change significantly the interactions between the SWNT and the eutectic molecules, and also did not influence the values of the interfacial thermal resistances. Hence, according to the literature data and the results from the present study, the cutoff distance used in this study exceeds the threshold value.

Hence, the intermolecular forces and can be neglected beyond the cutoff distance. As mentioned before, the graphite particles consist of significantly fewer numbers of carbon atoms than SWNT, and subsequently the small graphite particles could be more sensitive to the increase of the cutoff distance.

3.3.4 Comparison of the resistance calculation methods

Two methods for determining the interfacial thermal resistance was employed for the SWNT and the graphite sheets. As mentioned in the previous subsection, based on the lumped capacitance model, the interfacial thermal resistance was calculated by using the time constant, the material properties of the organic nanoparticles (density and specific heat capacity), and the estimated nanoparticle dimensions (surface area and volume) into Eq. (3.4), which is called Method 1 in this study. In another calculation, the value for the uniform heat capacity per unit area of an atomic layer of graphite was obtained from the literature [99], which is called Method 2 in this study.

Fig. 3.8 shows the comparison between the interfacial thermal resistance values obtained from both Method 1 and Method 2 for the SWNT and the graphite sheets. As shown in Fig. 3.8(A), distinctly different values for the interfacial thermal resistance for the SWNT were estimated (with increasing tube diameter) between the two calculation methods. For Method 1, fairly uniform values of interfacial thermal resistance were obtained for the range of diameters used in this study, but for Method 2 the interfacial thermal resistance values increased with the particle size. For small nanotubes, the interfacial thermal resistance values predicted by Method 1 are higher than that by

Method 2. Conversely, the interfacial thermal resistance values for large tubes predicted by Method 2 are higher than that by Method 1. In Fig. 3.8(B), however, the graphite nanoparticle demonstrates different behavior for the values of interfacial thermal resistance values. Almost identical resistances for the interfacial thermal resistance (which are about 25% lower than that by Method 1) were obtained from the simulations with the graphite nanoparticle.

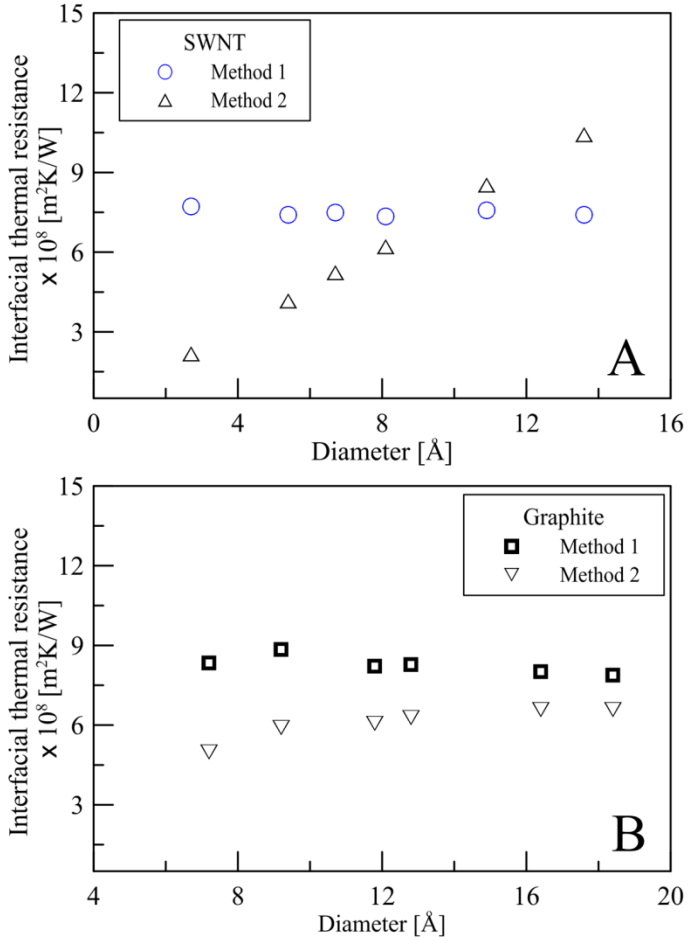

Fig. 3.8 Interfacial thermal resistance determined by two different methods: (A) SWNT and (B) graphite sheets

As show in Eq. (3.4), the time constant and the dimension of nanoparticle can significantly influence the interfacial thermal resistance values. It was observed that the time constant was increased with increase in the particle diameter (which might be attributed to the decrease in the ratio of the particle surface to volume). On the contrary, the ratio of the particle surface to volume was decreased by the same margin as the increase in the value of time constant. Thus, uniform values for interfacial thermal resistance was obtained regardless of the nanoparticle size. However, the magnitude of the degradation in the ratio (surface area to volume) is significantly different for SWNT and graphite. For the smallest case of the SWNT, the ratio of the surface to the volume is 1.48 [1/Å]. For the largest SWNT used in this study the value (for ratio of surface area to volume) is 0.29 [1/Å], which is about 20 % of the ratio of the smallest particle. The ratio change in the graphite is relatively smaller than in SWNT. The ratios of the surface to volume are 1.14 and 0.81 at the smallest particle and the largest particle, respectively. Since the parameters for nanoparticle dimension vary by different margins for the various shapes of the nanoparticles, this can help explain the variations in the results obtained by Methods. For SWNT, the interfacial thermal resistance was drastically increased due to the large change in the geometrical parameters (V/A). Hence, the value of the interfacial thermal resistance for graphite was increased significantly because of the small change in the geometrical parameters (V/A).

In Eq. (3.4) the only variable is time constant (using Method 2) even though the particle geometry (V/A) is changed as the particle diameter varies. In fact, as the particle diameter increases, thermal energy transport becomes less effective so that the time

constant increases. However, considering that the thermal resistance at the interface is a resistance per unit area, it has to be uniform regardless of the size of the nanoparticle. In this study it was found that the method to determine the thermal interfacial resistance at the interface of a particle with fluid could significantly affect the result. Hence, as a result of this study it can be concluded that Method 1 is more appropriate numerical method for applying the lumped capacitance technique to determine the value of the interfacial thermal resistance for the various cases considered in this study.

3.3.5 Interfacial layering of liquid molecules

Behavior of liquid atoms near the surface of the nanoparticles was investigated for the simulations involving the SWNT and the C_{60} fullerene. Fig. 3.9 shows the variations in the spatial density profiles for six different SWNT simulations (Fig. 3.9(A) - Fig. 3.9(F)) and C_{60} simulation (Fig. 3.9(G)), where the relative position (abscissa) refers to the distance from the outer surface of the nanoparticle. In previous studies, the existence of a semi-sold phase of the solvent molecules near the nanoparticle surface (called "compressed liquid layer"), was reported [73, 89]. The density plots for the SWNT show that the first peak occurs at a location of 3 Å away from the surface of the small nanotubes, while the first peak for SWNT with large diameter like (10, 10) was marginally displaced to a location of 4 Å away from the outer surface. That is, the void region - empty space between a particle and liquid molecules (equilibrium value of inter-molecular spacing) - marginally with increase of tube diameter, but those incremental changes were not significant. In addition, the radial thickness of the liquid layering

(defined by the distance up to the third peak and valley) plays an important role in modifying the thermal properties of the nanofluids. This thickness was observed to be nearly uniform for all sizes of SWNT. The thickness was estimated to be about 1 nm (10 Å). Similarly, the existence of the dense liquid layering was also confirmed for the C_{60} nanoparticle, where the void space and layering thickness were similar to that of SWNT.

The values for the thickness of the compressed layer that were obtained from simulations performed in this study are observed to be in good agreement with that of the literature values. The liquid argon molecules around a copper nanoparticle formed a dense layer of about 1 nm at a volume concentration of 1 % [119] of the nanoparticle. For MD simulations using gold nanoparticles in water, it was reported that the distance from the nanoparticle surface to third valley in the density plot was ~1 nm, and was found to be independent of particle size [120]. Furthermore, the thickness of the ordered liquid aluminum at the interface with sapphire was also experimentally measured to be ~1 nm using HRTEM [121]. As shown in Fig. 3.9, the thickness of the compressed liquid layers in all cases were ~1 nm, which indicated that the particle size and the particle shape do not influence the thickness of the compressed layer and therefore the solvent molecule behavior at the interface with the nanoparticles. Similarly the density variations of water molecules around the carbon particles were observed to be nearly identical for all the particles: SWNT, C_{60} and graphite. Hence, it can be concluded that the thickness of the dense liquid layer ("compressed layer") is constant for a given combination of nanoparticle and solvent composition, and is independent of the particle

size or shape (geometry). For the graphite sheets, density plots could not be obtained due to complications arising from the asymmetry in the shape of the nanoparticle.

Additional plots for the density profile for the various simulations reported in this section are provided in Appendix E. In addition, the plots for spatial distribution of chemical concentration for the various species are also provided in Appendix E. The results from the MD simulation shows that the local concentration gradients induced on the surface of the nanoparticles are affected by the bulk composition of the solvent. In addition, the thickness of the concentration "boundary layer" can be different (larger or smaller) than the thickness of the compressed phase. Hence there can be complex interactions between the concentration boundary layer and the density boundary layer (thickness of the "compressed phase"). Such interactions are likely to affect the resultant properties of the mixture of the nanoparticle and the solvent. The implications associated with the concentration gradients in the solvent molecules (or species) that are induced on the surface of the nanoparticle – will be explored in more detail in Section 7 and Section 8.

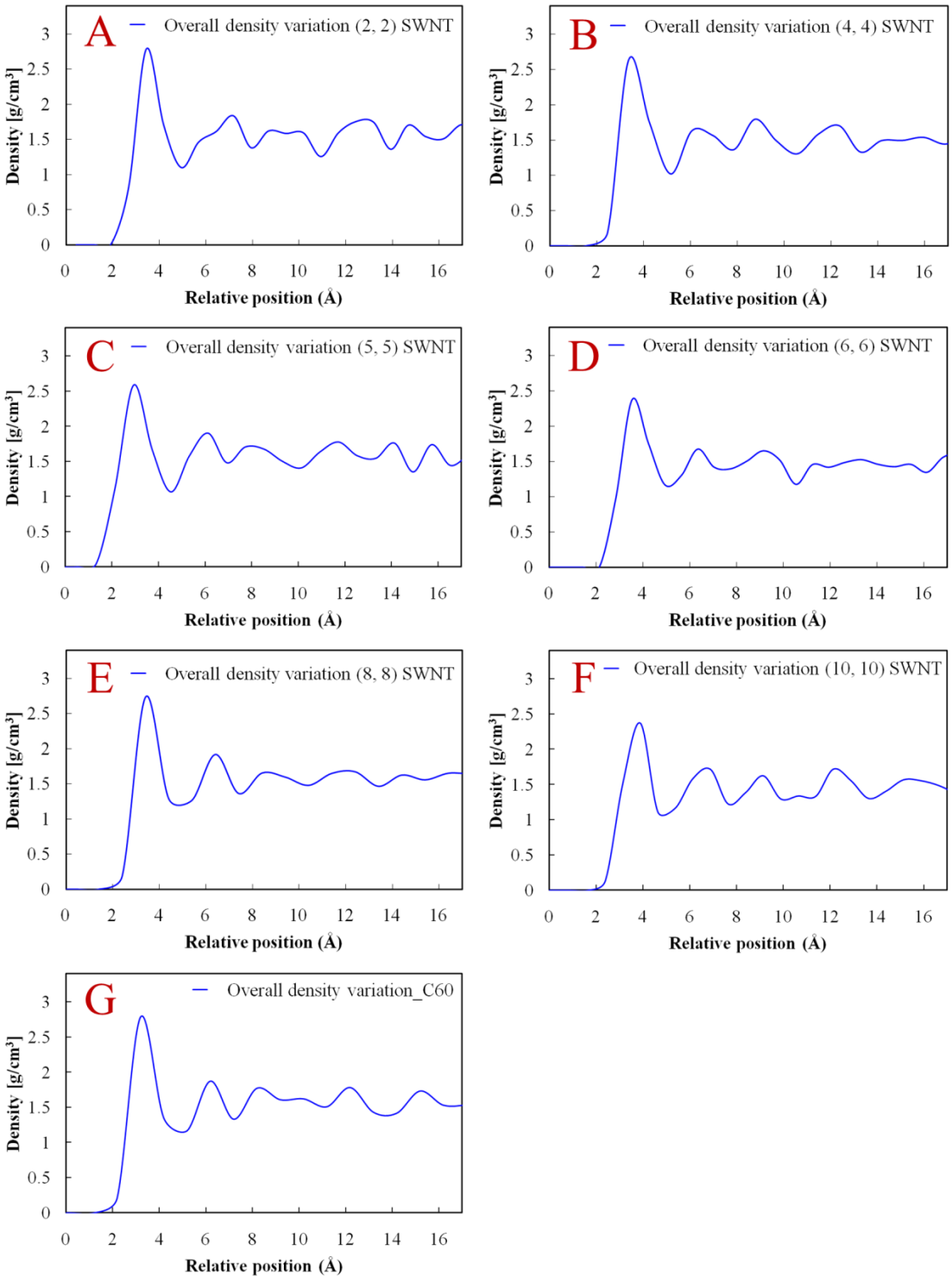

Fig. 3.9 Overall density profile: (A) (2, 2) SWNT, (B) (4, 4) SWNT, (C) (5, 5) SWNT, (D) (6, 6) SWNT, (E) (8, 8) SWNT, (F) (10, 10) SWNT, and (G) C_{60} fullerene

3.4 Conclusions

Molecular dynamics (MD) simulations were performed for the liquid carbonate salt as the solvent and three different carbon nanoparticles. Interfacial thermal resistance values at high temperature (for 900 - 1400 K) were estimated by monitoring the temperature decay of the nanoparticle and based on the lumped capacitance method. In order to examine the effect of nanoparticle shape on the values of the interfacial thermal resistance, three nanoparticle shapes were used in this study, which includes the single-walled carbon nanotubes, graphite sheets and C_{60} fullerene (i.e., configured as a cylinder, disk and sphere, respectively). The effect of the base fluid on the thermal resistance was also studied by changing the composition of the molten salt mixtures. Additionally, the effect of the cutoff length in the calculation of the Lennard-Jones potential was also investigated. In the determination of the interfacial thermal resistance, two distinct methods were employed to explore their suitability and consistency. Finally, the existence of the dense liquid layer ("compressed layer") around the nanoparticles was explored by plotting the local density values of the solvent. The knowledge gained from the simulation results is summarized as follows:

(a) The interfacial thermal resistance of the SWNT obtained in this study was observed to be in good agreement with other simulation results and the experimental measurements reported in the literature. The values for interfacial thermal resistance were estimated for the SWNT and the graphite nanoparticle. The values for interfacial thermal resistance were observed to be insensitive to variation in particle size for the SWNT and the graphite nanoparticle. However, the average value of the interfacial

thermal resistance for graphite was estimated to be about 10 % higher than that of SWNT.

(b) The interfacial thermal resistance was observed to linearly decrease with increase in concentration of lithium carbonate. This feature is attributed to the difference in LJ potential parameters between the lithium carbonate and the potassium carbonate. Increasing the mole fraction of lithium carbonate in the molten salt mixture enables the liquid molecules to be located closer to the surface of the nanoparticle.

(c) The values of cutoff radius did not significantly affect the values of the interfacial thermal resistance of the organic particles in liquid carbonate salt eutectic. In very small graphite nanoparticles (with size less than 1 nm), however, the resistance was decreased by increasing the cutoff distance from 12 Å to 15 Å. The variation of the value for the interfacial thermal resistance for the small graphite particles was attributed the enhancement of the geometrical parameters for the nanoparticle (e.g. surface area to volume ratio).

(d) Interfacial thermal resistance values determined by using the lumped capacitance model were found to be affected by the variations in the numerical procedure. Method 1 (using the material properties and the geometrical parameters for each particle shape) provided consistent predictions for the values of the interfacial thermal resistance. Another method, Method 2, (assuming the uniform heat capacity per unit area of an atomic layer of graphite without the incorporation of the particle geometry effects such as surface to volume ratio) showed that the interfacial thermal resistance increased with increasing particle size. Therefore, Method 1 was considered to be the more appropriate

method for determining the values of the interfacial thermal resistance using the lumped capacitance method.

(e) A dense layer of solvent molecules ("compressed layer") was found to self-assemble around the nanoparticle. The thickness of the compressed layer was estimated to be ~1 nm and was observed to be independent of the particle size for SWNT and C_{60} (fullerene). The void region (equilibrium molecular spacing between the nanoparticle and the first layer of solvent molecules), which plays the role of a barrier region for heat transfer from the particle to the solvent and vice versa, was also observed to be of constant thickness (i.e., independent of particle size and shape).

(f) Similar to the compressed layer – the nanoparticle was found to induce chemical concentration gradients on the surface of the nanoparticle due to preferential affinity of the nanoparticle material for a particular chemical species in the solvent molecules. This resulted in higher concentration of the preferred species on the nanoparticle surface (compared to that of the bulk composition). Thus, on the surface of the nanoparticle a chemical concentration gradient was established which would not exist in the absence of the nanoparticle. The size (thickness) of the chemical concentration boundary layer was found to be different than the thickness of the compressed layer (larger or smaller – depending on the bulk composition of the solvent). This complex interaction between the compressed layer and the chemical concentration boundary layer is likely to influence the resulting material properties of the mixture.

4. EXPERIMENTAL STUDY I: SPECIFIC HEAT CAPACITY OF PURE CARBONATE SALT MIXTURES

4.1 Objective

Comprehension of the thermo-physical properties of the base materials (neat solvents) is essential to the determination of the level of improvement in the properties of nanomaterials. Although various studies in the literature have reported on the thermo-physical properties of a variety of pure molten salts such as density, specific heat capacity, thermal conductivity, and latent heat of fusion [106, 122-125], the properties of their mixtures were measured only for limited cases. The aim of this study is to measure the thermo-physical properties of the carbonate salt mixtures using differential scanning calorimeter (DSC). We examined how the specific heat capacity values of the mixture change (for both liquid and solid phases) as the chemical compositions of the binary salt mixture were varied. Using the measured values of heat flow from the DSC experiments, the melting temperature and the heat of fusion were also explored as a function of the chemical composition. Finally, theoretical models for the prediction of the specific heat capacity (which are based on mass fraction and mole fraction) were employed to estimate that of the salt mixtures.

4.2 Experiments

The materials and experimental procedures were described in Section 2. The composition of the pre salt mixtures is described next.

The carbonate salt mixtures were synthesized by following the “two step” method as shown in Fig. 4.1. First, two salts were dissolved using distilled water in a vial. Considering solubility of each salt to water, enough water was added to fully dissolve the salts. In order to ensure homogeneous mixing of the two salts, the solution was ultra sonicated for 1 h in an ultrasonic bath (Model: 3510, Branson). The solution was then evaporated on a hot plate at 100 ℃ . Finally, dried powder of the salt mixtures was obtained. The composition ratio was varied to explore the effect of the composition on the specific heat capacity of the mixtures. Table 4.1 shows the molar and mass ratios of the lithium carbonate and the potassium carbonate for the samples which were tested in the present study.

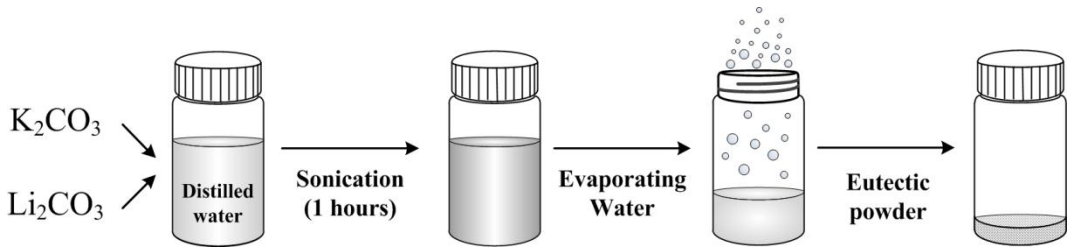

Fig. 4.1 Schematics of molten salt eutectic preparation

Table 4.1 Chemical composition of salt samples used in this study

Sample number	Group	Composition ratio (Li_2CO_3 : K_2CO_3) [mol. %]	Specific heat capacity [J/g·K]		
			at 250 [℃]	at 400 [℃]	liquid
1	Group 1	90.0 : 10.0	1.67	1.75	2.58
2		85.0 : 15.0	1.52	1.67	2.61
3		80.0 : 20.0	1.18	1.29	2.50
4		74.6 : 25.4	1.19	1.26	2.66
5		73.7 : 26.3	1.23	1.34	2.75
6	Group 2	68.0 : 32.0	1.13	1.24	2.50
7		67.0 : 33.0	1.26	1.35	2.09
8		66.0 : 34.0	1.19	1.22	1.68
9	Group 3	62.0 : 38.0	1.19	1.29	1.61
10		55.5 : 45.5	1.11	1.23	1.51
11		50.0 : 50.0	1.19	1.18	1.54
12		45.0 : 55.0	1.13	1.17	1.44
13		38.4 : 61.6	1.03	1.06	1.29
14		34.0 : 66.0	0.89	0.96	1.32

4.3 Results

4.3.1 Heat flow behaviors in liquid phase

Fig. 4.2 shows comparison for the heat flow for the carbonate salt mixtures obtained from experiments performed using DSC. The plots are obtained for the liquid phase. The figure shows that remarkable distinctions were found in the heat flow curves for the three groups listed in Table 4.1. Based upon the heat flow behaviors in liquid phase, the mixtures can be classified into three groups: (Group 1) increasing heat flow with temperature, (Group 2) dramatically decreased heat flow like glass transition, and

(Group 3) uniform heat flow with temperature. Group 1 which includes sample number 1 to 5 as listed in Table 4.1 is composed of salts with more than 68.0 % molar concentration of the lithium carbonate in the mixtures. For samples 6 to 8 in Group 2, the lithium carbonate concentration varied between 66 % and 68 % molar concentration. The rest of samples (9 to 14) were included in Group 3. On reducing the amount of the lithium carbonate salt, the heat flow (for Group 3) was decreased marginally with temperature. Since the mixtures were synthesized by following consistent protocols and DSC experiments were performed using standardized thermal-cycling protocols (using ASTM protocols), it can be concluded that these distinctly different behaviors observed in the heat flow curves is attributed to the amount of the lithium carbonate (i.e. composition of the mixture).

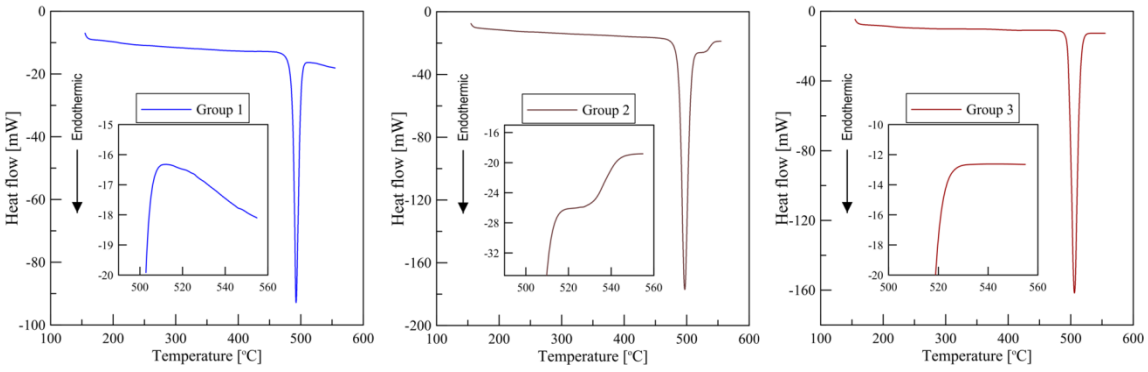

Fig. 4.2 Heat flows of carbonate salt mixtures for three different groups

4.3.2 Specific heat capacity

Specific heat capacity values of the carbonate salt mixtures in liquid phase were plotted as a function of the mole fraction of the lithium carbonate (as shown in Fig. 4.3).

The specific heat capacity values were segregated according to the three groups listed in Table 4.1 and consistent with the heat flow groups of Fig. 4.2. For Group 1, the specific heat capacity values converge to that of lithium carbonate in liquid state, which is 2.51 [J/g·K]. The lithium carbonate salt exists in liquid state at the temperature range that was chosen to obtain the average of the specific heat capacity values. For this temperature range lithium carbonate salt coexists with potassium carbonate in a mixture. It is, therefore, reasonable to predict that the salt mixture has a certain specific heat capacity that varies between those of the two pure salts. Nevertheless, almost the same values with that of the pure liquid lithium carbonate were obtained for the samples in Group 1. An additional feature in Group 1 is that the specific heat capacity value in liquid phase increased gradually with increase in temperature. On comparing the mean specific heat capacity values for the initial five degrees (525 - 530 ℃) with values that during the final five degrees (550 - 555 ℃) for the measurements, about 10 % augmentation of the average values were observed for sample 1 - 5.

In Group 2, two distinctive features were observed in the specific heat capacity measurements. First, as shown in Fig. 4.2, the heat flow of the mixtures was dramatically changed with temperature in the liquid phase. In other words, a huge decrease in the specific heat capacity was obtained in this study. In addition, it was found that the specific heat capacity values of the liquid mixtures in Group 2 were also drastically increased as the lithium carbonate concentration increased. That is, a temperature point at which the heat flow curve starts to go up shifts to a higher temperature as the mole fraction of the lithium carbonate increases. Similar to Group 1, sample 6 (with the

lithium carbonate molar concentration of 68 %) exhibits a marginal increase in the specific heat capacity value at lower temperatures in the liquid phase. Hence, Group 2 is confined within a narrow range of the lithium carbonate concentration. As shown in Fig. 4.3, the specific heat capacity of the mixtures in Group 3 also shows dependence upon the lithium carbonate concentration. While a sharp and huge degradation was measured for the Group 2 samples, the specific heat capacity of Group 3 was gradually decreased with decrease in mole fraction of lithium carbonate. The specific heat capacity starts to decrease linearly (from a value of 1.612 [J/g·K] for sample 9) with decreasing lithium carbonate concentrations (to a value of 1.289 [J/g·K] for sample 14 which is close to the specific heat capacity of potassium carbonate at 540 ℃ , i.e., in solid phase). The temperature dependence of the specific heat capacity of Group 3 was observed to be constant in the liquid state.

While the specific heat capacity of the liquid mixture exhibited obvious distinctions between the three groups, the specific heat capacity in solid phase was observed to follow a linear trend as shown in Fig. 4.4. However, there is an ambiguity in the linearity of the increase in the specific heat capacity values for the Group 2 region. The measured values increased with increase of the lithium carbonate concentration and the trend was observed to be identical at 250 ℃ and 400 ℃ . The specific heat capacity of the solid eutectics was significantly enhanced when the lithium carbonate was increased. The enhancements were as high as 66 % and 63 % at 250 ℃ and 400 ℃ , respectively. The values ranged from 0.893 to 1.670 [J/g·K] at 250 ℃ and from 0.956 to 1.750 [J/g·K] at

400 ℃ . The theoretical prediction for the specific heat capacity values are discussed in Discussion subsection.

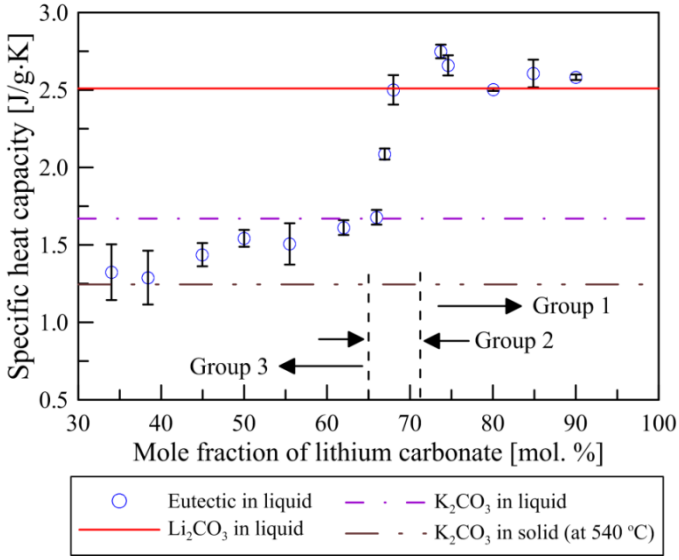

Fig. 4.3 Specific heat capacity of carbonate salt mixtures in liquid phase as a function of the mole fraction of lithium carbonate

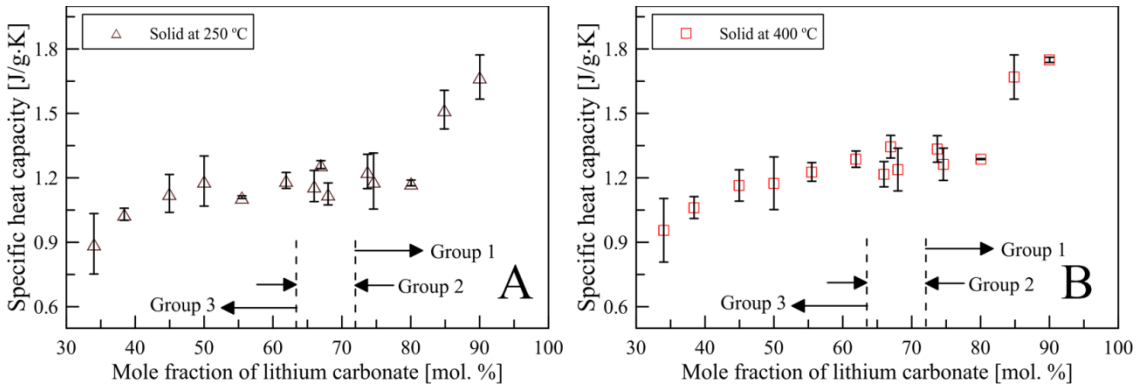

Fig. 4.4 Specific heat capacity in solid phase as mole fraction of lithium carbonate varies: (A) at 205 ℃ and (B) at 400 ℃

4.3.3 Heat of fusion

Heat of fusion is one of the most important properties of phase change materials (PCMs) which are often employed as TES media to harness solar thermal energy such as in the CSP systems. As an alternative TES material for CSP plants, the heat of fusion for the carbonate salt mixtures is of fundamental and practical utility. Moreover, since high heat of fusion enables efficiency of thermal systems to be enhanced, it is necessary to determine its variation as a function of the chemical composition. However, it is difficult to theoretically estimate the heat of fusion of the mixture from the current experiments because the melting point of each constituent salt and the mixtures are different. Therefore it is necessary to experimentally measure the heat of fusion. Fig. 4.5 shows the heat of fusion of the carbonate salt mixtures as a function of the chemical composition. As shown in this figure, the heat of fusion strongly depends on the composition for samples categorized in Group 1 and Group 2. The fusion enthalpy was measured to be 398.8 [J/g] for sample 8 (with 66 % molar concentration of lithium carbonate) and was decreased to about one third (135.0 [J/g]) for sample 1 (for lithium carbonate at 90 % molar concentration). Hence, increasing proportions of the potassium carbonate in the salt mixtures caused considerable enhancement of the heat of fusion for Group 1 and 2. On the other hand, there is no significant enhancement for Group 3 in spite of increasing mole fractions of the potassium carbonate. Rather the heat of fusion decreased from that of the eutectic point (42.7 % molar concentration of Li_2CO_3). The heat of fusion for sample 14 has a much smaller value (288.8 [J/g]) than mean value of Group 3 (sample 9

- 14), which is 361.6 [J/g]. Addition of extra potassium carbonate to the mixture, therefore, does not necessarily cause a uniform increase in the heat of fusion.

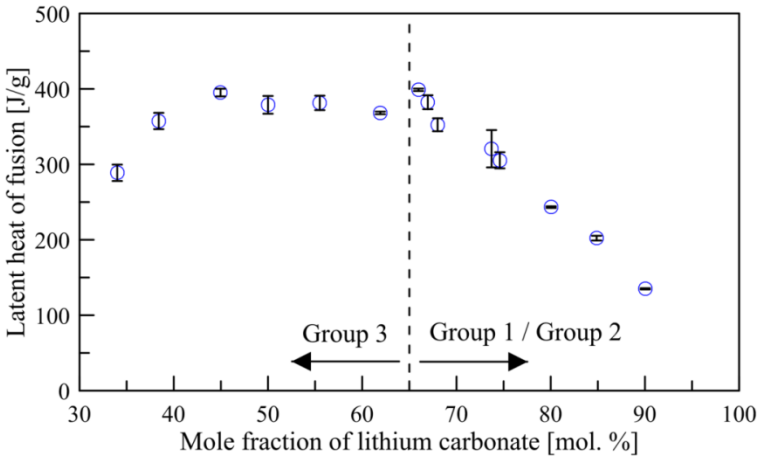

Fig. 4.5 Latent heat of fusion of carbon salt mixtures

4.3.4 Melting point

Melting point values of the carbonate salt mixture are listed in Fig. 4.6. According to Araki et al., the melting point is 488 ℃ for the eutectic composition of 62:38 molar ratio of the lithium carbonate and the potassium carbonate [123]. Assuming that the melting point corresponds to the peak temperature in a DSC endothermic curve, the melting point was measured to be ~500 ℃ (for the same eutectic of 62:38 ratio in this study). Hence, it is not appropriate for the present study to use the peak point of the DSC melting curve to define melting temperature of the carbonate eutectic, since a fast ramping rate was used, which can lead to significant uncertainties in the measurements. Therefore an alternative method was developed to determine the melting point more precisely from the heat flow curves obtained from the DSC experiments. The first

derivative (tangential slope) of heat flow curves with respect to temperature was used to define the melting point of the eutectic. For the eutectic corresponding to 62:38 composition ratio, the slope at 488 ℃ was estimated to be -4. The melting temperature for the salt mixtures was, therefore, determined for the value of the slope corresponding to a value of -4. Fig. 4.6 shows melting point estimated using this method for all the samples used in this study. As shown in the figure, the melting point was linearly decreased from 494 to 486 ℃ for increase in the mole fraction of the lithium carbonate (excluding the case of 50:50 ratio). The sample (corresponding to 50:50 ratio) showed the highest melting temperature of 502 ℃ . This characteristic was also observed by Araki and collaborators [123]. In the present study, it was observed that lithium carbonate concentration has a significant effect on the melting temperature of the carbonate salt mixtures and that the eutectic with 50:50 molar concentration has the highest melting temperature.

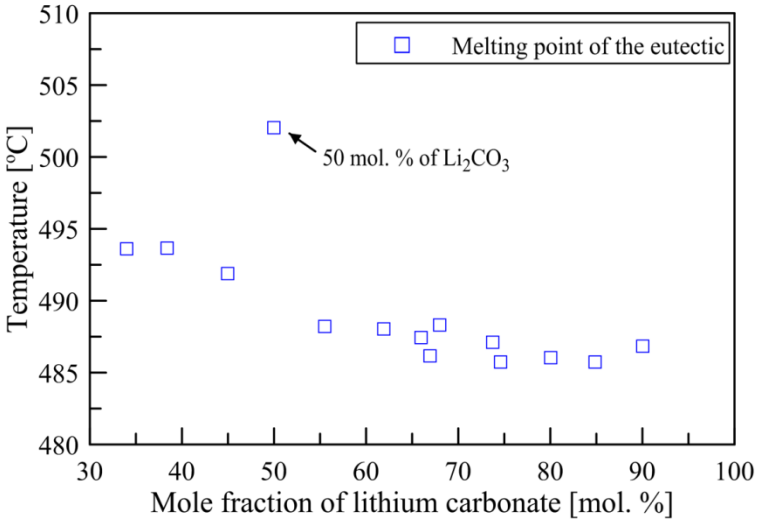

Fig. 4.6 Melting point variation of carbonate salt mixtures

4.4 Discussion

We categorized the carbonate salt eutectics into three groups according to the heat flow curves in the liquid phase. When considering only heat flow changes in the liquid state, the three groups demonstrated unique features. Group 1 showed continuous increase in heat flow with temperature (that is, specific heat capacity) in liquid phase. This can be attributed to the rise in the value of the specific heat capacity for each salt composition with temperature. In previous studies, the specific heat capacity of pure lithium carbonate and pure potassium carbonate in liquid phase were estimated by using two equations shown below [126, 127]. In these equations, t indicates temperature/1000 [K] and T indicates temperature [K].

$$C_P = A + B\cdot \mathrm{t} + C\cdot \mathrm{t}^2 + D\cdot \mathrm{t}^3 + \frac{E}{\mathrm{t}^2} \qquad [\mathrm{J/g\cdot K}] \qquad (4.1)$$

$$C_P = A + B\cdot \mathrm{T}^{-0.5} + C\cdot \mathrm{T}^{-2} + D\cdot \mathrm{T}^{-3} \qquad [\mathrm{J/g\cdot K}] \qquad (4.2)$$

Table 4.2 Coefficients of the correlations in Eq. (4.1), (4.2) and (4.3)

Materials in phase (Equation) [J/mol·K]	A	B	C	D	E
Li_2CO_3 in liquid (Eq. 4.1)	185.4350	-0.000051	0.000030	-0.000006	-0.000003
K_2CO_3 in liquid (Eq. 4.2)	442.6	-8,914	34,278,267	5.240×10^9	N/A
Li_2CO_3 in solid (Eq. 4.3)	68.33230	146.6390	-162.5730	248.0260	-0.702297

Equations (4.1) and (4.2) correlate the specific heat capacity of pure lithium carbonate and pure potassium carbonate in the liquid phase with temperature, respectively. The coefficients are listed in Table 4.2. According to Eq. (4.1) the specific heat capacity of the lithium carbonate is constant in the liquid phase for the temperature range used in this study, Eq. (4.2) shows a marginal increase in the specific heat capacity of the potassium carbonate with temperature. However, the increment is just about 2 %, which is too small to account for the 10 % increase observed in the mixtures. Since the eutectic composition is 62 % molar concentration of lithium carbonate [123], a portion of lithium carbonate in Group 1 might stay as solid (like slurry) at the temperature condition above 500 ℃ . Besides, as the temperature rises, the specific heat capacity of the solid lithium carbonate (as approximated by Eq. (4.3) [126]) is enhanced by 3 % between 525 and 555 ℃ . This could be responsible for the enhancement in the specific heat capacity values of the carbonate salt mixtures for Group 1 samples in the liquid phase.

$$C_P = A + B \cdot \mathrm{t} + C \cdot \mathrm{t}^2 + D \cdot \mathrm{t}^3 + \frac{E}{\mathrm{t}^2} \qquad [\mathrm{J/g \cdot K}] \qquad (4.3)$$

Although the enhancement of the specific heat capacity for the solid lithium carbonate is not as high as in the mixture, the specific heat capacity of the solid lithium carbonate is thought to be more influential on the distinct heat flow observed for samples in Group 1. Similarly, heat flow characteristics in Group 2 and Group 3 are hard to explain using just the temperature dependence of the specific heat capacity of the two

pure salts. Especially, strange heat flow curves in Group 2 were not expected before the tests were performed. As shown in Fig. 4.7, the threshold temperature for the sharp decrease in the specific heat capacity values occurred at high temperatures as the mole fraction of the lithium carbonate was increased. Above all, it was expected that the fluctuations would disappear for salt samples with 70 % molar concentration of lithium carbonate. Consequently the heat flow (specific heat capacity) behaviors of the carbonate salt mixture are not a monotonic function of the concentration of the constituent salts.

To enumerate the variation of specific heat capacity of the mixtures as a function of composition, Fig. 4.8 was plotted. Fig. 4.8 shows theoretical predictions for specific heat capacity of solid and liquid phase by using the simple mixing rule and the thermal equilibrium model.

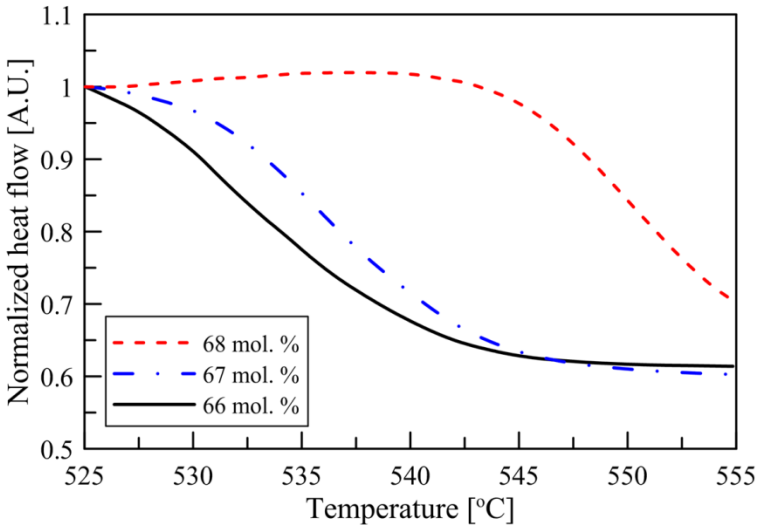

Fig. 4.7 Specific heat capacity of carbonate mixtures in Group 2 as a function of temperature and molar ratio of Li_2CO_3 (Shown in the legend)

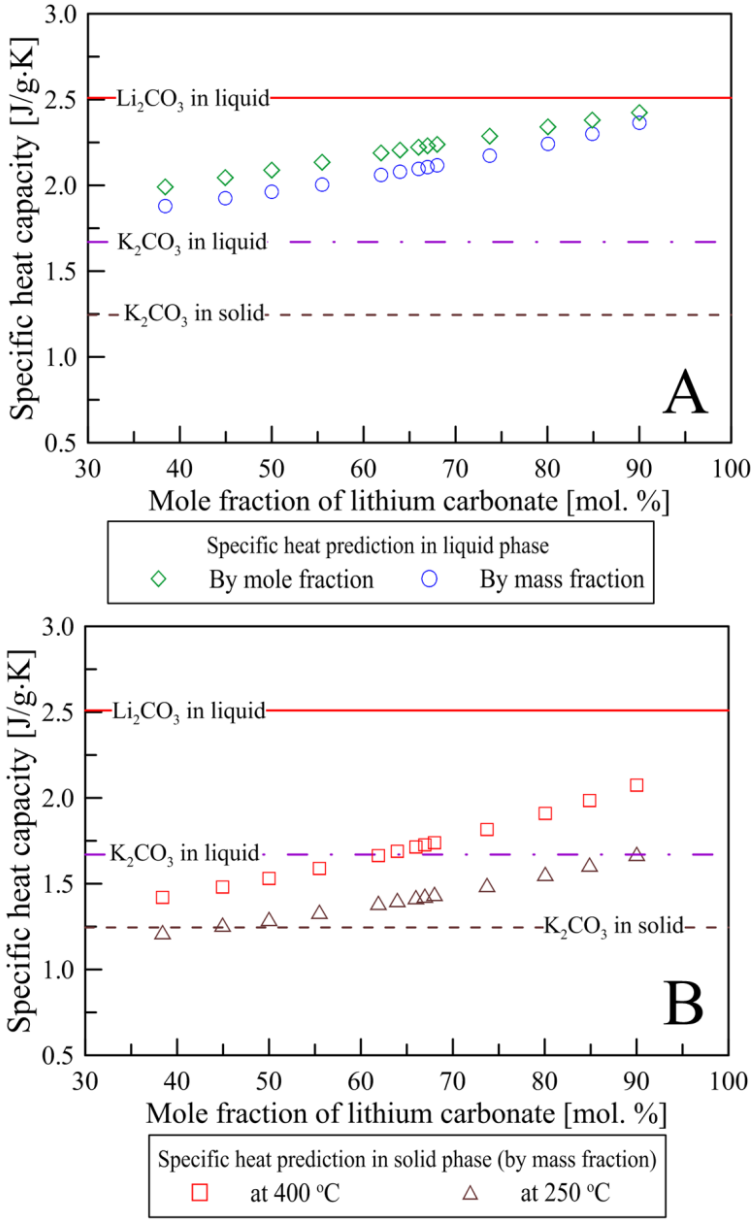

Fig. 4.8 Theoretical predictions of specific heat capacity of carbonate salt mixtures: (A) in liquid phase and (B) in solid phase (at 250 ℃ and 400 ℃)

In Fig. 4.8 (A), both models show linear increase in the specific heat capacity with increasing concentration of lithium carbonate. However, the measured data for the

samples (1-5) was almost uniform regardless of the mole fraction of lithium carbonate. Furthermore, the actual values for both predictions do not match the measured values for the specific heat capacity. The maximum values for the specific heat capacity from the predictions were 2.37 and 2.43 [J/g·K] for sample 1 at 90 % molar concentration of lithium carbonate. Both models predicted values of 2.17 and 2.29 [J/g·K] for sample 5 at 73.7 % molar concentration of lithium carbonate, while the experimental result was significantly higher at 2.50 [J/g·K]. Accordingly, the theoretical models used in this work failed to predict the variation in the specific heat capacity values of the carbonate mixture in Group 1. In addition the experiments showed that there is a threshold concentration of lithium carbonate at which the specific heat capacity values are enhanced drastically, yielding values that are almost identical to that of pure lithium carbonate.

The theoretical models were not able to predict the specific heat capacity of Group 2 as well. The measured results of Group 2 are widely distributed varying from 2.50 to 1.68 [J/g·K], but the models yield very small variations due to the narrow range of concentrations in Group 2. In Group 3, the theoretical models for binary mixtures also failed to predict the observed measurements for the specific heat capacity values (instead of mass fraction). Also, the theoretical estimates using volume fraction produce very similar values (not plotted in Fig. 4.8). Hence, simple mixing rule for predicting the specific heat capacity of the binary mixtures are not applicable to the carbonate salt samples.

Table 4.3 Comparison of the specific heat capacity for liquid phase for Group 3 samples

Measurement		Literature	
Composition ratio (Li_2CO_3 : K_2CO_3) [mol. %]	Specific heat capacity [J/g·K]	Composition ratio (Li_2CO_3 : K_2CO_3) [mol. %]	Specific heat capacity [J/g·K]
(45.0 : 55.0)	1.44	(42.7 : 57.3)	1.49
(50.0 : 50.0)	1.54	(50.0 : 50.0)	1.55
(62.0 : 38.0)	1.61	(62.0 : 38.0)	1.60

While there is no reference in the literature to verify all of these measurements, several specific cases (composition ratios) are available for comparing the specific heat capacity of the mixtures obtained in Group 3. Araki et al. reported the thermo-physical properties of the molten salt mixtures [113]. They tested three composition ratios of the lithium carbonate and the potassium carbonate (42.7:57.3, 50.0:50.0, and 62.0:38.0 in molar ratio), which belong to Group 3. Table 4.3 compares the values of specific heat capacity obtained from the literature with the measurements performed in this study for the same (or similar) composition ratios. They reported constant values of specific heat capacity for three samples in liquid phase, which were 1.49, 1.55, and 1.60 [J/g·K], respectively. These are in a good agreement with the specific heat capacity measured using DSC in this study. The results are 1.44, 1.54, and 1.61 [J/g·K], respectively. Similar values were obtained from the second and the third group of mixtures. For the first sample, a lower value was measured in this study. However, the difference is significantly low. Therefore, the sample preparation protocol and the experimental methods employed in the present study are consistent with the literature data.

Furthermore, the specific heat capacity results for Group 2 and Group3 were considered to be more reliable, since the measurement uncertainty for these samples was lower (compared to that of Group 3).

According to the reference by Janz et al., the latent heat of fusion for the carbonate eutectic with 50:50 mole fraction is reported to be 343 [J/g] [106]. For the mixture with the same composition, mean heat of fusion measured in this study is 379 [J/g]. Though this measurement was 10 % higher than the literature data, this difference is consistent with the measurements uncertainties corresponding to a heating rate used in DSC [128]. As shown in Fig. 4.5, the latent heat of fusion for the mixtures is strongly dependent on the compositions of the two salts. Reducing the proportion of lithium carbonate down to 67 % molar concentration increased the enthalpy of fusion of the mixture. However, the heat of fusion was observed to be constant for the mixtures with lithium carbonate concentration exceeding 67 % molar concentration. It is difficult to predict the liquid phase specific heat capacity of the carbonate mixtures for these two salts.

From the previous study, basically heat of fusion for lithium carbonate and potassium carbonate are 605.9 and 200 [J/g] with melting point of 720 ℃ and 901 ℃ , respectively [122]. Since the lower limit of the composition of the mixture at which the two salts are in liquid phase is 62 % molar concentration of the lithium carbonate, some lithium carbonate stays as solid at the temperature range above 500 ℃. For samples with concentrations significantly different from the eutectic range, the heat of fusion in Group 1 and Group 2 can be predicted by a simple algebraic equation by calculating the mass fractions of the two salts in the liquid phase (where the mass fraction is computed based

on the total mass of the mixture). In other words, the mass fraction of the salt mixture for the samples (which have different compositions from that of eutectic) was calculated by assuming that the liquid phase composition to be of the eutectic composition (62:38 mole fraction for Sample No. 1-8; 42.5:57.5 molar fraction for Sample No. 13-14). For Sample No. 9-12 it was assumed that the salt mixture was completely melted and therefore the liquid mass fraction was calculated based on the original mixing ratio of the two salts in the mixture. Subsequently, the heat of fusion for these samples was estimated by using a simple mixing rule based on the mass fraction of the two salts in the liquid phase only (where the total mass of the mixture consists of both the solid phase and the liquid phase, except for Sample No. 9-12).

Table 4.4 shows a comparison of the predictions for the heat of fusion using this technique for the different samples used in this study. The table shows that the predictions from this method have an error of ~10-20% for Group 1 samples and ~15% for Group 2 samples. In contrast the error is low for Group 3 samples (~5-10%) for composition values that are closer to the eutectic composition (Sample Nos. 9-11). However, larger errors from the prediction are observed (~20%) when the composition of the sample deviates by a large margin from that of the eutectic composition (Sample Nos. 12-14). Hence, this method provides a simple way to estimate the heat of fusion of carbonate salt mixtures within reasonable accuracy for compositions that are closer to the eutectic composition but can also be used for obtaining a preliminary estimate for other compositions of the mixture.

Table 4.4 Prediction and measurement values of heat of fusion

Group	No.	Original composition [mole fraction]		Composition of liquid [mass fraction]		Heat of fusion [J/g]		
		Li_2CO_3	K_2CO_3	Li_2CO_3	K_2CO_3	Prediction	Measurement	Error [%]
1	1	90.0	10.0	14.9	17.2	124.6	135.0	8
	2	84.9	15.1	21.7	25.0	181.7	202.2	10
	3	80.0	20.0	27.6	31.8	231.1	243.3	5
	4	74.6	25.4	33.8	38.9	282.7	320.7	12
	5	73.7	26.3	34.8	40.0	290.6	352.5	18
2	6	68.0	32.0	40.7	46.8	340.1	382.4	11
	7	67.0	33.0	41.7	48.0	348.8	398.8	13
	8	66.0	34.0	42.7	49.1	356.8	413.3	14
3	9	62.0	38.0	46.5	53.5	388.7	368.2	6
	10	55.5	44.5	40.0	60.0	362.4	381.4	5
	11	50.0	50.0	34.8	65.2	341.3	378.9	10
	12	45.0	55.0	30.4	69.6	323.4	395.2	18
	13	38.4	61.6	25.0	62.7	276.9	357.5	23
	14	34.0	66.0	21.6	54.2	239.3	288.8	17

Heat of Fusion: (1) Li_2CO_3 - 605.9 [J/g], (2) K_2CO_3 - 200.0 [J/g]

Janz et al. reported the melting temperatures at the two limits of the eutectic ratio: 498 ℃ for 42.7:57.3 and 488 ℃ for 62:38 [106]. Thus melting point for the samples with lithium carbonate concentration exceeding 62 % molar concentration should be at 488 ℃. As shown in Fig. 4.6, melting temperatures were consistent with this observation in Group 1, Group 2, and some of the mixtures in Group 3. The melting point for the rest of samples in Group 3 was increased with the mole fraction of

potassium carbonate. Much higher melting temperature was observed for the eutectic with 50:50 molar ratio, and is in good agreement with literature data [123].

4.5 Conclusion

For an alkali carbonate salt mixture which is composed of the lithium carbonate and the potassium carbonate, calorimetric measurements and analyses were performed for the thermo-physical property values for the both solid and liquid phase using a DSC. The specific heat capacity, the heat of fusion, and the melting temperature were measured from the DSC experiments. In order to examine the effects of the composition on the thermal properties, 14 samples with different chemical compositions were tested in this study. Based on the heat flow data in the liquid region, the samples were classified into 3 groups, which showed distinct behavior not only for specific heat capacity of the liquid carbonate salt mixtures but also for other properties, such as the heat of fusion and the melting temperature. The knowledge gained from the analytical exercise is summarized as follows:

(a) The specific heat capacity of the liquid mixtures, including that of the samples with lithium carbonate concentration exceeding 73.7 % molar concentration was increased with temperature (Group 1). For the samples with mole fractions between 68 % and 66 % molar concentration, specific heat capacity decreased drastically with temperature (Group 2). The remaining samples at the lithium carbonate molar

concentration less than 62 % demonstrated constant values of specific heat capacity in the liquid phase (Group 3).

(b) The specific heat capacity of the mixtures in the liquid phase was changed drastically on varying the mole fraction of lithium carbonate. For the Group 1 samples, the specific heat capacity values in the liquid phase matched that of pure lithium carbonate. For Group 2, the specific heat capacity in the liquid phase was drastically decreased with a decrease in concentration of the lithium carbonate. For Group 3 samples, the specific heat capacity values changed linearly. However, the specific heat capacity of the salt mixtures in solid phase (at 250 and 400 ℃) linearly increased with an increase in concentration of mole fraction of lithium carbonate for all the samples used in this study.

(c) The theoretical models (which are based on mass ratio and on molar ratio) failed to predict the specific heat capacity of the mixtures in both liquid and solid phases.

(d) The latent heat of fusion for the carbonate salt mixtures was significantly decreased for the samples with change in concentration, and was significantly different from that of the samples at the eutectic composition. For Group 1 and 2 samples, the lithium carbonate was not fully melted in the temperature range of interest. Hence, the heat of fusion was decreased with increasing mole fraction of lithium carbonate. A simple algebraic equation enables the prediction of the heat of fusion within reasonable accuracy for salt mixtures with composition similar to that of the eutectic mixture (and also provides a good estimate for the heat of fusion values for other compositions of the mixtures as well).

(e) Significant variation in the melting points of the carbonate mixtures was observed in the DSC experiments. Additionally, the highest melting point was observed for the sample of 50:50 composition ratio, whose melting temperature was measured to be about 502 ℃ from the DSC experiments.

5. EXPERIMENTAL STUDY II: EFFECT OF CNT CONCENTRATIONS

5.1 Objective

The effect of nanoparticle (carbon nanotube) concentrations on the specific heat capacity of the nanomaterials was examined for four concentrations. As described in the previous section, three different temperature ranges were chosen to compare the values of the specific heat capacity: in the sold phase (250 ℃ and 400 ℃) and in the liquid phase (525 ℃ to 555 ℃). Electron microscopy images were obtained for both pre-DSC samples and post-DSC samples in order to check the uniformity of dispersion of the nanotubes in the salt. Images were also used to verify if significant changes occurred in the post-DSC samples during repeated thermal cycles in DSC. Finally, the comparison of the specific heat capacity between the experimental measurements and the theoretical predictions by a classical model are also discussed.

5.2 Nanomaterial synthesis

Fig. 5.1 shows the schematic of the procedures that were used to synthesize the carbonate salt eutectic-CNT nanomaterials for specific heat capacity measurements, where the base material (solvent) has the eutectic composition (62:38 in molar ratio). Initially, the CNT was dispersed in distilled water. For uniform dispersion of the CNT in water, a surfactant, sodium dodecyl sulfate (SDS, Sigma Aldrich) was dissolved in pure water. The SDS (at a mass concentration of 1 %) with respect to the eutectic-CNT

nanomaterial was added and then the colloid was subjected to sonication in an ultrasonic bath for two hours. The aqueous salt solution was mixed with additional volumes of water and the aqueous CNT nanofluid. Then the suspension was sonicated again for three hours. Immediately after the sonication process, the water was evaporated using a syringe pump to obtain dry samples: the suspension was dispersed drop-by-drop on a beaker placed on a hot-plate at 250 ℃. Since SDS can be readily decomposed by prolonged heating at temperatures over 40 ℃ [129], the syringe method was employed to avoid agglomeration of the CNT. In order to confirm whether the CNT was well mixed with the salt eutectic, transmission electron microscope (TEM, JEOL JEM-2010) was used to obtain images of the nanomaterial for a pre-DSC sample. A TEM image for the pre-DSC sample is shown in Fig. 5.2. From this image it can be observed that the salt eutectic mixed homogeneously with the carbon nanotubes.

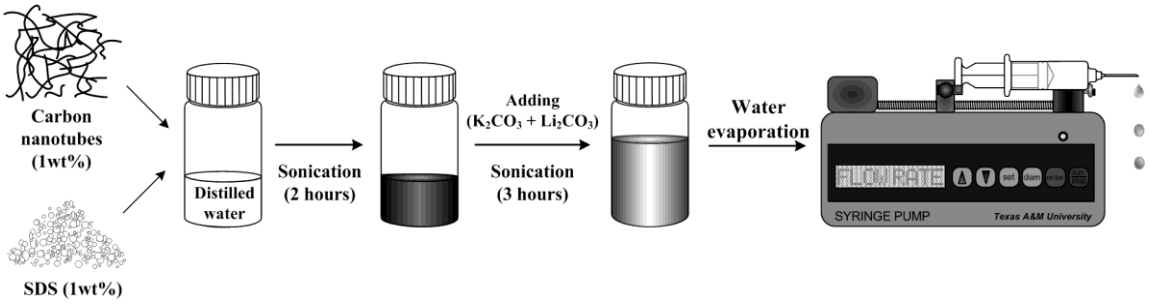

Fig. 5.1 Schematic of procedures for synthesizing nanomaterials

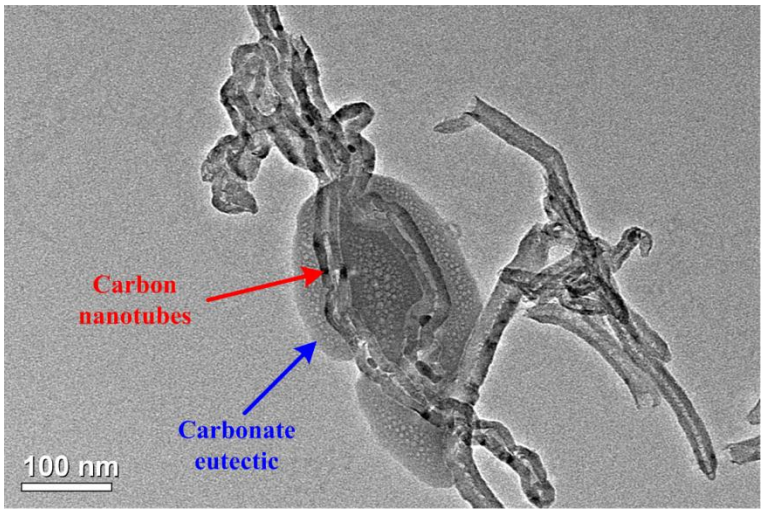

Fig. 5.2 TEM image of nanomaterials synthesized by mixing carbonate salt eutectic with CNT

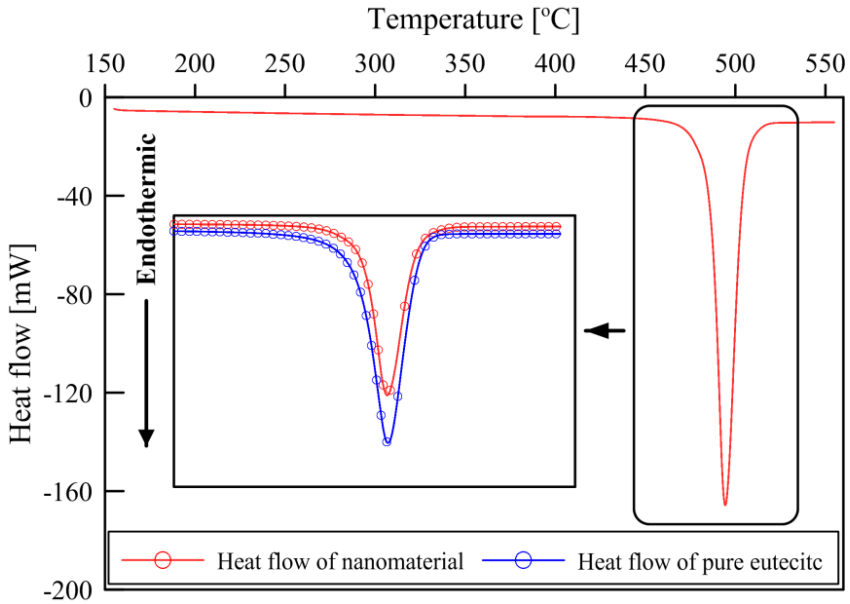

Fig. 5.3 Comparison of typical heat curves obtained from DSC experiments for a pure eutectic sample and a nanomaterial sample.

5.3 Results

5.3.1 Specific heat capacity of nanocomposites (nanomaterial in solid phase)

Fig. 5.3 shows the heat flow curves of a salt sample (molten-salt eutectic mixture) and a nanomaterial sample (containing CNT at mass concentration of 5 %). Comparing the two curves it is observed that there is only a marginal difference in the magnitude of the heat flow curves for the two samples and there was a slightly lower melting point for the nanomaterial sample. It should be noted that the magnitude of heat flow curves depends on the amount of samples loaded in the test pan. Accordingly, it can be presumed no chemical reaction occurred between the salt eutectic and the CNT (including SDS) over the whole temperature range in which measurements were performed.

The specific heat capacity of the nanocomposites and the enhancement at 250 °C for four different concentrations of CNT is shown in Fig. 5.4. A simple correlation for the specific heat capacity of the pure carbonate salt eutectic at a certain temperature range suggested by Araki et al. was presented in Eq. (5.1) [123].

$$c_P = 0.562 + 1.16\times10^{-3}\cdot T \quad \left[\mathrm{J/g\cdot K}\right] \left(365 \le T \le 631\mathrm{K}\right) \tag{5.1}$$

where, T indicated the absolute temperature. At 250 °C the literature value is 1.169 [J/g·K] and similarly, the experimental value obtained in our previous study was 1.188 [J/g·K], which is marginally different from the literature data but can be considered to be in reasonable agreement [60]. Compared with the specific heat capacity of the pure eutectic (1.188 [J/g·K]), the measured specific heat capacity for the various

concentrations of CNT were observed to be enhanced. As shown in Fig. 5.4, the specific heat capacity at the lowest concentration of CNT explored in this study (0.1 % mass concentration), was 1.236 [J/g·K], which corresponds to the enhancement of about 4.0 %; and is within the margins of the measurement uncertainty (~3 %). As the mass concentration of CNT was increased to 5 %, the specific heat capacity was also increased by up to 12 %.

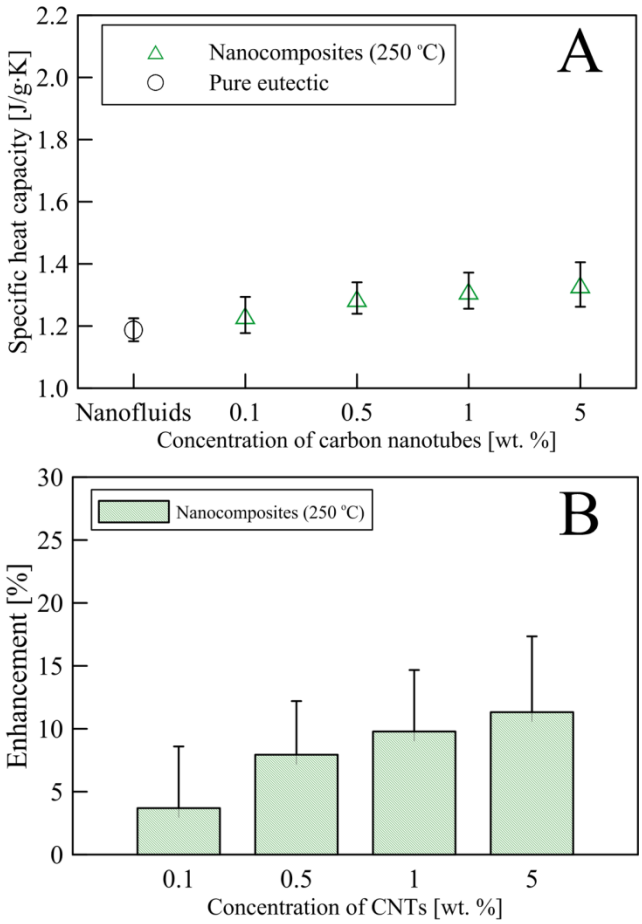

Fig. 5.4 (A) Specific heat capacity and (B) enhancements of the nanocomposites in solid phase (250 °C) as a function of CNT mass concentration.

A similar behavior in the specific heat capacity of the nanocomposites was obtained both for 400 ℃ and 250 ℃. Fig. 5.5 shows the specific heat capacity of the nanocomposites and the corresponding enhancements at 400 ℃. At the CNT mass concentration of 0.1 %, almost the same specific heat capacity as that of the pure eutectic was obtained. At higher concentration of CNT larger enhancement in the specific heat capacity values were observed. The highest enhancement obtained at 5 % mass concentration of CNT was 12.0 % (which is similar to 12.3 % observed at 250 ℃).

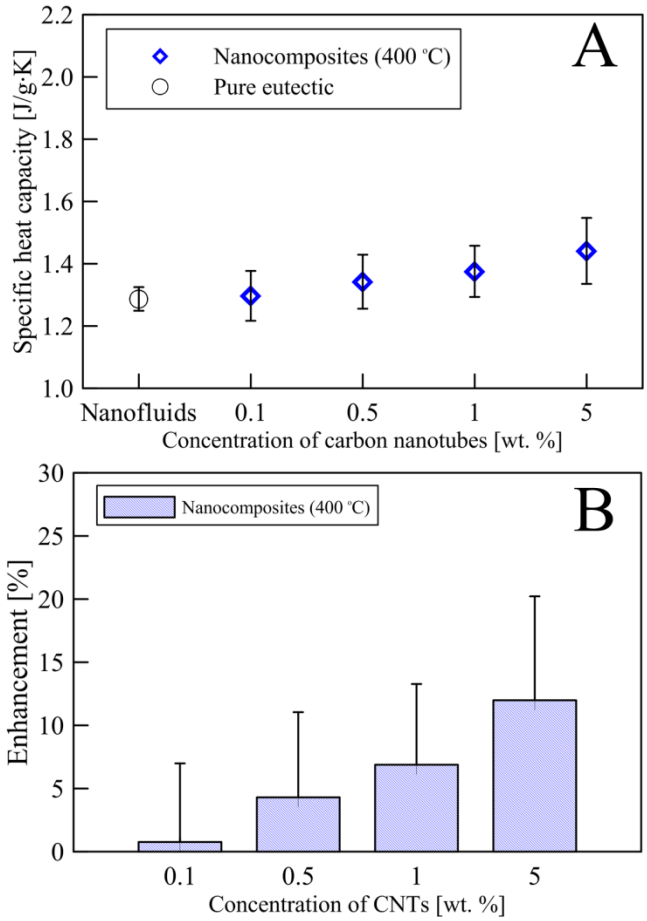

Fig. 5.5 Plots for (A) specific heat capacity and (B) enhancements for the nanocomposites (in solid phase) at 400 °C as a function of mass concentration of CNT

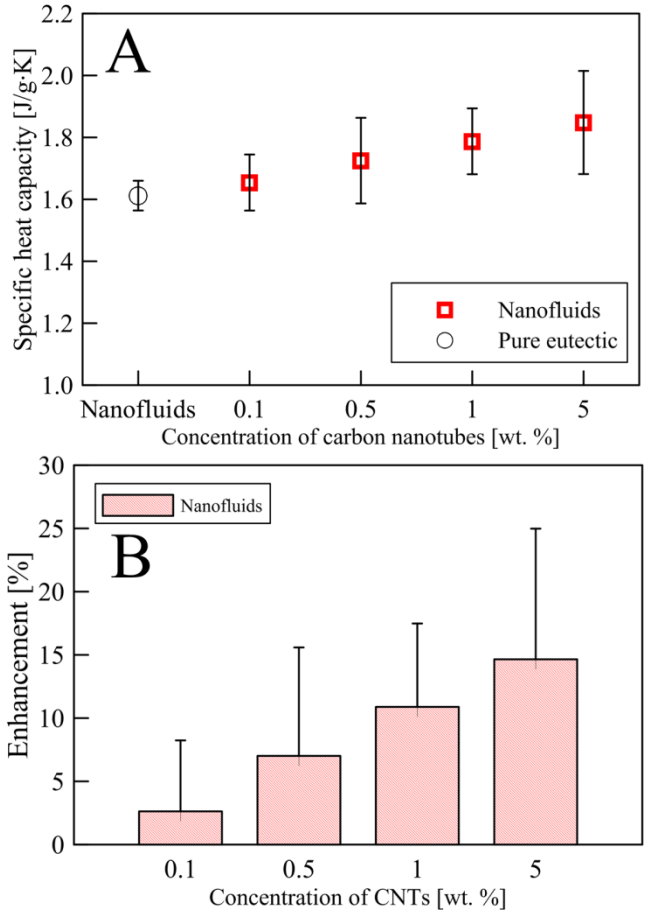

Fig. 5.6 Plots for (A) Specific heat capacity and (B) enhancements of the nanofluids as a function of CNT mass concentration

5.3.2 Specific heat capacity of nanofluids (liquid phase)

The specific heat capacity of the nanofluid samples (in liquid phase) was also measured in the present study. In the literature, Araki and collaborators experimentally measured the heat capacity of the pure carbonate salt eutectic and they reported a constant value of 1.6 [J/g·K] [123]. The specific heat capacity measured in this study was 1.612 [J/g·K] and was utilized to establish a baseline value for calculating the enhancements in the specific heat capacity for nanofluids [60]. Fig. 5.6 shows the results

for the enhancement of the specific heat capacity in the liquid phase. The concentration dependence of the nanofluid specific heat capacity (in liquid phase) was significant. The specific heat capacity values were enhanced significantly with increasing concentration of CNT. The most remarkable feature in the liquid phase was the relatively larger enhancements (than those in both at the solid phase results). In the liquid phase the specific heat capacity of the nanomaterial was significantly increased by up to 14.7 % on mixing with CNT at mass concentration at 5 %.

5.3.3 Theoretical prediction of specific heat capacity

A theoretical model (thermal equilibrium model), which is based on the mass fraction of nanoparticles (in the mixture) was proposed to predict the specific heat capacity of mixtures [130] and has been used to validate the experimental results for the specific heat capacity of several nanofluids in previous literatures [53], as shown in Eq. (5.2). This theoretical model was used in this study to predict the specific heat capacity of the nanomaterials and to compare these predictions with the experimental measurements for different concentrations.

$$c_{P,nf} = \frac{m_n \cdot c_{P,n} + m_{bf} \cdot c_{P,bf}}{m_n + m_{bf}} \tag{5.2}$$

where, m is the mass fraction, c_p is the specific heat capacity, subscript, n, indicates the nanoparticle, and subscript, bf, indicates the base fluid (solvent) properties. Using the

thermal equilibrium model in Eq. (5.2), the specific heat capacity of the nanofluids (nanomaterial samples in the liquid phase) was predicted as a function of the nanoparticle concentration. The specific heat capacity values of the eutectic, the graphite, and CNT at three different temperatures are listed in Table 5.1. The specific heat capacity for the nanoparticles (CNT) which is needed to theoretically estimate the specific heat capacity of the nanofluid was obtained from graphite value [115]. The theoretical predictions for the specific heat capacity values were plotted as a function of the temperature and the concentration of CNT in Fig. 5.7. As expected, larger enhancements in specific heat capacity of the nanofluids with increasing amounts of CNT were observed. However, the theoretical predictions did not match the experimental data. Also, when the specific heat capacity of CNT (generally referred to as C_v) was replaced with the higher value measured for single walled carbon nanotubes network [116], the prediction form the thermal equilibrium model did not match the experimental data.

Table 5.1 Specific heat capacity of pure carbonate salt eutectic, graphite and carbon nanotubes

Temperature	Carbonate eutectic [J/g·K]	Graphite [115] [J/g·K]	Carbon nanotube network [116] [J/g·K]
250 °C	1.188	1.25	1.79
400 °C	1.287	1.50	1.88
525 - 555 °C (Liquid phase)	1.612	1.66	1.97

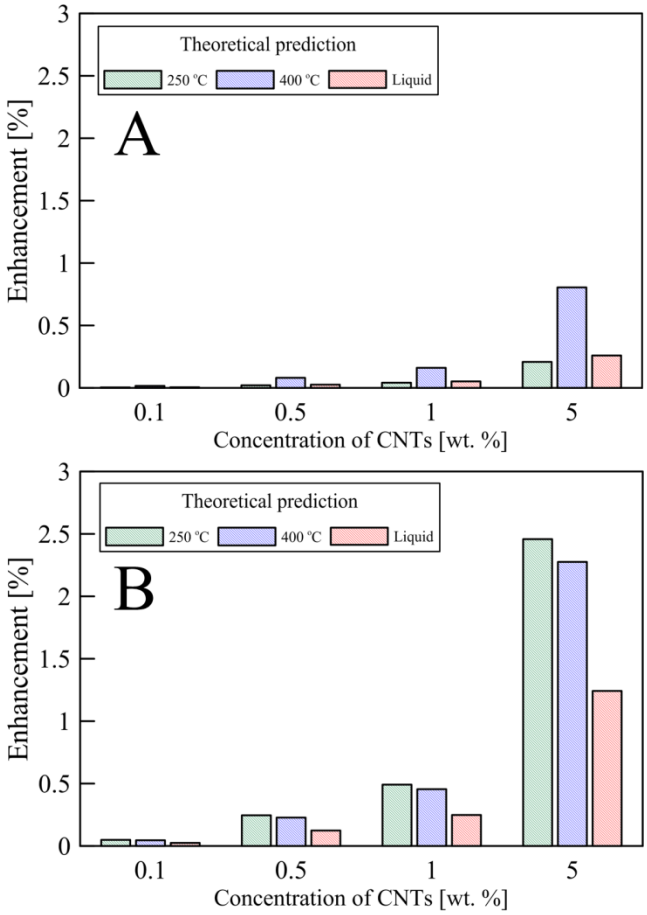

Fig. 5.7 Theoretical prediction for specific heat capacity in the nanomaterials using thermal equilibrium model: (A) using the specific heat capacity of graphite and (Bottom) using the specific heat capacity of single walled carbon nanotubes network

5.4 Discussion

The lack of agreement between predictions from the theoretical model and the experimental data can be explained to be due to several factors. First, the specific heat capacity of the nanoparticle (nanotubes in this study) is likely to be drastically increased. Wang et al., calculated the specific heat capacity of a nanoparticle and also investigated the effect of the particle size and the temperature [131]. In their paper, they showed that

the specific heat capacity can be enhanced with decrease in the size of the nanoparticle and with increasing temperature. Nelson et al. pointed out this effect as a possible reason for the enhanced specific heat capacity of the PAO-graphite nanofluids [56]. However, the specific heat capacity of the carbon nanotubes need to be enhanced by up to ~350 % (at the temperature where the eutectic exists in liquid), for the theoretical model to match the experimental results. Therefore, although the enhanced specific heat capacity of the nanoparticles might be a significant contributor, it does not account for the observed enhancements for the specific heat capacity of the nanofluids.

As shown in the MD simulations, a dense layer of liquid molecules ("compressed layer") is formed at the interface with the nanoparticles. As shown in Fig. 5.8, Oh et al. reported that the ordered liquid aluminum atoms adjacent to crystalline interface was experimentally observed at the interface with sapphire [121]. Many molecular dynamics simulations, as well as the experimental observation by Oh et al., showed the formation of a dense (compressed) layer with a certain thickness at the interface between a solid nanoparticle and liquid molecules, for instance at the water-CNT nanofluid [112]. This portion of the solvent phase (or layer) in which the solvent molecules acquire an ordered structure (forming a compressed phase) by mimicking the underlying lattice structure of the nanoparticle surface atoms (as opposed to the random motion of the molecules in the bulk liquid phase) can be regarded to acquire a quasi-crystalline structure and can amplify the capability for thermal energy storage (as well as other materials properties such as density and viscosity) in the nanofluid. Hence, the specific heat capacity of the nanofluid can be modified significantly by doping with a minute concentration of the

nanoparticles in the salt samples. The compressed region of the liquid molecules is expected to play a significant role for the enhancement of the specific heat capacity of the nanofluids. For the specific heat capacity enhancements in solid phase, the increase in the specific heat capacity of the nanotubes themselves with temperature might play a more dominant role in raising the specific heat capacity. Relatively small enhancements of the specific heat capacity in solid phase can support this particular hypothesis.

Based on the contribution from the interfacial compressed layer on the specific heat capacity, higher levels of enhancements are expected to occur in the liquid phase. Fig. 5.9 shows the SEM images of a pre-DSC sample and a post-DSC sample (with 5 % mass

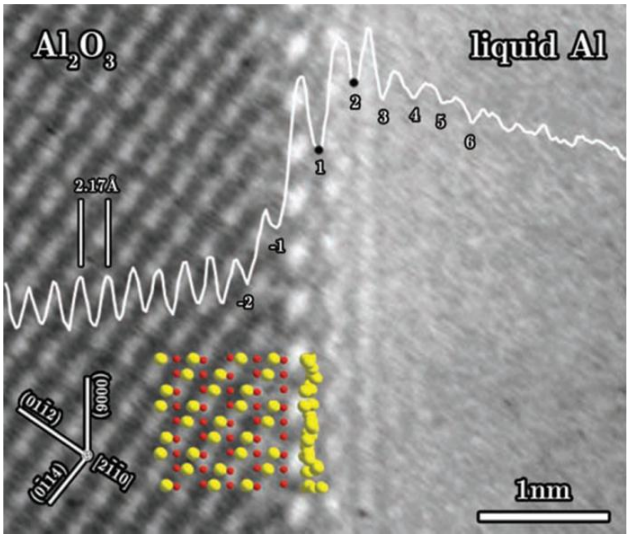

Fig. 5.8 Magnified area from a movie image by high-resolution transmission electron microscopy (HRTEM); atom positions in the Al_2O_3 (red for oxygen, yellow for aluminum) and an average intensity line scan perpendicular to the interface (white line)

Note: Reprinted with permission from "Ordered Liquid Aluminum at the Interface with Sapphire" by S. H. Oh, Y. Kauffmann, C. Scheu, W. D. Kaplan, M. Ruhle, 2005, *Science*, 310, pp. 661-663, Copyright 2005 by the American Association for the Advancement of Science (AAAS).

concentration of CNT). While some of the nanotubes are observed to exist individually in the eutectic, a large amount of agglomerated CNT is observed in the image. Hence, better dispersion of the CNT can enable larger enhancement in the specific heat capacity of the nanofluid. In previous studies, the effect of the liquid layering on the solid particle interface has been discussed to be a significant contributor to the dramatically enhanced thermal conductivity of nanofluids [94, 132, 133]. Accordingly, it can be expected that the thermal conductivity of the molten salt eutectic can also be augmented by dispersing nanoparticles.

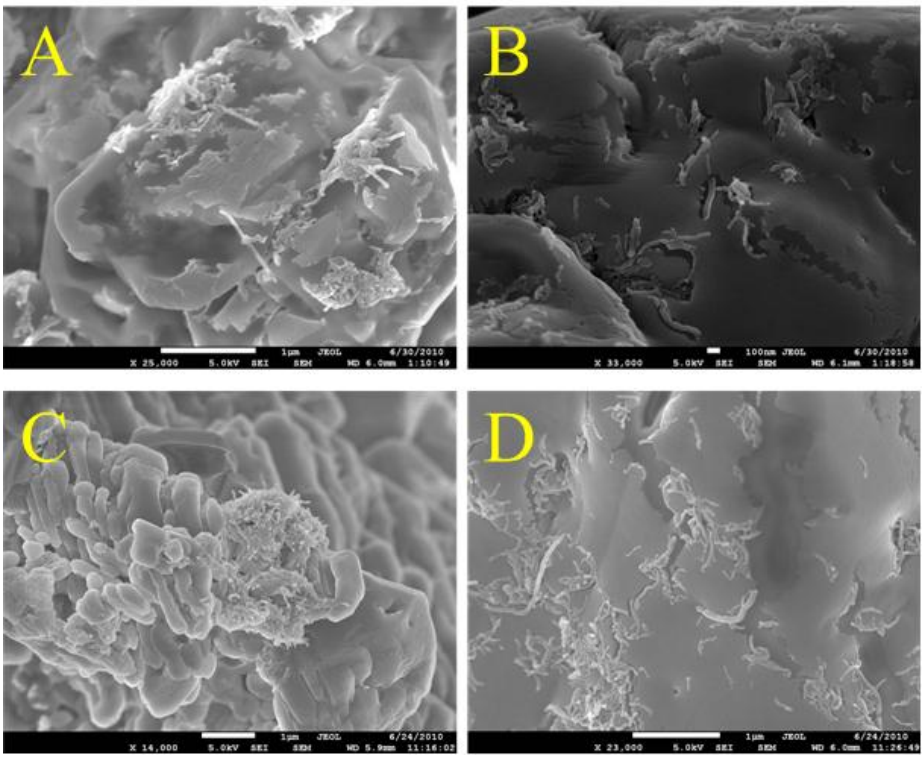

Fig. 5.9 SEM images of a pre –DSC sample (A, B) and a post-DSC sample (C, D)

In the present study, the specific heat capacity of the carbonate salt eutectic was enhanced by doping them with CNT and the level of enhancement was much higher than the theoretical predictions. Since the thermal equilibrium model for determining the specific heat capacity of mixtures is a function of the specific heat capacity and mass fractions of the constituents, variations in the specific heat capacity of the nanofluids are, to some extent, dependent on the amount of nanoparticles and their properties. Thus, the additions of CTN at small concentration cannot account for the significant level of enhancement of the specific heat capacity values that were observed in the experiments. Hence, there is a contradiction between the experimental results and the theoretical predictions. Although the theoretical model was in good agreement with the data for the specific heat capacity of aqueous nanofluids [53], these studies reported degradation in the specific heat capacity of the aqueous nanofluids. Consequently, it is expected that the theoretical model may be applicable only to limited cases, potentially in situations where the nanoparticles are agglomerated to form larger sized particles. Therefore, a new theoretical model which can be applicable for all nanofluids is needed.

5.5 Conclusion

The specific heat capacity enhancements for the carbonate salt eutectic based CNT nanomaterials were observed for both solid and liquid phase. The effect of the CNT concentrations was investigated in this section. In addition, the experimental results were compared with the theoretical predictions. The knowledge gained from these experiments is summarized as follows:

(a) The specific heat capacity was significantly enhanced by up to about 15 % in the liquid phase by dispersing multi-walled carbon nanotubes at 5 % mass concentration in the carbonate salt eutectic. Also, even at a minute level of mass concentration of CNT (0.1 %) the specific heat capacity was enhanced in liquid phase. Moreover, in solid phase, the specific heat capacity was enhanced by ~12 % for the nanomaterial samples obtained by mixing CNT at 5 % mass concentration.

(b) The specific heat capacity of the nanomaterials increased monotonically with the increase in concentration of CNT. The enhancement was higher in liquid phase than in solid phase. This implies that a potentially novel transport mechanism exists exclusively in the liquid phase (or the transport mechanism may be more dominant in the liquid phase).

(c) The uniformity of CNT dispersion was confirmed by TEM images for pre-DSC samples. In addition, no significant difference in the SEM images between the pre-DSC samples and the post-DSC samples were observed.

(d) Theoretical prediction for the specific heat capacity values was obtained using an analytical model (simple mixing rule). However, the prediction form the theoretical

model did not match the enhancement for the specific heat capacity values, as observed in the experimental measurements. This shows that the literature model (which is based on mixing properties of immiscible substances or phases) is limited in applicability. Better theoretical models are therefore required to estimate the specific heat capacity of mixtures, especially for the nanomaterial samples.

6. EXPERIMENTAL STUDY III: EFFECT OF SYNTHESIS CONDITIONS

6.1 Objective

To examine the effect of dispersion homogeneity of nanotubes in the base material, the evaporation temperature (for the hotplate settings) were varied from 120 ℃ to 160 ℃ in order to obtain the samples of dehydrated nanomaterials. It is expected that the amount of agglomerated nanotubes decreases with increasing evaporation temperature (shorter elapsed time for evaporation). Additionally, in order to obtain well dispersed water/CNT nanofluid, which is necessary for obtaining the salt/CNT mixture, several surfactants were used, which include: sodium dodecylbenzene sulfonate (SDBS), sodium dodecyl sulfate (SDS), and Gum Arabic (GA). All three surfactants are well known to be effective for dispersing carbon nanotubes in water [134]. The specific heat capacity values of the nanofluid samples for each surfactant composition were compared mutually for deciding the most appropriate surfactant composition for synthesizing the molten salt nanomaterials. The uniformity of CNT dispersion in the salt samples was discerned by using electron microscopy images for both pre-DSC and post-DSC samples. Finally, the theoretical predictions were compared with the experimental results.

6.2 Nanomaterial synthesis

Fig. 6.1 shows a schematic for the synthesis procedure for the carbonate salt-CNT nanomaterial. Initially, CNT at 1 % mass concentration was dispersed into distilled

water using a surfactant (1 % mass concentration) in order to prevent the agglomeration of the CNT. Then, the aqueous CNT suspension was sonicated in an ultrasonic bath for two hours. After the sonication step, water/salt solution was added to the aqueous CNT nanofluid. The suspension was sonicated again for three hours. Finally, in order to obtain the dehydrated samples, the suspension was evaporated on a hot plate. In this process, three settings on the hotplate were used for dehydration of the salt solution (nanofluids) - 120 ℃, 140 ℃, and 160 ℃. These temperature settings of the hotplate were varied to examine the effect of the evaporation temperature, or the evaporation time, on the specific heat capacity of the nanomaterials. Fig. 6.2 represents the durations for water to be evaporated completely at each temperature and for each surfactant. It was observed that the duration for complete evaporation linearly decreased with increase in the temperature setting of the hotplate. The durations were similar for the same temperature condition regardless of the surfactants used. In order to prevent undesired agglomerations of CNT, the procedure for the nanomaterial synthesis (shown in Fig. 6.1) was performed for each sample.

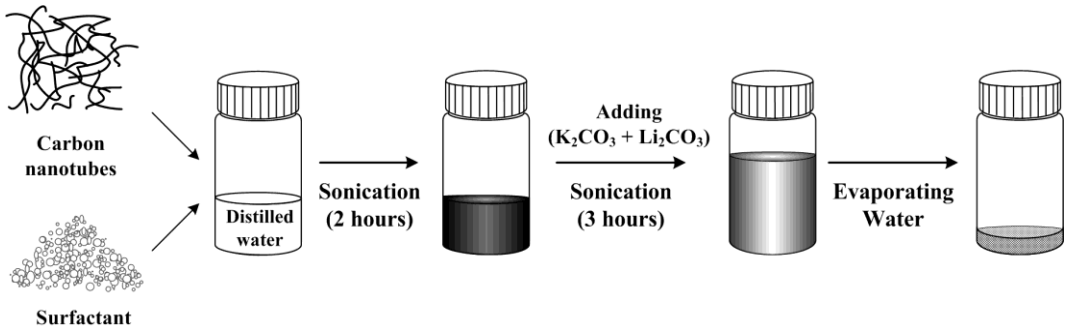

Fig. 6.1 Schematic for the synthesis procedure for nanomaterials

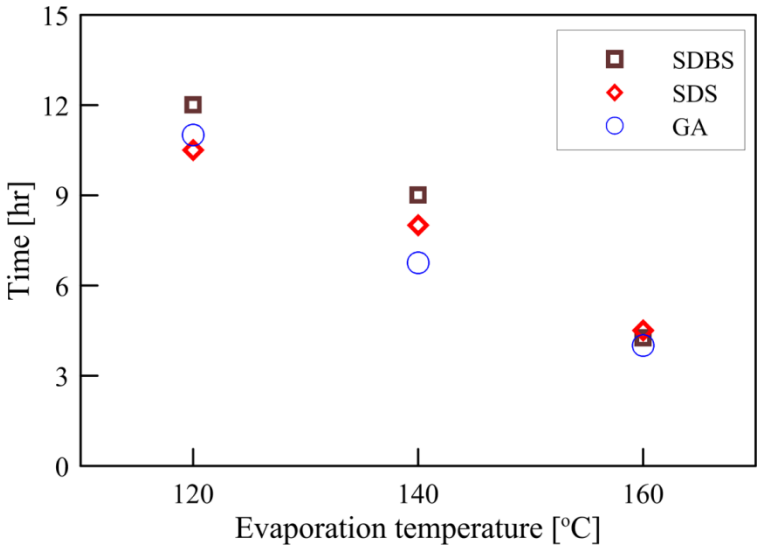

Fig. 6.2 Duration for water evaporation for nanomaterial sample with different surfactants

6.3 Results and discussion

6.3.1 Effects of surfactants and duration for complete evaporation

Fig. 6.3 shows the mean specific heat capacity of the nanofluids (in the liquid phase): using SDBS, SDS, and GA. The specific heat capacity was enhanced under all evaporation temperature conditions. However, the enhancements in the specific heat capacity were not identical among the nanofluids. Also, relations between the specific heat capacity and the evaporation temperature were observed to vary for different surfactants.

The specific heat capacity results of the nanofluids using SDBS are shown in Fig. 6.3. As shown in this figure, the enhancement in the specific heat capacity values was measured consistently regardless of the evaporation temperature even though a large standard deviation was obtained for the evaporation temperature of 120 ℃ . However,

there were no significant enhancements in the specific heat capacity values. Considering the uncertainty of DSC measurements, the specific heat capacity values obtained for the nanofluids using SDBS were not significantly different from that of the pure eutectic samples. The specific heat capacity of the nanofluids using SDS is shown in Fig. 6.3. The specific heat capacity was increased with increase of the evaporation temperature from 1.766 [J/g·K] at 120 ℃ to 1.901 [J/g·K] at 160 ℃ . Hence, SDS is more effective for dispersing the carbon nanotubes into the aqueous salt solution.

The results for nanofluids (synthesized using GA) are shown in Fig. 6.3. Compared with the previous results for the other two surfactants, the specific heat capacity of the nanofluids using GA were relatively higher and also show better stability for the evaporation temperature employed in this study. The highest specific heat capacity was 1.964 [J/g·K] at 160 ℃ , which corresponds to an enhancement of ~22 %. Interestingly, the specific heat capacity enhancement of the nanofluids using SDS was almost doubled by increasing the evaporation temperature from 120 ℃ to 160 ℃ . In contrast, upon using GA, the enhancement in the specific heat capacity of the nanofluids (in the liquid phase) was identical for all of the samples. The maximum enhancement was obtained for an evaporation temperature of 160 ℃ sample using GA. In other words, the faster evaporation did affect the specific heat capacity enhancement of the nanofluids using GA. Fig. 6.4 shows the specific heat capacity of the nanocomposites in the solid phase for the three surfactants. Similarly to the liquid phase, the nanocomposites using GA showed higher level of enhancements in the specific heat capacity than the other samples

using SDS or SDBS. The values were consistent regardless for the evaporation temperatures.

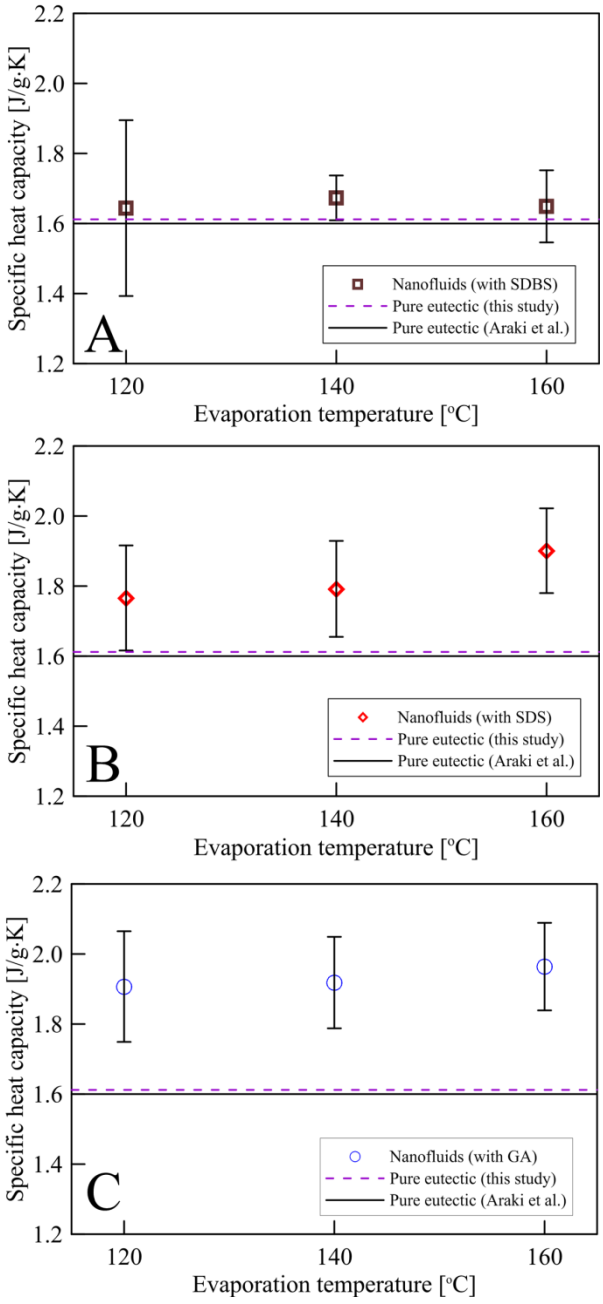

Fig. 6.3 Specific heat capacity of nanofluids for various evaporation temperatures using: (A) SDBS, (B) SDS, and (C) GA

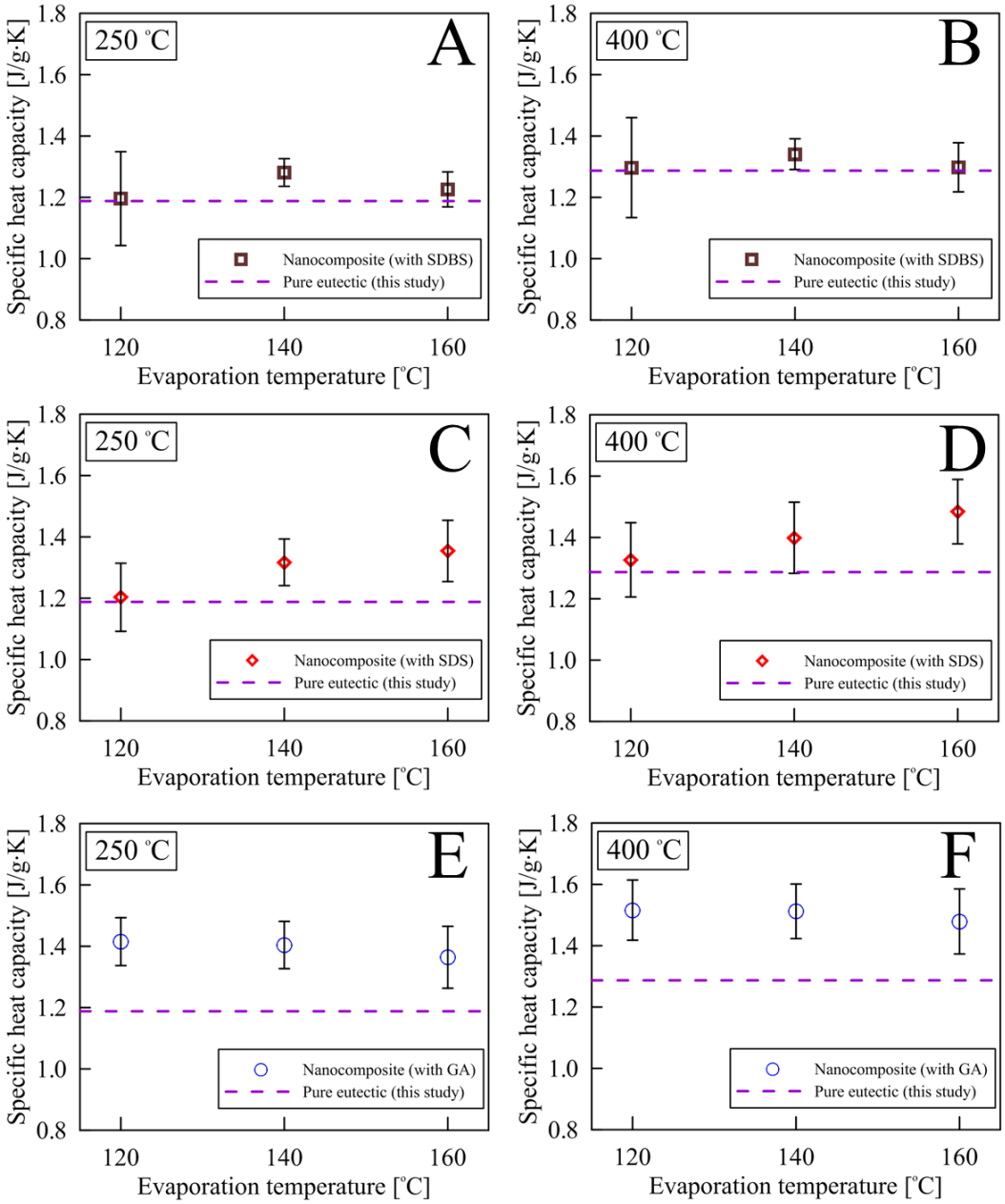

Fig. 6.4 Specific heat capacity of nanocomposites in solid phase for various evaporation temperature using: (A, B) SDBS, (C, D) SDS, and (E, F) GA

To examine whether SDS at 1 % mass concentration was suitable enough to homogeneously disperse CNT into salt samples, additional experiments were performed for the nanomaterials with SDS at 5 % mass concentration and for the same concentration of CNT [60]. As shown in Fig. 6.5, even though the specific heat capacity was enhanced in those samples, no significant difference in the specific heat capacity was found in the nanomaterials with SDS at 5 % mass concentration. That is, the addition of SDS didn't produce a favorable effect on the specific heat capacity enhancement rather the increase in concentration of SDS marginally decreased the specific heat capacity of the nanomaterial.

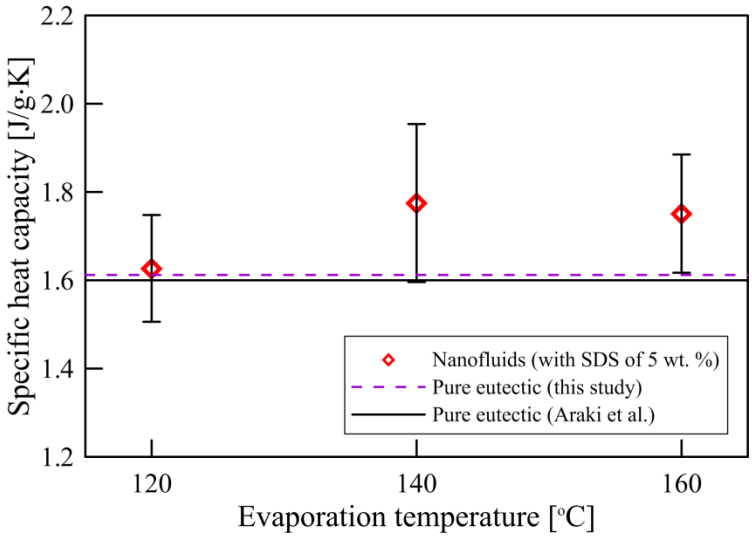

Fig. 6.5 Specific heat capacity of nanofluids in liquid phase once using SDS of 5 % mass concentration

Note: Reprinted from with permission from "Study of high temperature nanofluids using carbon nanotubes (CNT) for solar thermal storage applications" by B. Jo and D. Banerjee, 2010, ASME 2010 4th International Conference on Energy Sustainability ES2010-90299, Copyright 2010 by the American Society of Mechanical Engineering (ASME).

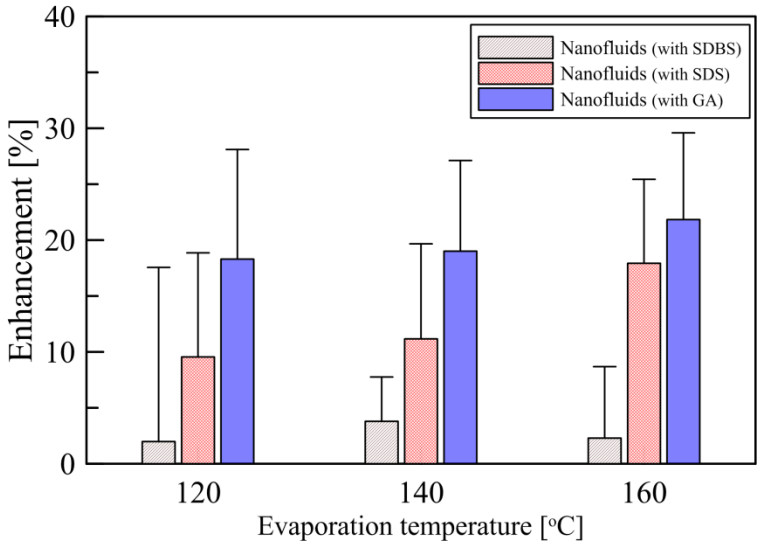

Fig. 6.6 Average enhancements in specific heat capacity of nanofluids for each evaporation temperature

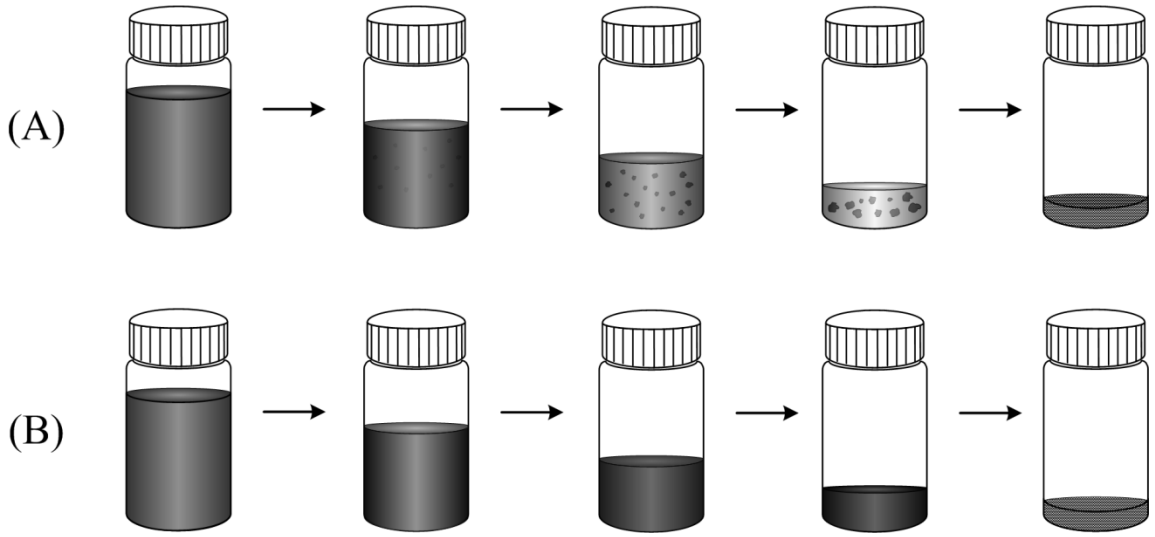

Fig. 6.7 Schematics of water evaporation process: (A) using SDS or SDBS, and (B) using GA

Average enhancements for each temperature and for each surfactant were plotted in Fig. 6.6. It can be presumed that GA is a more suitable surfactant for dispersing carbon nanotubes into the carbonate salt eutectic (in terms of both the enhancements and the variations in the specific heat capacity of the nanofluids as the evaporation temperature is varied). In fact, it was expected that the specific heat capacity of the nanomaterials using GA would show larger enhancement, because clustering of CNT was apparent (even by bare eyes) during the water evaporation process for the nanomaterials using SDS and using SDBS. Fig. 6.7 illustrates the distinction in the water evaporation procedure between GA and other surfactants (SDS and SDBS). Although SDS and SDBS are effective in dispersing CNT in water, these surfactants could not prevent the aggregations and precipitation of CNT from the aqueous solution (however, these surfactants retarded the agglomeration of CNT).

Fig. 6.8 shows SEM images for pre-DSC and post-DSC samples of nanomaterials using SDBS (A and B), SDS (C and D), and GA (E and F). These images show that the individual nanotubes and aggregated nanotubes coexisted in the solvent. The images confirm that the smallest amount of CNT aggregation was observed in the nanomaterials mixed with GA.

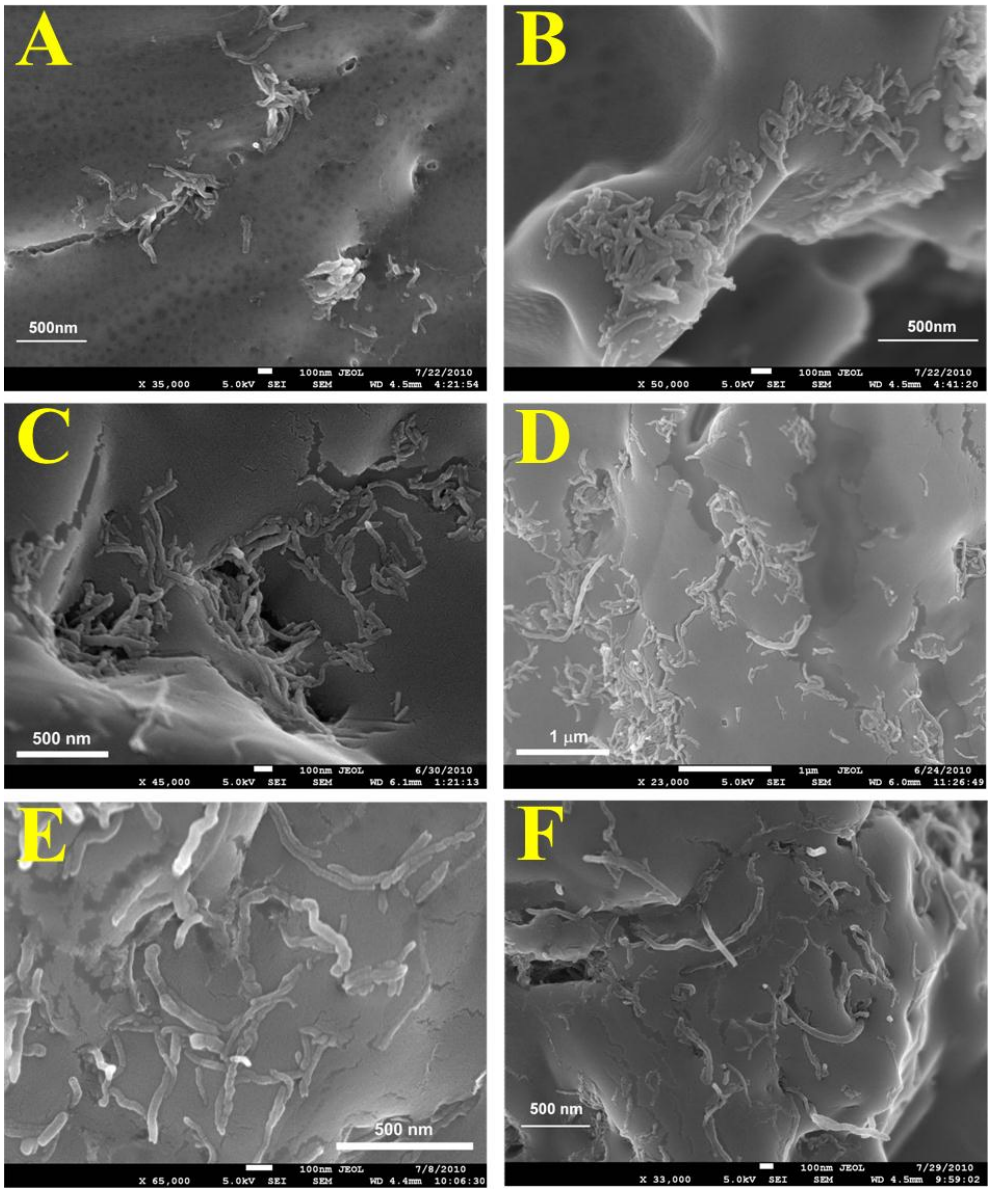

Fig. 6.8 SEM images of pre-DSC and post-DSC samples: using SDBS (Top - A, B), using SDS (Middle - C, D) and using GA (Bottom - E, F)

6.3.2 Theoretical predictions

Two correlations have been used in the literature to predict the specific heat capacity of the nanomaterials in the liquid phase (i.e. nanofluids) (for example, in reference [53]). The specific heat capacity of the nanomaterials can be estimated by using volume fractions of nanoparticles, densities, and specific heat capacity of both the base material (solvent) and nanoparticles. Equation (6.1), model 1, is based on volume fractions. Model 2 where densities of both the base material and nanoparticles are incorporated is based on mass fractions as in Eq. (6.2).

$$c_{P,nf} = \phi c_{P,n} + (1-\phi) \cdot c_{P,bf} \tag{6.1}$$

$$c_{P,nf} = \frac{\phi (\rho c_P)_n + \phi (\rho c_P)_{bf}}{\phi \rho_n + (1-\phi) \rho_{bf}} \tag{6.2}$$

where, C_p is the specific heat capacity, ρ is the density, and ϕ is the volume fraction of the nanoparticles. Subscripts, *bf*, *n*, and *nf* indicate the base fluid, the nanoparticle, and the nanofluid, respectively. Table 6.1 includes the material properties of the pure carbonate eutectic and the CNT to obtain the theoretical predictions for the specific heat capacity of the nanofluids. Since the material properties of the nanoparticles are the most important parameter that is used in both models, the theoretical predictions were obtained using the material properties of the graphite and the single walled carbon nanotube network (for the CNT).

Table 6.1 Theoretical prediction of specific heat capacity of nanofluids (1 % mass concentration) in liquid phase/ Material properties of salt eutectic, graphite and carbon nanotubes for theoretical predictions (a:[123], b:[118], c:[116] and d:[115])

Materials	Salt eutectic	CNT	Graphite	Nanofluids (by CNT)	Nanofluids (by graphite)
Density [g/cm^3]	1.97 [a]	1.74 [b]	2.2 [d]	N/A	N/A
Specific heat capacity [J/g·K]	1.612	1.97 [c]	1.66 [d]	1.616	1.612

As discussed in Section 5, the predictions from the simple mixing model (equilibrium mixing theory) did not match the experimental data for the nanofluids samples where GA was used as a dispersant for the nanoparticles (and the nanoparticles were largely unagglomerated). However, the predictions from the simple mixing rule matched the experimental data for samples with agglomerated (for SDS and SDBS as dispersants at lower values of evaporation temperatures). This conclusively demonstrates that the predictions from the simple mixing rule match the experimental data when the nanoparticles are agglomerated. However, for samples with uniformly dispersed and unagglomerated nanoparticles the experimental data for specific heat capacity violates the predictions from the simple mixing rule.

6.4 Conclusion

The specific heat capacity enhancements of the carbonate salt eutectic based CNT nanomaterial were observed even for minute concentration of the nanoparticles. The effect of the duration for complete evaporation on the specific heat capacity enhancement was investigated in this study. Additionally, three different surfactants were tested to identify the most appropriate surfactant for dispersing the nanoparticles in the molten salt. The knowledge gained from these experiments is summarized as follows:

(a) The specific heat capacity was significantly enhanced by up to 22% on dispersing multi-walled carbon nanotubes at 1 % mass concentration in the salt eutectic using Gum Arabic as a surfactant. At the highest evaporation temperature (the shortest duration), similar enhancements in the specific heat capacity was obtained for the nanofluids using SDS. There was no significant enhancement in the specific heat capacity of the nanofluids using SDBS.

(b) For the nanofluid samples which used SDS for dispersing CNT into the eutectic, the specific heat capacity was increased upon increasing the evaporation temperature. However, more consistent results for the specific heat capacity enhancement of the nanofluids were obtained by using Gum Arabic dispersant (the measured values of the specific heat capacity for the nanomaterial samples were consistent - regardless of the evaporation temperature used for sample preparation).

(c) The uniformity of CNT dispersion in the salt sample was confirmed by using SEM images of the pre-DSC and post DSC samples.

(d) Increasing surfactant mass concentration from 1 % to 5 % did not yield a higher enhancement of the specific heat capacity values. Rather the specific heat capacity measured for CNT nanomaterial with SDS at 5 % mass concentration was lower than the samples mixed with SDS at 1 % SDS mass concentration. This is potentially due to higher levels of agglomeration of the nanoparticles in the samples containing SDS at 5% mass concentration.

(e) The theoretical prediction for specific heat capacity was obtained using two different analytical models. However, both models could not match the enhancements of the specific heat capacity observed in the experiments for samples containing unagglomerated and fairly homogeneously dispersed nanoparticles. On the other hand, the experimental data for samples with agglomerated nanoparticles matched the predictions from the theoretical models.

7. EXPERIMENTAL STUDY IV: EFFECT OF SYNTHESIS PROTOCOL ON GRAPHITE NANOMATERIALS

7.1 Objective

The aim of this study is to investigate the effect of the synthesis protocol on the specific heat capacity for carbonate salt samples mixed with graphite nanoparticles. In literature there is a controversy about the effect of homogeneous dispersion of the nanoparticles on the level of enhancement of thermal conductivity [93, 135]. Nevertheless, it is presumed that the uniformity of dispersion of the particles leads to enhancement of the thermal conductivity of the nanofluids, due to the large surface to volume ratio of the nanoparticles. As we discussed in previous sections, experimental and computational studies have shown that a dense (compressed) liquid layer forms on the surface of the nanoparticles [112, 121]. A few reports suggested the energy storage mechanism that enhanced specific heat capacity for molten salt nanomaterials could arise from the formation of the compressed liquid layers on the surface of the nanoparticles. The increase in specific surface area of the nanoparticles is definitely significant [58, 59]. It is, therefore, presumed that the dispersion uniformity of the nanoparticles strongly affects the specific heat capacity of the nanofluids.

In this study, a new evaporation technique for synthesizing the nanomaterials was developed to substantially shorten the elapsed time for evaporation of water during the synthesis process (leading to less agglomeration of the nanoparticles). The effect of the base fluid composition (i.e., solvent consisting of the binary mixture of the carbonate salt)

was examined to explore the possible reasons for the enhanced specific heat capacity that was observed in these experiments. Finally, molecular dynamics (MD) simulations were performed to explore the nature of the compressed layers (and chemical/ species concentration gradients) as a function of the chemical properties of the solvent material.

7.2 Nanomaterial synthesis

Fig. 7.1 illustrates the two synthesis procedures for the molten salt nanomaterials used in this study. At first the graphite and the Gum Arabic (GA, Sigma Aldrich) were added to distilled water and the suspension was subjected to a sonication in an ultra-sonic bath for 2 hours. The carbonate salt eutectic was added into the aqueous graphite nanofluid prepared in the previous step and the aqueous salt-graphite nanofluid was sonicated again for 3 hours to avoid agglomerations of nanoparticles. In order to obtain dehydrated powder of the nanomaterial, water was evaporated on a hotplate set at 100 ℃. In the last step, the evaporation method was varied, which resulted in differing dispersion quality of the graphite nanoparticles. This is achieved using a large petri dish (Method 1) and using a vial (Method 2). It was expected that Method 1 would yield better uniformity in the nanoparticle dispersion because the petri dish method substantially reduces the duration for complete evaporation. The shorter duration for evaporation is conducive for GA to prevent the agglomeration of the graphite. In addition a large surface area of the petri dish is also beneficial for maintaining the homogeneity of the nanoparticle dispersion. Images of the dehydrated nanomaterials on

the petri dish are shown in Fig. 7.2. For the nanomaterials prepared by Method 1, finer salt powder formed on the periphery of the petri-dish (referred to as Nanomaterial 1) and coarser salt powder formed towards the center of the petri-dish (referred to as Nanomaterial 2). On the contrary, the nanomaterials obtained from Method 2 were collected from the vials without any separation. The neat salt mixtures (without addition of nanoparticles) were synthesized by using Method 2 only.

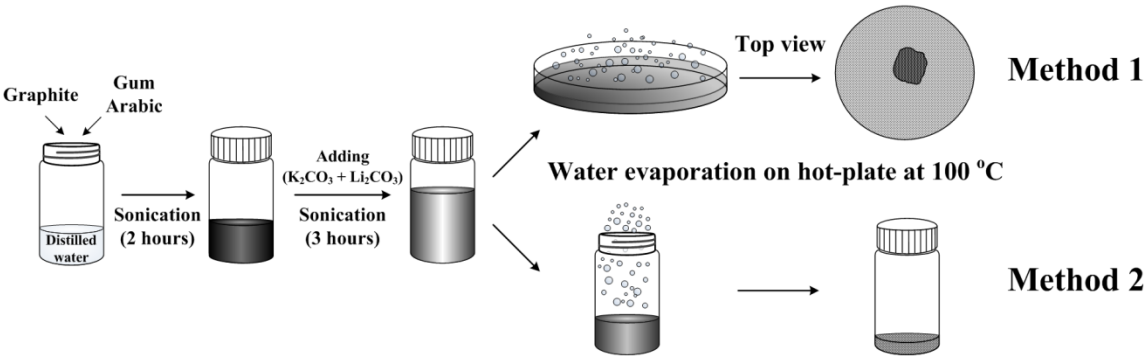

Fig. 7.1 Schematic of the synthesis methods for molten salt nanomaterials

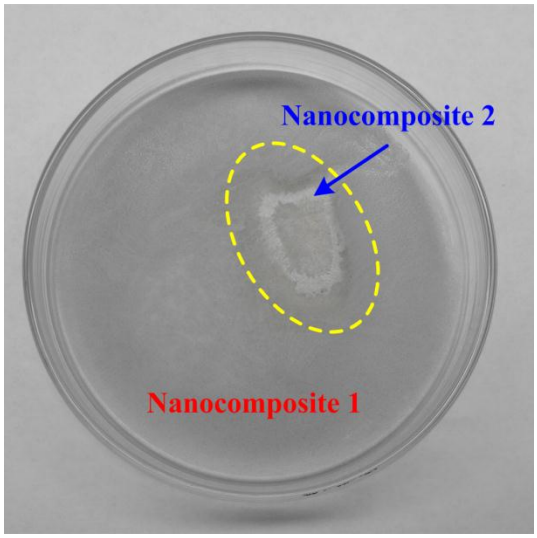

Fig. 7.2 Photo image of nanomaterials obtained after dehydration on a petri dish

7.3 DSC experiments and MD simulations

The experimental procedures for DSC and determination of the specific heat capacity were discussed in Section 2. The MD simulations conducted in this study also followed the same procedure as described in Section 3 [90].

7.4 Results and discussion

The results obtained from this study are presented in the same chronological order to clarify the logical steps that guided the activities in this study.

7.4.1 Nanomaterials synthesized using Method 1

Initially a carbonate salts eutectic sample with 62:38 molar ratio of the lithium carbonate and the potassium carbonate was chosen as the base material (solvent). The molten salt nanocomposites were dehydrated on a petri dish as shown in Fig. 7.2. The specific heat capacity measurements were performed for the Nanomaterial 1. Fig. 7.3 shows the specific heat capacity of the nanomaterial containing the graphite nanoparticles at 0.1 % mass concentration. The results showed significant enhancement in the specific heat capacity for both solid and liquid phases. It was observed that the specific heat capacity of the Nanomaterial 1 was dramatically increased in the liquid phase, which is 3.12 [J/g·K].

It was suspected that the chemical composition of Nanomaterial 1 could have changed due to the separation technique used in this study. In order to verify the exact

composition of the lithium carbonate and the potassium carbonate for the plain carbonate salt eutectic samples and the nanomaterial sample, Inductively Coupled Plasma-Mass Spectrometry (ICP-MS) was used. Surprisingly, it was observed that the chemical composition of the Nanomaterial 1 (by Method 1) was changed from that of the pure salt samples. That is, the mole fraction was not 62:38 (which was the intended composition). In contrast, the pure eutectic samples synthesized using Method 2 preserved originally intended composition. Table 7.1 presents the mole fractions of the lithium carbonate and the potassium carbonate measured by ICP-MS. In Table 7.1 the amount of the lithium carbonate in the Nanomaterial 1 (by Method 1) was much larger than that of the pure eutectic (by Method 2).

Similarly, the specific heat capacity of the Nanomaterial 2 (by Method 1) was also measured in this study. Fig. 7.3 shows the measured specific heat capacity capacities of the Nanomaterial 2 (by Method 1) for both solid and liquid phases. Fig. 7.3 shows that the specific heat capacities of the Nanomaterial 2 are lower than that of the Nanomaterial 1. As shown in Table 7.1, however, Nanomaterial 2 contains less amount of the lithium carbonate, compared with the Nanomaterial 1 and also the pure eutectic composition (62:38). Therefore, the specific heat capacity corresponding to these compositions has to be measured to determine the correct level of enhancements for the specific heat capacity values of these nanomaterials, especially for the liquid phase.

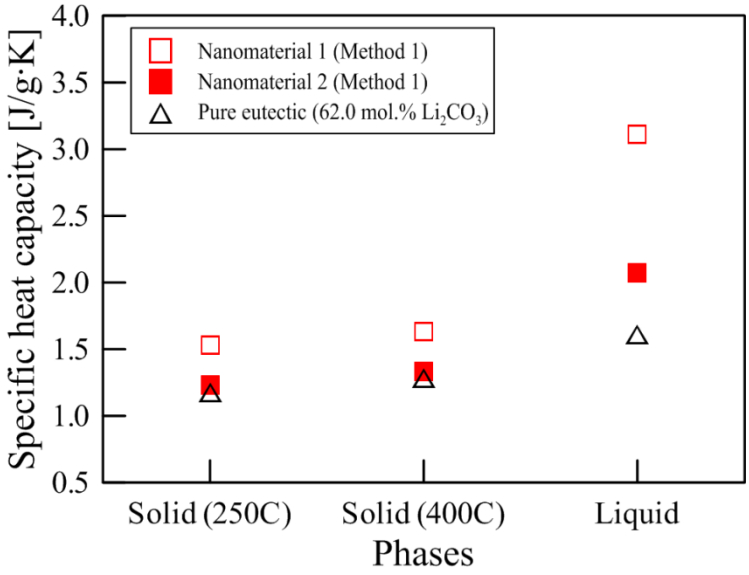

Fig. 7.3 Specific heat capacity of Nanomaterial 1 and Nanomaterial 2 synthesized by Method 1, and plain carbonate salt eutectic with 62:38 molar composition

Table 7.1 Compositions of tested samples by ICP-MS

Samples	Synthesis method	Molar ratio Li_2CO_3 : K_2CO_3
Plain carbonate salt mixture	Method 2	62.1 : 37.9
Nanomaterial 1	Method 1	74.6 : 25.4
Nanomaterial 2		34.0 : 66.0

7.4.2 Pure carbonate salt mixtures

As discussed in Section 4, the proportion of the lithium carbonate in the mixture strongly affects the specific heat capacity values, especially in the liquid phase. Hence, the specific heat capacity of the plain salt mixtures was measured corresponding to the chemical composition measured for the samples obtained for Nanomaterial 1 and Nanomaterial 2. These experiments were performed to verify the correct level of enhancement in the specific heat capacity of the nanomaterials obtained in this study. Fig. 7.4 shows the specific heat capacity of the plain salt mixture samples for a molar ratio of 74.6:25.4 (Li_2CO_3 : K_2CO_3). These results were compared to the property values for samples of Nanomaterial 1 (by Method 1) and for the pure eutectic with a molar ratio of 62:38 (Li_2CO_3 : K_2CO_3). As expected, the specific heat capacity of the pure binary mixture (74.6:25.4) in the liquid phase is much higher than that of the eutectic (62:38). The results in the solid phase for the pure salt samples with two different chemical compositions were observed to be almost identical (Fig. 7.4). The measured values for solid and liquid phases show that the specific heat capacities of the pure salt mixtures are lower than that of the nanomaterials. Hence, it can be concluded that the specific heat capacity values were enhanced significantly on dispersing the nanoparticles into the salt samples. Fig. 7.5 shows the specific heat capacity of the pure salt mixture (34.0:66.0), Nanomaterial 2 (by Method 1) and pure eutectic (62:38). In contrast to the pure salt mixture (74.6:25.4) - the pure salt (34.0:66.0) has a lower value of specific heat capacity compared to that of the pure eutectic (62:38). That is, the specific heat capacity value was effectively enhanced for Nanomaterial 2 (made by Method 1) as well.

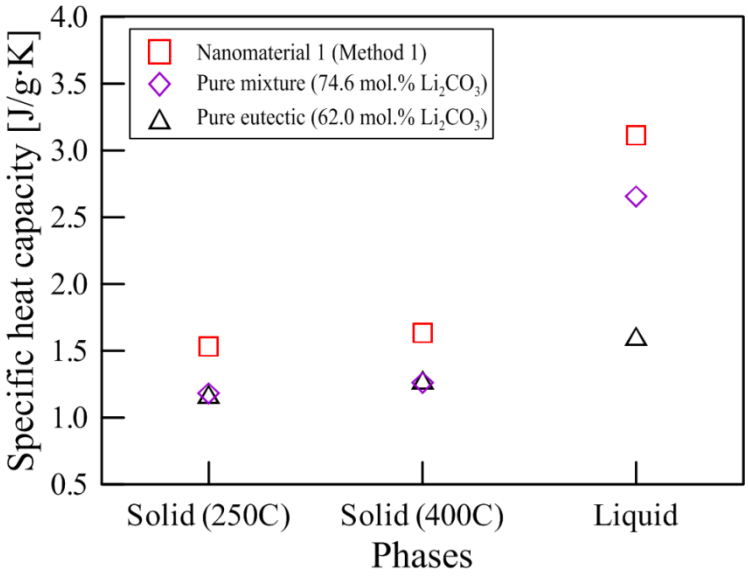

Fig. 7.4 Specific heat capacity of Nanomaterial 1 (synthesized by Method 1), pure salt mixture with 74.6:25.4 molar ratio (Li_2CO_3 : K_2CO_3), and plain eutectic with 62:38 molar ratio (Li_2CO_3 : K_2CO_3)

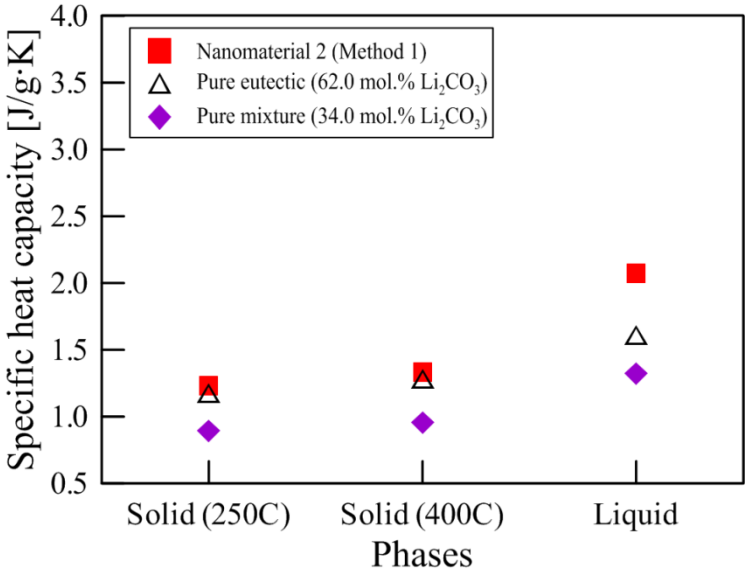

Fig. 7.5 Specific heat capacity of Nanomaterial 2 (synthesized by Method 1), plain eutectic with 62:38 molar ratio (Li_2CO_3 : K_2CO_3), and plain salt mixture with 34.0:66.0 molar ratio (Li_2CO_3 : K_2CO_3).

Table 7.2 Specific heat capacity of nanomaterials (1, 2) and pure mixture (eutectic)

Materials	Specific heat capacity [K/g·K]		
	at 250 [℃]	at 400 [℃]	Liquid phase
Nanomaterial 1 (Method 1)	1.53 (29.7%)* (28.6%)**	1.63 (27.3%)* (29.4%)**	3.12 (93.8%)* (17.3%)**
Pure mixture (74.6 mol. % Li_2CO_3)	1.19	1.26	2.66
Pure eutectic (62.0 mol. % Li_2CO_3)	1.18	1.28	1.61
Nanomaterial 2 (Method 1)	1.24 (5.1%)* (39.3%)**	1.34 (4.7%)* (39.6%)**	2.07 (28.6%)* (56.8%)**
Pure mixture (34.0 mol. % Li_2CO_3)	0.89	0.96	1.32

KEY:

* Enhancement in nanomaterial property compared to that of pure eutectic

** Enhancement in nanomaterial property compared to that of pure mixture

7.4.3 Nanomaterials by Method 2

Fig. 7.6 shows the comparison for the specific heat capacity of the Nanomaterial 1 (that was synthesized using Method 1) to that of the pure salt mixture (74.6:25.4) and the Nanomaterial 3 (using Method 2). The property values for Nanomaterial 3 were found to be intermediate between that of the Nanomaterial 1 and the pure salt mixture (74.6:25.4). In solid phase the measured values for specific heat capacity for Nanomaterial 3 (by Method 2) were 1.26 and 1.42 [J/g·K] at 250 ℃ and 400 ℃, respectively. In contrast the

corresponding values for Nanomaterial 1 (by Method 1) were 1.53 and 1.63 [J/g·K], respectively. Hence, the specific heat capacity of the Nanomaterial 3 (by Method 2) were higher in the solid phase than that of the pure mixture (1.19 and 1.26 [J/g·K], respectively), but were lower than that of the Nanomaterial 1 (by Method 1) samples. Similar trend was observed in the liquid phase with these samples, but the differences were even more pronounced.

The specific heat capacity of Nanomaterial 4 (synthesized using Method 2) are compared with that of the pure salt mixtures (34:66) and Nanomaterial 2 (by Method 1) in Fig. 7.7. Similar trends were observed in these results (Fig. 7.6) when compared to Fig. 7.7. Comparing Fig. 7.6 and Fig. 7.7 it is observed that lowering the composition of the Li_2CO_3 results in more dramatic enhancements in the specific heat capacity values for the nanomaterials for both Method 1 and Method 2. Also, Method 1 yields higher levels of enhancement in specific heat capacity than Method 2 for both salt compositions. As mentioned before, Method 2 results in reduced homogeneity (and dispersion uniformity) for the nanoparticles due to longer duration required for complete dehydration of the samples during the synthesis process (i.e., Method 2 provides more opportunity for nanoparticle agglomeration in the aqueous solution). Hence, this conclusively demonstrates that the uniformity of dispersion of the nanoparticles is a significant factor that influences the level of enhancement for the specific heat capacity of the salt nanomaterials (both in solid phase and more effectively in the liquid phase). All results are tabulated in Table 7.3.

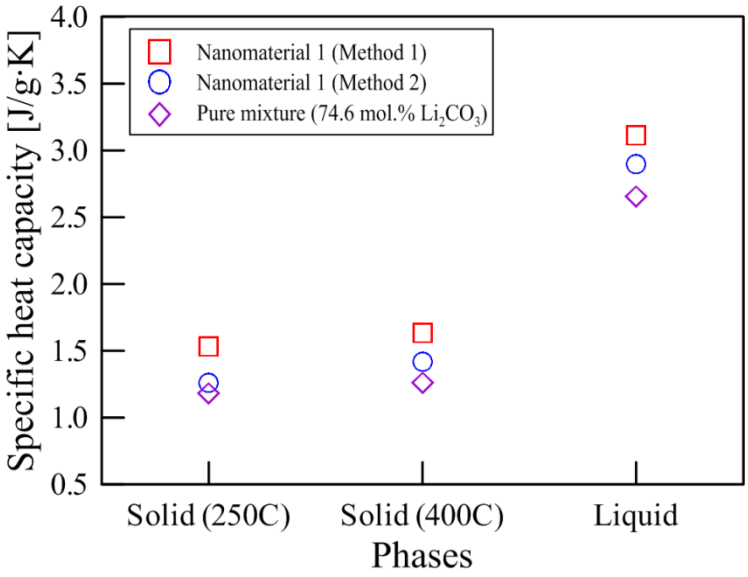

Fig. 7.6 Specific heat capacity of Nanomaterial 1 synthesized by Method 1 and Method 2, and plain salt mixture with 74.6:25.4 molar ratio

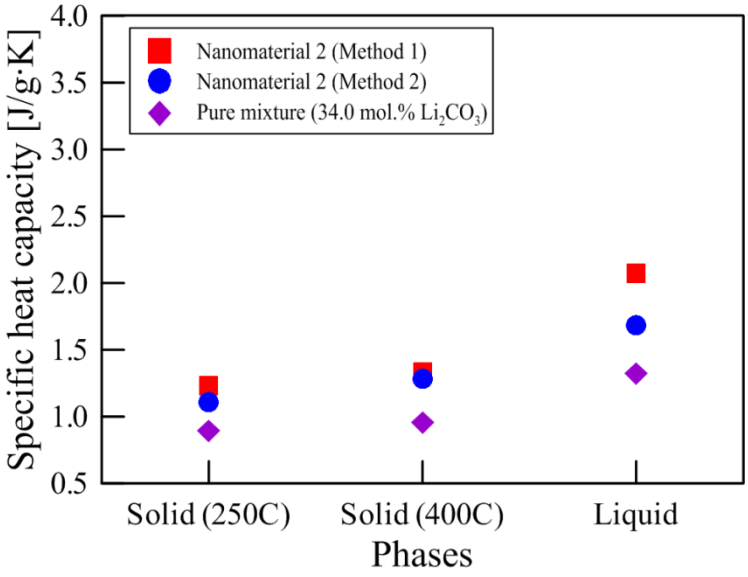

Fig. 7.7 Specific heat capacity of Nanomaterial 2 synthesized by Method 1 and Method 2, and plain salt mixture with 34.0:66.0 molar ratio

Table 7.3 Specific heat capacity of nanomaterials (3, 4) and pure mixture (eutectic)

Materials	Specific heat capacity [K/g·K]		
	at 250 [℃]	at 400 [℃]	Liquid phase
Nanomaterial 3 (Method 1)	1.26 (6.8%)* (5.9%)**	1.42 (10.9%)* (12.7%)**	2.90 (80.1%)* (9.0%)**
Pure mixture (74.6 mol. % Li_2CO_3)	1.19	1.26	2.66
Pure eutectic (62.0 mol. % Li_2CO_3)	1.18	1.28	1.61
Nanomaterial 4 (Method 1)	1.11 (-5.9%)* (24.7%)**	1.28 (0.0%)* (33.3%)**	1.69 (5.0%)* (28.0%)**
Pure mixture (34.0 mol. % Li_2CO_3)	0.89	0.96	1.32

KEY:

* Enhancement in nanomaterial property compared to that of pure eutectic

** Enhancement in nanomaterial property compared to that of pure mixture

7.4.4 Discussion

This section explores the potential energy storage mechanisms responsible for the observed enhancement in the specific heat capacity of the nanomaterial samples, especially for the liquid phase (i.e., for the nanofluid samples).

As mentioned before (in Section 1) controversies exist in the literature on the enhancement or degradation of the specific heat capacity of nanomaterials. The specific heat capacity of aqueous nanofluids (in de-ionized water or ethylene glycol solutions)

were reported to degrade when compared to that of the neat solvent and the level of decrement was reported to be linearly proportional to the concentration of the nanoparticles [53]. These results were found to be consistent with the simple mixing rules (Eq. 6.1 and Eq. 6.2).

In recent studies, however, the specific heat capacity of high temperature solvents (which were subjected to phase-change at elevated temperatures exceeding 490 ℃) was enhanced on doping with nanoparticles [57-60, 72-78]. These results were observed to violate the predictions from the simple mixing rules (Eq. 6.1 and Eq. 6.2) [60]. Hence, new theoretical models need to be developed that are consistent with the observed phenomena reported in this study.

To account for the additional energy storage mechanisms that are responsible for the anomalous enhancements in the specific heat capacity of nanomaterials, results from MD simulations were explored. The results from the MD simulations clearly show the existence of the compressed liquid layer that forms at the interface with nanoparticles (i.e., on the surface of the nanoparticles) [102, 112, 119]. This compressed layer is a result of the interactions due to intermolecular forces (adhesive forces) between the nanoparticle atoms and the liquid molecules. The existence of the compressed liquid layer was also verified by electron microscopy images obtained from various experiments. However, the implication of the compressed liquid layer for heat transfer and thermal energy storage has not been explored in as much detail in the literature.

Keblinski et al. [93] suggested that ordered liquid layering at the nanoparticle interface could increase the thermal conductivity of nanofluids. Even though the specific

heat capacity is a different thermo-physical property compared to thermal conductivity, the formation of the compressed liquid layer on the surface of the nanoparticles could have an effect on both property values. This was precisely the argument propounded in recent literature reports [57-59] (it may be noted that the same salt mixtures were used in this study but different types of nanoparticles were used as additives and similar levels of enhancements were observed for the property values of the nanomaterials that were synthesized using similar synthesis protocols as in the current study).

Basically, a critical parameter in accounting for the effect of the compressed liquid layer for the experimental data is the specific heat capacity value of the compressed liquid layer (which is currently unknown since no literature reports exist for calculating or measuring this property value for the compressed layer). In order to account for the increase (or decrease) in the specific heat capacity of the nanomaterials in the liquid phase (i.e., for the nanofluid samples) the ordered liquid layer should have a significantly elevated (or degraded) property value than that of the bulk property values for the solvent material (i.e., in the bulk phase of the liquid molecules that are located far away from the nanoparticle interface). Presumably the dense layer behaves like a semi-crystalline solid (i.e., it has property values that are almost identical to the property values of the solid phase of the solvent and corresponding to the temperature value that is close to the melting point). This assumption partially incorporates the heat of fusion in the net value of the specific heat capacity for the semi-solid layer (i.e., for the compressed liquid layer). Hence it can be postulated that this semi-solid compressed liquid layer (for non-aqueous solvents) has higher specific heat capacity than that of the

bulk phase of the solvent (in the liquid phase) by partially accounting for the enthalpy of fusion that is incorporated in these "loosely" structured molecules in the semi-solid layer that forms on the surface of the nanoparticle (or for that matter, on any crystalline interface). On the basis of this hypothesis, the enhancement in the effective (or total) specific heat capacity of the non-aqueous nanofluids was explored by accounting for both the mass fraction and the specific heat capacity of the compressed liquid layer. In addition, the total volume of the compressed liquid layer (i.e., the mass fraction) is affected by the effective size and shape of the nanoparticles (which in turn is affected by the amount of agglomeration and uniformity of the dispersion of the nanoparticles).

As shown in Fig. 7.8 (as well as Fig. 7.6 and Fig. 7.7), both the composition of the salt mixture and the synthesis method (i.e., uniformity of dispersion and level of agglomeration of the nanoparticles) significantly influences the property values of the nanomaterials. Also, the contribution from the compressed layer to the effective (net) specific heat capacity is reduced at higher the levels of agglomeration of the nanoparticles. On a similar note, the contribution from the compressed layer to the effective (net) specific heat capacity is reduced for nanoparticle shapes that have lower surface to volume ratio. In other words, for the same mass fraction and uniformly dispersed as well as unagglomerated nanoparticles with similar size ranges - a disc shaped/ lamellar nanoparticle (e.g., graphite nanoparticles) would demonstrate higher levels of enhancement, compared to tube shaped/ cylindrical nanoparticle (e.g., CNT), which in turn will demonstrate higher levels of enhancement compared to spherical nanoparticles (e.g., C_{60} fullerenes as well as inorganic and ceramic nanoparticles such as

titania, ceria, magnesia, alumina, etc.). These effects were explored further using MD simulations, which will be discussed in the next subsection.

The discussion in the previous paragraph has significant implications that are counter-intuitive (compared to the macro-scale transport phenomena typically used in relationships or equations for thermodynamics as well as heat and mass transfer). For example, for proper design of the nanomaterials (i.e., in order to maximize the effective thermo-physical property values of the nanomaterials) the mass concentration of the nanoparticles is required to be very low (i.e., less than 1% or less than 5%) in order to minimize the agglomeration of the nanoparticles and for ensuring homogeneity or uniformity in the dispersion of the nanoparticles. Low concentration of the nanoparticles also implies that the material (thermo-physical) properties of the nanoparticles are of a secondary importance compared to the nanoparticle shape, nanoparticle size as well as the adhesive intermolecular interactions between the nanoparticle and solvent material. In other words, the geometrical properties and the chemical properties of the nanoparticles are of primary importance and the physical properties are of secondary importance.

Similarly the chemical properties of the solvent material (e.g., adhesive intermolecular interactions, chemical composition and chemical structure) are more important compared to the physical properties of the solvent material (e.g., cohesive intermolecular forces). The chemical structure of the solvent molecules can have significant effects as well. For example, for organic solvents the relevant factors can be the degree of polymerization (i.e., size of polymer chains such as for monomer, dimer,

trimer, etc.), the isomers (i.e., straight chain versus branched chain structures) as well the composition ratio of their mixtures. These factors were reported in an earlier study to significantly affect the interfacial thermal resistance of the nanoparticles as well as the nature of the compressed layer (such as the thickness, peak density and the effective mass fraction) [68]. Similarly for inorganic fluids (e.g., polar solvents such as water, and ionic liquids such as molten salts) the chemical properties such as molecular reordering (e.g., hydrogen bonding), dielectric effects (e.g., formation of electric double layers), pseudo chemical bonding (e.g., chemical hydration and chelating complexes), pH and concentration of dispersant agents (surfactants) can be significant factors in determining the stability and effective properties of the nanofluids. Thus for inorganic solvents the chemical properties are of primary importance while the physical properties can play a secondary role.

On this same note, it may be mentioned that for aqueous nanofluids the net specific heat capacity values are expected to decrease due to the formation of the compressed liquid layer from the solvent molecules. The compressed liquid layer is expected to have semi-solid properties - akin to that of ice at a temperature close to the melting point. Ice has significantly smaller value of specific heat capacity (~ 2 J/g-K) compared to that of water (~ 4.2 J/g-K). Therefore, the synthesis of aqueous nanofluids potentially results in the formation of a “ice” layer on the nanoparticles (which is expected to survive even at room temperature or even at elevated temperatures). This was also verified by experimental measurements (using x-ray diffraction studies) that were reported in the literature for both aqueous solvents and organic solvents [136-141]. Hence, the net result

is the degradation in the effective specific heat capacity of the aqueous nanofluid mixture - now composed of three types of materials - the nanoparticle, solvent phase (i.e., water molecules in the bulk phase - that are far away from the nanoparticle interface) and “ice” phase that forms on the nanoparticle interface. Hence this model is consistent with the experimental results and is able to resolve the apparent controversies in the literature for the experimental measurement of the specific heat capacity values for aqueous nanofluids (degradation in the property values) and non-aqueous nanofluids (enhancements in the property values).

The discussions in the previous paragraphs (in this section) are counter-intuitive compared to the physical constitutive equations that are used for macro-scale engineering applications and for estimating the material property values in the bulk phase of these materials. For example, in typical heat transfer equations the thermo-physical property values are of primary importance (e.g., thermal conductivity, density, viscosity, etc.) while the chemical properties, such as molecular structure, are not explicitly incorporated in these constitutive equations (e.g., thermal resistance values for macro-scale conduction and convection heat transfer are not explicitly dependent on the molecular structure of the materials). In contrast, the discussions in this section show that for nanomaterials the chemical properties are more dominant factors that need to be incorporated in the constitutive equations and the physical property values play a less significant role (e.g., the molecular structure of the solvent and consequently the adhesive intermolecular forces can significantly affect the estimated values for interfacial thermal resistance or Kapitza resistance for the nanoparticles).

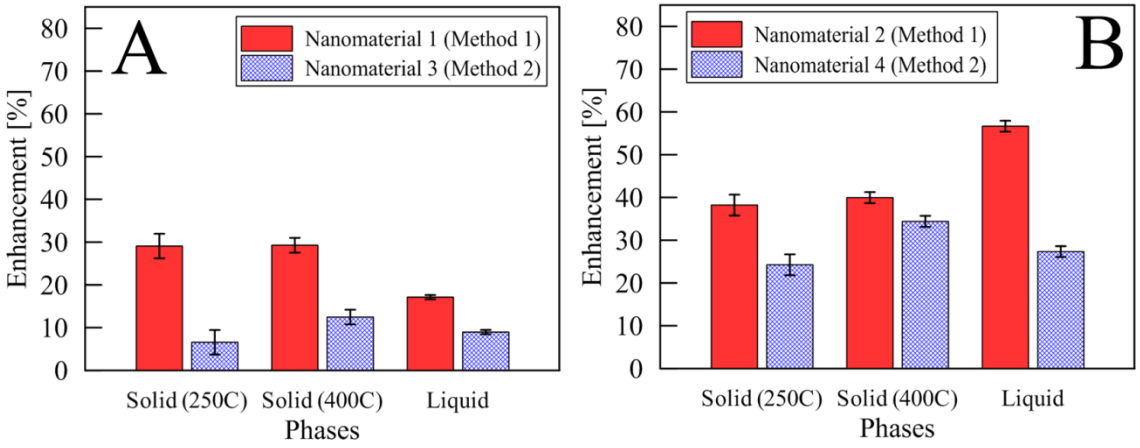

Fig. 7.8 Comparison of the specific heat capacity enhancements between Method 1 and Method 2 at solid phases and liquid phase: (A) Nanomaterial 1 / Nanomaterial 3 and (B) Nanocomposite 2 / Nanomaterial 4

7.4.5 MD simulation

MD simulations were performed to explore the effect of the following factors on the material property values of the nanomaterial samples:

(1) Formation of the compressed liquid layer. This was required to estimate the size (e.g., thickness) and density of the compressed layer.

(2) Size of the void space between the compressed layer and the nanoparticle.

(3) Change in chemical composition (molar ratio) of the lithium carbonate and the potassium carbonate in the binary salt mixture for the compressed liquid layer compared to that in the bulk.

Primarily, the first two factors (and to some extent, all of the factors) enumerated above should be considered in order to determine the effective mass fraction and material property values for the compressed layer. The chemical concentration gradients established as a result of the change in the chemical composition in the compressed liquid (compared to the bulk solvent phase) can result in additional material transport mechanisms (e.g., by thermophoresis) which can affect the effective values of thermal conductivity (and viscosity) of the nanomaterial samples. In addition, the local chemical concentration gradients on the surface of the nanoparticles can enable additional thermal storage mechanisms for the nanomaterial samples (e.g., contributions from local variations in the chemical potential distribution) - which are primarily non-existent for the pure salt mixtures.

Fig. 7.9 shows the plots for density variation as a function of the relative position from the center of the graphite nanoparticle. The plots were obtained for two different chemical compositions of the salt mixtures (i.e., corresponding to the two different bulk compositions of the solvent phase). In Fig. 7.9, it was observed that the first peak in each density plot (which is also the highest peak) is more pronounced for Nanomaterial 2. In Nanomaterial 1, the density peak of the compressed region was relatively less pronounced (compared to the neighboring peaks in the spatial distribution of the density values). In other words, the density of the solvent phase in the compressed layer is higher in Nanomaterial 2 than in Nanomaterial 1. The shape of the lamellar graphite nanoparticle used in the MD simulations was not perfectly symmetrical. As a result, the density peaks were not as pronounced. However, the MD simulations for Nanomaterial 2

did display the formation of the solid compressed region. The thickness of the compressed liquid layer is defined in this study to be the distance between the locations of the first valley (corresponding to the first density peak - counting from the surface of the nanoparticle) to the location of the fourth valley. According to this definition, the figure shows that the thickness of the compressed liquid layer for Nanomaterial 2 is larger than that of Nanomaterial 1. The figure shows that the thickness of the compressed liquid layer to be 10.5 [Å] and 13.5 [Å] for Nanomaterial 1 and Nanomaterial 2, respectively. It was, therefore, apparent from these simulations that the thickness and effective density (and therefore the mass fraction) of the compressed liquid layer that forms on the surface of the nanoparticle depends on the chemical composition and chemical properties of the solvent material.

The spatial distribution of the concentration (molar ratio) for the salts in the binary mixture for the solvent phase was plotted in Fig. 7.10 for two different nanomaterials. This figure shows that the local value of the molar ratio in the vicinity of the nanoparticle is significantly different, compared to the bulk values (and that of the corresponding pure salt mixtures). Hence, this result shows that addition of nanoparticles creates local concentration gradients. The length scale for the concentration gradients within the compressed liquid layer is smaller than the thickness of the compressed layer itself. This implies huge magnitudes for the local values of the chemical concentration gradients which is likely to affect the heat and mass transfer from the nanoparticle into the solvent due to thermophoresis (e.g., Soret effect and Duffour effect). In both nanomaterials, surprisingly, the ratio of the potassium atom in the compressed region is

higher than the average value (i.e., for the bulk phase values or for that of the corresponding pure salt mixtures). This is probably due to greater adhesion forces between potassium (i.e., potassium carbonate) and the graphite nanoparticle. The values for the L-J potential parameters and the Coulomb interaction terms for the atomic interactions between K, Li and graphite that were used in the MD simulations are responsible for the dominance of the intermolecular adhesive forces for K and graphite (compared to that of Li). As shown in the figure, the maxima in the proportion of the potassium atoms occur in the vicinity of the nanoparticle surface, and the fluctuations gradually decreases to the overall (average or bulk) composition away from the surface of the nanoparticle. This implies that the chemical composition of the compressed liquid layer is comprised of higher concentration of potassium carbonate than in the bulk solvent phase. As a consequence of the different chemical composition and higher relative density of the compressed phase the material property values of the compressed layer is expected to be significantly different compared to that of the pure solvent material of the same composition (i.e., for pure salt mixtures of the same chemical composition as the compressed layer). In addition the chemical potential values corresponding to these values of chemical composition and density for the compressed layer are expected to be significantly different than that of the pure salt mixture (of the same chemical composition as the compressed layer but may have a different density value). Hence, these factors can serve as an additional energy storage mechanism that is non-existent in the absence of the nanoparticle (i.e., in the pure salt mixtures).

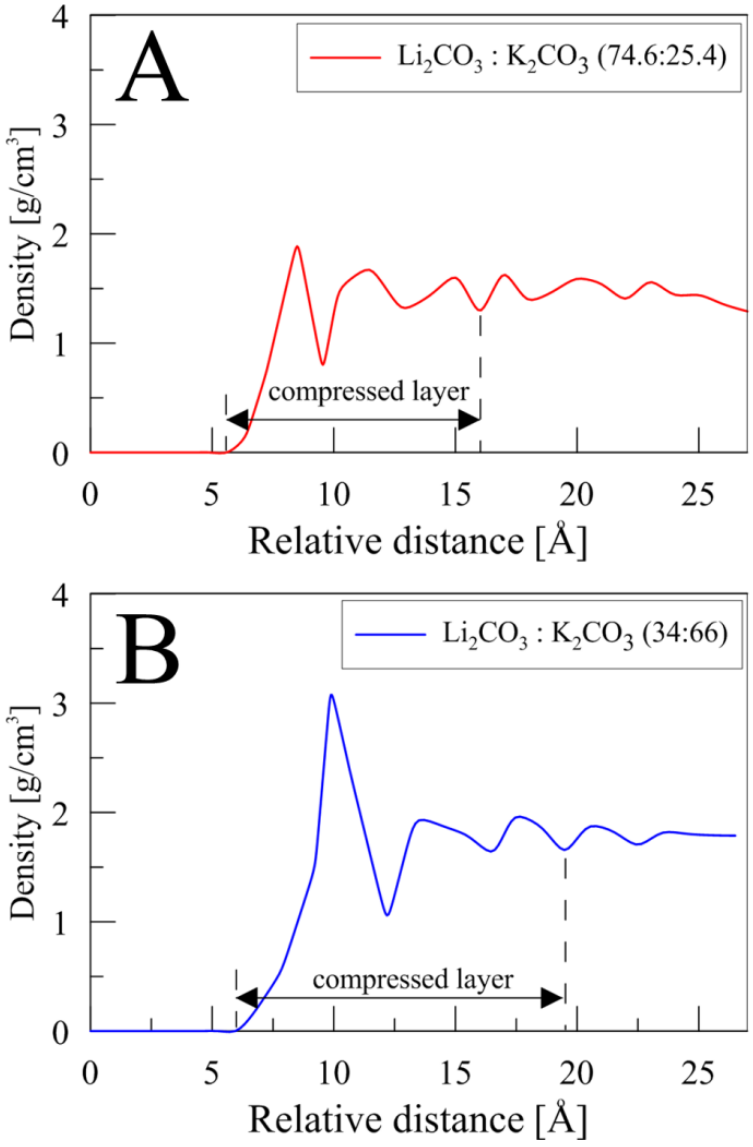

Fig. 7.9 Spatial distribution of density values for carbonate salt mixtures obtained from MD simulation results for: (A) Nanomaterial 1 and (B) Nanomaterial 2

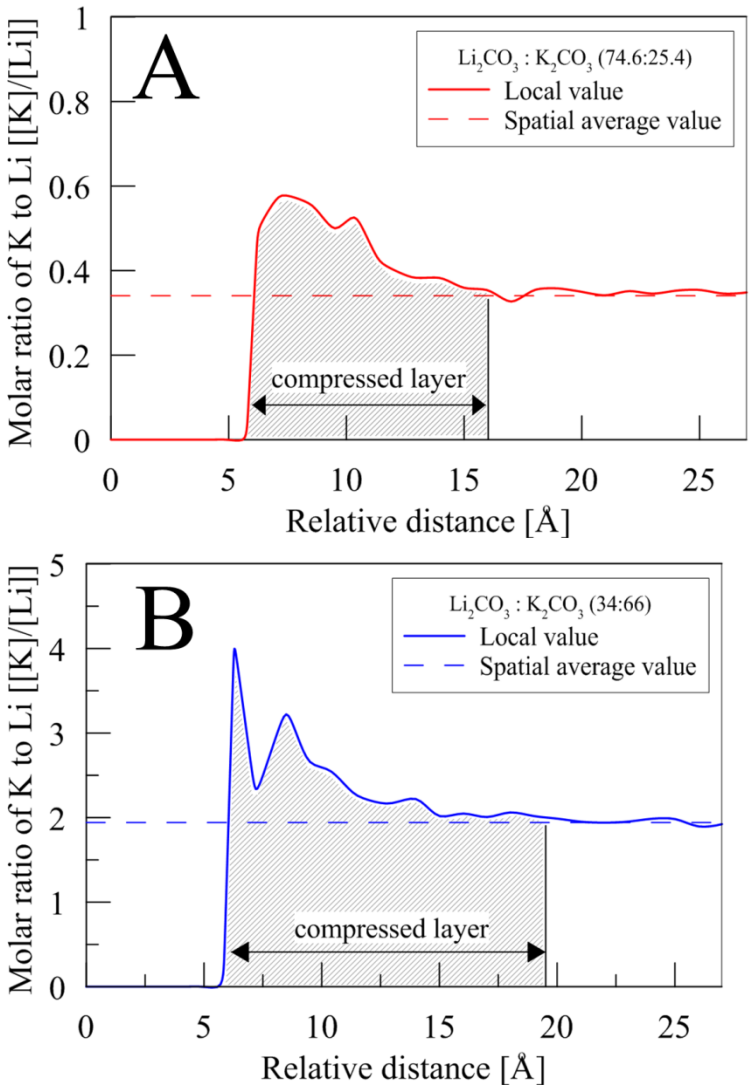

Fig. 7.10 Spatial distribution of the species concentration (molar ratio of potassium to lithium) for the carbonate salt mixtures obtained from MD simulations for: (A) Nanomaterial 1 and (B) Nanomaterial 2

7.4.6 Specific heat capacity enhancement

The MD simulation results imply that the experimental observations for enhancement of the specific heat capacity are a consequence of a combination of several factors. As shown in Fig. 7.8, the enhancement in the specific heat capacity is larger in Nanomaterial 2 than in Nanomaterial 1. In liquid phase, especially, the level of enhancement for the property values between the two samples (of two different chemical compositions) was significantly different. In the prior subsection it was mentioned that the thickness, density and chemical composition (proportion of potassium or potassium carbonate) of the compressed liquid layer for Nanomaterial 2 was larger than that of Nanomaterial 1. Those factors act favorably for enhancing the specific heat capacity of Nanomaterial 2. Furthermore, the partial contribution from the enthalpy of fusion to the formation of the compressed layer (and therefore the effective specific heat capacity of the compressed layer) can be different for the two salt mixtures. In the experimental measurements it was observed that the enthalpy of fusion of the carbonate salt mixtures linearly decreases when the mole fraction of the lithium carbonate exceeds 70 %. The measured values for the enthalpy of fusion for the two solvents used in Nanomaterial 1 and Nanomaterial 2 are 305 and 289 [J/mol], respectively. The higher proportion of potassium carbonate in the compressed liquid layer favors the property values for Nanomaterial 1 compared to that of Nanomaterial 2. Since from Fig. 7.10 it is apparent that the compressed liquid layer is composed of larger concentration of potassium carbonate salts, the enthalpy of fusion for Nanomaterial 1 may be somewhat larger than observed for that of the pure salt mixture of the same chemical composition. This factor

can be responsible for marked improvement in the specific heat capacity of the Nanomaterial 1, in spite of the relatively narrow and less dense compressed layer that exists for Nanomaterial 1.

Additionally, the shorter duration for dehydration obtained by using Method 1 (for synthesis of the nanomaterials) minimizes the agglomeration of the nanoparticles resulting in smaller mean size of the nanoparticles (compared to the nanomaterials synthesized by using Method 2). Since the smaller values of the mean for the particle size distribution causes a significant enhancement in the net surface area of the nanoparticles (for the same mass fraction of the nanoparticles) – as a consequence the volume fraction (or mass fraction) of the compressed liquid layer is also enhanced significantly. This enables sharp enhancement in the value of the specific heat capacity for nanomaterials synthesized using Method 1 (compared to that of Method 2). Moreover, the long durations for sonication (for more than 5 hours) for the aqueous solutions that were employed for the synthesis procedure can also help to reduce the mean values for the size distribution of the nanoparticles. As reported by Karthikeyan et al. [142] - the better homogeneity (or uniformity) for nanoparticle dispersion in the solvent results in higher levels of enhancement in the thermal conductivity values for nanofluid samples. Similar trends in the results were observed in this study for the measurement of specific heat capacity of the nanomaterial samples. The results imply that better uniformity in the dispersion of the nanoparticles - maximizes the physical volume (and the mass fraction) of the compressed liquid layer and causes more

pronounced levels of enhancements in the measured values for specific heat capacity of the nanomaterials.

As a final comment for this section, the existence (or transformation/ survival) of the distinct compressed liquid layer is not known when the nanomaterial solidifies from the liquid state. Hence, it is not clear what energy storage mechanisms are responsible for the enhanced specific heat capacity values observed in the solid state measurements for the nanomaterials. It is possible that the adhesive forces arising from the existence of the nanoparticles can induce re-ordering of the solvent molecules just prior to solidification (e.g., similar to nucleation and growth of dendrite structures during crystallization) [58, 79, 80]. Recent experimental results allude to this type of behavior for nanomaterials [80]. It was observed that solid state property values (specific heat capacity values) of nanomaterials was higher for samples undergoing melting and re-solidification – compared to nanomaterial samples (salt mixtures doped with nanoparticles) that did not undergo melting and re-solidification.

7.5 Conclusion

The specific heat capacity measurements were performed using Differential Scanning Calorimetry for solid and liquid phases of the pure binary salt mixtures and the corresponding nanomaterials (by mixing with graphite nanoparticles). Small variations in the synthesis protocols (e.g., dehydration temperature and containers used for the dehydration step that in turn affected the time required for complete dehydration) were

found to cause significant variations in the property values of the resulting nanomaterials. The effect of the nanomaterial composition on the level of enhancement in the specific heat capacity values was examined by employing two distinct synthesis protocols. This phenomenon was explored further by performing MD simulations for the different nanomaterial compositions. The MD simulations showed that the formation and chemical composition of the compressed liquid layer on the surface of the nanoparticles is highly sensitive to the chemical composition of the solvent phase. This in turn can significantly affect the effective thermo-physical property values (especially specific heat capacity values) for the nanomaterial. The knowledge gained from the experiments and numerical simulations reported in this section are summarized as follows:

(a) The specific heat capacity of the carbonate salt mixtures in both solid and liquid phases was enhanced significantly by doping with graphite nanoparticles at minute concentrations (mass fraction of 0.1 %). Small variations in synthesis protocol were found to cause significant change in the measured property values. The maximum enhancements in the values of specific heat capacity for the nanomaterials (over that of the corresponding pure salt mixtures) were 40 % and 57 %, in the solid and liquid phase, respectively.

(b) The uniformity of nanoparticle dispersion was found to affect the level of enhancement of the specific heat capacity of the nanomaterials. Method 1 (which had a significantly smaller duration required for complete dehydration compared to that of Method 2) yielded higher levels of enhancement in the property values for the all the

nanomaterial samples used in this study. However, Method 1 was found to cause variations in the chemical composition of the solvent.

(c) Nanomaterial 2 (with smaller net concentration of the lithium carbonate in the solvent material) demonstrated higher levels of enhancement for the measured values of the specific heat capacity. However, the absolute values of the measured specific heat capacity are lower for Nanomaterial 2 compared to that of Nanomaterial 1. For both nanomaterial samples, the level of enhancements in the property values is higher in the liquid compared to that of the solid phase data. The difference in heat of fusion (corresponding to the two different chemical compositions of the solvents) was attributed for the different levels of enhancements in the specific heat capacity values in the liquid phase.

(d) MD simulations were performed to explore the effect of the variation in chemical composition of the solvent material on the formation of the compressed liquid layer and therefore on the resulting properties of the nanomaterials. A thicker and denser compressed layer (with higher concentration of potassium carbonate) was obtained for the Nanomaterial 2. As a result, higher levels of enhancement in specific heat capacity for Nanomaterial 2 were expected. A consequence of the higher concentration of potassium carbonate in the compressed layer for Nanomaterial 2 is a lower effective specific heat capacity of Nanomaterial 2 (compared to that of Nanomaterial 1) even though the thickness and density of the compressed layer is higher for Nanomaterial 2. These predictions from the numerical models are consistent with the experimental measurements.

(e) A potential mechanism for the observed enhancements in the measured values of specific heat capacity was proposed owing to the formation of the compressed liquid layer on the surface of the graphite nanoparticles. Based on the variations in the spatial distribution of local density values and the variations in the spatial distribution of the local chemical compositions, as predicted by the MD simulations for the compressed layer, the variations in the level of enhancement of the specific heat capacity measurements for the various nanomaterials were found to be consistent with the numerical predictions. The formation (and mass fraction) of the compressed liquid layer was predicted to be dependent on the total surface area of the nanoparticles. Hence, the enhancement in specific heat capacity values was predicted to be a surface phenomenon which is affected by the uniformity of dispersion of the nanoparticles and the amount of agglomeration of the nanoparticles. This is consistent with the experimental observations where the uniformity of dispersion and amount of agglomeration of the nanoparticles (which is a function of the time required for complete dehydration of the aqueous solution of the nanomaterials in the synthesis protocols) was found to affect the level of enhancement of the property values. Hence, uniformity of dispersion and stability of the nanoparticles (i.e., minimizing agglomeration) as well the chemical composition of the solvent are key factors for maximizing the specific heat capacity of the nanomaterials.

8. EXPERIMENTAL STUDY V: EFFECT OF SOLVENT PROPERTIES ON SPECIFIC HEAT CAPACITY ENHANCEMENT

8.1 Objective

The aim of this study is to investigate the effect of solvent composition on the specific heat capacity enhancement for carbonate salt nanomaterials mixed with multi-walled carbon nanotubes. As reported in the previous section, it was found that the enhancement in the specific heat capacity of the carbonate salt-based graphite nanomaterials was affected by the chemical composition of the two constituent salts for the solvent phase, lithium carbonate and potassium carbonate. It was also observed that the thermal properties of the pure carbonate salt mixtures were significantly affected by the variation in the mass concentration of the two salts. In order to verify the effect of the composition of the solvent phase on the specific heat capacity – additional experimental measurements were performed for a wide range of chemical compositions of the carbonate salt mixtures. These measurements help to explore how the thermal and chemical properties of the pure solvent (salt mixture) influence the specific heat capacity of the nanomaterials that are synthesized by mixing nanoparticles with the neat solvent.

In the present study, similar synthesis techniques for the molten salt nanomaterials were employed (e.g., using a large petri dish in the water evaporation step). The chemical composition of each nanomaterial was obtained by using ICP-MS (after specific heat capacity measurements were performed using DSC). This is similar to the sequence of experiments performed for the nanomaterial samples synthesized by mixing

graphite nanoparticles with carbonate salt mixtures. Based on both of the results for the specific heat capacity (by DSC) and the chemical composition of the two carbonate salts (by ICP-MS), the effect of the chemical composition on the thermal properties of the solvent are resolved.

8.2 Nanomaterial synthesis

The same synthesis protocol for the molten salt nanomaterials which is called Method 1 as shown in Fig. 7.1 was employed for the carbonate salt mixture-CNT nanomaterials. The Gum Arabic (GA) was used as a surfactant to homogeneously disperse the CNT powder in distilled water, similar to the studies discussed in the previous sections. Of the two synthesis methods mentioned in Section 7, Method 1 was chosen for the current study for dehydrating the samples (i.e., the aqueous solutions were dehydrated using a large petri dish placed on a hotplate, and the dehydrated sample was then used in the DSC experiments). More detailed explanation about the synthesis protocol is presented in the previous section.

8.3 Experiments

The experimental procedures for DSC and determination of the specific heat capacity were discussed in Section 2. The same procedures were followed in this study.

As reported in Section 7, the samples dehydrated on the petri-dish were separated into two regions for sample collection which were then subsequently used for specific heat capacity measurements (using DSC) and testing for chemical composition (using ICP-MS). The ICP-MS measurements were performed by Dr. Taylor's research group in the Department of Veterinary Integrative Biosciences at Texas A&M University. Five samples of the solvent (for different mass concentration ratio) were obtained from the ICP-MS measurements and correlated with the results of the specific heat capacity measurements.

8.4 Results

Fig. 8.1 compares the specific heat capacity of CNT nanomaterials in liquid phase with that of pure carbonate salt mixtures as a function of chemical composition. It was observed that the specific heat capacity of the nanomaterials was significantly enhanced for all cases of the samples. Hence, this shows that the enhancement in the specific heat capacity of nanomaterials was influenced by the solvent (or chemical composition).

The chemical composition of the samples measured by using ICP-MS varied from 36.6 % to 79.2 % in molar fraction of the lithium carbonate. For some of the samples used in this study literature data was not available for specific heat capacity of the neat solvent (salt mixtures). The specific heat capacity values of the pure salt mixtures for those compositions were estimated by interpolation from the measured values shown in the Section 4. The specific heat capacity of the pure solvent (for these compositions)

varied from 1.35 [J/g·K] to 2.53 [J/g·K]. For the nanomaterials, the specific heat capacity was measured to vary from 1.71 [J/g·K] to 3.27 [J/g·K]. All results for the specific heat capacity measurements and the chemical compositions are summarized in Table 8.1. As shown in Fig. 8.1, the level of enhancement in the specific heat capacity of the nanomaterial samples (red circle) compared to that of the pure salt mixture (black triangle) increases as the chemical composition of the neat solvent increasingly derivates from that of the eutectic composition (i.e., Li_2CO_3 and K_2CO_3 in molar ratio of 62:38). While the enhancement of the specific heat capacity for the Case 3 in Table 8.1 (64.3:35.7) was limited to 6.0 %, the enhancements for the Case 1 (79.2:20.8) and Case 5 (36.6:63.4) was obtained to be 29.3 % and 26.7 %, respectively.

Table 8.1 Chemical compositions and specific heat capacity of pure salt mixtures and nanomaterials

Cases	Molar composition (Li_2CO_3:K_2CO_3)	Pure salt mixtures [J/g·K]		Nanomaterials [J/g·K]	
		Solid (400 °C)	Liquid	Solid (400 °C)	Liquid
1	79.2:20.8	1.284	2.526	1.612	3.266
2	68.0:32.0	1.239	2.501	1.359	3.015
3	64.3:35.7	1.218	1.676	1.312	1.777
4	42.5:57.5	1.126	1.410	1.161	1.700
5	36.6:63.4	1.070	1.348	1.219	1.707

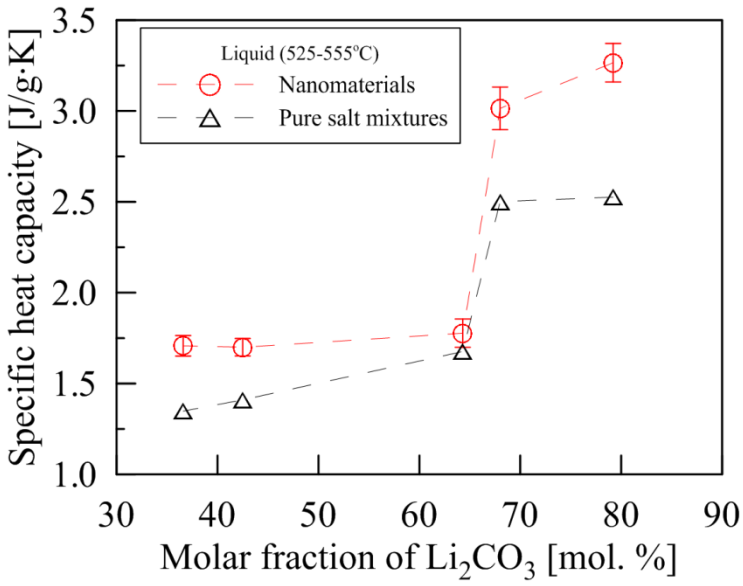

Fig. 8.1 Specific heat capacity of pure carbonate salt mixtures and nanomaterials in liquid phase for five different chemical compositions

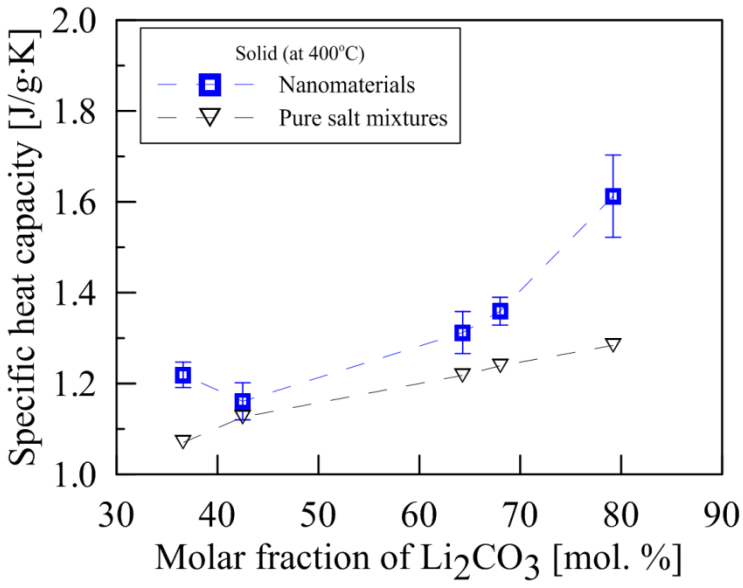

Fig. 8.2 Specific heat capacity of nanomaterials and pure salt mixtures in solid phase (400 ℃) for 5 chemical compositions of solvent

A similar feature was observed in solid phase at 400 ℃ , as shown in Fig. 8.2. However the composition in the solid phase (at which the level of enhancement is minimum) does not correspond to that at the liquid phase. The level of enhancement in the specific heat capacity of the nanomaterial samples (red circle) compared to that of the pure salt mixture (black triangle) increases as the chemical composition of the neat solvent increasingly deviates from that of the eutectic composition (i.e., Li_2CO_3 and K_2CO_3 in molar ratio of 62:38). The plot of the specific heat capacity for the pure carbonate mixture is a monotonically increasing and fairly linear function of the lithium carbonate concentration. However, a similar the plot for the nanomaterial shows a concave (upward) shape.

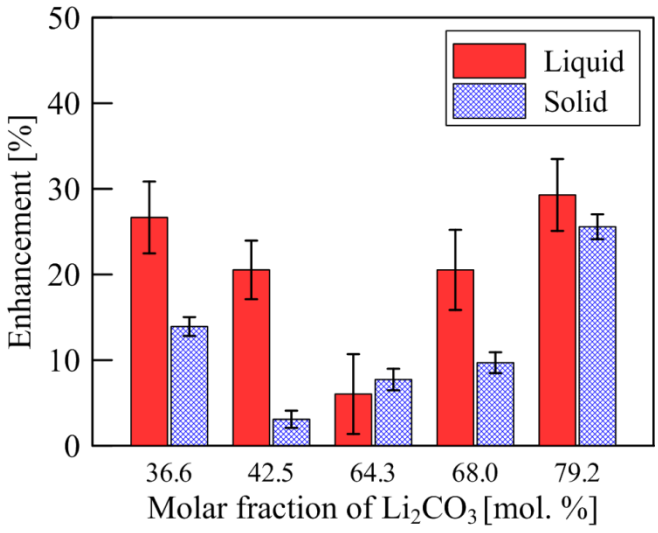

Fig. 8.3 Enhancements of specific heat capacity of CNT nanomaterials in liquid and solid phase for five different chemical compositions of solvent

The enhancements in the specific heat capacity of the carbonate salt mixture-CNT nanomaterials were plotted for both liquid and solid phase in Fig. 8.3. The enhancement plots are V-shaped as the mole fraction of lithium carbonate in the mixture is increased. As mentioned above, the level of enhancement in the specific heat capacity was affected by the chemical composition of the solvent. The minimum level of enhancements in the specific heat capacity for the samples tested in this study was obtained for the chemical composition of 64.3:35.7 which is the closest to the eutectic composition (62:38) of lithium carbonate and potassium carbonate. The enhancements at both ends of the concentration range (36.6 % and 79.2 % of Li_2CO_3 in molar ratio) were usually the highest, which were 26.7 % and 29.3 % in liquid phase and 13.9 % and 25.6 % in solid phase, respectively.

8.5 Discussion

The specific heat capacity measurements were performed for the nanomaterials obtained by mixing carbonate salts mixtures with CNT, where the chemical composition of the solvent material (salt mixture) was varied parametrically. All of the nanomaterial samples showed varying levels of enhancements in the specific heat capacity. In previous sections, it was discussed that the existence of the compressed liquid layer in the vicinity of nanoparticles can affect thermal property of the whole system (i.e., of the mixture). In addition, in Section 7 it was mentioned that the resultant material properties of the compressed layer arising from the spatial variation in the molar concentration ratio

of the constituent salts within the compressed layer (compared to that in the bulk of the solvent phase) could potentially affect the enhancement in the specific heat capacity of the nanomaterials. In order to estimate the specific heat capacity of these nanomaterials, in the same way (as in previous sections), MD simulations were performed. The mole fraction of lithium carbonate (i.e. chemical composition) was varied from 34.0 % to 85.7 %. This chosen range for the MD simulations encompasses the range of molar ratios used in the experiments for the DSC measurements of the samples (36.6 % - 79.2 %).

Figure 8.4 shows the density variation of the solvent (carbonate salt mixtures) adjacent to a CNT for six chemical compositions of the solvent. The results show that compressed layer was formed in the vicinity of the nanotubes. Among the six cases explored in the numerical simulations, two mole fractions (85.7:14.3 and 74.6:25.4) have relatively weak intensity in the first density peak whereas other four cases have significantly higher values for the first peaks in the density plots. In particular, the magnitude of the first peak of the density plot increases as the molar ratio of lithium carbonate in the salt mixture decreases. These trends and results are consistent with the previous results for the graphite nanomaterials, in which higher magnitude of density peak was observed in the simulation results for nanomaterial samples containing lower mole fraction of lithium carbonate in the salt mixture (solvent phase). Based on these two results, it can be concluded that for the molten salt mixture of carbonate salts the magnitude of the density peak decreases with an increase of the mole fraction of the lithium carbonate salt. Hence, at certain value of the mole fraction of the salt mixture the

formation of the compressed phase may be hindered due to the inherent nature of the inter-molecular interactions.

Nevertheless, the nanomaterial samples explored in this study demonstrated significant levels of enhancement in the specific heat capacity values. These enhancements are observed to be affected by several sets of parameters and features. One notable feature is the spatial variation of the concentration of the constituents (salts) within the compressed layer (compared to that of the bulk composition). Figure 8.5 shows the concentration plots demonstrating significant spatial variation in the concentration of the constituent salts (i.e., mole fraction of potassium atoms to lithium atoms) within the compressed layer. It was observed that more potassium molecules per unit volume were contained within the compressed layer (than in the bulk of the solvent phase) for all the numerical simulations explored in this study. Thus, the compressed region definitely has different thermo-physical properties compared to those of the bulk phase of the solvent (i.e., for the pure salt mixture). It should be pointed out that a pure salt mixture having the same composition as that of the compressed layer is likely to have different physical and chemical properties, since the material in the compressed layer is likely to have anisotropic properties due to semi-crystalline ordering of the molecules that is induced by the presence of the nanoparticle (and the ordering is influenced by the underlying lattice structure of the nanoparticle in consideration). For example, the lattice induced ordering of the semi-crystalline compressed layer can be different for CNT as compared to that for graphite or fullerene). As mentioned in Section 7, additionally local fluctuations in the transport mechanisms, such as heat and mass/

species transfer, due to the spatial concentration gradient (i.e., thermophoresis) may be responsible for the effective specific heat capacity enhancement of the nanomaterials (as well as modification of the effective values of other material properties such as density, viscosity and thermal conductivity).

The effect of the chemical composition on the specific heat capacity enhancement was also explored by constructing the concentration plots, as shown in Figure 8.5. Four plots - (A), (B), (E), and (F) - show relatively wide thickness of the potassium atom dominant regions where concentrations of potassium atoms are higher than that of the bulk composition of the solvent. On the contrary, the other two plots, (C) and (D), have narrow regions where the concentration of the potassium atoms is higher than that of bulk composition of the solvent. The four nanomaterials (A, B, E, F) showed significant enhancements of the specific heat capacity whereas the other two samples (C, D) showed lower enhancements. In other words, the nanomaterials (labeled as A, B, E, and F in Figure 8.4 and Figure 8.5) that displayed wider regions of concentration variation showed dramatically higher levels of enhancement in the specific heat capacity, but the nanomaterials (labeled as C and D) that displayed narrow regions of concentration variation showed lower levels of enhancements. Therefore, the imbalance of the molar concentration of the two salts (lithium carbonate and potassium carbonate) in the compressed layer can be considered to have significant influence on the specific heat capacity of the nanomaterials.

The solvent composition can influence the specific heat capacity of the nanomaterials through different transport mechanisms. Several nanomaterial samples

that were tested experimentally in this study were comprised of salt mixtures with molar ratios that were significantly different from the eutectic composition. For these samples, it is expected that a portion of the constituent salts remained unmelted for the range of temperatures that were used in the measurements for the experiments performed using DSC apparatus. Hence, the samples are expected to behave like a slurry for temperatures exceeding the eutectic temperature. In DSC measurements, the specific heat capacity enhancement was increased as the composition of the salt mixture increasingly deviated from the eutectic point. Therefore it is expected that as the proportion of the solid salt phase (i.e., mass fraction of the unmelted material) increases, the level of enhancement in the specific heat capacity was also observed to increase. Hence, the state of the solvent material (completely melted or slurry) is expected to be an important factor for determining the level of the specific heat capacity enhancement. However, additional studies are needed to verify the formation of the slurry and its effect (e.g., mass fraction of the slurry) on the resultant properties of the nanomaterial samples in the solid/ liquid states.

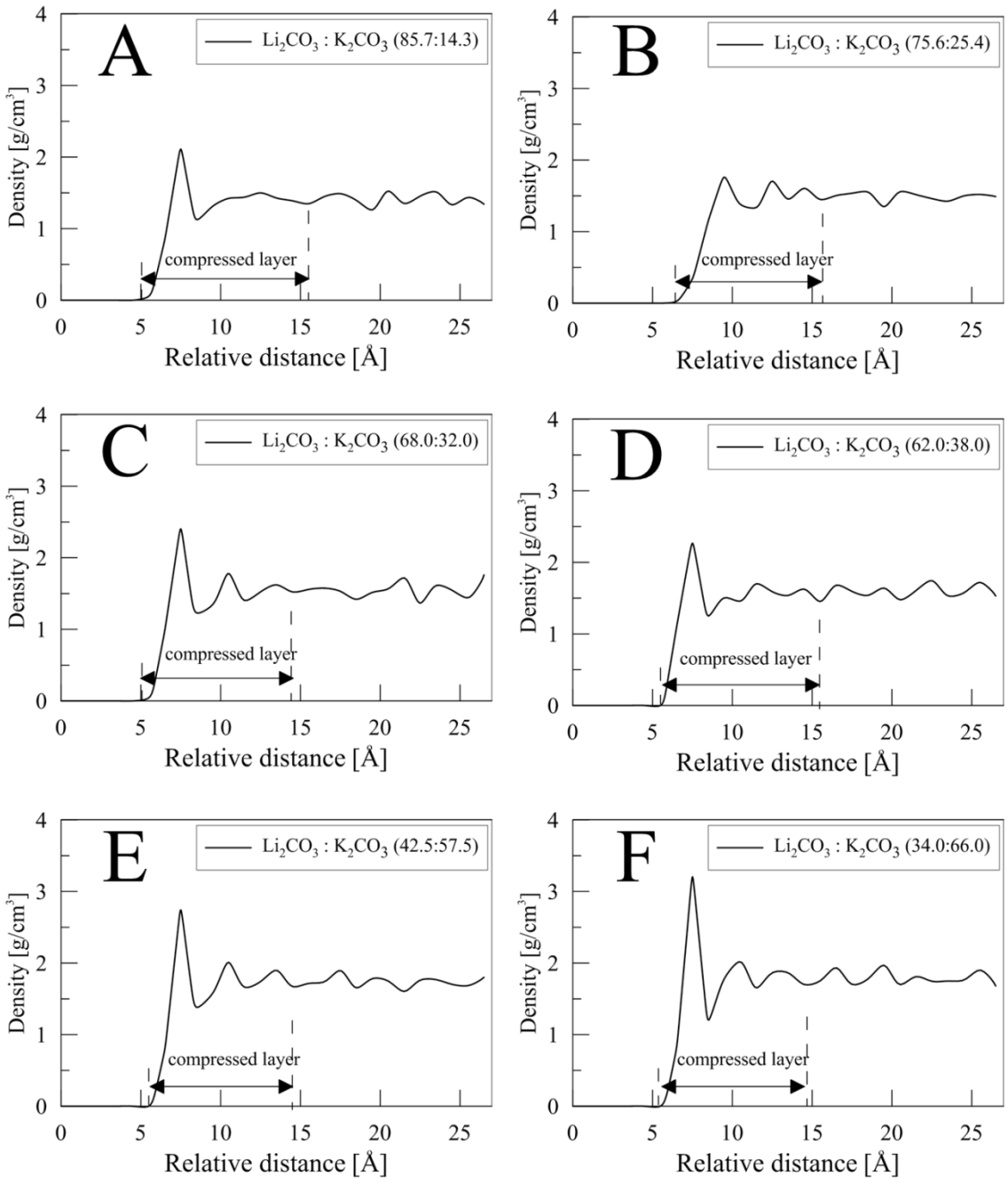

Fig. 8.4 Density variations of solvent material (carbonate salt mixture) as a function of chemical composition

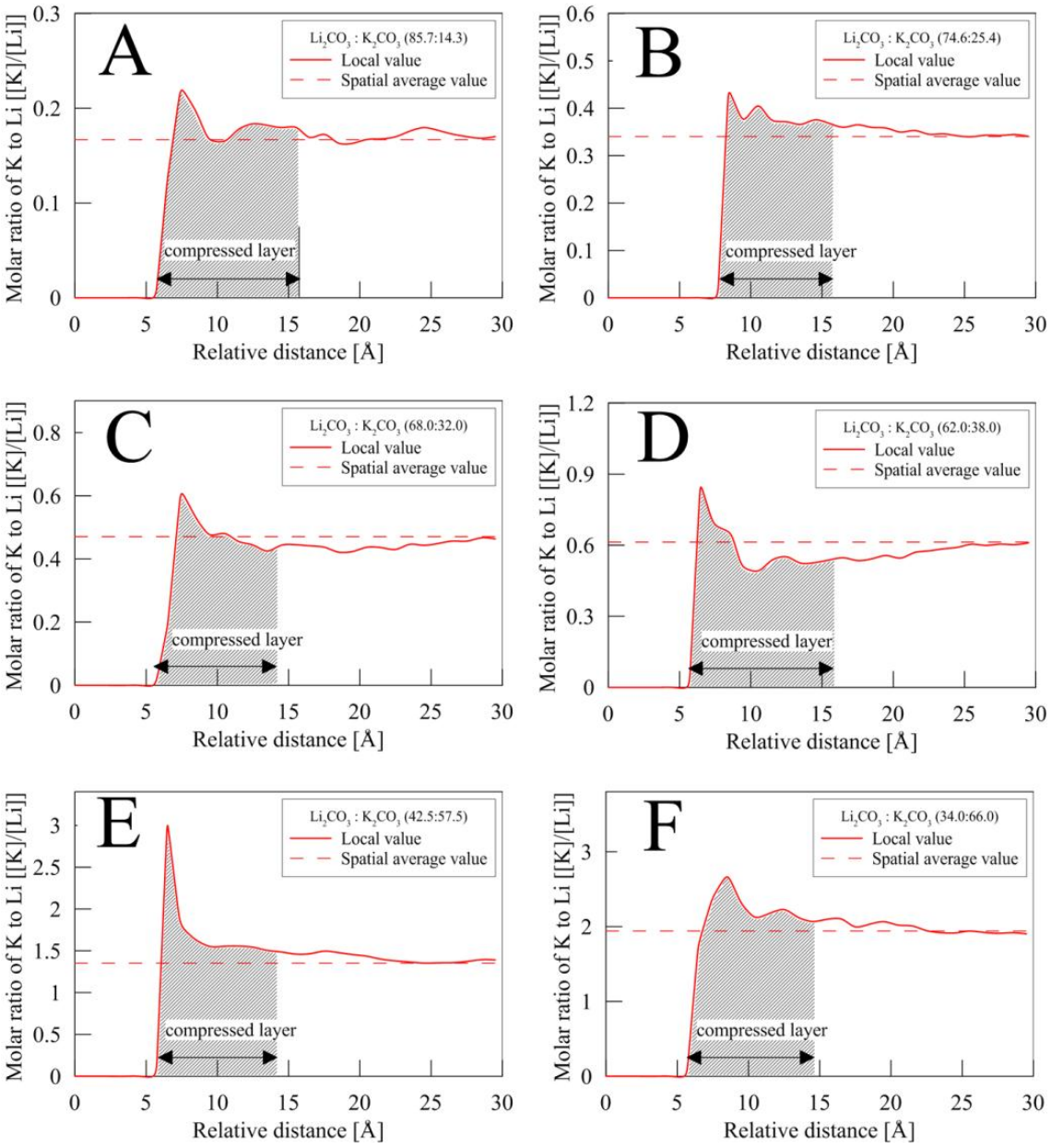

Fig. 8.5 Molar ratio of potassium to lithium along relative position as function of chemical composition

8.6 Conclusion

The specific heat capacity values were measured using Differential Scanning Calorimetry (DSC) for nanomaterials synthesized by mixing carbonate salt mixtures with CNT. The synthesis protocol described in Section 7 (separation of samples using a large petri-dish for dehydration of the resulting nanomaterials) was employed in this study. The effect of the chemical composition of the solvent phase (salt mixture) was examined by measuring mole fractions of the two constituent salts (lithium carbonate and potassium carbonate). The concentrations of the two salts were measured by using ICP-MS technique. MD simulations were also performed for a wider range of the chemical composition of the solvent (compared to the range explored in the experimental measurements). The experimental results showed that the chemical composition of the solvent strongly affected the specific heat capacity. The knowledge gained from the experiments and numerical simulations conducted in this section are summarized as follows:

(a) The specific heat capacity of the carbonate salt mixtures in both solid and liquid phases was significantly enhanced by doping with multi-walled carbon nanotubes. The enhancements varied from 6.0 % to 29.3 % in liquid phase and from 3.1 % to 25.6 % in solid phase (at 400 ℃). However, the maximum enhancement in the molten salt-CNT nanomaterials was smaller than that in the graphite nanomaterials.

(b) The chemical composition of the solvent (carbonate salt mixture) was observed to affect the specific heat capacity enhancement of the nanomaterials. It was observed that as the solvent chemical composition of the solvent deviates increasingly from the

eutectic composition, the level of enhancement of the specific heat capacity was increased.

(c) The MD simulations show that the compressed liquid layer that forms in the solvent in the vicinity of the nanoparticles has different values (as well as spatial variation in the values) of mass density and molar ratio of the constituent salts (compared to that in the bulk phase). This is expected to affect the properties of the nanomaterial samples. The results from the MD simulations show the formation of density peaks in the compressed layer. The magnitude of the first density peak in the compressed layer was observed to increase in magnitude with decrease in the molar ratio of lithium carbonate. Hence, the molar ratio of the solvent phase (salt mixtures) may have a significant influence on the formation of the compressed layer and thereby, the properties of the resulting nanomaterials.

(d) Based on the experimental results (from both Section 7 and this section), it can be deduced that the composition of the solvent phase can significantly influenced the resulting specific heat capacity of the nanomaterials. It is expected that a portion of the salt mixture for the nanomaterials can exist in solid phase even after the melting point has been exceeded in the DSC experiments, resulting in the formation of a slurry in the testing pans used in the experimental measurements. The nanomaterial samples that were likely to form a slurry - showed higher levels of enhancement in the specific heat capacity values. Additionally, the magnitude of the enhancement was higher for the samples with chemical composition (molar ratio) that increasingly deviated from the eutectic composition. Additional studies are required to verify the formation of the

slurry-phase in the nanomaterial samples for the temperature ranges used in the specific heat capacity measurements. The influence of the slurry materials (size, morphology, composition, etc.) on the resulting material properties of the samples also need to be explored in future studies.

9. EXPERIMENTAL STUDY VI: SURFACTANT ADDED MOLTEN SALT MIXTURES

9.1 Objective

Control experiments were performed to estimate the contribution of the surfactants (utilized for homogeneous dispersion during sample preparation) to the total specific heat capacity of the nanomaterial samples.

As discussed in the previous sections, several types of organic surfactants were used to improve the uniformity of the nanoparticle dispersion in water. As a consequence of homogeneous dispersion – unagglomerated nanoparticles were obtained in the nanomaterials with a concomitant enhancement in the specific heat capacity values of the nanomaterials. To ascertain the contribution of the surfactant material to the total specific heat capacity of the nanomaterials – control experiments were designed and implemented. In the control experiments – the pure salt mixtures were doped with the same mass fraction of the surfactants but without nanoparticles. The specific heat capacity values of these salt samples were measured. However, it was observed that the level of enhancement for salt samples with surfactants was much higher than for salt samples with surfactants in which nanoparticles were also added to the mixture. Materials characterization of these samples (with surfactants but without addition of nanoparticles to the mixture) demonstrated the formation of organic nanoparticles – potentially from chemical degradation of the surfactants themselves. Materials characterization techniques involved micro-Raman Spectroscopy (mRS) and Tunneling

Electron Microscopy (TEM). These nanoparticles that were formed in-situ during the thermocycling experiments (repeated melting and solidification) resulted in higher levels of enhancement – compared to samples where nanoparticles were added during the sample preparation step. Additionally, a necessary condition for the formation of the organic nanoparticles was also suggested in this study.

9.2 Sample preparation

The same base material (solvent) composed of the eutectic composition of the carbonate salt mixture (as mentioned in previous sections) was used in this study. Two surfactants, SDS and SDBS, were homogeneously dispersed into the aqueous solution of the pure salt mixture – followed by complete dehydration of the samples. Fig. 9.1 shows the sample preparation for the salt-surfactant mixtures. It is similar to one of the protocols for nanomaterials synthesis as shown in Fig. 6.1. In the water evaporation step, the hotplate temperature was set to 120 ºC.

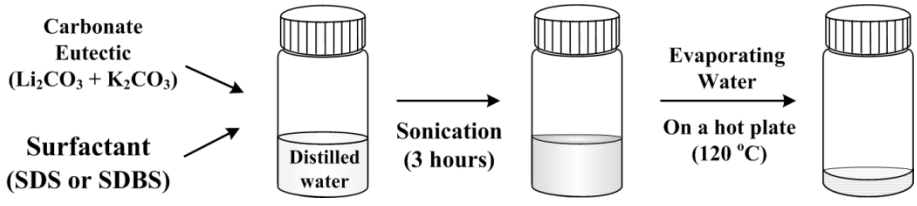

Fig. 9.1 Schematic diagram for preparation of molten salt-surfactant mixtures

9.3 Experiments

9.3.1 Specific heat capacity measurements

The experimental procedure for the DSC experiments (thermocycling involving repeated melting-solidification of the samples) and calculation procedure of estimating the specific heat capacity of the samples - were already discussed in Section 2. The same procedures were followed in this study. The effect of the water evaporation step on the specific heat capacity was explored for the salt-SDBS mixtures. For some of the samples, complete dehydration was achieved in 4 hours. However, for some of the other samples the dehydration step was continued for 24 hours (even after complete dehydration of the samples was achieved).

9.3.2 Materials characterization of samples

Raman spectrometer (Model: Horiba Jobin-Yvon LabRam IR) was used to confirm the existence of carbon nanoparticles in the samples by scanning changes in chemical structures of the surfactants. Raman measurements were performed with powder samples of the salt-surfactant mixtures – both before and after the experiments. He-Ne laser (632 nm) was chosen as a light source for optical excitation of the samples. The spectrometer is equipped with a charge coupled detector device (CCD) cooled by liquid nitrogen. The spectral resolution was about 0.16 cm^{-1} for the experimental conditions used in this study.

In order to compare Raman spectra of post-DSC samples to pre-DSC samples, three sample groups were prepared: (1) pure surfactants – both SDS and SDBS (Specimen I); (2) surfactant (SDS) mixed with eutectic salt mixture (Specimen II); and (3) surfactant

(SDBS) mixed with eutectic salt mixture (Specimen III) that was subjected to short heating duration and long heating duration for dehydration step. Specimen I was pure surfactant and was used as received. The sample preparation protocol for Specimen II and Specimen III involved the preparation of an aqueous solution of the surfactants mixed with the eutectic salt followed by dehydration on a hotplate at 120 °C to obtain the dry powder of the nanomaterial samples. For Sample II the dehydration step was limited to 4 hours. For Specimen III – the dehydration step was fixed at 4 hours for one set of experiments and 24 hours for another set of experiments.

To ensure the reliability of the Raman Spectra measurements the results for the Specimen I were compared with the reference data provided by the manufacturer (Sigma-Aldrich) and were found to be consistent. Subsequently, Raman Spectra measurements for salt samples mixed with surfactants (Specimen II and Specimen III) were performed. The differences in the Raman Spectra measurements for the two specimens were then evaluated. Appearance of additional peaks like a carbon-carbon bonding in Specimens II and III were used to prove the existence (or formation) of carbon nanoparticles (graphitic nanoparticles).

Transmission Electron Microscope (TEM; Model: JEOL, JEM-2010) equipped with ATW type Energy Dispersive Spectroscopy (EDS) detector (Oxford Instruments) was employed as another independent method to verify the formation of carbon nanoparticles in Specimen III. Using the TEM images and EDS results, existence of carbon nanoparticles were ascertained in the post-DSC samples. EDS spectra for the nanoparticles on silicon monoxide grids were measured to confirm that the observed

nanoparticles in the TEM images were indeed due to carbon-carbon bonding, which proved the formation of carbon nanoparticles from the chemical degradation of the surfactant molecules.

9.4 Results and discussion

9.4.1 Specific heat capacity of eutectic-SDS mixtures

Fig. 9.2 shows the specific heat capacity values of the carbonate salt eutectic-SDS mixtures for three different concentrations. Compared to the specific heat capacity of the pure salt eutectic, the specific heat capacity values were significantly enhanced for all of the concentrations of SDS used in this study. The enhancement of the specific heat capacity for the sample prepared using SDS at 0.5 % mass concentration was 11.6 %. With increase in the concentration of SDS from 0.5 % to 1 %, the specific heat capacity of the mixture was increased from 1.761 [J/g·K] to 1.836 [J/g·K], which corresponds to an enhancement of 11.6% to 16.3%, respectively. For the sample prepared using SDS at a mass concentration of 5 %, however, the specific heat capacity was decreased to 1.659 [J/g·K], where the level of enhancement was within the margins of the measurement uncertainty – hence it can be conclusively ascertained if there was any net enhancement in the specific heat capacity values. Additionally, it was observed that the standard deviation of the result for the samples (prepared using SDS at mass concentration of 5 %) was large relative to the results for the other samples (i.e., at lower mass concentrations of SDS). This result was attributed to the degradation of the specific heat capacity in

successive cycles while the thermocycling experiments were in progress in the DSC – in order to check the repeatability of the measurements for multiple cycles of melting-solidification.

The specific heat capacity values for samples (SDS at mass concentration of 5%) are shown in Fig. 9.3 – where the progressive degradation in the measured values for successive cycles for the different measurement experiments conducted on different days. Fig. 9.3 (A) shows the plots with original values of the specific heat measured in these experiments. The normalized values of the specific heat capacity (normalized to the first value obtained in successive thermocycles) are shown in Fig. 9.3 (B). As shown in the figures, the huge degradation of the specific heat capacity of the samples (SDS mass concentration of 5 %) was observed. The degradation in the final value (compared to the first value) was as much as 34%. For other concentrations of SDS, however, almost uniform specific heat capacity values were obtained in successive cycles for the thermocycling experiments. For the other samples (SDS mass concentration of 0.5 % and 1 %) the measured values of the specific heat capacity were within 98 % and 93 % of the first value, respectively.

From the enhanced specific heat capacity values measured in the DSC experiments and the anomalous variation in specific heat capacity with variation mass concentration of SDS in the salt samples, it can be expected that the thermocycling (repeated melting and solidification of the salt samples) induced changes in the chemical structure of SDS. The thermocycling experiments involved operation at high temperatures ranging from 150 °C to 560 °C. The carbon chains of SDS which were attached to sulfate groups were

potentially disrupted at these high temperature conditions leading to consolidation of the carbon-carbon bonds to form carbon (e.g., graphite) nanoparticles. As mentioned before, doping carbonate salt mixtures (including eutectic) with small amounts of organic nanoparticles resulted in enhancement of the specific heat capacity of the salt mixtures. Therefore, the carbon nanoparticles formed in-situ in these thermocycling experiments are also expected to enhance the specific heat capacity values of the resulting nanomaterials (even though the samples did not contain any nanoparticles – to begin with – during the sample preparation step).

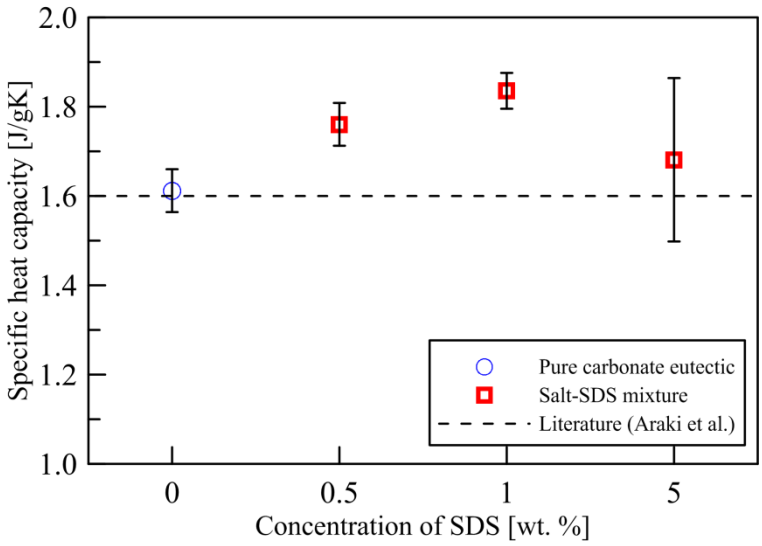

Fig. 9.2 Specific heat capacity of samples of carbonate salt eutectic mixed with SDS at different mass concentrations of SDS

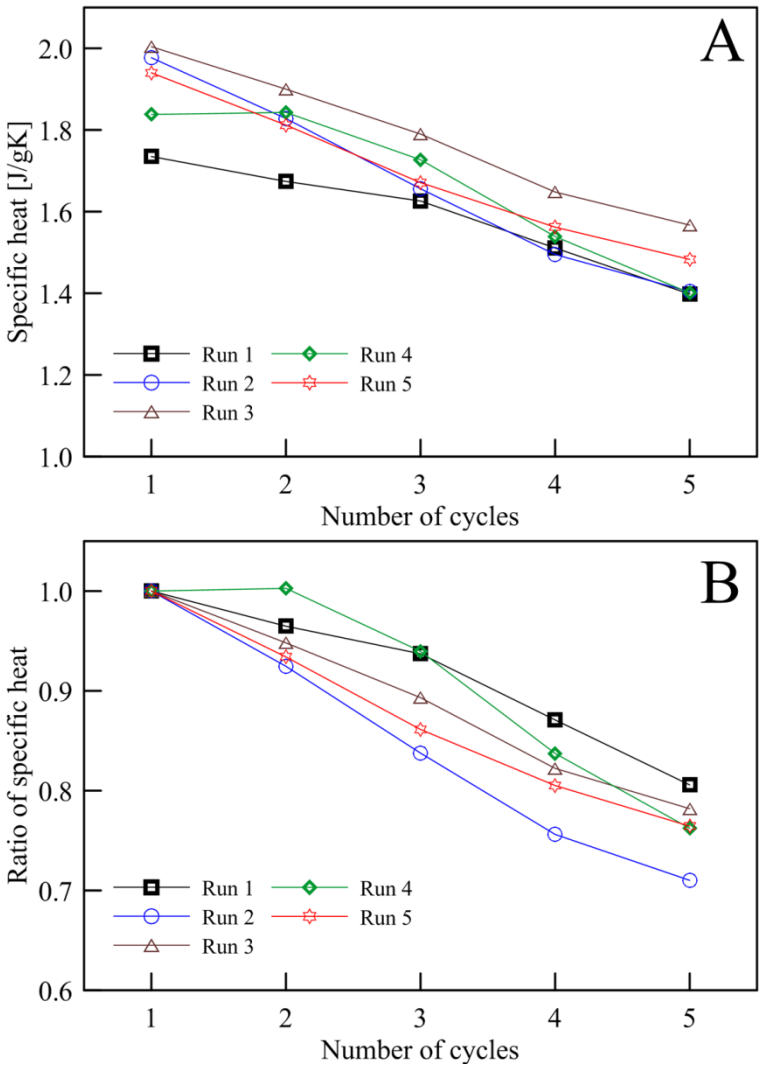

Fig. 9.3 Specific heat capacity values for salt samples (with SDS at mass concentration of 5%) plotted for successive cycles during thermocycling experiments performed in the DSC: (A) Raw values, and (B) Normalized values (normalized with the first value in each thermocycle experiment)

9.4.2 Specific heat capacity of eutectic-SDBS mixtures

Another organic surfactant, SDBS, was used to verify whether the same technique can be used for other surfactant materials. The specific heat capacity of salt eutectic-SDBS mixture was measured in the liquid phase. The same protocol was employed to prepare the mixtures, and experimental conditions were also the same as salt-SDS mixtures. Fig. 9.4 shows the specific heat capacity of the salt-SDBS mixtures as a function of the SDBS mass concentration. Surprisingly, the specific heat capacity was not enhanced by adding SDBS in the carbonate salt eutectic, and rather was marginally degraded compared to that of the pure eutectic sample. The increase in the concentration of SDBS did not significantly affect the specific heat capacity of the mixtures. This discrepancy in behavior for the samples mixed with the two different surfactants (SDS and SDBS) can be rationalized by the fact that there is a large difference in the decomposition temperature for SDBS compared to that of SDS. As reported in previous studies, SDS is easily decomposed by prolonged heating at over 40 °C [129]. On the other hand, the decomposition temperature of SDBS is known to exceed 238 °C [143, 144].

Hence to cause chemical decomposition of SDBS, prolonged heating of the samples containing SDBS is required at elevated temperatures. Therefore, the salt-SDBS mixtures were heated for additional durations even after the complete dehydration of the salts-SDBS water solution was achieved. Heating duration of the salt-SDBS mixtures were prolonged to 24 hours at 120 °C. Fig. 9.5 shows the specific heat capacity values of these samples containing SDBS surfactant that were heated for longer duration. In

contrast to the samples heated for shorter duration, the specific heat capacity was significantly enhanced for all mass concentrations of SDBS for the samples with prolonged heating during the dehydration step. For the samples with prolonged thermal treatment during dehydration step (containing SDBS at mass concentration of 0.5% and 1%) the specific heat capacity enhancement exceeded 18% - compared to that of the pure eutectic samples. Interestingly, the specific heat capacity for the samples subjected to prolonged heat treatment during dehydration step (containing SDBS at mass concentration of 5%) was lower than the samples containing SDBS at lower concentrations. Nevertheless, there was no significant degradation in the specific heat capacity values for successive cycles during thermocycling experiments for this sample.

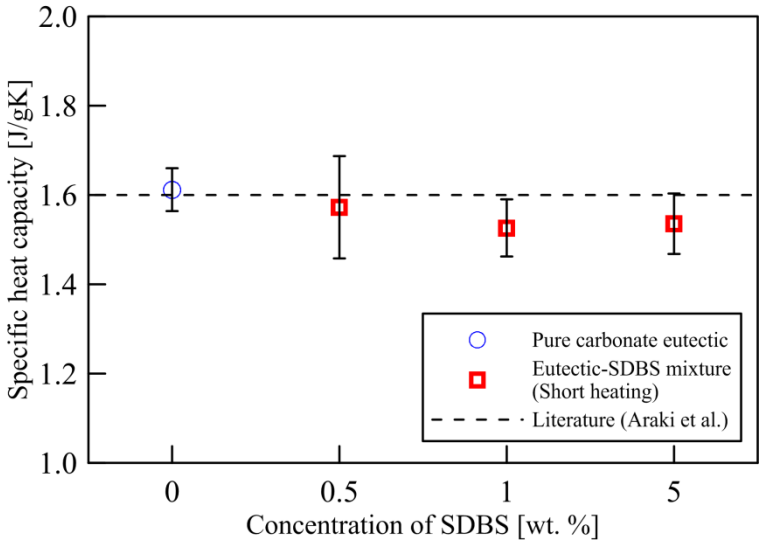

Fig. 9.4 Specific heat capacity of carbonate salt eutectic-SDBS mixtures (short heating)

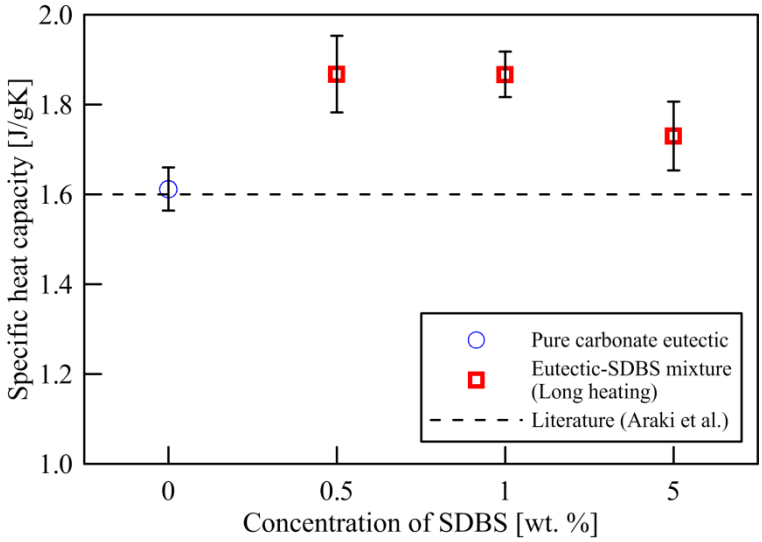

Fig. 9.5 Specific heat capacity of carbonate salt eutectic-SDBS mixtures (long heating)

9.4.3 Trace of carbon nanoparticles: Raman spectrum

As mentioned in the Experiments subsection above, Raman Spectra were obtained for the three different sample groups: (1) Specimen I (pure surfactants SDS and SDBS, used as received), (2) Specimen II (eutectic salt mixed with SDS, dehydrated at 120 °C for 4 hours), and (3) Specimen III (eutectic salt mixed with SDBS, dehydrated at 120 °C for 4 hours or 24 hours).

Fig. 9.6 shows the Raman Spectra for Specimen I (SDS and SDBS) measured in present study. Each spectrum of two surfactants was compared with references provided by the manufacturer (Sigma-Aldrich) to conform the reliability of the measurements and purity of the as-received surfactant samples. The Raman spectrum of pure SDS in Fig. 9.6 (A) consists of sharp peaks at around 2900 cm^{-1} and several week peaks at around

1450 cm^{-1}, 1300 cm^{-1}, 1130 cm^{-1}, and 1175 cm^{-1}, including peaks that occurred in shoulder regions of the other peaks. The spectrum of pure SDBS shows a series of peaks located at around 2900 cm^{-1} and a relatively weak peak at 3060 cm^{-1}. It also includes some sharp and weak peaks between 1600 cm^{-1} and 500 cm^{-1}. These were consistent with the manufacturer data for Raman Spectra for these surfactants.

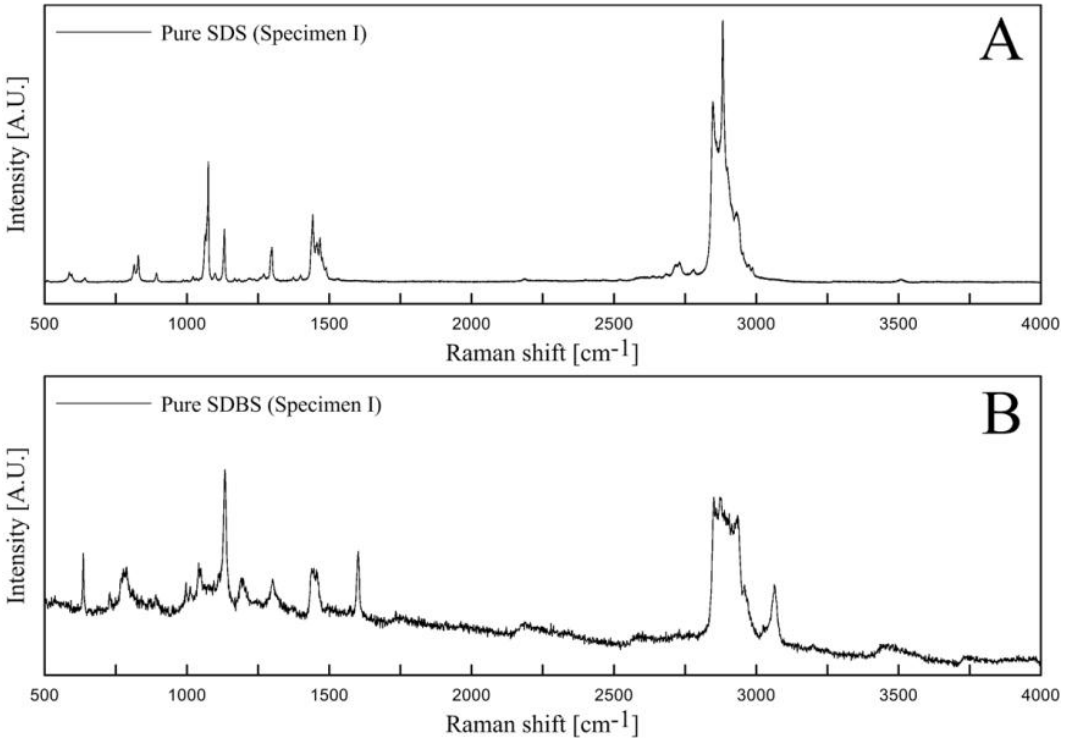

Fig. 9.6 Raman spectra of Specimen I: (A) pure SDS and (B) pure SDBS

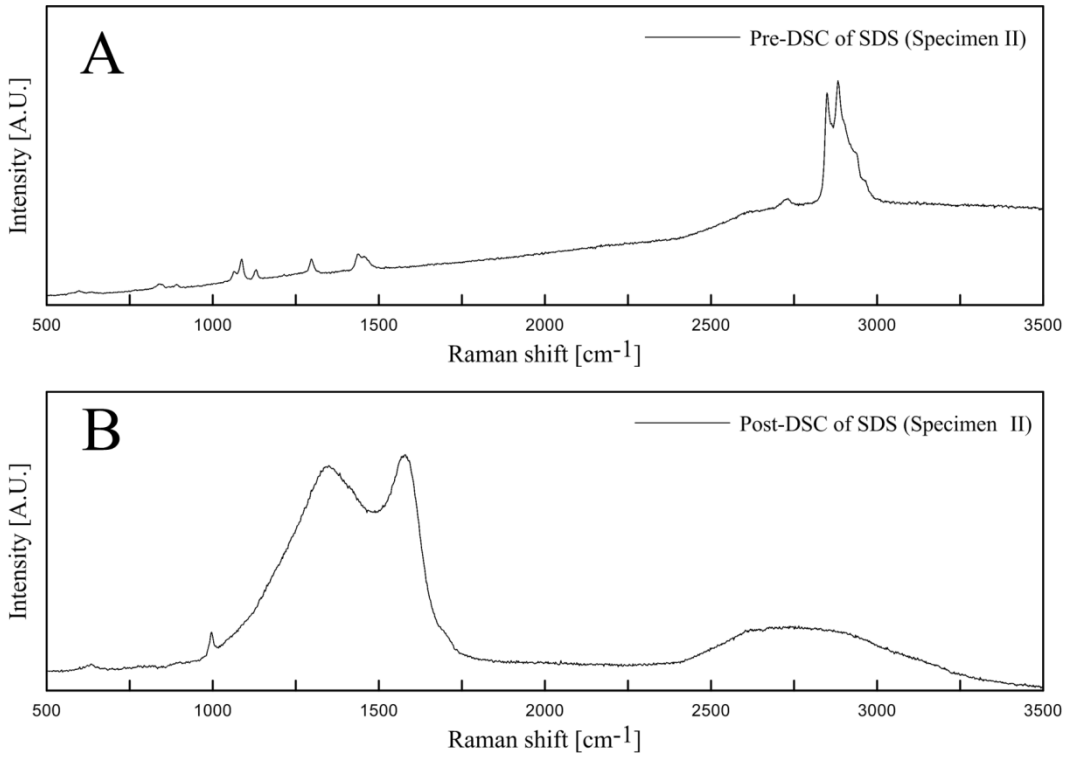

Fig. 9.7 Raman spectra of Specimen II samples containing SDS: (A) pre-DSC sample and (B) post-DSC sample

Prior to measuring Raman spectra of Specimen III (salts-surfactant mixtures), Raman spectra of pre-DSC and post-DSC samples were measured for Specimen II in order to examine the occurrence (or absence) of specific peaks in the spectra – both before and after the thermocycling experiments were performed using the samples in a DSC. Fig. 9.7 shows the Raman Spectra of SDS (Specimen II) for pre-DSC and post-DSC samples. Comparing with Fig. 9.6 (A), the Raman spectrum of the pre-DSC SDS sample (Specimen II) appeared to be similar to the spectrum of Specimen I, as shown in Fig. 9.6 (A). In other words, there is no significant difference between pure SDS samples (Specimen I) and pre-DSC samples (Specimen II). However, the Raman spectra in Fig.

9.7 (B) obtained from the post-DSC sample was totally different from the pre-DSC sample in Fig. 9.7 (A), where two main features were observed in the Raman spectrum measurements. As shown in Fig. 9.7 (B), most of peaks (observed in the pre-DSC samples) vanished and two broad-band peaks at 1566 cm^{-1} and 1335 cm^{-1} appeared for the post-DSC sample. The Raman shifts of 1566 cm^{-1} and 1335 cm^{-1} are in accordance with G band and D band in carbon structures such as carbon nanotubes and graphite nanoparticles [145-147]. From the Raman Spectra measurements of Specimen II, it can be deduced that the surfactants were decomposed due to the high temperature condition in the DSC and that carbon atoms of the surfactants spontaneously formed carbon nanoparticles during the DSC experiments.

Finally, Raman spectra for the Specimen III samples were also obtained in this study. The results for both salt-SDS mixtures and salt-SDBS mixtures are shown in Fig. 9.8 and in Fig. 9.9, respectively. For the pre-DSC samples (Specimen III), most of the peaks in Raman Spectra were observed to have disappeared except for two peaks located between 1000 cm^{-1} and 1150 cm^{-1}. From this result it can be expected that the chemical structures may have changed during sample preparation (e.g. during dehydration step). Fig. 9.8 (B) and Fig. 9.9 (B) show Raman spectra for the post-DSC samples for the two mixtures. Surprisingly, the G and D band peaks were observed in the Raman Spectra (at 1592 cm^{-1} and 1323 cm^{-1}). Consistent with the Raman Spectra observed for the Specimen II samples, the same peaks were also obtained for the Specimen III samples (eutectic salt-SDBS mixture); however the G band and D band peaks were slightly shifted to 1556 cm^{-1} and 1321 cm^{-1}.

Hence the Raman Spectra measurements conclusively proved the formation of carbon nanoparticles in this study. However, there were small differences in the peaks observed in the Raman Spectra for the position for G band and D band for the Specimen II and Specimen III samples. The shift in the location of the peaks in the Raman Spectra can be explained by the variation of the extent of structure disorder and clustering in the two samples [148].

9.4.4 Trace of carbon nanoparticles: Transmission electron microscope

Using Raman spectroscopy, the existence of the carbon nanoparticles in the salt-surfactant mixtures (post-DSC samples) was established. To determine the size of the nanoparticles formed in-situ – Tem measurements were performed. Fig. 9.10 shows electron microscopy images of carbon nanoparticles found in the salt-surfactant mixtures (Specimen III). Fig. 9.10 (A) and (B) obtained from TEM demonstrate the formation of carbon nanoparticles. These TEM images are consistent with similar images of carbon nanoparticles reported in the literature [149, 150]. The TEM images were obtained by placing the samples on TEM grids (supported by Silicon monoxide films). Additionally, the elemental composition of the nanoparticles was also analyzed by using EDS. As shown in Fig. 9.10 (C) and (D), the EDS results confirmed that the nanoparticles observed in the TEM images were made of carbon. This conclusively establishes the formation of carbon nanoparticles in-situ during the thermocycling experiments for the eutectic salt samples mixed with surfactants.

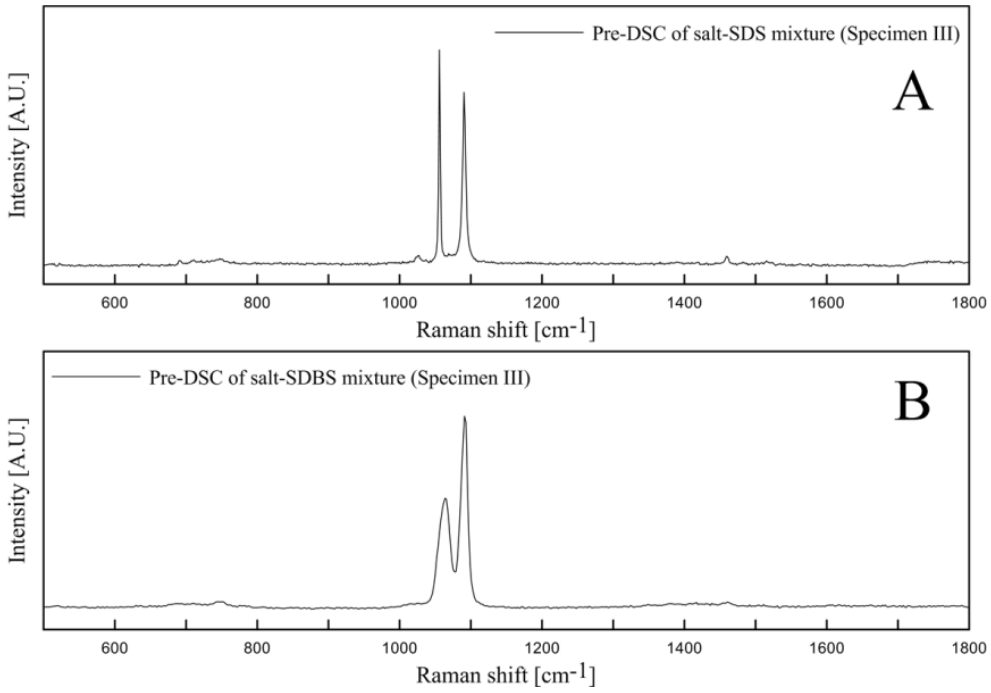

Fig. 9.8 Raman spectra of Specimen III (salt-SDBS mixture, heat treatment for 4 hours): (A) pre-DSC sample (B) post-DSC sample.

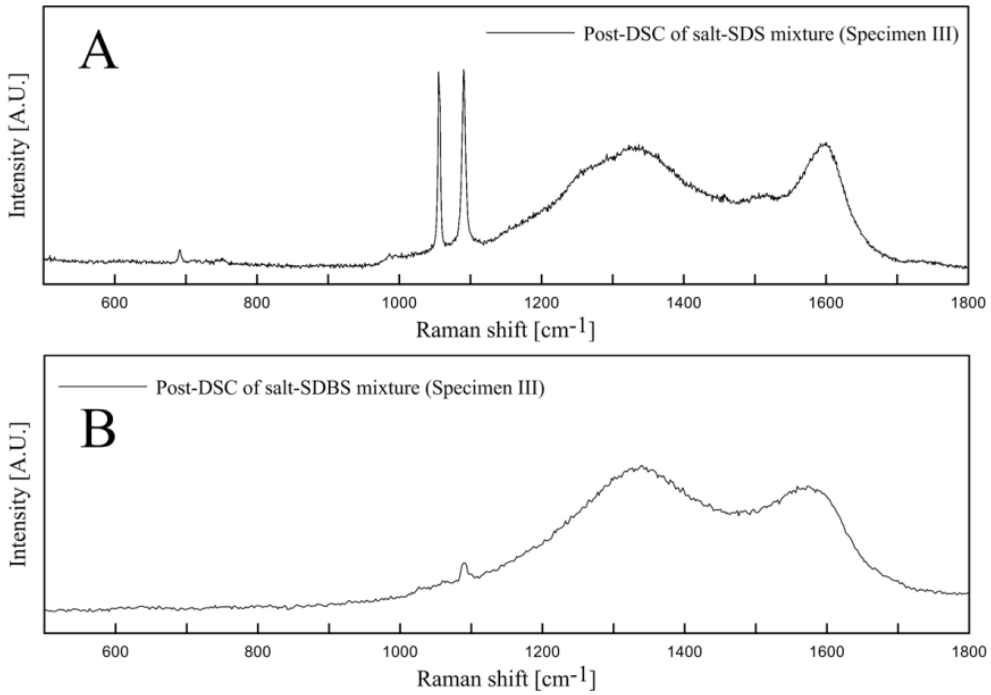

Fig. 9.9 Raman spectra of Specimen III (salt-SDBS mixture, heat treatment for 24 hours): (A) pre-DSC sample and (B) post-DSC sample

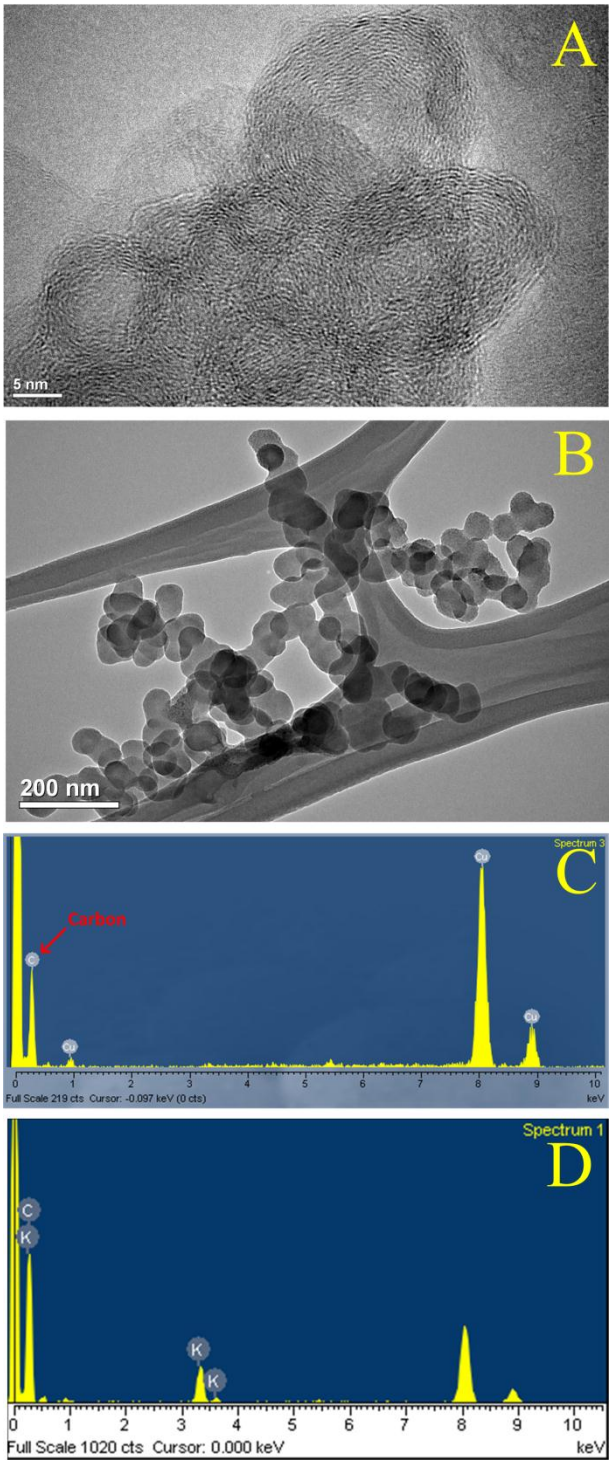

Fig. 9.10 TEM images of carbon nanoparticles: (A) sample containing SDS and (B) sample containing SDBS, and EDS results: (C) for sample containing SDS and (D) for sample containing SDBS

9.5 Conclusion

Specific heat capacity enhancements of carbonate salts eutectic samples (mixed with surfactants) were obtained from DSC experiments that were performed for two different surfactants (SDS and SDBS). In-situ synthesis of carbon nanoparticles were demonstrated in these studies. In-situ synthesis of carbon nanoparticles in these eutectic salt samples was accompanied by significant enhancement of the specific heat capacity of these samples. Materials characterization experiments were performed using Raman Spectroscopy, visualization using TEM and elemental composition analyses using EDS. The knowledge gained from these experiments is summarized as follows:

(a) Enhancement of specific heat capacity exceeded 18% by adding organic surfactants at mass concentration of 0.5% and 1% to carbonate salt mixtures at eutectic composition. This enhancement values are comparable with the experimental measurements for the nanomaterials (described in the previous sections in this study).

(b) The increase in the amount of surfactants (to mass concentration of 5%) leads to a decrease in the specific heat capacity of the salt-surfactant mixtures. Additionally, huge degradation in the specific heat capacity values were observed for the Specimen II samples (salt-SDS mixture) in successive cycles during the thermocycling experiments performed in the DSC apparatus.

(c) It was found that the duration of heating during the dehydration step (for sample preparation) affected the specific heat capacity enhancement for salt-SDBS mixtures. While there was no enhancement of the specific heat capacity for the Specimen III samples heated for the short periods (less than 4 hrs. at 120 °C), the Specimen III

samples which were heated for extended periods (about 24 hrs) showed significant enhancement of specific heat capacity values.

(d) The Raman Spectra for the Specimen III samples - for both pre-DSC and post-DSC samples – demonstrated the existence of carbon nanoparticles

(e) The nanoparticles that were formed in-situ in these experiments were visualized using TEM.

(f) Elemental composition analyses using EDS conclusively showed that carbon nanoparticles were formed in-situ in these experiments.

10. EXPERIMENTAL STUDY VII: VISCOSITY OF MOLTEN SALTS-CNT NANOFLUIDS

10.1 Objective

The aim of this study is to measure the rheological behavior of the nanomaterials in the liquid phase. The nanomaterials were synthesized by dispersing carbon nanotubes (CNT) in pure salt mixtures using the synthesis protocols described earlier.

The motivation for performing these measurements is to resolve issue of considerable engineering significance. Rheological properties of the nanomaterials in the liquid state are important for determining the efficacy (e.g., overall plant efficiency and thermodynamic efficiency) of these materials for TES in energy harvesting applications, such as in CSP plants (as well as geothermal and nuclear power plants). The rheological properties are also important in determining the efficacy of nanofluids for thermal management applications (such as for developing novel coolants and HTF). Since the pumping cost of these fluids is a significant factor governing the economics of various engineering applications, the results presented in this section have wide applicability and are helpful for determining the optimum concentration of the nanoparticles for obtaining the desired rheological properties (in conjunction with the desired levels of enhancement in the values for thermal conductivity and specific heat capacity). For example, these experimental data can be useful for the development of novel heat exchanger configurations (e.g., liquid-to-liquid and liquid-to-gas) where nanofluids are used as the HTF.

Controversies abound in the literature pertaining to the rheological behavior of nanofluids, where some studies reported experimental measurements for the rheological properties by assuming Newtonian behavior while other experimental studies conclusively demonstrated Non-Newtonian behavior in the experimental measurements for various nanofluids (e.g., shear thinning behavior). Hence the effective viscosity of the nanomaterials was measured over a wide range of shear rates. The effect of the nanoparticle (CNT) concentration was also investigated by performing the experiments for three different values of the mass concentrations for the nanoparticles: 1 %, 2 % and 5 %. Also, it is logical to expect that the amount of agglomerated nanoparticles will also affect the rheological properties of the resulting nanofluids. Hence the synthesis protocol was tweaked to obtain two different nanomaterials for a mass concentration of the nanoparticles fixed at 1 %. A surfactant (Gum Arabic or "GA") was used to uniformly disperse the nanoparticles (CNT) into the aqueous solution of the eutectic salt (prior to ultra-sonication and dehydration of the mixture). In the other sample, GA was not used and therefore the uniformity of dispersion (and agglomeration) of the CNT was different. The enhancement in the measured value of viscosity was smaller for the surfactant dispersed nanomaterials (compared to the nanomaterial without surfactant dispersion). Finally, the level of aggregation of the nanotubes was estimated for the samples of the two nanomaterials by using a theoretical model obtained from the literature.

10.2 Sample preparation

The same nanomaterials (used for specific heat capacity measurements) were also used in this study. The pure eutectic salt mixture consists of lithium carbonate and potassium carbonate by 62:38 molar ratio. The high temperature nanofluids were synthesized by using the protocol depicted in Fig. 6.1.

10.3 Experimental apparatus and procedure

A rotational rheometer and a cone-and-plate test section were used for the viscosity measurements. The measurements were performed over a wide range of shear rates varying from 1 to 1000 [1/s]. The temperature for the measurements was fixed at 550 ℃ for ensuring that the molten salt eutectic samples were in the liquid state. The temperature of the samples was controlled by an external convection-radiation oven, which was integrated with the rheometer instrument for enabling measurements at elevated temperatures. Nanoparticle mass concentrations were fixed at 1%, 2%, and 5%. The mass concentration of the GA was fixed at 1 %. To examine the effect of agglomeration of the nanoparticles on the rheological behavior of the nanomaterials, the samples were also synthesized by mixing the nanoparticles with the eutectic salt samples at a mass concentration of 1 % and without using any surfactant. The rheological properties of all the samples (pure eutectic salt mixtures and the nanomaterials) were measured for identical test conditions in the rheometer (temperature, shear rates and

cone-plate configuration). The cone-plate configuration enabled the imposition of uniform shear rates throughout the volume of the test samples.

10.4 Results and discussion

10.4.1 Rheological behavior of nanomaterials

Fig. 10.1 shows the results from the viscosity measurements for the pure carbonate eutectic samples and the nanomaterial samples. The measurements were performed as a function of the shear rate at 550 ℃. It is observed that the results for the pure eutectic are in good agreement with the literature data [151] except for values from the measurements that were performed at very low shear rate. For the low shear rate measurements, the exceptionally high values for viscosity for both the pure eutectic and the nanofluids can be attributed to the high measurement uncertainty associated with the small values of torque in the measurement instrument. Fig. 10.1 shows highly non-linear rheological behavior for the nanomaterial samples which is akin to properties of shear thinning liquids (non-Newtonian). The shear thinning behavior was more pronounced for higher values of mass concentration of the nanoparticles. In other words, the non-Newtonian shear thinning behavior was extended to higher shear rates with increase in the mass concentration of the nanoparticles in the samples. At a shear rate of 1000 [1/s] where asymptotic behavior for the viscosity values was observed, the enhancements in the viscosity values were 11 %, 93 %, and 1130 % for the CNT mass concentrations of 1 %, 2 %, and 5 %, respectively. Comparing these results with the results for a nitrate

salt mixture-silica nanofluid [80], the viscosity of CNT nanofluids was more sensitive to the concentration of the nanoparticles. It can be explained using the fact that the carbon nanotubes are much larger in size than silica nanoparticles. Moreover, in the previous study [80] on the viscosity of nitrate-silica nanofluids which were tested for similar concentrations (0.5 % and 1.0 % in mass concentration), the effect of the nanoparticle concentrations were not explored thoroughly.

In recent reports [46, 47, 152], the enhancement in the viscosity of nanomaterial samples was attributed to the level of agglomeration of the nanoparticles. In this study the effect of agglomeration of nanoparticles on the rheological properties of the nanomaterials was examined where the mass concentration of the nanoparticles was fixed at 1%. The viscosity of the two nanomaterials was measured in this study as a function of shear rate at a temperature of 550 ℃. One sample was synthesized using surfactant (GA) for enhancing the uniformity of the dispersion of the nanoparticles with the intent of minimizing the level of agglomeration. The other sample was synthesized without using any surfactants and therefore the uniformity of the nanoparticle dispersion as well as the level of agglomeration was compromised in this sample. The results from the measurement for the two different nanomaterial samples are compared in Fig. 10.2. It was observed that the viscosity of the nanomaterial samples synthesized without using GA was ~18 % higher than that of the nanomaterial samples synthesized by using GA. GA was used to ensure better uniformity in dispersing the CNT in the aqueous solution of the eutectic salt mixture. GA was reported in the literature for its effectiveness in obtaining homogeneous dispersion of MWCNT in distilled water [37, 153]. Images

obtained from the electron microscopy of the nanomaterial samples confirmed that the synthesis protocol using GA resulted in more homogeneous dispersion (and less agglomeration) of CNT, as shown in Fig. 10.3. For Samples synthesized without using surfactants more agglomeration and less homogeneity in the dispersion of the nanoparticles was observed. Consequently, the rheological property values (shear thinning behavior) of these nanomaterials were elevated by ~18 % compared to that of the samples synthesized using surfactant.

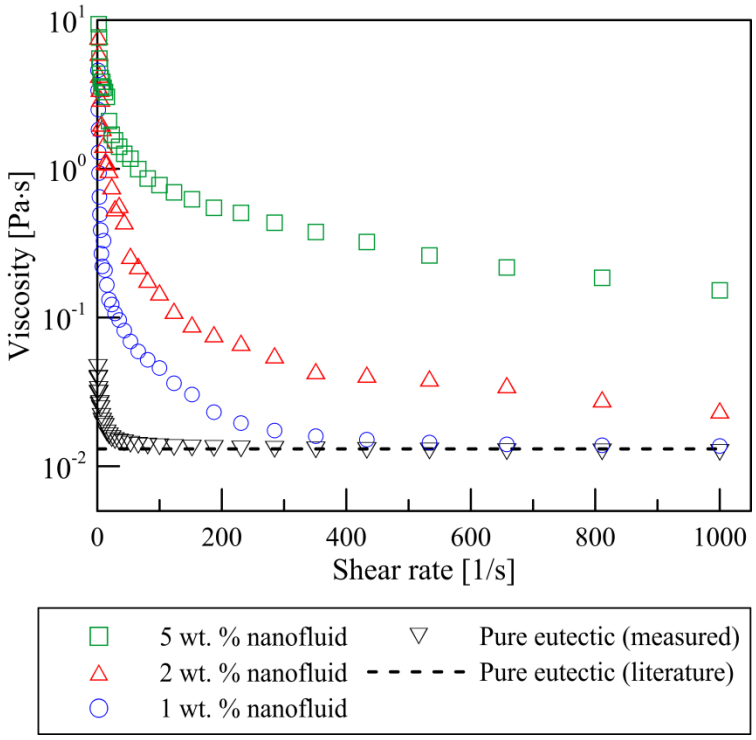

Fig. 10.1Viscosity of high temperature nanofluids as a function of shear rate for various nanotube concentrations at 550 ℃

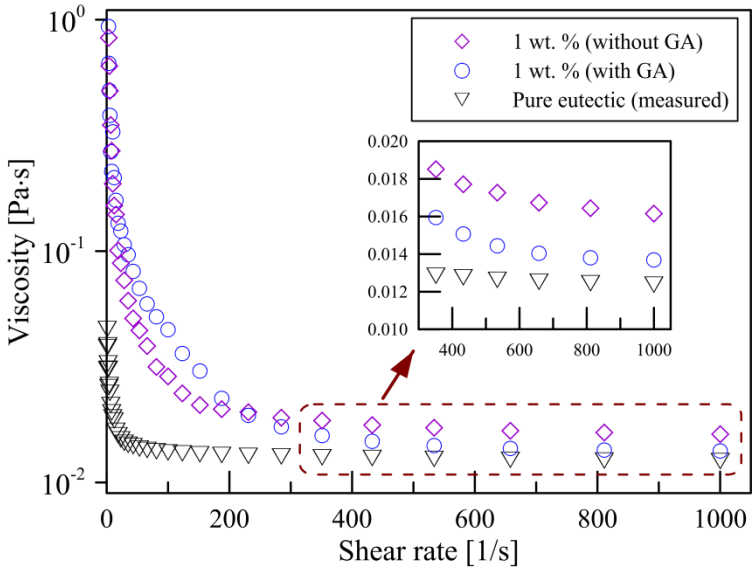

Fig. 10.2 Effect of nanoparticle dispersion on the viscosity of nanofluids

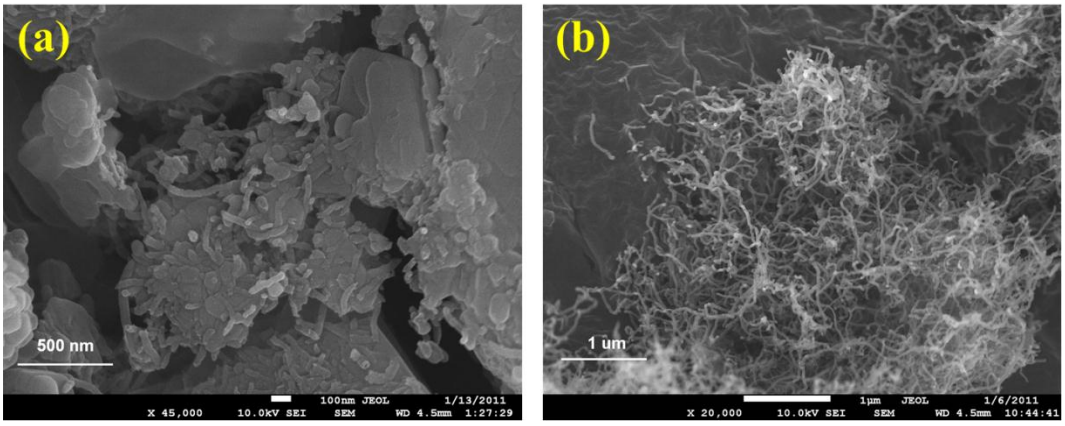

Fig. 10.3 Scanning electron microscopy (SEM) images of nanomaterials for a mass concentration of CNT of 1 %, synthesized: (a) using surfactant (GA at mass concentration of 1 %) and (b) without using surfactants

10.4.2 Predictions from theoretical model

Einstein [49] suggested a simple model (and is expressed in Eq. (10.1)) for estimating the viscosity of Newtonian fluids containing suspension of spherical particles at very low concentrations. In 1952, Brinkman proposed a modified model for higher concentration of the suspension of spherical particles [50]. This is a generalized form of the Einstein equation, and is shown in Eq. (10.2). However, the predictions from both of these analytical models did not agree with the experimental measurements performed in this study [154].

$$\eta_r = \frac{\eta_{nf}}{\eta_{bf}} = 1 + 2.5\phi \tag{10.1}$$

$$\eta_r = \frac{1}{(1-\phi)^{2.5}} \tag{10.2}$$

In both of these equations, η indicates the viscosity, ϕ is the volume concentration of the spherical particles, while subscripts, *r*, *nf*, and *bf*, refer to the relative ratio, nanofluid, and base fluid (solvent) property values, respectively. As mentioned before, the nanoparticle agglomeration can significantly enhance the viscosity of the nanofluids. Hence, a modified theoretical model that accounts for this effect is needed to explore the observed rheological behavior in the experimental measurements. The Krieger-

Dougherty model [51] (expressed in Eq. 10.3) was selected to analyze the experimental results for the viscosity measurements [46, 47].

$$\eta_r = \frac{\eta_{nf}}{\eta_{bf}} = \left(1 - \frac{\varphi_a}{\varphi_m}\right)^{-[\eta]\varphi_m} \tag{10.3}$$

In this model, typically, the maximum concentration (φ_m) at which the flow can occur is assumed to be 0.605, and the value for intrinsic viscosity ($[\eta]$), which is a measure of contribution by a solute, is assumed to be 2.5 for monodisperse systems [152]. The effective volume fraction of the aggregates (φ_a) is expressed as a function of the ratio of radii for the aggregates to that of the primary (or unagglomerated) nanoparticles (a_a/a), and is expressed using the following functional relationship [24, 155]:

$$\varphi_a = \phi \cdot \left(a_a/a\right)^{3-D} \tag{10.4}$$

In Eq. (10.4), *D* is the fractal index that is usually chosen to be 1.8 for a spherical nanoparticle [46, 47, 152]. However, a few studies have also reported the fractal index for the rod-shaped nanoparticles and these values have wide range of variability. In this study the value of the fractal index was chosen to be 1.8 based on a previous report in the literature [156]. Based on these values for the various parameters, Eq. (10.5) was expressed as follows:

$$\eta_r = \left(1 - \frac{\phi}{0.605}\left(\frac{a_a}{a}\right)^{1.2}\right)^{-1.5125} \tag{10.5}$$

The volume concentration of MWCNT was determined by using the following relationship $\phi = (w/\rho_n)\cdot\left[w/\rho_n + (1-w)/\rho_{bf}\right]$, where (W) is the mass concentration, and (ρ_n , ρ_{bf}) are the densities of the nanoparticles and base fluid (solvent), respectively.

Eq. (10.5) was plotted in Fig. 10.4 as a function of the mass concentration at certain values for the relative ratio of the radius of the aggregates (compared to that of the ratio of the unagglomerated nanoparticles). The experimental measurements performed in this study matched the predictions from the theoretical model for $a_a/a = 4.7$. In previous studies [46, 47], the values for this ratio ranged from 3.34-4 for ethylene glycol-based titania nanofluid and the value for this ratio was chosen to be 9.46 for titanate nanofluids in order to match the theoretical predictions from Eq. 10.5 with the experimental data. Considering the previous studies reported in the literature, the value of 4.7 for the relative ratio for radius is considered to be quite reasonable value for characterizing the rheological behavior of the nanomaterials used in this study. In the plots shown in the inset of Fig. 10.4, the predictions from the theoretical model were found to be in good agreement with the experimental data for nanomaterials synthesized using surfactant (GA at mass concentration of 1% and nanoparticle at mass concentration of 1%). For this nanomaterial sample, the value of the ratio (a_a/a) that provided the best match

between the numerical predictions and the experimental data was calculated to be 2.1. Hence, it can be concluded that using the surfactant in the synthesis process resulted in a better uniformity of dispersion of the MWCNT and therefore reduced the enhancements in the measured values of the viscosity.

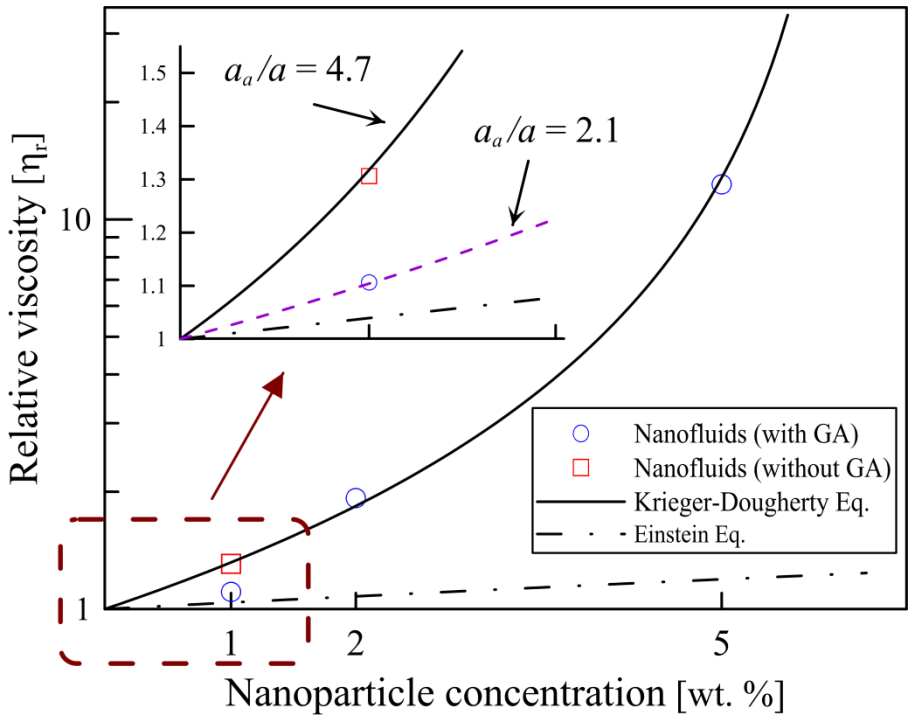

Fig. 10.4 Relative viscosity of the nanofluids at a shear rate of 1000 [1/s] compared with predictions from the theoretical model

10.5 Conclusion

The rheological behavior of the nanomaterials were measured and characterized for a wide range of shear rates using a rotational rheometer instrument and utilizing a cone-and-plate test section. The viscosity values were drastically elevated for the

nanomaterials. The knowledge gained from the experimental measurements and numerical modeling performed in this study is summarized as follows:

(a) Non-Newtonian behavior (shear thinning behavior) was observed in the nanomaterial samples. For lower values of shear rate, the viscosity values were enhanced by a huge margin (probably due to higher measurement uncertainties for the low values of the torque measured by the instrument). In contrast the measured values for viscosity were reduced drastically at higher shear rates.

(b) At the shear rate of 1000 [1/s], the viscosity was enhanced by ~11 % for nanomaterial samples containing carbon nanotube at mass concentration of 1%. The level of enhancement was dramatically elevated as the concentration of the nanoparticle was increased.

(c) The effect of the nanoparticle aggregation on the increase in the viscosity of the nanofluids was examined in this study. Higher viscosity values were observed for nanomaterials synthesized without surfactants.

(d) Using the Krieger-Dougherty model (which incorporates the effect of the nanoparticle agglomeration) the aggregation factor was calculated from the experimental data. The model showed that the aggregation factor was increased at higher concentration of the nanoparticles resulting in higher values for the viscosity values that were observed in the experimental measurements.

11. CONCLUSION

11.1 Summary

In order to reduce the unit cost for power generation, thermal energy storage (TES) systems are necessary for the operation of CSP plants. Molten salts are considered to provide attractive options as materials for thermal energy storage – especially at elevated temperature conditions. However, the relatively poor thermal properties are an impediment to their application for the CSP. Hence, nanomaterial samples using binary salt mixtures were synthesized in this study to address this issue. The material properties of these nanomaterial samples (and pure salt mixture samples) were characterized using a combination of experimental measurements and numerical investigations. Various types of organic nanoparticles were explored for the synthesis of the nanomaterials (such as CNT, graphite/graphene and fullerene).

Small variations in the synthesis protocols were found to cause significant variations in the material properties of the nanomaterials. Differential Scanning Calorimetry (DSC) was used to perform specific heat capacity measurements of the samples. The chemical composition of the solvent material was observed to significantly influence the level of enhancements in the property values of the nanomaterials. The level of enhancements was observed to be significantly higher in the liquid phase of the nanomaterials (compared to that of the solid phase). The variation in the chemical concentration of the solvent material was verified by performing ICP measurements.

The hypothesis developed in this study is that the chemical properties along with the thermo-physical properties of the solvent material (and the chemical composition of binary salt mixtures) dominate the level of enhancement in the specific heat capacity of the organic nanomaterials. From the wide range of parameters that were explored in this study, the effect of the solvent composition is found to play a significant and influential role in the observed enhancements in the values of the specific heat capacity of the nanomaterials, and therefore can play a more dominant role than the material properties of the nanomaterials *per se*. However, the nanoparticles can play an implicit role in modifying the properties of the compressed layer – since the ordering of the liquid molecules in the compressed layer can be influenced by the underlying lattice structure of the nanoparticle itself. It is a meaningful observation in course of exploration of the thermal properties of the nanomaterials (or nanofluids), because the previous studies in the literature invariably attributed the anomalous enhancements in the thermo-physical properties of nanomaterials to the material properties of the nanoparticles and assumed that the material properties of the solvent phase played a more passive role. From the results obtained from experimental and numerical investigations employed in this study, however, it can be concluded that the material properties of the solvent materials play a more significant role in determining the level of specific heat capacity enhancement of the nanomaterials. Consistent with the results reported in the literature, it was observed that the uniformity (and homogeneity) of the dispersion of the nanoparticles favorably influenced the level of specific heat capacity enhancement as well as the rheological properties of the nanomaterials.

Molecular dynamics (MD) simulations were performed to estimate the interfacial resistance (also known as Kapitza resistance) between the nanoparticle and the solvent molecules. The various parameters that were observed to affect the numerical results are nanoparticle shape, size, and material properties of the solvent (thermo-physical properties as well as chemical properties such as inter-molecular adhesive forces, and molecular structure). The MD simulations showed that the morphology and the chemical composition of the compressed layer that forms on the surface of the nanoparticles can significantly affect the material properties of the resulting nanomaterials. The morphology and chemical composition of the compressed liquid layer was found to be highly sensitive to the chemical composition of the solvent material. Hence it was concluded that the observed enhancements in the specific heat capacity values was a direct outcome of the total surface area of the nanoparticles which in turn is affected by the dispersion uniformity and stability (or level of agglomeration) of the nanoparticles.

Rheological behavior of the nanomaterials was characterized experimentally as a function of the concentration of the nanoparticles and dispersion uniformity or agglomeration of the nanoparticles (i.e., with or without using surfactants in the synthesis protocols). Shear thinning behavior (non-Newtonian) behavior was observed. The viscosity was enhanced at higher concentration of nanoparticles. Using numerical models from the literature it was concluded that higher viscosity values observed in the experimental measurements arise from higher level of agglomeration of the nanoparticles (which can occur at higher nanoparticle concentrations or for synthesis protocols that avoid the use of surfactants).

Materials characterization using electron microscopy was also performed to complement the experimental measurements and to confirm the uniformity of dispersion and level of agglomeration of the nanoparticles in the various nanomaterial samples used in this study. Agglomeration and uniformity of nanoparticle dispersion in the nanomaterial samples were observed to significantly affect the resulting material properties.

11.2 Future directions

11.2.1 C_{60} fullerene nanomaterials

Among the various organic nanoparticles presented in this study (such as CNT and graphite), the measurement of the specific heat capacity of the nanomaterials using C_{60} (Fullerene) was omitted in this study due to malfunctioning of the experimental apparatus. As reported in Appendix C, the C_{60} nanoparticles were dispersed in aqueous solution by a mechanical mixing (stirring) method, despite the extremely low solubility in water. Hence, this demonstrates the feasibility for synthesizing molten salt nanomaterials using methods similar to those employed in this study. Although the concentration of C_{60} nanoparticles in this aqueous solution is unknown, the specific heat capacity of the C_{60} nanoparticles can be measured, and also the effect of the C_{60} fullerene on that thermal property of the molten salt nanomaterials can be investigated by using the dispersion techniques explained in Appendix C.

11.2.2 Functionalization of nanoparticles

A theoretical investigation for the specific heat capacity of nanomaterials [80] showed that the enhancement of the specific heat capacity was strongly dependent upon the properties and morphology of the compressed liquid layer. Since the total volume of the compressed layer is amplified significantly with concomitant decrease in the nanoparticle size (for the same mass concentration of the nanoparticles), progressive reduction in the size of nanoparticles leads to amplification in the specific heat capacity of the nanomaterials. Fig. 11.1 shows the theoretical prediction of the specific heat capacity for four different nanomaterials based on this model [80]. As shown in Fig. 11.1 (C), for instance, the critical diameter of the carbon nanotubes is 20 nm, since for CNT diameter less than 20 nm the specific heat capacity is enhanced dramatically with increase in mass concentration or decrease in CNT diameter.

In this study, the specific heat capacity enhancement was explored for carbonate salt mixtures. However, thermal conductivity is also an important thermal property for determining the efficacy of the nanomaterials for TES applications. In previous studies in the literature [30], the critical diameter of nanoparticles for enhancing thermal conductivity was expressed by the following equation:

$$D_{np} = 2R_{np}k_f \tag{11.1}$$

In the Eq. (11.1), D is the diameter of nanoparticles, R is the interfacial thermal resistance (or "Kapitza resistance") between the solvent and nanoparticle, and k is the

thermal conductivity of the solvent fluid. Subscripts - *np* and *f* - indicate the property values for the nanoparticle and the solvent (fluid), respectively. Substituting the thermal conductivity of the carbonate salt eutectic (0.75 W/m·k) and the interfacial thermal resistance values of the organic nanoparticles obtained in Section 3 (~ 10^{-8} m^2K/W), the critical diameter can be determined as shown in Table 11.1. For the carbon nanotubes, the mean value of the critical diameter was estimated to be ~113 nm (for enhancing the thermal conductivity of the nanofluid), which is much larger than the critical size for enhancing the specific heat capacity of the nanofluids (~ 20 nm or less).

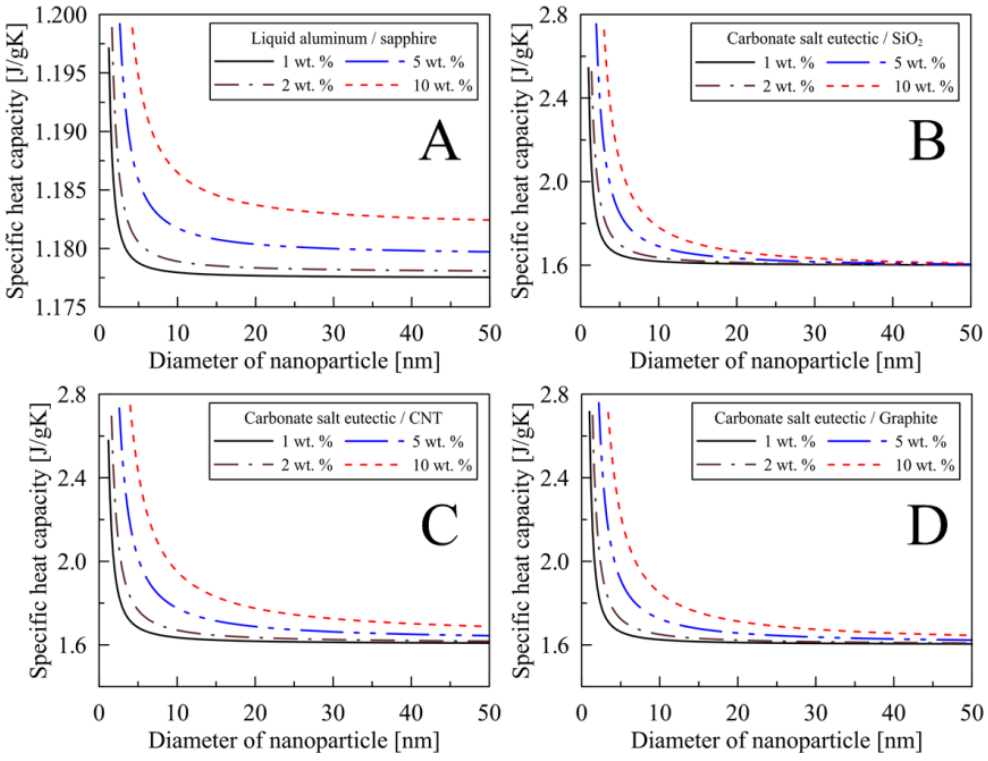

Fig. 11.1 Prediction of specific heat capacity for several nanofluids: (A) Sapphire-liquid aluminum, (B) Silica-carbonate salt eutectic, (C) CNT-carbonate salt eutectic, and (D) graphite-carbonate salt eutectic

In order to optimize the critical diameter of nanoparticles for simultaneously maximizing thermal conductivity and specific heat capacity, functionalization (or chemical modification) of the nanoparticles was explored theoretically in this study. In previous literature [157], it was reported that the functionalization of nanoparticles decreased the interfacial thermal resistance of the nanoparticles and also increased the rate of heat transfer. As shown in Fig. 11.2, two functional groups (carboxylic group and amine group) were employed for functionalizing single-walled carbon nanotubes (SWNTs). MD simulations were performed, using the same procedure described in Section 3.

Table 11.1 Interfacial thermal resistances and critical diameter for enhancing thermal conductivity of nanofluids

Nanoparticle	Diameter [A]	Interfacial thermal resistance x 10^8 [m^2K/W]	Critical diameter [nm]
Carbon nanotubes	2.7	7.72	116
	5.4	7.41	111
	6.7	7.50	113
	8.1	7.36	110
	10.9	7.58	114
	13.6	7.41	111
Graphite sheet	7.2	8.34	125
	9.2	8.85	133
	11.8	8.23	123
	12.8	8.29	124
	16.4	8.02	120
	18.4	7.88	118
C_{60} fullerene	7.1	6.94	104

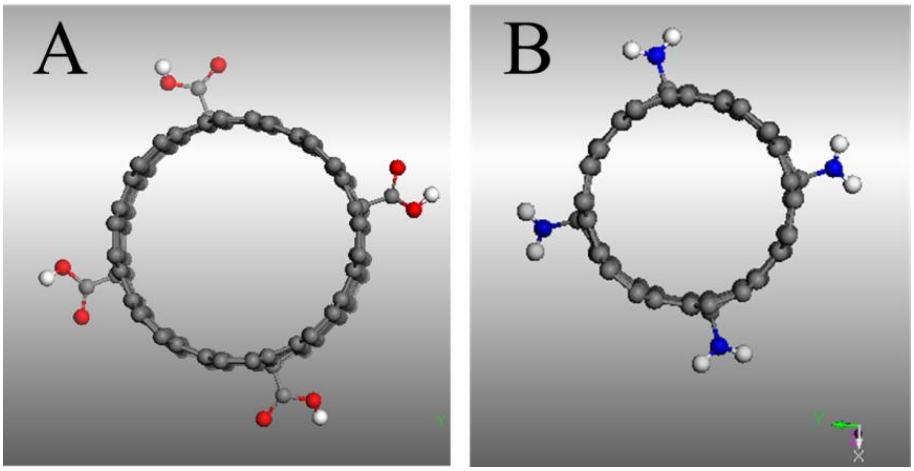

Fig. 11.2 Configuration of functionalized single-walled carbon nanotubes: (A) carboxyl group and (B) amine group

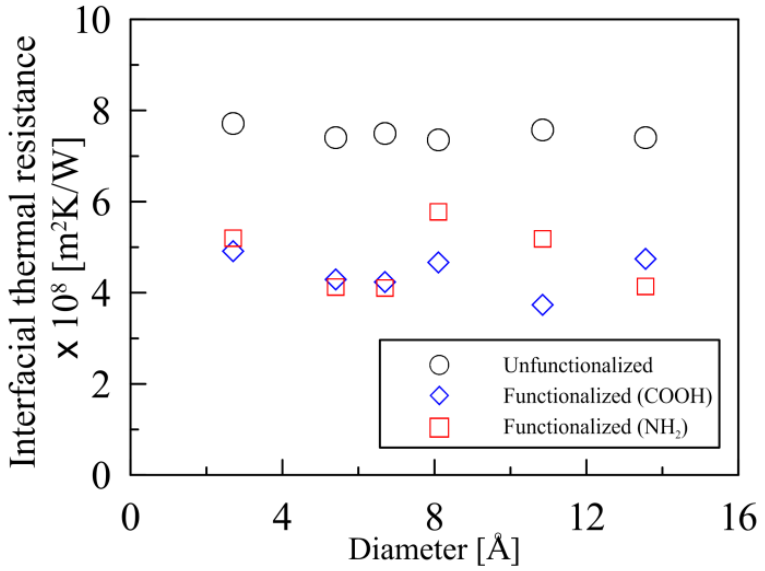

Fig. 11.3 Interfacial thermal resistances for the pristine SWNT and the functionalized SWNT

Table 11.2 Interfacial thermal resistance and critical diameter of functionalized SWNTs

Functional group	Diameter [A]	Interfacial thermal resistance x 10^8 [m^2K/W]	Critical diameter [nm]
Carboxyl (COOH)	2.7	4.92	74
	5.4	4.30	65
	6.7	4.24	64
	8.1	4.67	70
	10.9	3.74	56
	13.6	4.75	71
Amine (NH_2)	2.7	5.20	78
	5.4	4.13	62
	6.7	4.11	62
	8.1	5.78	87
	10.9	5.19	78
	13.6	4.14	62

Fig. 11.3 shows the interfacial thermal resistances of the functionalized SWNT. As shown in this figure, the interfacial thermal resistances were significantly decreased by chemically modifying SWNTs. Table 11.2 presents the interfacial thermal resistance values and the critical diameters. The critical diameter for the thermal conductivity was decreased up to 41 % after chemical functionalization of SWNTs. Hence, the chemical functionalization of nanoparticles can help to decrease the critical size of the nanoparticles for maximizing the thermal conductivity, such that for the same size of the nanoparticles the specific heat capacity is also maximized. Hence, these results show a preliminary roadmap for optimizing nanoparticle size, shape and concentration – in order to maximize both thermal conductivity and specific heat capacity of the mixture (nanofluids).

11.3 Conclusion

In this study the enhancement in the specific heat capacity of a binary molten salt mixture was achieved by doping with organic nanoparticles. Unique features were identified, such as: (1) the solvent properties (chemical and thermo-physical) play more dominant role in enhancing the specific heat capacity of nanomaterials, (2) the chemical composition and the physical properties of the liquid layer on the surface of the nanoparticle can be significantly different from that of the pure solvent (i.e., in the absence of the nanoparticle), and (3) concentration gradient induced on the surface of the nanoparticle can be different in size than the size of the compressed layer (which was estimated computationally in this study). This suggests that such interactions between the compressed phase and the chemical concentration "boundary layer" can enable alternate mechanisms for energy storage on the nano-scale and potentially aid in enhancing the specific heat capacity of the molten salt nanomaterials. Nevertheless, additional investigations are required to enhance the comprehension of these complex interactions and ultimately lead to development of more robust theoretical framework for exploring the properties of nanomaterials. Molecular dynamics simulation can be used to enable better comprehension of the interactions between nanoparticles and the solvent molecules.

There are several implications that can be explored based on the results obtained from this study which require further investigation for better comprehension of the underlying mechanisms responsible for the specific heat capacity enhancement of the nanomaterials. As discussed in Section 8, the concentration gradient induced by the

solvent molecules (or species) on surface of the nanoparticle and in the vicinity of the compressed layer of the solvent can mutually interact to play a decisive role in enhancing the thermal energy storage in these nanoparticle mixtures. Preferential attraction of the potassium ions and lithium ions by the nanoparticle surface atoms as well as different values of diffusivity (mass or chemical) for these ions in the solvent can lead to thermophoretic transport phenomena in the vicinity of nanoparticles. The localized concentration imbalance of the solvent molecules (or ions) in the vicinity of nanoparticles can also induce additional transport mechanism (or energy storage mechanisms) within the nanofluid. Therefore, the study of the diffusivity of the solvent molecules would probably be meaningful in order to fully comprehend the implications of the experimental results presented in this study.

As suggested above, the functionalization of the nanoparticles can provide an attractive strategy for optimizing the thermal properties of nanomaterials. The results showing the effect of the surfactants in the enhancing the properties of the nanomaterials can be considered to be another manifestation of this same effect. Surfactant molecules have a unique chemical structure – composed of a hydrophobic “tail” and hydrophilic “head”. For CNT nanofluids, for example, the hydrophobic tail of surfactant molecules attaches to the carbon nanotubes and the hydrophilic head interacts with the solvent molecules. In other words, these surfactant molecules can play a similar role to the chemical functional groups that was explored in this study for the CNT nanofluids. Additionally, the effect of the surfactant concentration should be studied, because high concentration of surfactants can lead to the formation of large micelles in the nanofluids.

Since increase in the effective size of the nanoparticles (e.g., Stokes Diameter) reduces the volume of compressed layer, chemical functionalization (or treatment using surfactants) could be unfavorable to enhancing the specific heat capacity of the nanomaterials. Finally, the spontaneous formation of nanoparticles from organic surfactants (that was observed in this study) also needs further investigation.

Comparing the measured enhancements for the specific heat capacity of the nanomaterials (from this study) with the cost analysis reported in the literature – it is estimated that the commercial implementation of these enhancement techniques has the potential to reduce the cost of power generated in CSP plants by 20-50%. The cost analyses used to infer such operational improvements is based on parametric analyses for the variation in the cost of power generation as a function of the enhancement in the specific heat capacity of TES materials that can occur at the expense of relative rise in the total cost (fixed and operation costs) due to additional cost burden associated with incorporating the nanomaterials in the CSP plant [158]. However, the incorporation of the nanomaterials can lead to even more dramatic cost reduction for power generation in CSP plants if the associated size reductions (and material cost reductions) for various devices are considered such as: the heat exchangers, storage tanks, piping networks, etc. Higher pressure penalty can be expected due to the higher viscosity values of the nanomaterials (thus resulting in higher pumping power requirements). However this effect is expected to be of marginal significance for operation of the TES devices in CSP plants, such as for power tower configurations, since the nanomaterials are typically pumped between the storage tanks only twice a day (between the hot storage tank and

cold storage tank, for a two-tank TES system). The effect of pressure penalty on the overall plant efficiency is expected to be more significant for continuous operation of the pumps (if the nanomaterials are used as HTF, such as in parabolic trough systems). Incorporation of nanomaterials for TES in dish (Stirling) systems has the best potential for performance improvements and reduction in the unit cost for power generation – since these systems are more compact and therefore the effect of pump penalty is minimal while the material property enhancements (e.g., demonstrated for thermal conductivity and specific heat capacity) can substantially improve the operational performance of the compact heat exchangers (e.g., liquid-to-gas heat exchangers) and enhance the cycle time for utilizing the TES units while imposing marginal increase in the fixed cost. Hence the results presented in this study can have deep and far reaching impacts on the technical and economic feasibility for energy harvesting technologies involving TES (e.g., in CSP pants, geothermal, nuclear and hybrid platforms such as high temperature fuel cell/ hydrogen generation technologies).

REFERENCES

[1] Richter, C., Teske, S., and Short, S., 2009, "Global Concentrating Solar Power Outlook 09" Greenpeace International Solar Paces and ESTELA, Amsterdam, The Netherlands.

[2] Leitner, A., 2002, "Fuel from the Sky: Solar Power's Potential for Western Energy Supply," NREL/SR-550-32160, NREL, Golden, Colorado.

[3] Tanaka, N., 2010, "Technology Roadmap: Concentrating Solar Power," International Energy Agency, Paris, France.

[4] Pacheco, J. E., Showalter, S. K., and Kolb, W. J., 2002, "Development of a Molten-Salt Thermocline Thermal Storage System for Parabolic Trough Plants," J. Sol. Energy Eng., **124**(2), pp. 153-159.

[5] Kearney, D., Herrmann, U., Nava, P., 2003, "Assessment of a Molten Salt Heat Transfer Fluid in a Parabolic Trough Solar Field," J. Sol. Energy Eng., **125**(2), pp. 170-176.

[6] Ozerinc, S., Kakac, S., and YazIcIoglu, A. G., 2010, "Enhanced Thermal Conductivity of Nanofluids: A State-of-the-Art Review," Microfluid. Nanofluid., **8**(2), pp. 145-170.

[7] Hong, T. K., Yang, H. S., and Choi, C. J., 2005, "Study of the Enhanced Thermal Conductivity of Fe Nanofluids," J. Appl. Phys., **97**(6), pp. 064311.

[8] Hwang, Y. J., Ahn, Y. C., Shin, H. S., 2006, "Investigation on Characteristics of Thermal Conductivity Enhancement of Nanofluids," Curr. App. Phys., **6**(6), pp. 1068-1071.

[9] Zhu, H. T., Zhang, C. Y., Tang, Y. M., 2007, "Novel Synthesis and Thermal Conductivity of CuO Nanofluid," J. Phys. Chem. C, **111**(4), pp. 1646-1650.

[10] Beck, M. P., Yuan, Y., Warrier, P., 2009, "The Effect of Particle Size on the Thermal Conductivity of Alumina Nanofluids," J. Nanopart. Res., **11**(5), pp. 1129-1136.

[11] Wang, X., Xu, X., and Choi, S. U. S., 1999, "Thermal Conductivity of Nanoparticle-Fluid Mixture," J. of Thermophysics Heat Transfer, **13**(4), pp. 474-480.

[12] Czarnetzki, W. and Roetzel, W., 1995, "Temperature Oscillation Techniques for Simultaneous Measurement of Thermal Diffusivity and Conductivity," Int. J. Thermophys., **16**(2), pp. 413-422.

[13] Ju, Y. S., Kim, J., and Ming-Tsung Hung, 2008, "Experimental Study of Heat Conduction in Aqueous Suspensions of Aluminum Oxide Nanoparticles," J. Heat Transfer, **130**(9), pp. 092403.

[14] Putnam, S. A., Cahill, D. G., Braun, P. V., 2006, "Thermal Conductivity of Nanoparticle Suspensions," J. Appl. Phys., **99**(8), pp. 084308.

[15] Masuda, H., Ebata, A., Teramae, K., 1993, "Alteration of Thermal Conductivity and Viscosity of Liquid by Dispersing Ultra-Fine Particles (Dispersion of γ-Al_2O_3, SiO_2, and TiO_2 Ultra-Fine Particles)," Netsu Bussei, **4**(4), pp. 227-233.

[16] Lee, S., Choi, S.U.S., and Li, S., 1999, "Measuring Thermal Conductivity of Fluids Containing Oxide Nanoparticles," J. Heat Transfer, **121**(2), pp. 280-289.

[17] Murshed, S. M. S., Leong, K. C., and Yang, C., 2005, "Enhanced Thermal Conductivity of TiO_2-Water Based Nanofluids," Int. J. Therm. Sci., **44**(4), pp. 367-373.

[18] Choi, S. U. S., Zhang, Z. G., Yu, W., 2001, "Anomalous Thermal Conductivity Enhancement in Nanotube Suspensions," Appl. Phys. Lett., **79**(14), pp. 2252-2254.

[19] Chopkar, M., Sudarshan, S., Das, P. K., 2008, "Effect of Particle Size on Thermal Conductivity of Nanofluid," Metall. Mater. Trans. A, **39**(7), pp. 1535-1542.

[20] Wang, X., and Mujumdar, A. S., 2007, "Heat Transfer Characteristics of Nanofluids: A Review," Int. J. Therm. Sci., **46**(1), pp. 1-19.

[21] Keblinski, P., Eastman, J. A., and Cahill, D. G., 2005, "Nanofluids for Thermal Transport," Mater. Today, **8**(6), pp. 36-44.

[22] Das, S. K., Choi, S. U. S., and Patel, H. E., 2006, "Heat Transfer in Nanofluids - A Review," Heat Transfer Eng., **27**(10), pp. 3-19.

[23] Yu, W., and Choi, S. U. S., 2004, "The Role of Interfacial Layers in the Enhanced Thermal Conductivity of Nanofluids: A Renovated Hamilton-Crosser Model," J. Nanopart. Res., **6**(4), pp. 355-361.

[24] Wang, B., Zhou, L., and Peng, X., 2003, "A Fractal Model for Predicting the Effective Thermal Conductivity of Liquid with Suspension of Nanoparticles," Int. J. Heat and Mass Transfer, **46**(14), pp. 2665-2672.

[25] Xue, Q., and Wen-Mei Xu, 2005, "A Model of Thermal Conductivity of Nanofluids with Interfacial Shells," Mater. Chem. Phys., **90**, pp. 298-301.

[26] Xie, H., Fujii, M., and Zhang, X., 2005, "Effect of Interfacial Nanolayer on the Effective Thermal Conductivity of Nanoparticle-Fluid Mixture," Int. J. Heat Mass Transfer, **48**(14), pp. 2926-2932.

[27] Xuan, Y., Li, Q., and Hu, W., 2003, "Aggregation Structure and Thermal Conductivity of Nanofluids," AIChE J., **49**(4), pp. 1038-1043.

[28] Bhattacharya, P., Saha, S. K., Yadav, A., 2004, "Brownian Dynamics Simulation to Determine the Effective Thermal Conductivity of Nanofluids," J. Appl. Phys., **95**(11), pp. 6492-6494.

[29] Jang, S. P., and Choi, S. U. S., 2004, "Role of Brownian Motion in the Enhanced Thermal Conductivity of Nanofluids," Appl. Phys. Lett., **84**(21), pp. 4316-4318.

[30] Prasher, R., Bhattacharya, P., and Phelan, P. E., 2005, "Thermal Conductivity of Nanoscale Colloidal Solutions (Nanofluids)," Phys. Rev. Lett., **94**(2), pp. 025901.

[31] Eastman, J. A., Choi, S. U. S., Li, S., 2001, "Anomalously Increased Effective Thermal Conductivities of Ethylene Glycol-Based Nanofluids Containing Copper Nanoparticles," Appl. Phys. Lett., **78**(6), pp. 718-720.

[32] Xie, H., Wang, J., Xi, T., 2002, "Thermal Conductivity of Suspensions Containing Nanosized SiC Particles," Int. J. Thermophys., **23**(2), pp. 571-580.

[33] Xie, H., Wang, J., Xi, T., 2002, "Dependence of the Thermal Conductivity of Nanoparticle-Fluid Mixture on the Base Fluid," J. Mater. Sci. Lett., **21**(19), pp. 1469-1471.

[34] Das, S. K., Putra, N., Thiesen, P., 2003, "Temperature Dependence of Thermal Conductivity Enhancement for Nanofluids," J. Heat Transfer, **125**(4), pp. 567-574.

[35] Assael, M. J., Metaxa, I. N., Arvanitidis, J., 2005, "Thermal Conductivity Enhancement in Aqueous Suspensions of Carbon Multi-Walled and Double-Walled Nanotubes in the Presence of Two Different Dispersants," Int. J. Thermophys., **26**(3), pp. 647-664.

[36] Liu, M., Ching-Cheng Lin, M., Huang, I., 2005, "Enhancement of Thermal Conductivity with Carbon Nanotube for Nanofluids," Int. Commun. Heat and Mass Transfer, **32**(9), pp. 1202-1210.

[37] Ding, Y., Alias, H., Wen, D., 2006, "Heat Transfer of Aqueous Suspensions of Carbon Nanotubes (CNT Nanofluids)," Int. J. Heat Mass Transfer, **49**, pp. 240-250.

[38] Hong, K. S., Tae-Keun Hong, and Ho-Soon Yang, 2006, "Thermal Conductivity of Fe Nanofluids Depending on the Cluster Size of Nanoparticles," Appl. Phys. Lett., **88**(3), pp. 031901.

[39] Turgut, A., Tavman, I., Chirtoc, M., 2009, "Thermal Conductivity and Viscosity Measurements of Water-Based TiO 2 Nanofluids," Int. J. Thermophys., **30**(4), pp. 1213-1226.

[40] Mintsa, H. A., Roy, G., Cong, T. N., 2009, "New Temperature Dependent Thermal Conductivity Data for Water-Based Nanofluids," Int. J. Therm. Sci., **48**(2), pp. 363-371.

[41] Das, S. K., Putra, N., and Roetzel, W., 2003, "Pool Boiling Characteristics of Nano-Fluids," Int. J. Heat Mass Transfer, **46**(5), pp. 851-862.

[42] Xuan, Y., and Li, Q., 2003, "Investigation on Convective Heat Transfer and Flow Features of Nanofluids," J. Heat Transfer, **125**(1), pp. 151-155.

[43] Prasher, R., Song, D., Wang, J., 2006, "Measurements of Nanofluid Viscosity and its Implications for Thermal Applications," Appl. Phys. Lett., **89**(13), pp. 133108.

[44] He, Y., Jin, Y., Chen, H., Ding, Y., Cang, D., and Lu, H., 2007, "Heat Transfer and Flow Behaviour of Aqueous Suspensions of TiO_2 Nanoparticles (Nanofluids) Flowing Upward through a Vertical Pipe," Int. J. Heat Mass Transfer, **50**, pp. 2272-2281.

[45] Kwak, K., and Kim, C., 2005, "Viscosity and Thermal Conductivity of Copper Oxide Nanofluid Dispersed in Ethylene Glycol," Korea-Aust. Rheol. J., **17**(2), pp. 35-40.

[46] Chen, H., Ding, Y., and Tan, C., 2007, "Rheological Behaviour of Nanofluids," New J. Phys., **9,** pp. 367-382.

[47] Chen, H., Ding, Y., Lapkin, A., 2009, "Rheological Behaviour of Ethylene Glycol-Titanate Nanotube Nanofluids," J. Nanopart. Res., **11**(6), pp. 1513-1520.

[48] Chen, H., and Ding, Y., 2009, "Heat Transfer and Rheological Behaviour of Nanofluids - A Review," Adv. Transp. Phenomena, **1**, pp. 135-177.

[49] Einstein, A., 1906, "A New Determination of Molecular Dimensions; Eine Neue Bestimmung Der Molekul-Dimensionen," Ann. Phys., **19**(2), pp. 289-306.

[50] Brinkman, H. C., 1952, "The Viscosity of Concentrated Suspensions and Solutions," J. Chem. Phys., **20**(4), pp. 571-581.

[51] Krieger, I. M., and Dougherty, T. J., 1959, "A Mechanism for Non-Newtonian Flow in Suspensions of Rigid Spheres," Trans. Soc. Rheol., **3**(1), pp. 137-152.

[52] Namburu, P. K., Kulkarni, D. P., Dandekar, A., 2007, "Experimental Investigation of Viscosity and Specific Heat of Silicon Dioxide Nanofluids," Micro Nano Lett., **2**(3), pp. 67-71.

[53] Zhou, S., and Ni, R., 2008, "Measurement of the Specific Heat Capacity of Water-Based Al_2O_3 Nanofluid," Appl. Phys. Lett., **92**(9), pp. 093123.

[54] Vajjha, R. S., and Das, D. K., 2009, "Specific Heat Measurement of Three Nanofluids and Development of New Correlations," J. Heat Transfer, **131**(7), pp. 071601.

[55] Zhou, L., Wang, B., Peng, X., 2010, "On the Specific Heat Capacity of CuO Nanofluid," Adv. Mech. Eng., **2010**, pp. 172085.

[56] Nelson, I. C., Banerjee, D., and Ponnappan, R., 2009, "Flow Loop Experiments using Polyalphaolefin Nanofluids," J. Thermophys. Heat Transfer, **23**(4), pp. 752-761.

[57] Shin, D., and Banerjee, D., 2010, "Effects of Silica Nanoparticles on Enhancing the Specific Heat Capacity of Carbonate Salt Eutectic (Work in Progress)," Int. J. Struc. Chang. Solids, **2**(2), pp. 25-31.

[58] Shin, D., and Banerjee, D., 2011, "Enhanced Specific Heat of Silica Nanofluid," J. Heat Transfer, **133**(2), pp. 024501.

[59] Shin, D. and Banerjee, D., 2011, "Enhancement of Specific Heat Capacity of High-Temperature Silica-Nanofluids Synthesized in Alkali Chloride Salt Eutectics for Solar Thermal-Energy Storage Applications," Int. J. Heat Mass Transfer, **54**, pp. 1064-1070.

[60] Jo, B. and Banerjee, D., 2010, "Study of high temperature nanofluids using carbon nanotubes (CNT) for solar thermal storage applications," ES 2010-90299, *ASME 2010 4th International Conference on Energy Sustainability*, May 17-22, Phoenix, AZ, USA.

[61] Bridges, N. J., Visser, A. E., and Fox, E. B., 2011, "Potential of Nanoparticle-Enhanced Ionic Liquids (NEILs) as Advanced Heat-Transfer Fluids," Energy Fuels, **25**(10), pp. 4862-4864.

[62] Ahn, H. S., Sinha, N., Zhang, M., 2006, "Pool Boiling Experiments on Multiwalled Carbon Nanotube (MWCNT) Forests," J. Heat Transfer, **128**(12), pp. 1335-1342.

[63] Ahn, H. S., Sathyamurthi, V., and Banerjee, D., 2009, "Pool Boiling Experiments on a Nano-Structured Surface," IEEE Trans. Compon. Packag. Technol., **32**(1), pp. 156-165.

[64] Sathyamurthi, V., Ahn, H. S., Banerjee, D., 2009, "Subcooled Pool Boiling Experiments on Horizontal Heaters Coated with Carbon Nanotubes," J. Heat Transfer, **131**(7), pp. 071501.

[65] Singh, N., Sathyamurthy, V., Peterson, W., 2010, "Flow Boiling Enhancement on a Horizontal Heater using Carbon Nanotube Coatings," Int. J. Heat Fluid Flow, **31**(2), pp. 201-207.

[66] Jeon, S., Jo, B., and Banerjee, D., 2011, "Enhancement of Saturation Boiling of PF-5060 on Microporous Surface," AJTEC2011-44408, *ASME/JSME 8th Thermal Engineering Joint Conference*, March 13-17, Honolulu, Hawaii, USA.

[67] Sriraman, S. R., 2007, "Pool Boiling on Nano-Finned Surfaces," M.S. Thesis, Texas A&M University.

[68] Singh, N., 2010, "Computational Analysis of Thermo-Fluidic Characteristics of a Carbon Nano-Fin," Ph. D. Thesis, Texas A&M University.

[69] Unnikrishnan, V. U., Banerjee, D., and Reddy, J. N., 2008, "Atomistic-Mesoscale Interfacial Resistance Based Thermal Analysis of Carbon Nanotube Systems," International Journal of Thermal Sciences, **47**(12), pp. 1602-1609.

[70] Singh, N., Unnikrishnan, V. U., and Banerjee, D., 2011, "Analysis of Thermal Interfacial Resistance between Nanofins and various Coolants," Int. J. Comput. Methods Eng. Sci. Mech., **12**(5), pp. 254-260.

[71] Shin, D. and Banerjee, D., 2009, "Investigation of Nanofluids for Solar Thermal Storage Applications," ES2009-90465, *ASME Energy Sustainability Conference*, July 20- 25, San Francisco, CA, USA.

[72] Shin, D. and Banerjee, D., 2010, "Enhanced Thermal Properties of PCM Based Nanofluid for Solar Thermal Energy Storage," ES2010-90293, *4th International Conference on Energy Sustainability*, May 17-22, Phoenix, AZ, USA.

[73] Shin, D. and Banerjee, D., 2010, "Enhanced Specific Heat Capacity of Molten Salt-metal Oxide Nanofluid as Heat Transfer Fluid for Solar Thermal Applications," SAE-10PSC-0136, *SAE Power Systems Conference*, November 2-4, Fort Worth, Texas, USA.

[74] Shin, D., and Banerjee, D., 2011, "Experimental Investigation of molten salt nanofluid for solar thermal energy application," AJTEC2011-44375, *ASME/JSME 8th Thermal Engineering Joint Conference*, March 13-17, Honolulu, Hawaii, USA.

[75] Kwak, H., Shin, D., and Banerjee, D., 2010, "Enhanced Sensible Heat Capacity of Molten Salt Based Nanofluid For Solar Thermal Energy Storage Application," ES2010-90295, *ASME 4th International Conference on Energy Sustainability*, May 17-22, Phoenix, AZ, USA.

[76] Shin, D., Jo, B., Kwak, H., 2010, "Investigation of high temperature nanofluids for solar thermal power conversion and storage applications," IHTC14-23296, *14th International Heat Transfer Conference*, August 8-13, Washington D.C., USA.

[77] Jung, S. and Banerjee, D., 2011, "Enhancement of Heat Capacity of Nitrate Salts using Mica Nanoparticles," Developments in Strategic Materials and Computational Design II: Ceramic Engineering and Science Proceedings, **32**, pp. 127-137.

[78] Jo, B., and Banerjee, D., 2011, "Enhanced Specific Heat Capacity of Nanocomposites using Organic Nanoparticles," IMECE2011-64001, *ASME 2011 International Mechanical Engineering Congress and Exposition*, November 11-17, Hyatt Regency Denver & Colorado Convention Center, USA.

[79] Shin, D., 2011, "Molten Salt Nanomaterials for Thermal Energy Storage and Concentrated Solar Power Applications," Ph. D. Thesis, Texas A&M University.

[80] Jung, S., 2012, "Numerical and Experimental Investigation of Inorganic Nanomaterials for Thermal Energy Storage (TES) and Concentrated Solar Power (CSP) Applications," Ph. D. Thesis, Texas A&M University.

[81] Jo, B. and Banerjee, D., 2011, "Enhanced Viscosity of Aqueous Silica Nanofluids," Developments in Strategic Materials and Computational Design II: Ceramic Engineering and Science Proceedings, **32**, pp. 139-146.

[82] Jo, B., Jung, S., Shin, D., 2011, "Anomalous Rheological Behavior of Complex Fluids (Nanofluids)," IMECE2011-64091, *ASME 2011 International Mechanical Engineering Congress and Exposition*, November 11-17, Hyatt Regency Denver & Colorado Convention Center, USA.

[83] Jung, S., Jo, B., Shin, D., 2010, "Experimental Validation of a Simple Analytical Model for Specific Heat Capacity of Aqueous Nanofluids," SAE-10PSC-0134, *SAE Power Systems Conference*, November 2-4, Fort Worth, Texas, USA.

[84] Jung, S. and Banerjee, D., 2011, "A Simple Analytical Model for Specific Heat of Nanofluid with Tube Shaped and Disc Shaped Nanoparticles," AJTEC2011-44372,

ASME/JSME 8thThermal Engineering Joint Conference, March 13-17, Honolulu, Hawaii, USA.

[85] Yu, J., Kang, S., Jeon, S. and Banerjee, D., 2012, "Heat Transfer Measurements for Flow of Nanofluids in microchannels using Temperature Nano-Sensors," Front. Heat Mass Transfer (Special Issue on Microchannels), **3**, pp. 013004.

[86] Ahn, H. S., Lee, S. W., Lau, S. C., 2007, "Mass (Heat) Transfer Downstream of Blockages with Round and Elongated Holes in a Rectangular Channel," J. Heat Transfer, **129**(12), pp. 1676-1685.

[87] Sunder, M., and Banerjee, D., 2009, "Experimental Investigation of Micro-Scale Temperature Transients in Sub-Cooled Flow Boiling on a Horizontal Heater," Int. J. Heat Fluid Flow, **30**(1), pp. 140-149.

[88] Sinha, N., Ahn, H. S., Williams, R., 2009, "Packaging of Surface Micromachined Thin Film Thermocouples (TFT): Comparison of the Resistance Arc Microwelding Technique with Wire Bonding," IEEE Trans. Compon. Packag. Technol., **32**(2), pp. 252-260.

[89] Sathyamurthi, V., and Banerjee, D., 2009, "Non-Linear Dynamical Analyses of Transient Surface Temperature Fluctuations during Subcooled Pool Boiling on a Horizontal Disk," Int. J. Heat Mass Transfer, **52**, pp. 5608-5623.

[90] Jo, B. and Banerjee, D., 2011, "Interfacial thermal resistance between organic nanoparticles and alkali molten salt eutectic: Effect of material properties, particle shapes and sizes," AJTEC2011-44373, *ASME/JSME 8th Thermal Engineering Joint Conference*, March 13-17, Honolulu, Hawaii, USA.

[91] Evans, W., Prasher, R., Fish, J., Meakin, P., Phelan, P., and Keblinski, P., 2008, "Effect of Aggregation and Interfacial Thermal Resistance on Thermal Conductivity of Nanocomposites and Colloidal Nanofluids," Int. J. Heat Mass Transfer, **51**, pp. 1431-1438.

[92] Keblinski, P., Phillpot, S. R., Choi, S.U.S., and Eastman, J. A., 2002, "Mechanisms of Heat Flow in Suspensions of Nano-Sized Particles (Nanofluids)," Int. J. Heat Mass Transfer, **45**(4), pp. 855-863.

[93] Keblinski, P., Prasher, R., and Eapen, J., 2008, "Thermal Conductance of Nanofluids: Is the Controversy Over?" J. Nanopart. Res., **10**(7), pp. 1089-1097.

[94] Yu, W. and Choi, S. U. S., 2003, "The Role of Interfacial Layers in the Enhanced Thermal of Nanofluids: A Renovated Maxwell Model," J. Nanopart. Res., **5**, pp. 167-171.

[95] Che, J., Cagin, T., and Goddard III, W. A., 2000, "Thermal Conductivity of Carbon Nanotubes," Nanotechnology, **11**(2) pp. 65-69.

[96] Osman, M. A. and Srivastava, D., 2001, "Temperature Dependence of the Thermal Conductivity of Single-Wall Carbon Nanotubes," Nanotechnology, **12**(1), pp. 21-24.

[97] Guo, C. Y., Pettitt, B. M., and Wheeler, L. T., 2006, "Force Field Comparisons of the Heat Capacity of Carbon Nanotubes," Mol. Simul., **32**, pp. 839-848.

[98] Tummala, N. R., and Striolo, A., 2009, "SDS Surfactants on Carbon Nanotubes: Aggregate Morphology," ACS Nano, **3**(3), pp. 595-602.

[99] Huxtable, S. T., Cahill, D. G., Shenogin, S., Xue, L., Ozisik, R., Barone, P., Usrey, M., Strano, M. S., Siddons, G., Shim, M., and Keblinski, P., 2003, "Interfacial Heat Flow in Carbon Nanotube Suspensions," Nat. Mater., **2**(11), pp. 731-734.

[100] S. Maruyama, Y. Igarashi, Y. Taniguchi, 2004, "Molecular Dynamics Simulations of Heat Transfer Issues in Carbon Nanotubes," *Proceedings of the 1st International Symposium on Micro & Nano Technology*, March 14-17, Honolulu, Hawaii, USA.

[101] Zhong, H. and Lukes, J. R., 2006, "Interfacial Thermal Resistance between Carbon Nanotubes: Molecular Dynamics Simulations and Analytical Thermal Modeling," Phys. Rev. B: Condens. Matt.), **74**(12), pp. 125403.

[102] Li, L., Bedrov, D., and Smith, G. D., 2006, "Water-Induced Interactions between Carbon Nanoparticles," J. Phys. Chem. B, **110**(21), pp. 10509-10513.

[103] Habasaki, J., 1990, "Molecular Dynamics Simulation of Molten Li_2CO_3 and Na_2CO_3," Mol. Phys., **69**(1), pp. 115-128.

[104] Koishi, T., Kawase, S., Tamaki, S., and Ebisuzaki, T., 2000, "Computer Simulation of Molten Li_2CO_3-K_2CO_3 Mixtures," J. Phys. Soc. Jpn., **69**(10), pp. 3291-3296.

[105] Costa, M. F., 2008, "Molecular Dynamics of Molten Li_2CO_3-K_2CO_3," J. Mol. Liq., **138**, pp. 61-68.

[106] Janz, G. J., Allen, C. B., Bansal, N. P., 1979, "Physical Properties Data Compilations Relevant to Energy Storage - 2. Molten Salts: Data on Single and Multi-component Salt Systems," US Nat. Bur. Stand., Nat. Stand. Ref. Data Ser. NSRDS-NBS 61, New York.

[107] Pop, E., Mann, D., Wang, Q., 2006, "Thermal Conductance of an Individual Single-Wall Carbon Nanotube above Room Temperature," Nano Lett., **6**(1), pp. 96-100.

[108] Dhawan, A., Taurozzi, J. S., Pandey, A. K., 2006, "Stable Colloidal Dispersions of C_{60} Fullerenes in Water: Evidence for Genotoxicity," Environ. Sci. Technol., **40**(23), pp. 7394-7401.

[109] Hyung, H. and Kim, J., 2009, "Dispersion of C_{60} in Natural Water and Removal by Conventional Drinking Water Treatment Processes," Water Res., **43**(9), pp. 2463-2470.

[110] ASTM E1269, 2005, Standard Test Method for Determining Specific Heat Capacity by Differential Scanning Calorimetry, American Society for Testing and Materials.

[111] Kline, S. J. and McClintock, F. A., 1953, "Describing Uncertainties in Single Sample Experiments," Mech. Eng., **75**(1), pp. 3-8.

[112] Walther, J. H., Jaffe, R., Halicioglu, T., 2001, "Carbon Nanotubes in Water: Structural Characteristics and Energetics," J. Phys. Chem. B, **105**(41), pp. 9980-9987.

[113] Girifalco, L. A., Hodak, M., and Lee, R. S., 2000, "Carbon Nanotubes, Buckyballs, Ropes, and a Universal Graphitic Potential," Phys. Rev. B: Condens. Matt., **62**(19), pp. 13104-13110.

[114] Kim, B. H., Beskok, A., and Cagin, T., 2008, "Molecular Dynamics Simulations of Thermal Resistance at the Liquid-Solid Interface," J. Chem. Phys., **129**(17), pp. 174701.

[115] Billings, B.H., and Gray, D.E., 1972, "American Institute of Physics Handbook," McGraw-Hill, New York.

[116] Li, Y., Qiu, X., Yin, Y., Yang, F., and Fan, Q., 2009, "The Specific Heat of Carbon Nanotube Networks and their Potential Applications," J. Phys. D: Appl. Phys., **42**(15), pp. 155405.

[117] Diky, V. V., Zhura, L. S., Kabo, A. G., Markov, V. Y., and Kabo, G. J., 2001, "High-Temperature Heat Capacity of C_{60} Fullerene," Fullerene Sci. Technol., **9**(4), pp. 543-551.

[118] Kim, S. H., Mulholland, G. W., and Zachariah, M. R., 2009, "Density Measurement of Size Selected Multiwalled Carbon Nanotubes by Mobility-Mass Characterization," Carbon, **47**(5), pp. 1297-1302.

[119] Li, L., Zhang, Y., Ma, H., and Yang, M., 2010, "Molecular Dynamics Simulation of Effect of Liquid Layering around the Nanoparticle on the Enhanced Thermal Conductivity of Nanofluids," J. Nanopart. Res., **12**(3), pp. 811-821.

[120] Chang, C. I., Lee, W. J., Young, T. F., Ju, S. P., Chang, C. W., Chen, H. L., and Chang, J. G., 2008, "Adsorption Mechanism of Water Molecules Surrounding Au Nanoparticles of Different Sizes," J. Chem. Phys., **128**(15), pp. 154703.

[121] Oh, S. H., Kauffmann, Y., Scheu, C., Kaplan, W. D., and Ruhle, M., 2005, "Ordered Liquid Aluminum at the Interface with Sapphire," Science, **310**(5748), pp. 661-663.

[122] Chase, M. W. J., 1988, "NIST-JANAF Thermochemical Tables 4th Ed. Part 1, Al-Co," J. Phys. Chem. Ref. Data, Monograph 9, pp. 1-1951.

[123] Araki, N., Matsuura, M., Makino, A., 1988, "Measurement of thermophysical properties of molten salts: mixtures of alkaline carbonate salts," Int. J. Thermophys., **9**(6), pp. 1071-1080.

[124] Osman, M. B. S., Dakroury, A. Z., Dessouky, M. T., Kenawy, M. A., El-Sharkawy, A. A., 1996, "Measurement of Thermophysical Properties of Ammonium Salts in the Solid and Molten States," J. Therm. Anal., **46**(6), pp. 1697-1703.

[125] Ito, H., Hasegawa, Y., and Ito, Y., 2001, "Densities of Eutectic Mixtures of Molten Alkali Chlorides Below 673 K," J. Chem. Eng. Data, **46**(5), pp. 1203-1205.

[126] NIST Standard Reference Database 69, 2000, NIST Chemistry Web Book.

[127] Liu, Q., Tenner, T. J., and Lange, R. A., 2007, "Do Carbonate Liquids Become Denser than Silicate Liquids at Pressure? Constraints from the Fusion Curve of K_2CO_3 to 3.2 GPa," Contrib. Mineral. Petrol., **153**(1), pp. 55-66.

[128] Wang, G. and Harrison, I. R., 1994, "Polymer Melting: Heating Rate Effects on DSC Melting Peaks," Thermochim. Acta, **231**(10), pp. 203-213.

[129] Dubska, L., 1968, "Influence of Temperature on the Decomposition of Technical Alkyl Sulfates," Veda Vyzk. Prum. Potravin., **18**, pp. 79-94.

[130] Buongiorno, J., et al., 2006, "Convective Transport in Nanofluids," J. Heat Transfer, **128**(3), pp. 240-250.

[131] Wang, B., Zhou, L., and Peng, X., 2006, "Surface and Size Effects on the Specific Heat Capacity of Nanoparticles," Int. J. Thermophys., **27**(1), pp. 139-151.

[132] Leong, K. C., Yang, C., and Murshed, S. M. S., 2006, "A Model for the Thermal Conductivity of Nanofluids - the Effect of Interfacial Layer," J. Nanopart. Res., **8**(2), pp. 245-254.

[133] Lemire, B., Neumaier, K., and Andres, K., 1990, "Grain Size-Dependence of the Spezific Heat of $YBa_2Cu_3O_7$-Sinters," Physica B, **165-166**, pp. 1353-1354.

[134] Hilding, J., Grulke, E. A., Zhang, Z. G., 2003, "Dispersion of Carbon Nanotubes in Liquids," J. Dispersion Sci. Technol., **24**(1), pp. 1-41.

[135] Murshed, S. M. S., 2009, "Correction and Comment on "Thermal Conductance of Nanofluids: Is the Controversy Over?"," J. Nanopart. Res., **11**(2), pp. 511-512.

[136] Yu, C. J., Richter, A. G., Datta, A., Durbin, M. K., Dutta, P., 2000, "Molecular Layering in a Liquid on a Solid Substrate: An X-Ray Reflectivity Study," Physica B, **283**(1), pp. 27-31.

[137] Wang, L., Tan, Z., Meng, S., Liang, D., and Li, G., 2001, "Enhancement of Molar Heat Capacity of Nanostructured Al_2O_3," J. Nanopart. Res., **3**, pp. 483-487.

[138] Turanov, A. N. and Tolmachev, Y. V., 2009, "Heat- and Mass-Transport in Aqueous Silica Nanofluids," Heat Mass Transfer, **45**(12), pp. 1583-1588.

[139] Gerardi, C., Cory, D., Buongiorno, J., Hu, L. W., and McKrell, T., 2009, "Nuclear Magnetic Resonance-Based Study of Ordered Layering on the Surface of Alumina Nanoparticles in Water," Appl. Phys. Lett., **95**(25), pp. 253104.

[140] Feibelman, P. J., 2010, "The First Wetting Layer on a Solid," Phys. Today, **63**(2), pp. 34-39.

[141] Ocko, B. M., Hlaing, H., Jepsen, P. N., Kewalramani, S., Tkachenko, A., Pontoni, D., Reichert, H., and Deutsch, M., 2011, "Unifying Interfacial Self-Assembly and Surface Freezing," Phys. Rev. Lett., **106**(13), pp. 137801.

[142] Karthikeyan, N. R., Philip, J., and Raj, B., 2008, "Effect of Clustering on the Thermal Conductivity of Nanofluids," Mat. Chem. Phys., **109**(1), pp. 50-55.

[143] Jakab, E., Meszaros, E., and Omastova, M., 2007, "Thermal Decomposition of Polypyrroles," J. Therm. Anal. Calorim., **88**(2) pp. 515-521.

[144] Wang, J., Sun, J., Gao, L., Liu, Y., Wang, Y., Zhang, J., Kajiura, H., Li, Y., and Noda, K., 2009, "Improving the Conductivity of Single-Walled Carbon Nanotubes Films by Heat Treatment," J. Alloys Comp., **485**, pp. 456-61.

[145] Reich, S., and Thomsen, C., 2004, "Raman Spectroscopy of Graphite," Philos. Trans. R. Soc. London, Ser. A, **362**(1824), pp. 2271-2288.

[146] Jawhari, T., Roid, A., and Casado, J., 1995, "Raman Spectroscopic Characterization of some Commercially Available Carbon Black Materials," Carbon, **33**(11), pp. 1561-1565.

[147] Sidorov, A. N., Pabba, S., Hewaparakrama, K. P., Cohn, R. W., and Sumanasekera, G. U., 2008, "Side-by-Side Comparison of Raman Spectra of Anchored and Suspended Carbon Nanomaterials," Nanotechnology, **19**(19), pp. 195798.

[148] Ferrari, A. C., and Robertson, J., 2000, "Interpretation of Raman Spectra of Disordered and Amorphous Carbon," Phys. Rev. B: Condens. Matt., **61**(20), pp. 14095-14107.

[149] Yan, A., Lau, B. W., Weissman, B. S., Kulatos, I., Wang, Y. C., Kane, A. B., and Hurt, R. H., 2006, "Biocompatible, Hydrophilic, Supramolecular Carbon Nanoparticles for Cell Delivery," Adv. Mat., **18**(18), pp. 2373-2378.

[150] Song, C., Du, J., Zhao, J., Feng, S., Du, G., and Zhu, Z., 2009, "Hierarchical Porous Core-Shell Carbon Nanoparticles," Chem. Mat., **21**(8), pp. 1524-1530.

[151] Sato, Y., Yamazaki, T., Kato, H., Zhu, H., Hoshi, M., and Yamamura, T., 1999, "Viscosities of Li_2CO_3-Na_2CO_3 and Li_2CO_3-K_2CO_3 Binary Melts," Netsu Bussei, **13**(3), pp. 162-167.

[152] Chen, H., Ding, Y., He, Y., and Tan, C., 2007, "Rheological Behaviour of Ethylene Glycol Based Titania Nanofluids," Chem. Phys. Lett., **444**, pp. 333-337.

[153] Bandyopadhyaya, R., Nativ-Roth, E., Regev, O., and Yerushalmi-Rozen, R., 2002, "Stabilization of Individual Carbon Nanotubes in Aqueous Solutions," Nano Lett., **2**(1), pp. 25-28.

[154] Masoumi, N., Sohrabi, N., and Behzadmehr, A., 2009, "A New Model for Calculating the Effective Viscosity of Nanofluids," J. Phys. D: Appl. Phys., **42**(5), pp. 055501.

[155] Hui, P. M. and Stroud, D., 1986, "Complex Dielectric Response of Metal-Particle Clusters," Phys. Rev. B: Condens. Matt., **33**(4), pp. 2163-2169.

[156] Mohraz, A., Moler, D. B., Ziff, R. M., and Solomon, M. J., 2004, "Effect of Monomer Geometry on the Fractal Structure of Colloidal Rod Aggregates," Phys. Rev. Lett., **92**(15), pp. 155503.

[157] Shenogin, S., Bodapati, A., Xue, L., 2004, "Effect of Chemical Functionalization on Thermal Transport of Carbon Nanotube Composites," Appl. Phys. Lett., **85**(12), pp. 2229-2231.

[158] Malik, D. R., 2010, "Evaluation of Composite Alumina Nanoparticle and Nitrate Eutectic Materials for use in Concentrating Solar Power Plants," M.S. Thesis, Texas A&M University.

APPENDIX A

(Specific heat capacity and viscosity of aqueous nanofluids)

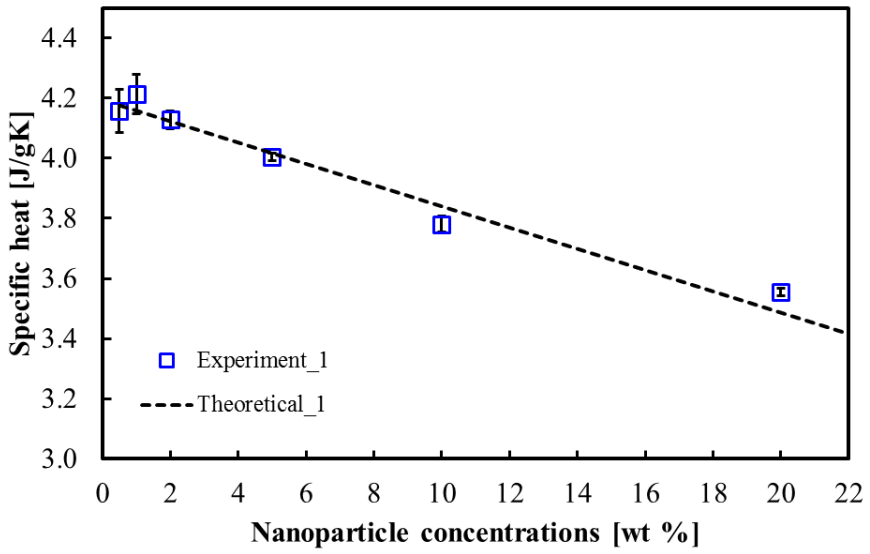

Fig. A 1 Specific heat capacity of aqueous TiO_2 nanofluids as a function of nanoparticle concentration

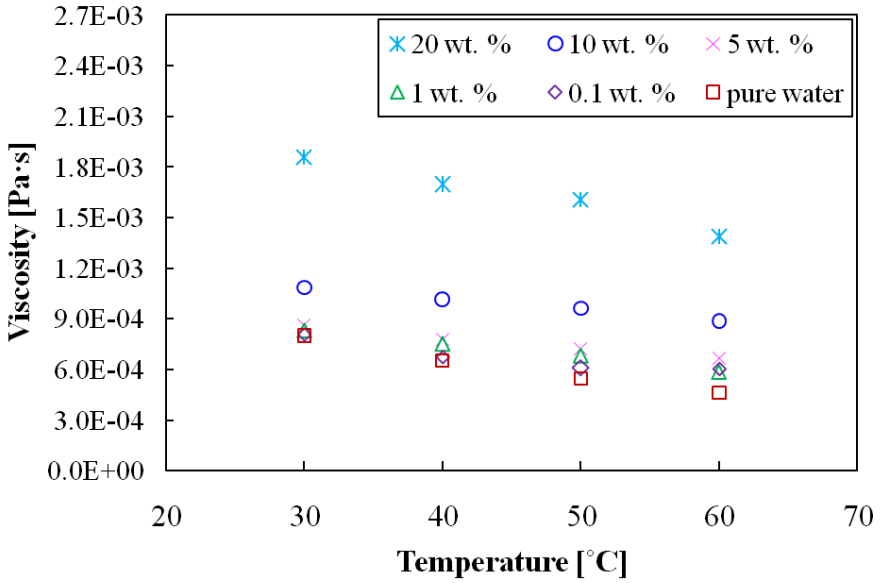

Fig. A 2 Viscosity of aqueous SiO_2 nanofluids as a function of temperature and nanoparticle concentration

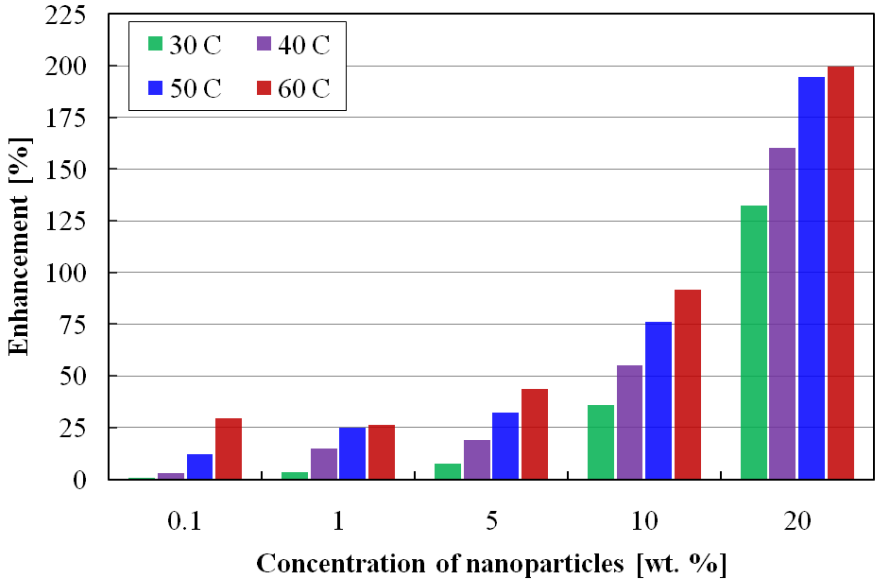

Fig. A 3 Enhancements in the viscosity of aqueous SiO_2 nanofluids

APPENDIX B

(Scanning microscopy images of graphite nanomaterials)

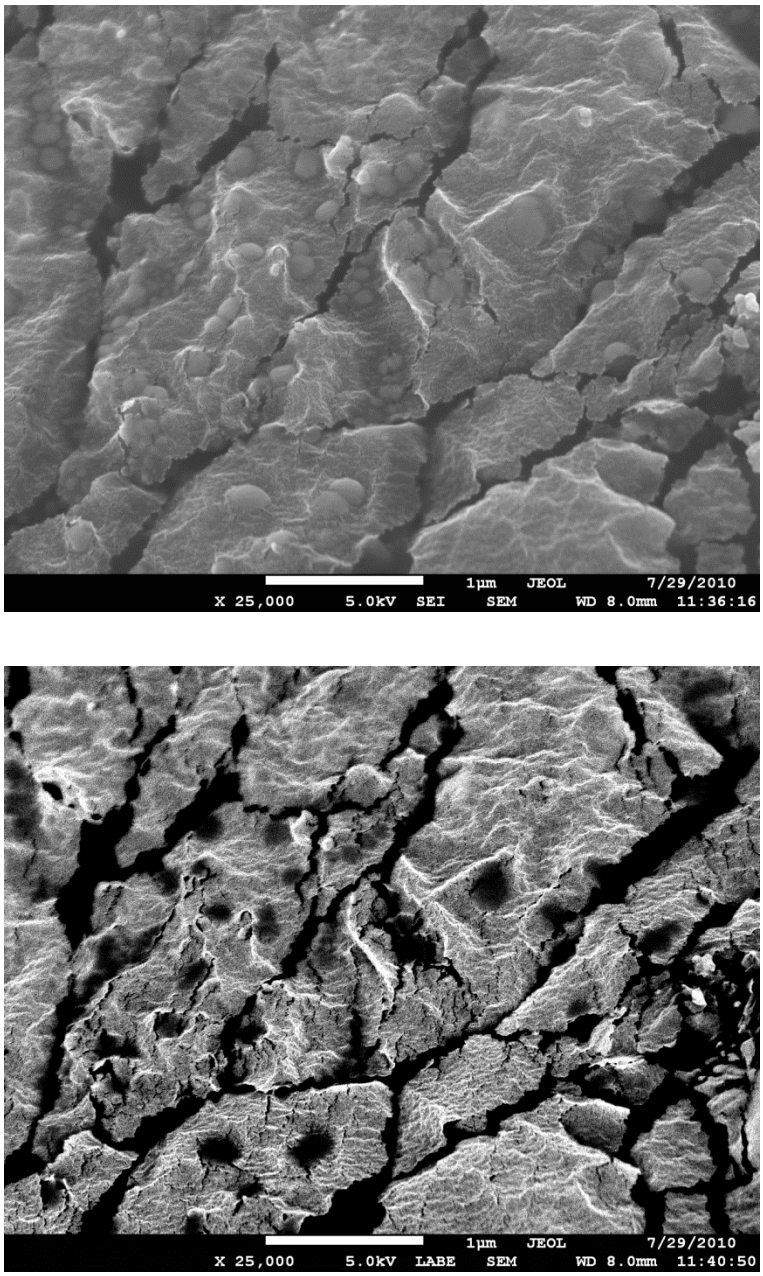

Fig. B. 1 SEM images-A of graphite nanomaterial (Top) Secondary electron image and (Bottom) Backscatter image for Nanomaterial 1 (Method 1)

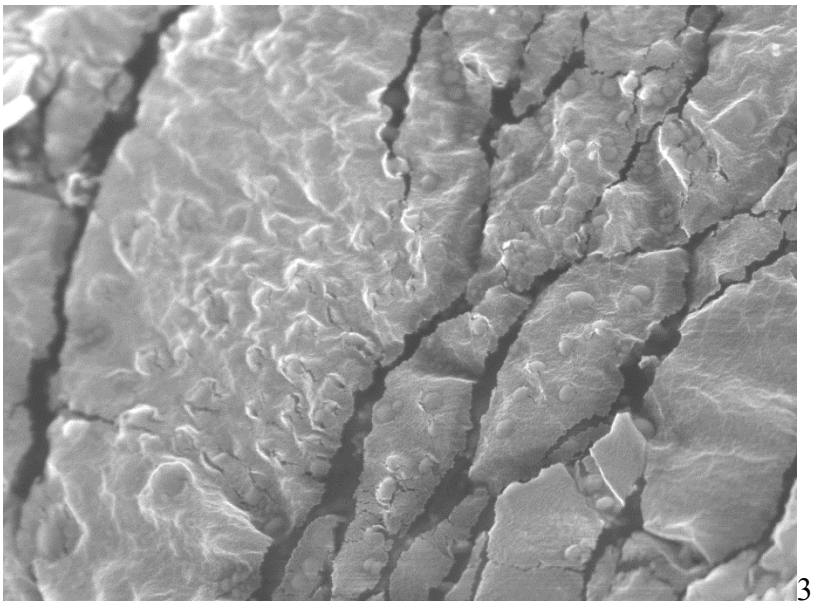

3

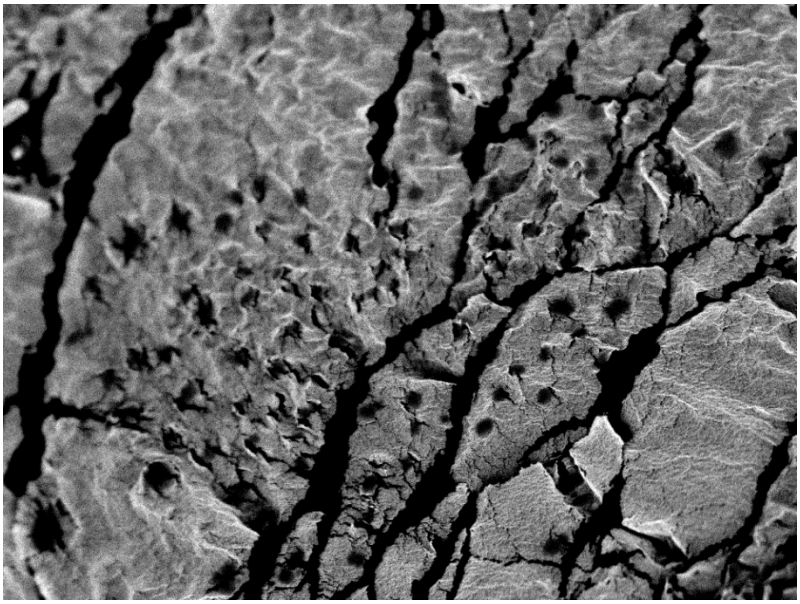

Fig. B. 2 SEM images of graphite nanomaterial (Top) Secondary electron image and (Bottom) Backscatter image for Nanomaterial 1 (Method 1)

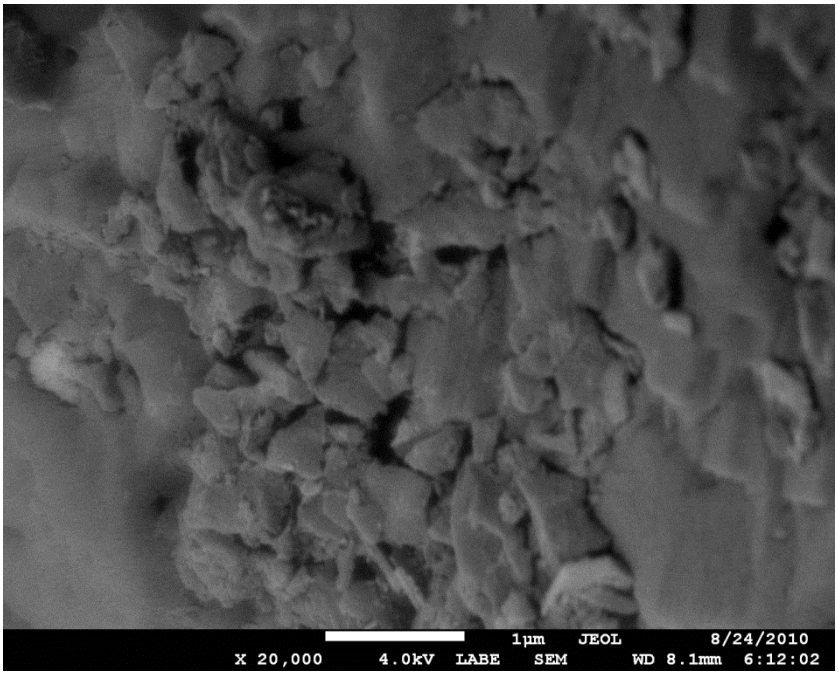

Fig. B. 3 SEM images of graphite nanomaterial: low-angle backscatter image for Nanomaterial 1 (Method 1)

APPENDIX C

(Size distribution and zeta potential of C_{60} fullerene nanoparticle in distilled water)

C_{60} fullerene (also known as "Buckyballs") has an extremely low solubility in water [80]. Hence, it is difficult to disperse the C_{60} fullerene particles in water. Conventional strategies - such as adding surfactants to the solvent and applying ultrasound for agitation - are not effective in improving the dispersion of fullerenes in water. This trait has been an impediment to the synthesis of aqueous solutions of fullerene. In this study, dispersion of the fullerene nanoparticles in water was studied by using a mechanical mixing technique (i.e., using a rotating a magnetic stirring bar). The time for mixing was varied from 1 week to 4 weeks, and two different durations for settling time was explored (1 week or 2 weeks). These studies were performed to compare the size distribution and zeta potential of the fullerene nanoparticles dispersed in water. A surfactant (SDS, 1.0 % mass concentration) was added to distilled water to facilitate the dispersion. The effect of the surfactant dispersion was explored by comparing the size distribution and zeta potential values for these samples using SDS with those obtained from the samples without using SDS.

Table C. 1 Experimental conditions for C_{60} fullerene dispersion

Set No.	C_{60} fullerene [Mass fraction. %]	SDS [mg]	Solvent	Mixing RPM
1	0.01	1.0	Distilled water	800
2	0.01	N/A	Distilled water	800

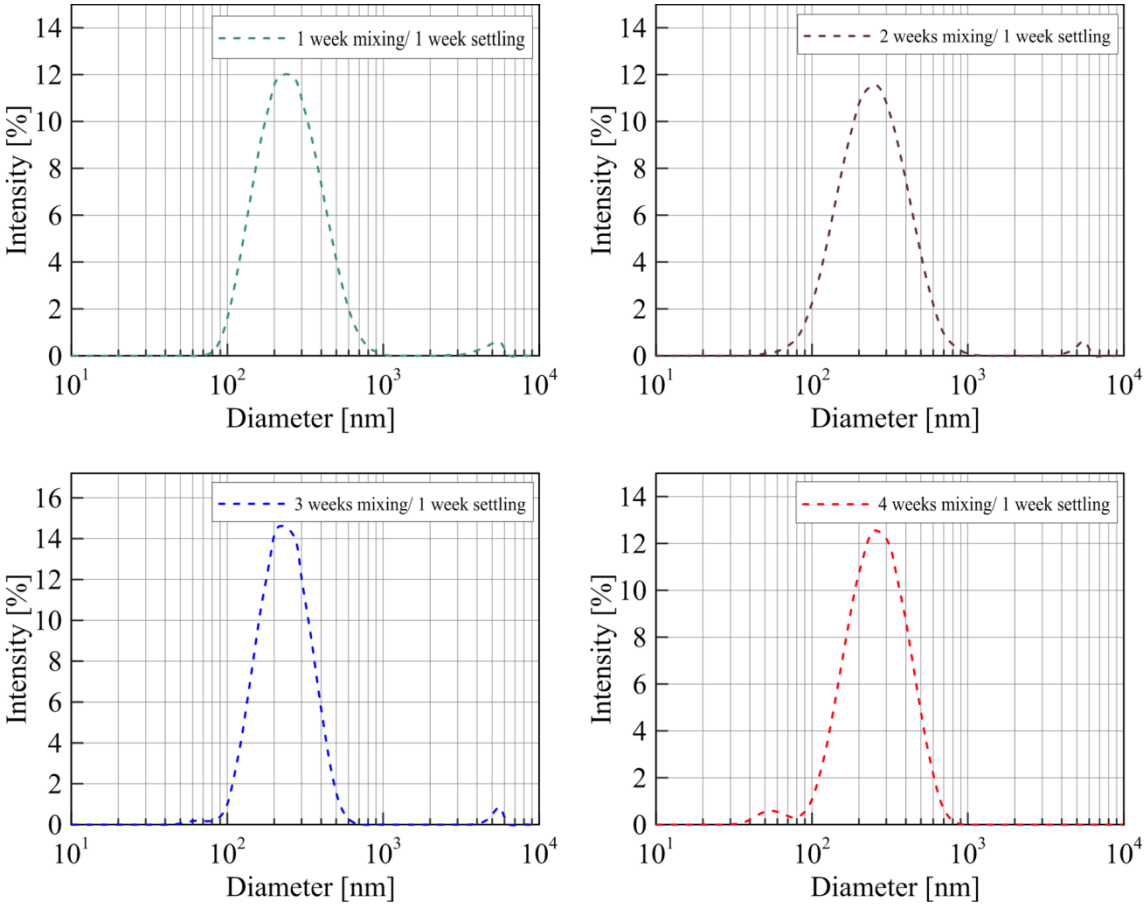

Fig. C. 1 Nanoparticle size distribution for set No. 1 (1 week for settlement of the nanoparticles)

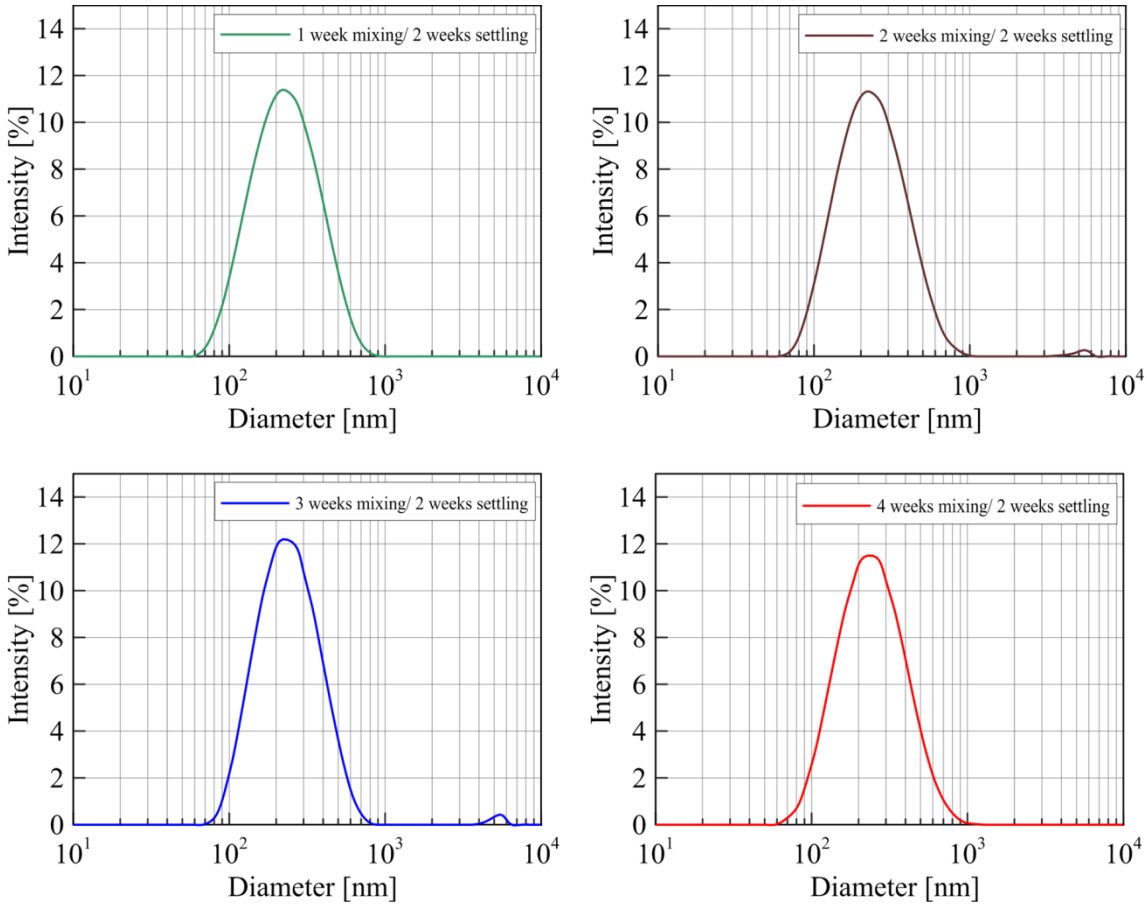

Fig. C. 2 Nanoparticle size distribution for set No. 1 (2 weeks for settlement of the nanoparticles)

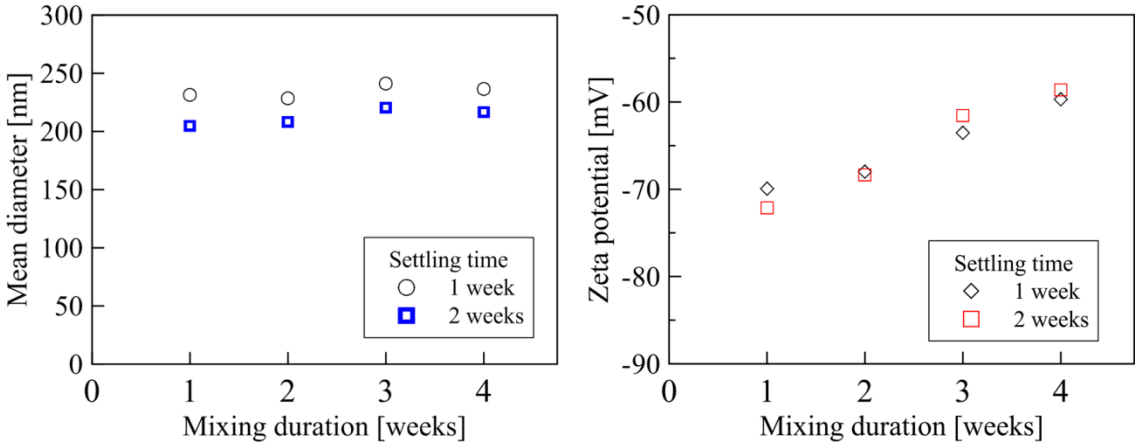

Fig. C. 3 Average diameter and zeta potential of C_{60} fullerene for set No. 1

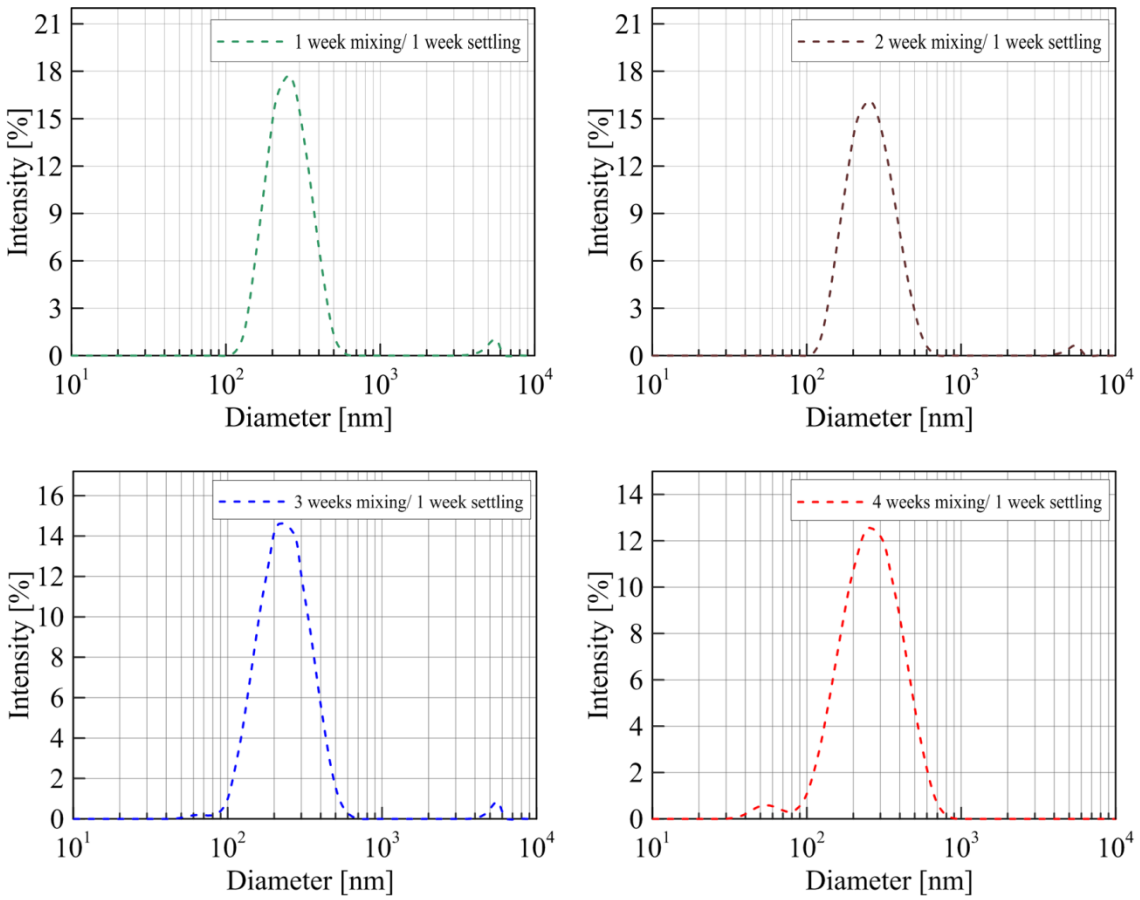

Fig. C. 4 Nanoparticle size distribution for set No. 2 (1 week for settlement of the nanoparticles)

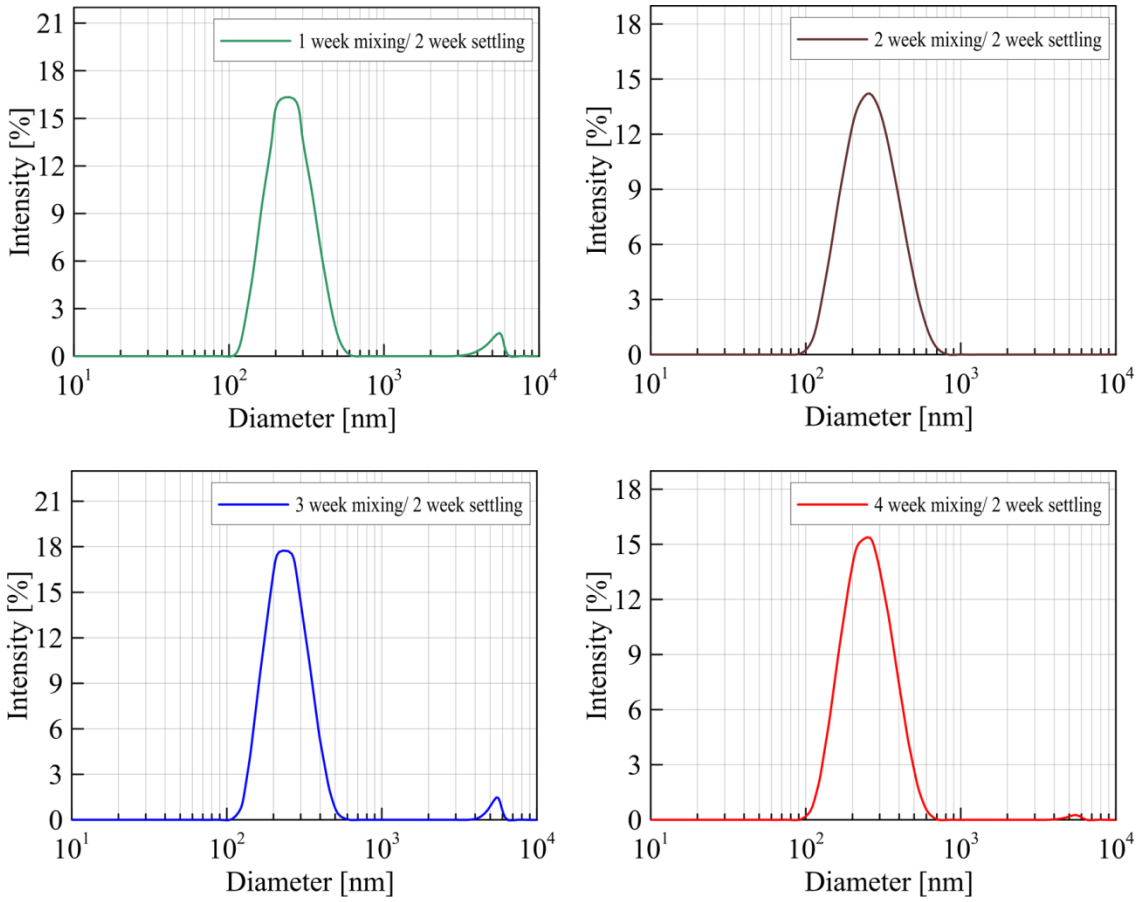

Fig. C. 5 Nanoparticle size distribution for set No. 2 (2 weeks for settlement of the nanoparticles)

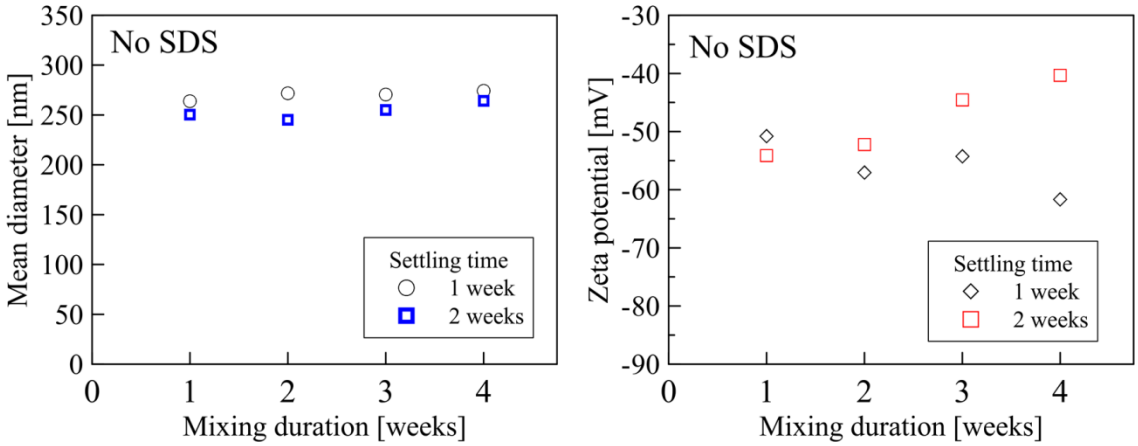

Fig. C. 6 Average diameter and zeta potential of C_{60} fullerene for set No. 2

Table C. 2 Average diameters and standard deviation of C_{60} fullerene dispersed in water

Mixing duration [weeks]	SDS		No SDS	
	1 week settling	2 week settling	1 week settling	2 week settling
1	231 (1.0)	205 (1.7)	264 (6.9)	251 (7.3)
2	229 (1.7)	208 (2.5)	272 (13.5)	245 (4.1)
3	242 (2.4)	221 (0.6)	271 (3.8)	255 (0.3)
4	237 (1.0)	217 (1.7)	274 (7.1)	264 (9.1)

Table C. 3 Average zeta potential and standard deviation of C_{60} fullerene dispersed in water

Mixing duration [weeks]	SDS		No SDS	
	1 week settling	2 week settling	1 week settling	2 week settling
1	-69.9 (1.8)	-72.1 (0.8)	-50.7 (0.6)	-54.1 (0.9)
2	-68.0 (1.1)	-68.3 (1.6)	-57.0 (0.8)	-52.2 (1.5)
3	-63.5 (1.8)	-61.5 (1.0)	-54.2 (1.9)	-44.5 (0.8)
4	-59.7 (2.5)	-58.6 (1.4)	-61.7 (0.6)	-40.3 (0.7)

APPENDIX D

Fig. D. 1 show the specific heat capacity of two organic nanomaterials in which the nanoparticles were highly agglomerated in the solvent. Due to the agglomeration of the nanoparticles, the specific heat capacity values were decreased drastically with each successive cycle when thermocycling experiments (repeated melting and re-solidification) were performed in a DSC. As shown in the Fig. D. 1, the specific heat capacity value was higher than the pure eutectic value for the first two or three runs, but the value decreased to less than that of the pure eutectic at the end of the thermocycling experiment. The mass concentration of the nanoparticles for these two nanomaterials was 1 %. Fig. D. 2 shows a SEM image of agglomerated carbon nanotubes in these samples that were used in the thermo-cycling experiments. The SEM images were obtained from the samples after the experiments were performed.

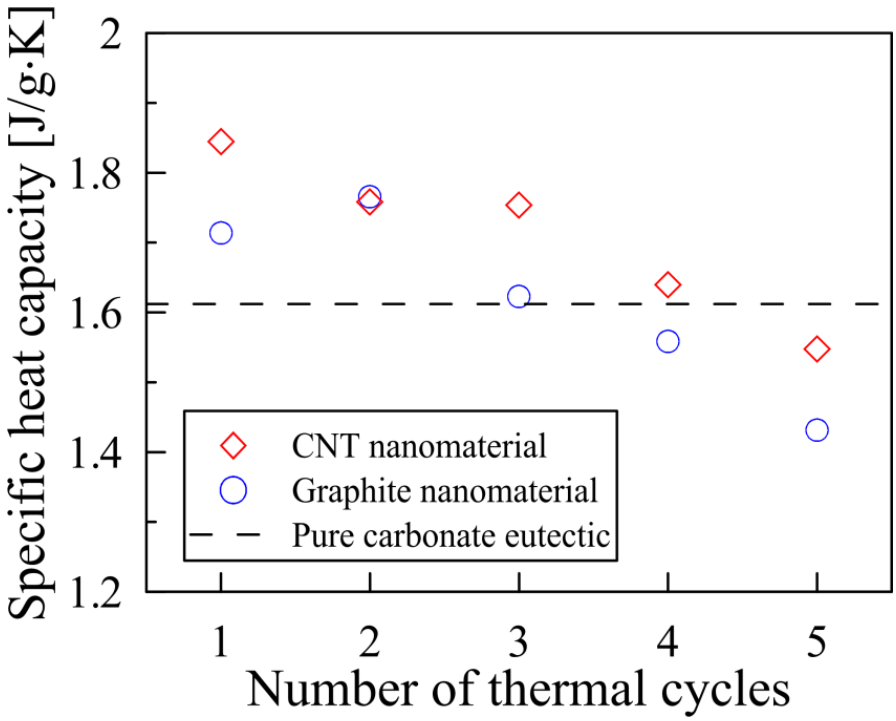

Fig. D. 1 Specific heat capacity of carbonate salt eutectic-CNT nanomaterials in liquid phase as repeating thermal cycles in DSC

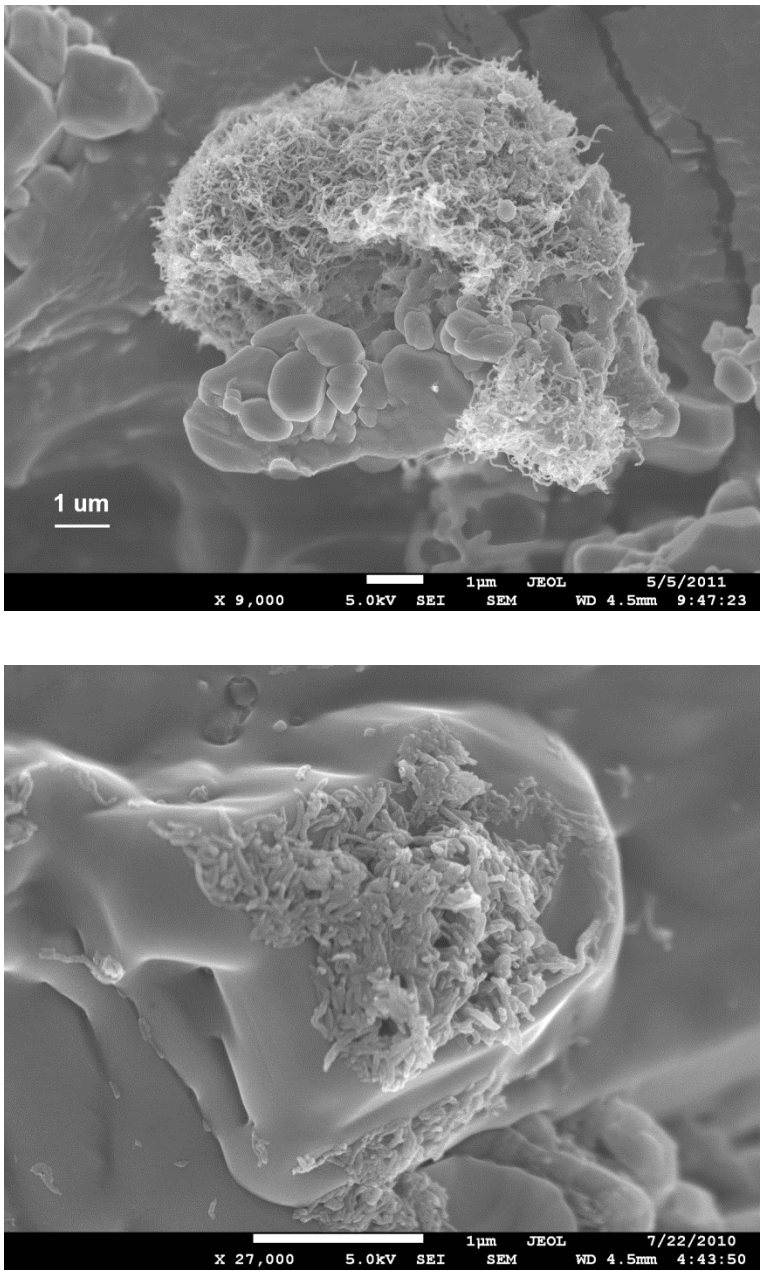

Fig. D. 2 Scanning electron microscopy (SEM) images of nanomaterials with large agglomeration of carbon nanotubes

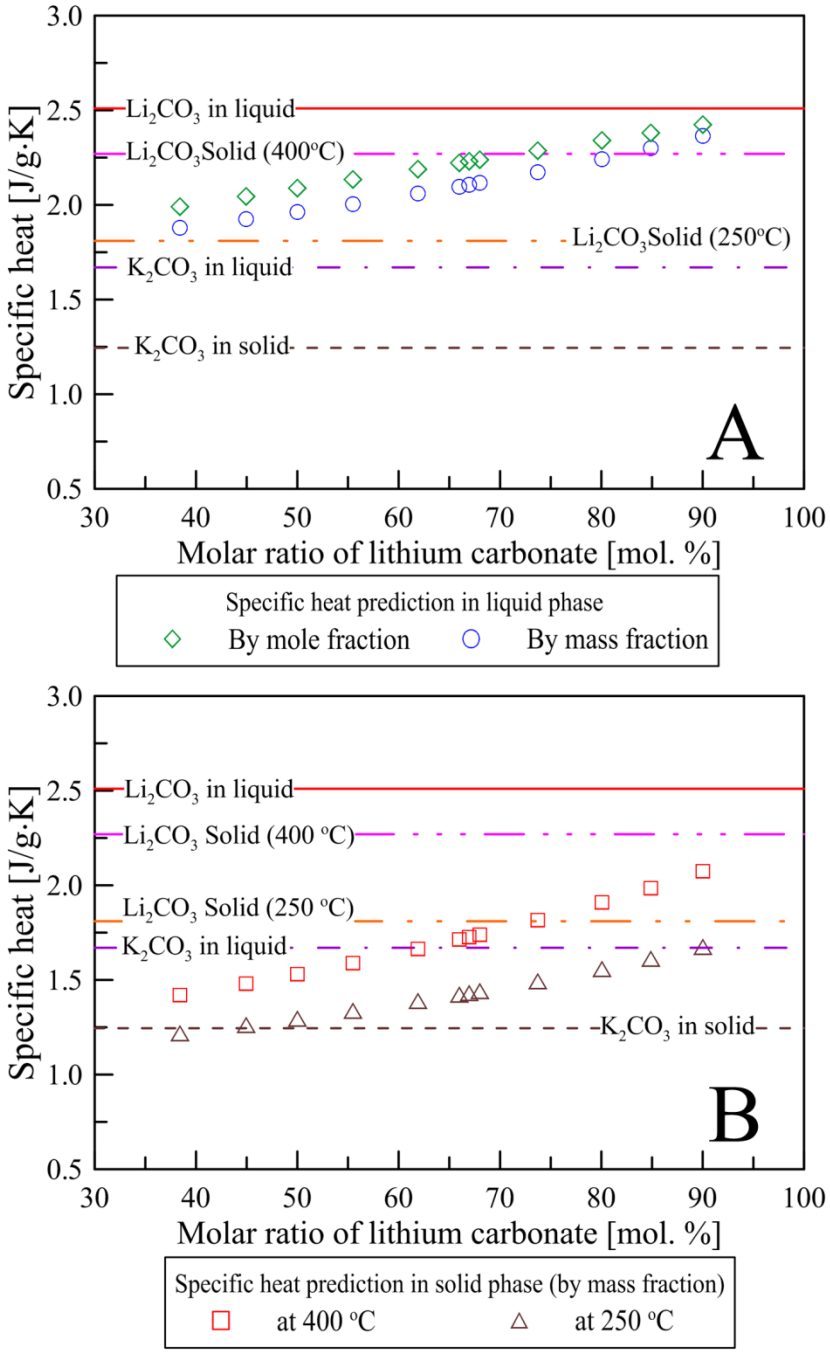

Fig. D. 3 Theoretical predictions of specific heat capacity of carbonate salt mixtures: (A) in liquid phase and (B) in solid phase (at 250 ℃ and 400 ℃) (which are the same as in Fig. 4.8)

APPENDIX E

(Discretized density and concentration plots of the carbonate salt mixtures in CNT nanomaterials using pristine carbon nanotubes or using functionalized carbon nanotubes)

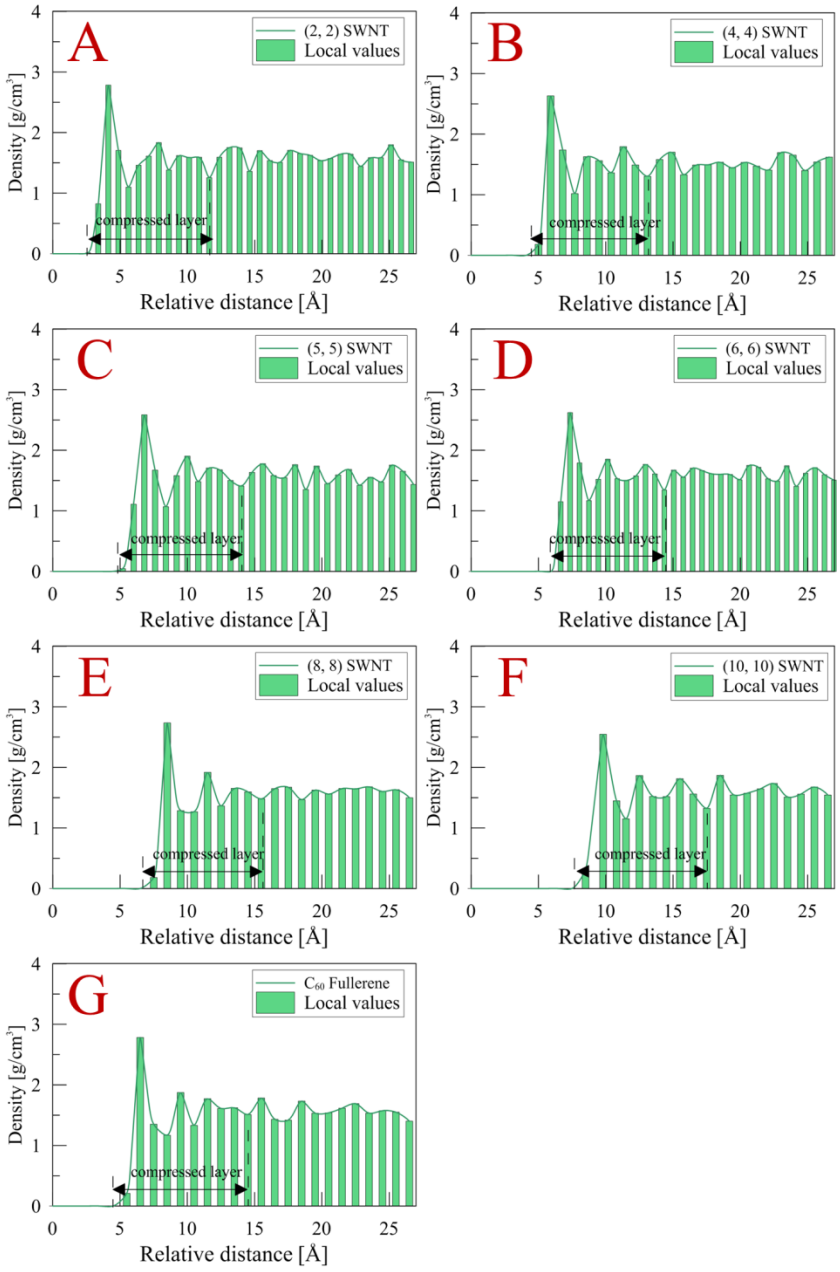

Fig. E. 1 Density variations of solvent material (carbonate salt mixture) for carbon nanotubes and C_{60} fullerene (which are the same as in Fig. 3.9)

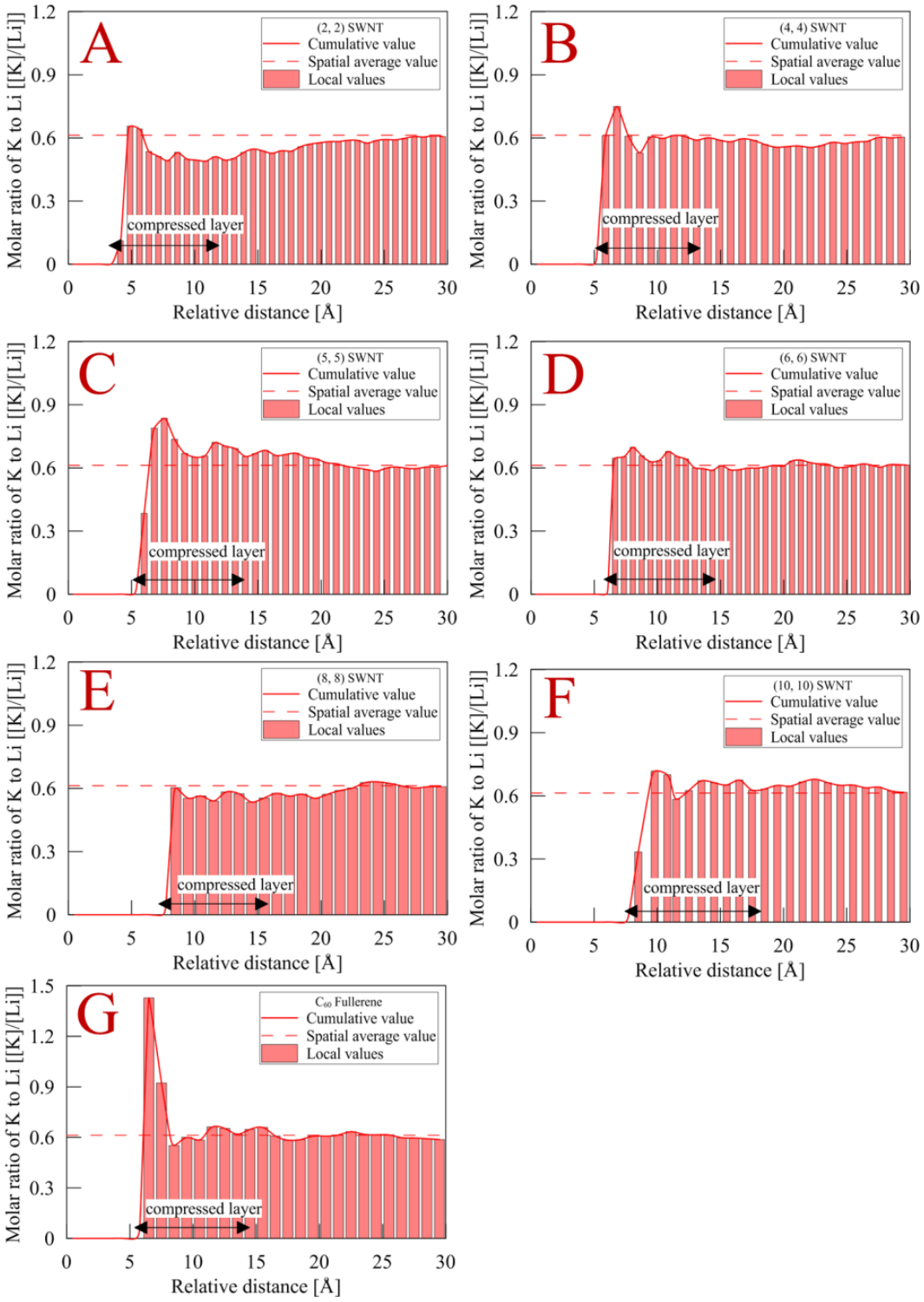

Fig. E. 2 Molar ratio of potassium to lithium along relative position for carbon nanotubes and C_{60} fullerene

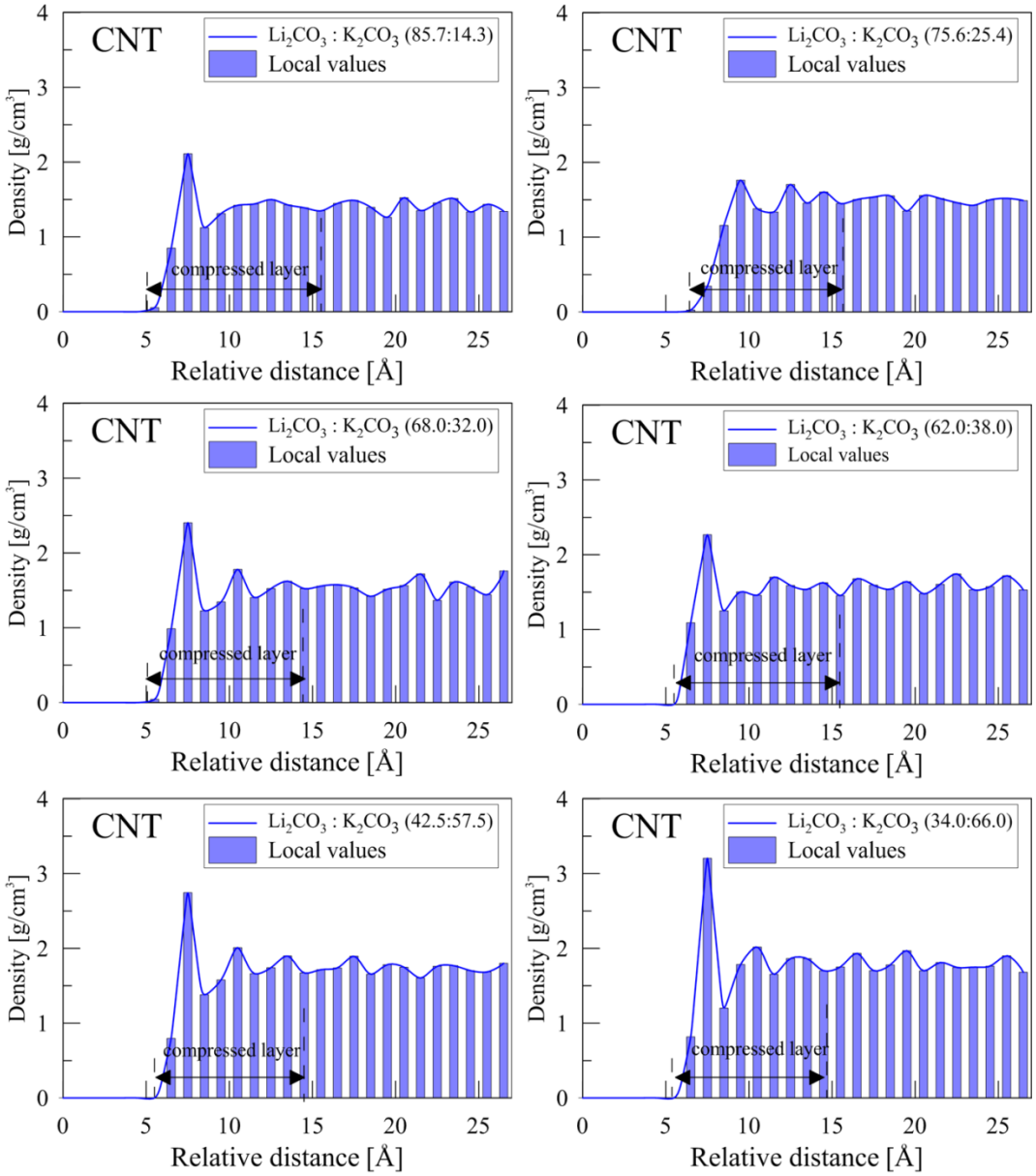

Fig. E. 3. Density variations of solvent material (carbonate salt mixture) as a function of chemical composition (which are the same as in Fig. 8.4)

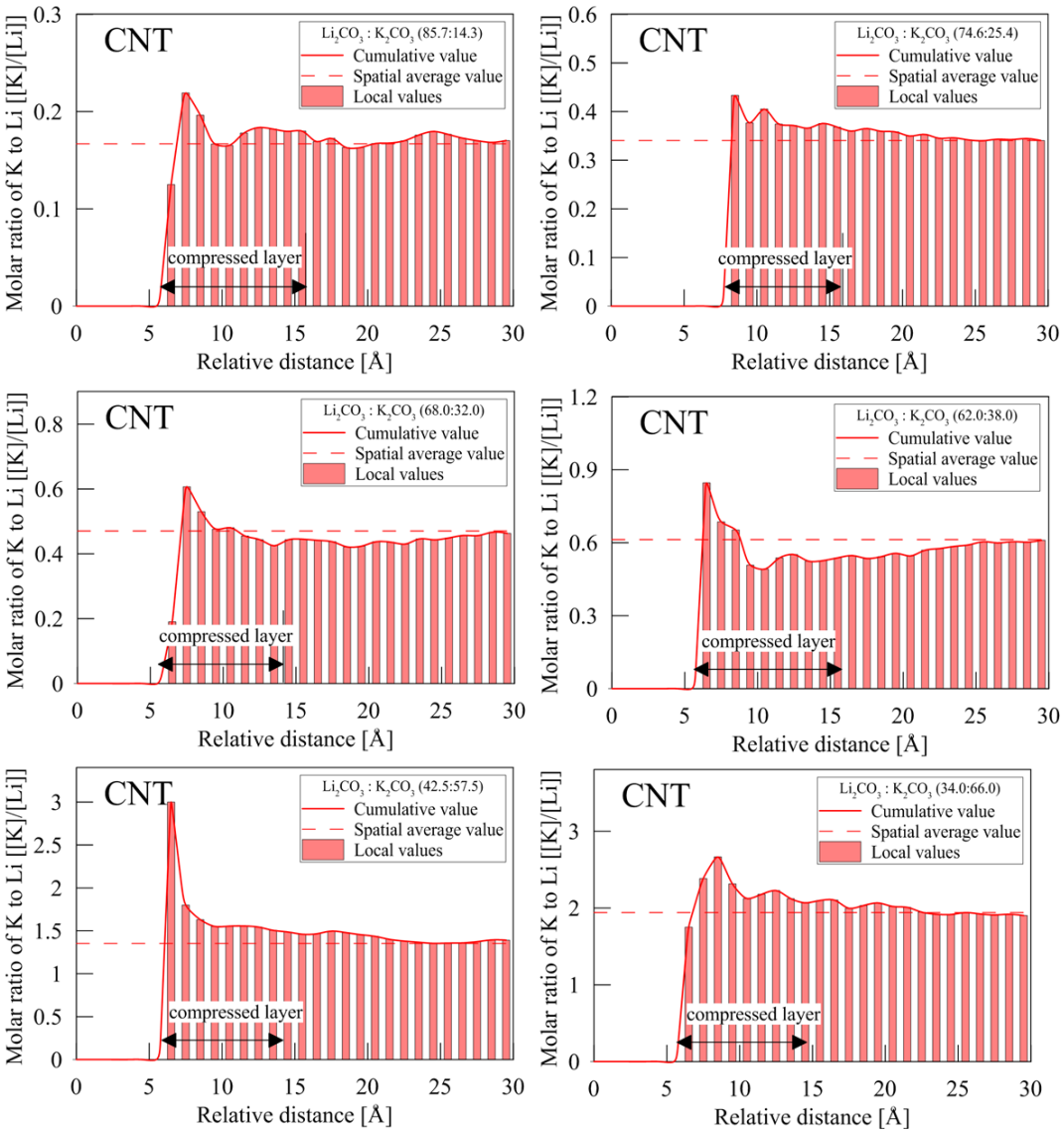

Fig. E. 4 Molar ratio of potassium to lithium along relative position as function of chemical composition (which are the same as in Fig. 8.5)

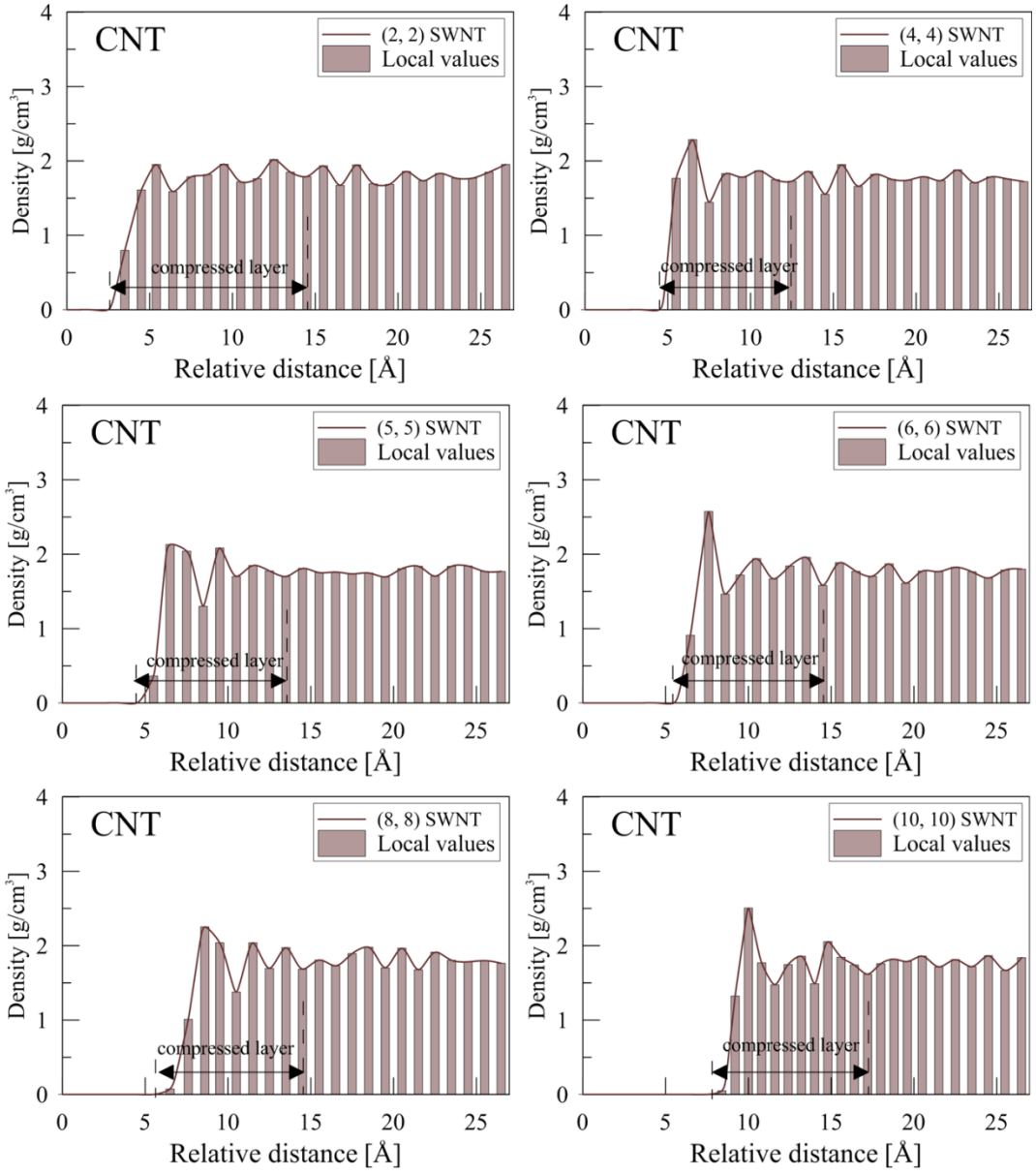

Fig. E. 5 . Density variations of solvent material (carbonate salt mixture) near a functionalized carbon nanotube by carboxyl (COOH) groups

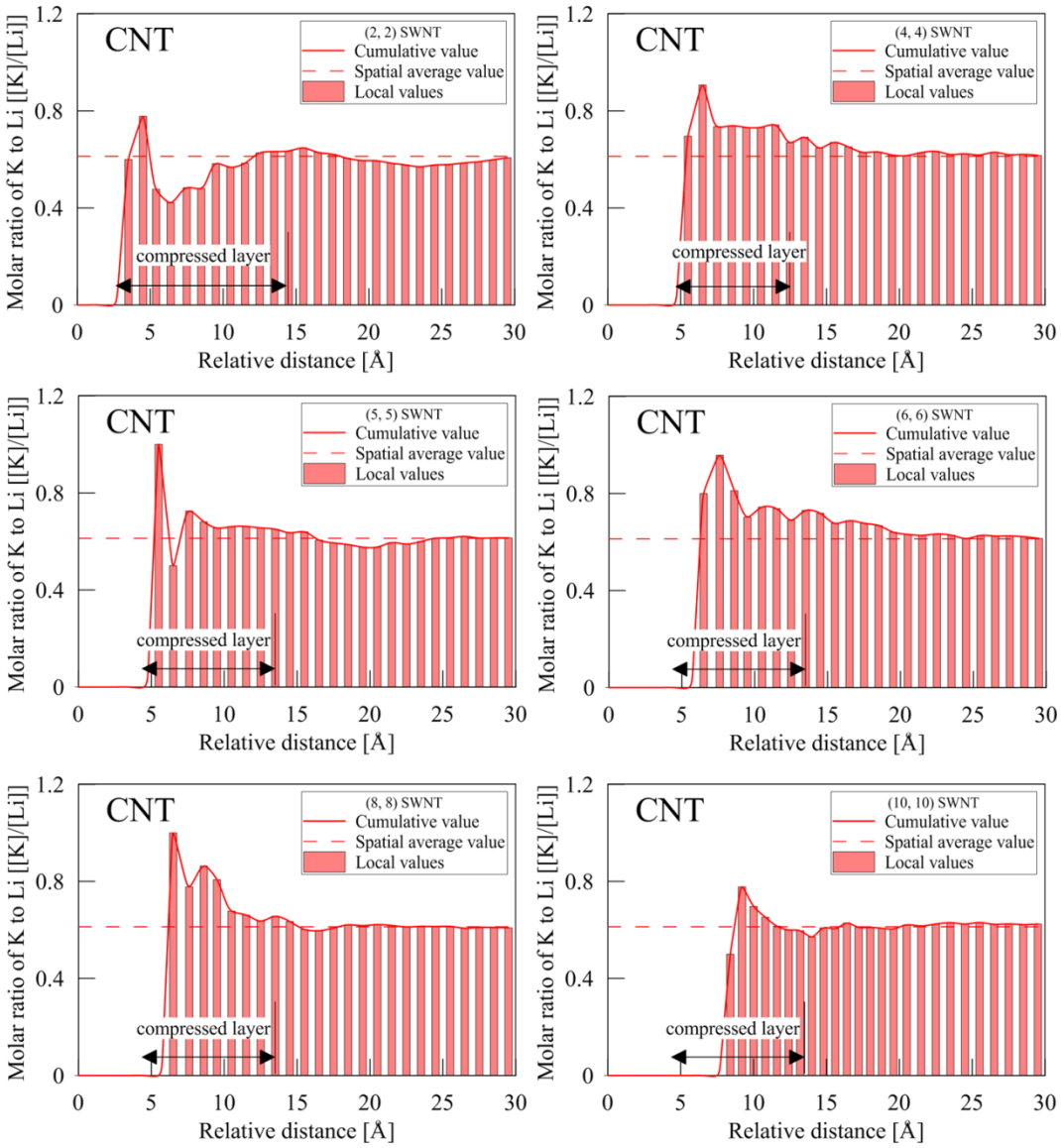

Fig. E. 6 Molar ratio of potassium to lithium along relative position: nanofluids with functionalized carbon nanotubes by amine (NH2) groups

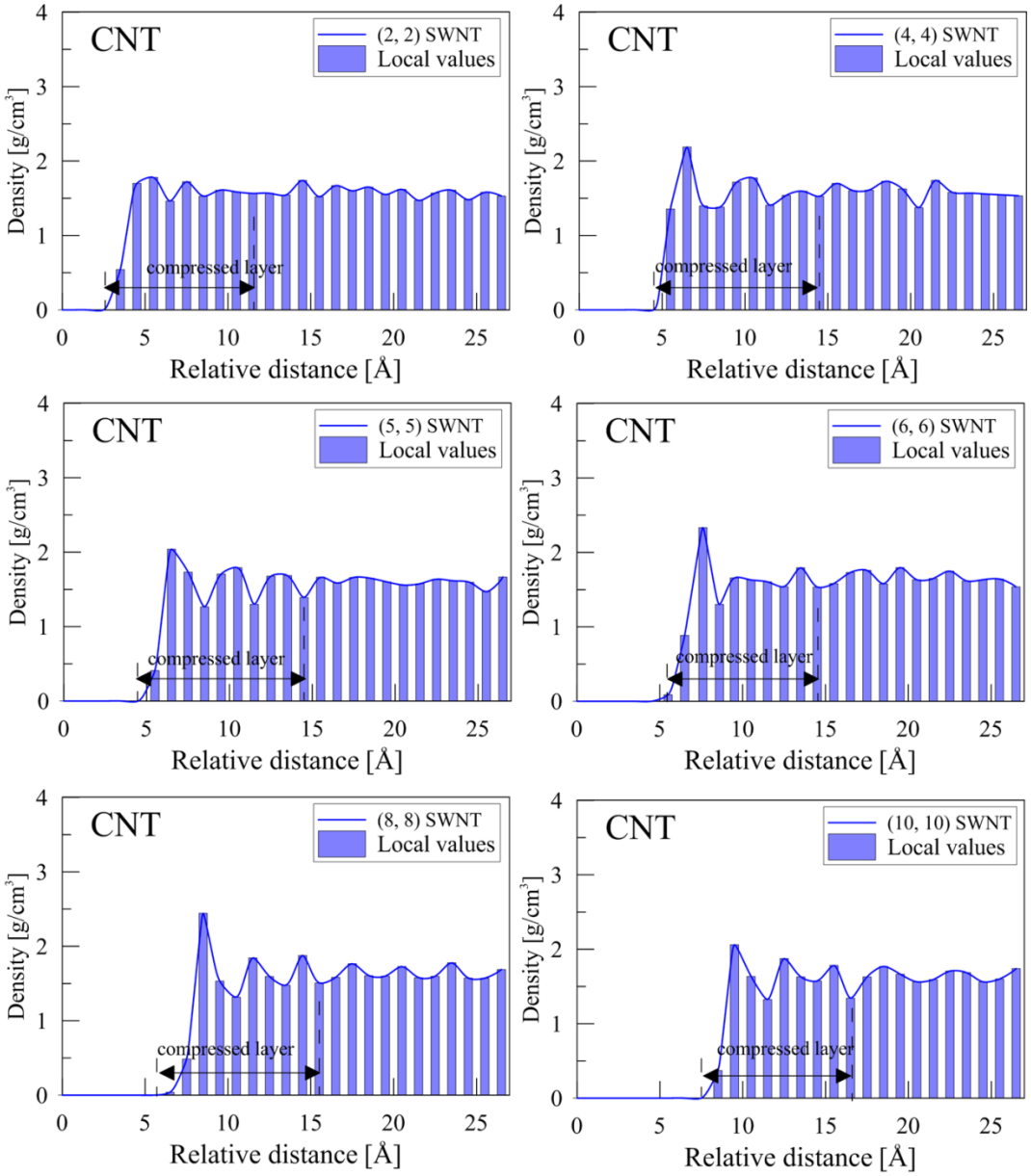

Fig. E. 7 Density variations of solvent material (carbonate salt mixture) near a functionalized carbon nanotube by amine (NH_2) groups

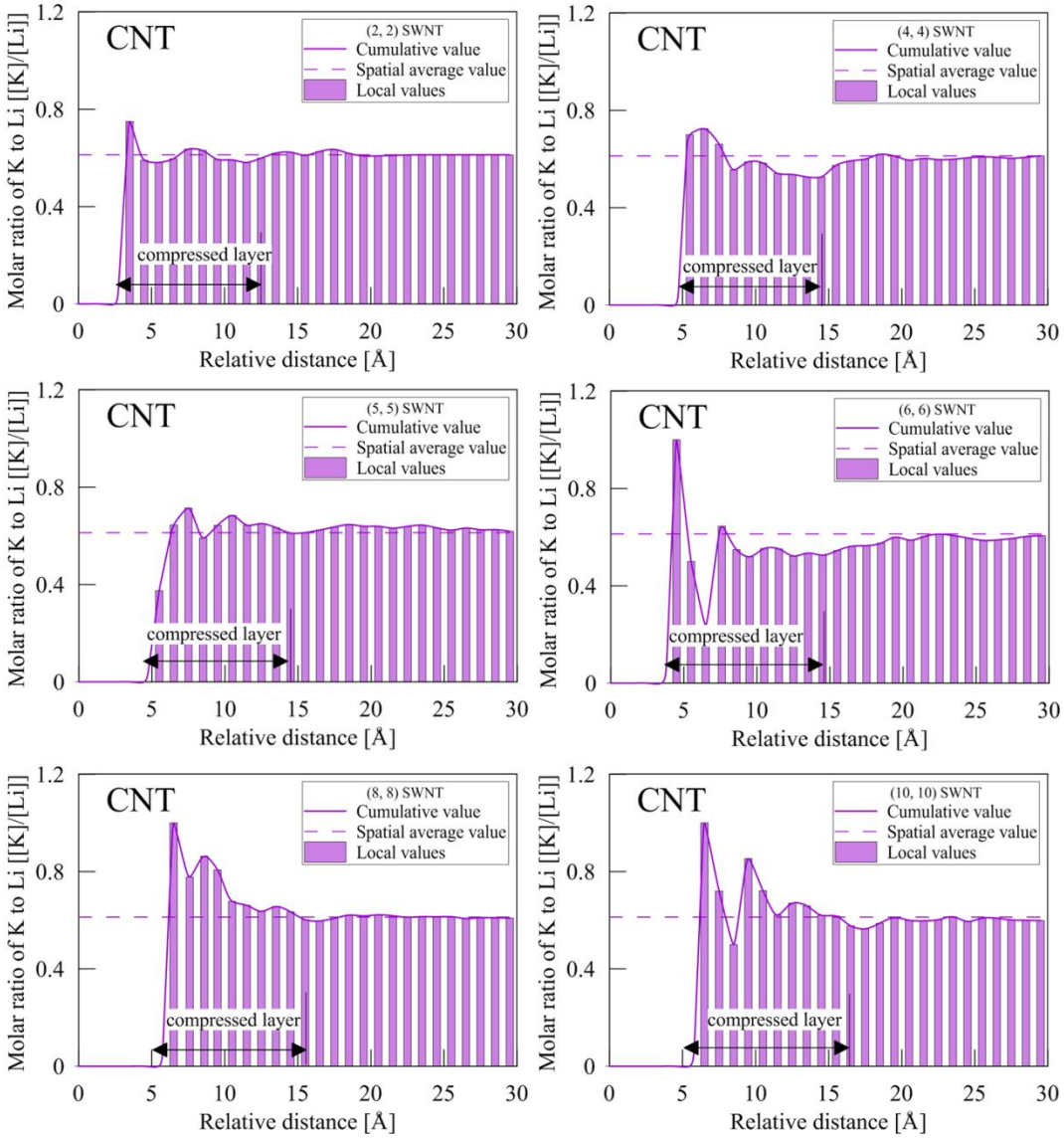

Fig. E. 8 Molar ratio of potassium to lithium along relative position: nanofluids with functionalized carbon nanotubes by amine (NH_2) groups

VITA

Name: Byeongnam Jo

Address: Texas A&M University
Department of Mechanical Engineering
3123 TAMU, College Station, TX 77843-3123

Email Address: jo7908@gmail.com

Education:

Ph. D., Mechanical Engineering,
Texas A&M University, College Station, August 2012

M.S., Mechanical Engineering,
University of Minnesota-Twin Cities, Minneapolis, May 2009

M.S., Mechanical Engineering,
Ajou University, Suwon, Rep. Korea, February 2007

B.S., Mechanical Engineering,
Ajou University, Suwon, Rep. Korea, February 2005

Publications

- **B. Jo** and D. Banerjee, *ASME 2011 International Mechanical Engineering Congress & Exposition*, IMECE2011-64001, November 11-17, Denver, Colorado, USA.
- **B. Jo**, S. Jung, D. Shin, and D. Banerjee, *ASME 2011 International Mechanical Engineering Congress & Exposition*, IMECE2011-64091, November 11-17, Denver, Colorado, USA.
- **B. Jo** and D. Banerjee, *ASME/JSME 8thThermal Engineering Joint Conference*, AJTEC2-11-44373, March 13-17, 2011, Honolulu, Hawaii, USA.
- S. Jeon, **B. Jo**, and D. Banerjee, *ASME/JSME 8thThermal Engineering Joint Conference*, AJTEC2-11-44373, March 13-17, 2011, Honolulu, Hawaii, USA.
- **B. Jo** and D. Banerjee, *34th International conference and Exposition on Advanced Ceramics and Composites*, ICACC-S10-001-2011, January 23-28, 2011, Daytona Beach, Florida, USA.
- S. Jung, **B. Jo**, D. Shin, and D. Banerjee, *SAE Power System Conference*, November 2-4, 2010, 2010-01-1731, Fort Worth, Texas, USA.
- D. Shin, **B. Jo**, H. Kwak, and D. Banerjee, *International Heat Transfer Conference*, IHTC14-23296, August 8-13, 2010, Washington D.C., USA.
- **B. Jo** and D. Banerjee, *ASME 2010 4th International Conference on Energy Sustainability*, ES2010-90299, May 17-22, 2010, Phoenix, Arizona, USA.